Loads Induced by Overtopping Bores on Vertical Walls
at the End of Sea Facing Promenades: A Laboratory Study

Maximilian Streicher

Promotor: prof. dr. ir. A. Kortenhaus
Proefschrift ingediend tot het behalen van de graad van
Doctor in de ingenieurswetenschappen: bouwkunde

UNIVERSITEIT
GENT

Vakgroep Civiele Techniek
Voorzitter: prof. dr. ir. P. Troch
Faculteit Ingenieurswetenschappen en Architectuur
Academiejaar 2018 - 2019

ISBN 978-94-6355-247-9
NUR 956
Wettelijk depot: D/2019/10.500/55

Examination board

Supervisor:

prof. Andreas Kortenhaus
Coastal Engineering Research Group
Department of Civil Engineering
Faculty of Engineering and Architecture
Ghent University
Technologiepark 60
B-9052 Ghent, Belgium

Voting members:

prof. Patrick De Baets	Ghent University, Belgium	chairman
prof. Peter Troch	Ghent University, Belgium	secretary
prof. Mia Loccufier	Ghent University, Belgium	
prof. Adam Bezuijen	Ghent University, Belgium	
prof. Bas Hofland	TU Delft, The Netherlands	
prof. Nils Goseberg	TU Braunschweig, Germany	
dr. Tomohiro Suzuki	Flanders Hydraulics Research, Belgium	

Internal defence (Ghent University): 28 May 2019
Public defence (Ghent University): 5 July 2019

A word of thanks

Travelling through the past four years of PhD has been a challenging and rewarding journey. It has carried me a long way and I want to thank the people who were part of it.

The journey started in the harbour. During the past four years that was clearly the core group of the coastal engineering research group: Thank you Ellen Vyncke for the skilled support in all practical and organisational matters; Lien De Backer for sharing exciting travel experiences and both for fighting with our budgets in the background. Thanks to the A-Team from the flume. Herman Van der Elst, for the technical master pieces and as a man of world welcoming us internationals so warmly. David Derynck, I don't know how many horse power there are in you but everything you construct in the flume was 'de max'. Sam Meurez, thank you for picking me up in Delft again and the quality work. If it is true that a genius needs chaos, than Tom Versluys is the perfect example. No measurement difficult enough to not have a friendly talk besides. Stylish thanks to Peter Devriese for bringing the COB to live and showing me how to wear gentleman gloves all year long. Vicky Stratigaki, thanks for the funny talks we had during the lunch breaks and the good citroen 2CV ride. Bedankt ook allemaal om mij Nederlands te leren.

Then there are the lighthouses, standing rock solid just at the entrance of the harbour and providing guidance based on their vision. Here, I would like to thank my promoter Andreas Kortenhaus first for accepting me as a PhD student. The freedom you gave me in conducting my research came with an increased responsibility to make things work. This let me grow professionally and as a person. I always had the feeling that you had my back and when I asked for a meeting they were to the point and constructive. I want to thank the head of our research group Peter Troch for providing a stable environment in which I could conduct research at my best. In one of our research meetings Peter Troch suggested me to apply for the international research project WALOWA. To fill the Delta Flume with sand made me sceptical at first but let to the best thing which could possibly have happened during this journey.

I left the harbour and soon got involved during the WALOWA project with researchers across Europe. Many fruitful meetings and discussions followed and I want to thank especially Corrado Altomare for the strong and friendly support during the experiments; Bas Hofland for bringing in his research experience and

insisting on the right measurement set-up; Tomohiro Suzuki for joining later in the analysis stage and providing quietly most powerful results; Lorenzo Cappietti for an enthusiastic scientific exchange; Alessandra Saponieri for accepting to be an essential part of WALOWA; Davide Pasquali who's support was fundamental; Mark Klein Breteler and his team from the Delta Flume, my friend Dorothea Kaste for the expert advise. Many more were involved who are acknowledged hereby greatly for the success of the WALOWA project!

With the acquired WALOWA data my journey was heading west where I was welcomed most generously by Steven Hughes and his wife Patty Hughes. The stay in Colorado widened my horizon in many aspects and I miss the view from the patio towards Longs Peak and the Rocky Mountains. It felt like backwind in the sails to discuss with one of the experts in the field and at the same time to do grocery shopping together. Living in the international house of Colorado State University brought me in touch with the most diverse people, who have enriched my life.

I would like to say thanks to the other sailors. Brecht Devolder, Tim Verbrugghe, David Gallach-Sánchez, you were already out on sea when I arrived and I could not have wished for a more capable trio in who's lee zone I could catch up and push through the four years of PhD. Brecht Devolder you are a machine and a good spirit to be around with. Tim, I was happy to leave you the chocolate. What you did with your keyboard and camera is amazing. David, thanks for your friendship and being the first of the international group to organize things and many delicious Spanish dinners. At the same height are sailing Gael Verao Fernandez and Philip Balitsky. Gael Verao Fernandez, the name Galicia for me is now connected with generosity, hospitality, compassion and many "Esmorgas", thanks for sharing them (and the good movies) with me. Philip Balitsky, the talks we had and your honesty to look for the truth are refreshing. We really kept 4 years of continuous cross country up in Belgium, that's where the island is! Just behind us are catching up with high speed Ine Vandebeek, thanks for making Limburg a spot on the map; Vincent Gruwez thanks for the good collaboration on the physical-numerical modelling edge, for correcting my Dutch summary and introducing me to Annick Heugens and Arthur; Panagiotis Vasarmidis and Myrsini Michalaki for many good moments at Bar Bricolage, excursions to Antwerp or Wallonie; Carlos Arboleda Chavez, thanks for making SABA safe again and together with Nina Dalla Bernardina for having such an open house for your friends; Minghao Wu, thanks for your curiosity in my research and preparing the best dish during OMAE conference. Timothy Vervaet and Nicolas Quartier, in the short time we had together it was a lot of fun to get to know you. You both seem crazy enough to take up this PhD journey - as long as there is enough food and drink provided off course.

Corinna Hohls, Sofie De Wilde, Jean-Baptiste Carpentier, Matthias Hirt and Krasimir Marinov it was a pleasure to work with you as master students. I want to thank you for your companionship on this journey and the contributions you have made to the completion of my PhD research. In this context I also want to thank the members of the examination board. The manuscript improved greatly after their careful revision and I am happy that you have accepted to be part of

the jury. I want to thank Nicolas Silin and his family for an unforgettable time in Argentina. Varjola Nelko for being a part of this journey. A word of thanks also for the bridges I have passed. Gilles van Staen for practising Portuguese together; Evy Van Puymbroek for being there the entire way together; the many international friends for sharing their experiences of living abroad. When I started this journey there were already one streamline cruiser and a big yacht in the same waters: Thank you Xuexue Chen and Koen Van Doorslaer for offering your expertise in this specific field of research, it was a pleasure to learn from your example. Finally, a special thanks to Hocine Oumeraci and Darshana Dassanayake, who were the vivid triggers to start working as a coastal engineer.

Heather Mary Sills, thanks for proofreading my manuscript, the Namur beer festival and introducing me to the Square Ghent community. Jakob Kuhs, kayaking the Leie, discussing PhD life and climbing have shaped a really good memory. Marco Rossi, thank you for your friendship and the best talks during our weekly swim sessions and the obligatory fries afterwards.

Mama, die kreativen Gedanken und Grafiken der Arbeit gehen auf deine Kappe, das Design des Boots. Danke dass du immer für mich da warst und für die Hilfe beim Buffet. Papa, danke für den offenen Austausch, du hast mir gezeigt dass es sich lohnt mutig auf Entdeckungsreise zu gehen. Kerstin und dir vielen Dank für die Hilfe beim Sektempfang. Dominik und Patrick, ohne euch wäre es unvorstellbar. Ich möchte der Familie Meures danken, die für mich immer ein lebhaftes Vorbild war. Meinem Opa, der mit 92 Jahren fast im Bus nach Ghent gekommen wäre, um bei der Verteidigung dabei zu sein. Danke an alle die nicht dabei sein können. Familie Peters für die guten Gedanken und den Wein. Familie Streicher für die vielen schönen Erinnerungen an gemeinsame Treffen. Fabian Holle, danke für deine Freundschaft und um mich immer wieder ins Wasser zu stoßen. Der ganzen Braunschweiger Crew und besonders Jonas Leimcke, Eike Leszczensky und Max Brück die mich noch immer überall besucht haben. Luciane Sopchenski Santos, obrigado por colocar as coisas em perspectiva, as deliciosas refeições enquanto eu estava escrevendo e o apoio do vento sul durante este tempo, beijos.

Maximilian Streicher
July 2019

Contents

1 Introduction **1**
- 1.1 Background and Motivation . . . 3
- 1.2 Main objective and methodology . . . 6

2 Fundamental processes and scientific state-of-the-art **9**
- 2.1 Bores in shallow water and mildly sloping foreshore conditions . . . 10
- 2.2 Bore interaction and bore impact processes . . . 12
- 2.3 Experimental studies on overtopped bore loading of vertical walls . . . 14
  - 2.3.1 Studies involving the overtopping discharge . . . 15
  - 2.3.2 Studies in shallow waters and mild foreshore conditions . . . 17
  - 2.3.3 Other related studies . . . 17
- 2.4 Review of existing prediction formulas for bore-induced impact forces 20
  - 2.4.1 Empirical prediction formulas . . . 20
  - 2.4.2 Statistical prediction formulas . . . 26
- 2.5 Scale- and model effects in laboratory experiments on bore impacts 30
- 2.6 Research gaps and specific objectives . . . 34
- 2.7 Thesis outline . . . 35

3 Experimental set-up **39**
- 3.1 Ghent University wave flume . . . 40
  - 3.1.1 Geometrical set-up . . . 41
  - 3.1.2 Hydraulic conditions . . . 44
  - 3.1.3 Test programme . . . 46
- 3.2 Deltares Delta Flume . . . 48
  - 3.2.1 Geometrical set-up . . . 49
  - 3.2.2 Hydraulic conditions . . . 51
  - 3.2.3 Test programme . . . 52
- 3.3 Measurement techniques . . . 53
  - 3.3.1 Water surface elevation measurement . . . 53
  - 3.3.2 Overtopping measurement . . . 55
  - 3.3.3 Flow thickness and velocity measurement . . . 57
  - 3.3.4 Impact load measurement . . . 59
  - 3.3.5 Synoptic measurement . . . 61
- 3.4 Data processing . . . 63

3.4.1 Unique test identifier (TestID) . . . 64
3.4.2 Wave parameters . . . 65
3.4.3 Average overtopping . . . 70
3.4.4 Flow thickness and velocity . . . 70
3.4.5 Impact force and pressure . . . 72

4 Analysis of scale effects in laboratory impact force measurement 79
4.1 Specific objectives . . . 79
4.2 Data analysis and methods . . . 80
4.2.1 Similarities of geometrical model set-up . . . 80
4.2.2 Similarities of hydraulic boundary condition . . . 82
4.3 Results and discussion . . . 84
4.3.1 Repeatability of laboratory impact force measurements . . . 85
4.3.2 Scale effects in laboratory impact force measurements . . . 88
4.4 Conclusions . . . 93

5 Analysis of bore interaction and bore-induced impact process 95
5.1 Specific objectives . . . 96
5.2 Data analysis and methods . . . 96
5.2.1 Bore interaction patterns . . . 98
5.2.2 Bore run-up at wall . . . 101
5.2.3 Bore impact type classification . . . 102
5.3 Results and discussion . . . 103
5.3.1 Impulsive impact type . . . 103
5.3.2 Dynamic impact type . . . 104
5.3.3 Quasi-static impact type . . . 106
5.3.4 Distribution of impact types . . . 107
5.3.5 Link between bore impact type and bore interaction pattern 108
5.3.6 Implications on force predictions . . . 109
5.4 Conclusions . . . 111

6 Analysis of empirical & theoretical impact force prediction 113
6.1 Specific objectives . . . 114
6.2 Data analysis and methods . . . 114
6.2.1 Horizontal bore properties on promenade . . . 114
6.2.2 Statistical error estimator . . . 115
6.3 Results and discussion . . . 117
6.3.1 Semi-empirical prediction of dynamic impact type . . . 117
6.3.2 Semi-empirical prediction of quasi-static impact type . . . 120
6.3.3 Theoretical prediction of impact signal shape . . . 122
6.4 Conclusions . . . 128

7 Analysis of statistical impact force prediction 131
7.1 Review of existing approaches . . . 132
7.2 Specific objectives . . . 134
7.3 Data analysis and methods . . . 134
7.3.1 Choice of statistical distribution function . . . 135

7.3.2 Generation of data-samples for statistical analysis 135
7.3.3 Sensitivity of sample size for statistical analysis 139
7.3.4 Sensitivity of the fitting threshold for statistical analysis . . 140
7.3.5 Statistical fitting of Weibull distribution to the samples . . 140
7.4 Results and discussion 144
7.4.1 Prediction method for maximum overtopped bore loads . . 144
7.4.2 Example calculation for prediction methodology 147
7.5 Conclusions 151

8 Summary of key findings and recommendations for future research 153
8.1 Summary of key findings 153
8.2 Recommendations for future research 156

A Model Geometry 'UGent2' - 'UGent3' 159

B Wall set-up 'DeltaFlume' 161

C Parameters for testID 492 and testID 500 163

D Sensitivity Sample Size S_1, S_2, S_3, S_5 166

E Impact-Analysis-Toolbox (IAT) - Load cell 169

F Impact-Analysis-Toolbox (IAT) - Pressure sensor 175

List of Figures

Figure 1.1 Measured mean high tide water level at level Cuxhaven in Germany (red line in the left figure). Sea level rise scenarios as predicted by the IPCC (2014) (right figure). 2
Figure 1.2 Windfield from 'Deutscher Wetterdienst' (DWD) for storm Christian (28.10.2013) and storm Xaver (06.12.2013). Xaver showed the highest measured storm surge water level at Pegel Norderney Riffgat since 1906. 2
Figure 1.3 Storm water level reaching the dike in Ostend, Belgium (right figure). Before the beach nourishments were carried out starting from 2007 (Van Doorslaer et al., 2017). Typical coastal set-up for the Belgian coastline (left figure). With the soft-structure mild foreshore, followed by the hard-structure dike, promenade and wall (photo by Nicolas Milot). 3
Figure 1.4 Flooding of the harbor in Norden (Germany) during a storm surge (left figure). Wave overtopping of the dike and impact at coastal structures on the barrier island Norderney (middle figure). Overtopping wave splash at the Belgian coast before the nourishment starting from 2007. 5
Figure 1.5 Storm walls on the barrier island Norderney during regular conditions (left figure) and during a storm surge with overtopping bore-induced loads on the wall elements (right figure). The storm fotos were taken 09.11.2007 (source: NLWKN). 6

Figure 2.1 Overview of geometrical and hydraulic parameters 9
Figure 2.2 Process overview of overtopping bores impacting a vertical wall on top of a promenade. I) wave breaking, II) wave overtopping and formation of overtopping bore, III) transformation of bore along promenade, IV) initial impact at the wall and upward deflection, V) wave catch-up and VI) sequential overtopping, VII) anticipated collision of incoming and reflected bore. 15
Figure 2.3 Thesis outline 37

Figure 3.1 Side-view (upper figure) and top-view (lower-figure) sketch of the geometrical model set-up 39

Figure 3.2 Ghent University wave flume facility with glass front along 15m flume width (left figure) and piston type wave paddle (right figure). 41
Figure 3.3 Geometrical set-up of 'UGent3' model test with distinct features: transition slope, foreshore, dike, promenade and wall. 43
Figure 3.4 Geometrical set-up for 'UGent1' model to measure impact load (upper), overtopping (middle) and incident waves (lower). . . 45
Figure 3.5 Split of wave flume in 'UGent2' model test starting from 10m offshore of the dike toe using a thin metal plate (left figure). Dike, promenade and wall were installed in the 0.7m left section of the split-up (right figure). 46
Figure 3.6 Deltares Delta Flume for prototype testing (left figure) and its 9m high blue piston type wave paddle (right figure). 48
Figure 3.7 Geometrical set-up of 'DeltaFlume' model tests with distinct features: wall, promenade, dike, foreshore and transition slope. . . 50
Figure 3.8 $\sim$1.000 m^3 of sand were installed and compacted in layers of 1 m (A). The foreshore evolution was monitored during the experiments with a mechanical bed profiler (B), measuring the total length in main flume axis of the foreshore. The sand was levelled up to 2cm accuracy before the start of the 'DeltaFlume' model tests. 51
Figure 3.9 a) An incoming wave broke on the shallow and sandy foreshore. b) Two bore crests at the start of the overtopping process over the dike crest and c) consecutive impact of the bores against the vertical wall. d) After the impact process the bores were reflected and travel shoreward again. 53
Figure 3.10 Resistive type wave gauges in the Ghent University flume. Offshore wave measurement in the flat bottom part (A) and wave measurement along the foreshore (B) until the incident wave measurement at the dike toe (C). 55
Figure 3.11 Water surface elevation measurement in the Delta Flume with resistive type wave gauges mounted on the flume wall. The foot of the wave gauges was partly covered in a protective box to prevent the finished foreshore layer to interfere with the measurement (A and B). The reference electrode to compensate for changes in water temperature and salinity during the sometimes 4h long experiment (C). 56
Figure 3.12 Overtopping measurement set-up for the 'UGent1'-'UGent3' data-sets. The overtopping water over the dike crest was guided via the overtopping tray in the overtopping box. The overtopped water was measured by a weigh cell installed below the overtopping box. 57

Figure 3.13 The flow thicknesses in the 'UGent1'-'UGent2' data-set was measured with resistive type wave gauges (WG), flash-mounted on the promenade. The flow velocities were derived with transit-time techniques. A frontal image of the wave gauges installed on the promenade (A) and a close up with distances between the wave gauges indicated (B). 58
Figure 3.14 The measurement of flow thickness and velocity on the promenade in the 'DeltaFlume' data-set. Ultrasonic distance sensors (UDS) and resistive type wave gauges (WLDM) were used to measure the flow thickness and electro-magnetic current meter (EMS) and paddle wheel (PW) to measure the flow velocities. 59
Figure 3.15 Impact force measurement with strain gauge load cells in the Ghent University flume. The strain gauge load cell was attached to a alluminium measurement plate flash mounted in the wall and supported towards the back of the flume with a rigid metal beam 60
Figure 3.16 Impact force measurement with compression load cells (left) and pressure measurement with piezo-electric pressure sensors (right) 61
Figure 3.17 The SICK LMS 511 laser profiler was mounted to the left flume wall (when standing with the back to the paddle) approximately at the dike toe location (A). A slant angle of 23 degree was used to prevent oversaturated return signal strength due to reflections in nadir (B). 62
Figure 3.18 Three GoPro 5 Black were deployed during the 'DeltaFlume' experiment. The views from the overview camera (A), the sideview camera (B) and the camera filming through the observation window in the wall (C) were provided. 63
Figure 3.19 Wave spectrum computed based on measured water surface elevation time-series, for testID 500 from 'DeltaFlume' data-set, at WG2 (close to paddle, offshore) and WG7 (close to dike toe). Locations for WG2 and WG7 are given in Table 3.4. 67
Figure 3.20 Relative water depth at the dike toe (x-axis) and flattening of the spectral wave period from offshore to the dike toe (y-axis) after Hofland et al. (2017). The prediction after Hofland et al. (2017) was given as the black line together with the 95% confidence interval as two times the standard deviation σ. 69
Figure 3.21 Non-dimensional overtopping vs. non-dimensional freeboard (left) and predicted/measured overtopping vs non-dimensional water depth showed that the measured values are within comparable (between data-sets) and predicted (Altomare et al., 2016) range . 71
Figure 3.22 Time-series of layer thickness gauges (WLDM1-WLDM4) with incoming η_i and reflected η_r flow thickness measured at location 1-4 (A). Time-series of paddle wheels (PW1-PW4) with incoming bore velocity u_i at location 1-4 (B). 72

Figure 3.23 Force time-series before (black) and after filtering (red). A zoom on the two highest impacts was provided in the lower figures.The signal from the lower load cell (0.18 m above the promenade) of testID 500 from the 'DeltaFlume' data-set was displayed. 73
Figure 3.24 Pressure sensor time-series before (black) and after filtering (red). A zoom on the two highest impacts was provided in the lower figures. The signal from pressure sensor P3 (0.16 m above the promenade) of testID 500 from the 'DeltaFlume' data-set was displayed. 74
Figure 3.25 A total horizontal force from the pressure sensor signals was obtained by applying rectangular pressure integration (Equation 3.2). The distances Δ_i and pressures P_i were used during the calculation. 76
Figure 3.26 Selected peak events for test testID 500 from the 'DeltaFlume' data-set for the integrated pressures (upper figure) and force measurement (lower figure). 77
Figure 3.27 Plotting positioning of the force peaks for all impacts from 'UGent1'-'UGent3' and 'DeltaFlume' model tests. 78

Figure 4.1 Dike, promenade and wall in large-scale (A) and small-scale (C) experiment. The impact forces were measured in the area highlighted in red, with two compression load cells in large-scale (B) and a strain gauge load cell in small-scale. 81
Figure 4.2 Beginning of water surface elevation time-series (left) and wave spectrum calculated for the entire time-series (right) for test testID 492. The measurements in the upper row were obtained at the location close to the paddle and in the lower row at the dike toe location. Small-scale (blue) and large-scale (red) measurements were compared in prototype. 83
Figure 4.3 Beginning of water surface elevation time-series (left) and wave spectrum calculated for the entire time-series (right) for test testID 500. The measruements in the upper row were obtained at the location close to the paddle and in the lower row at the dike toe location. Small-scale (blue) and large-scale (red) measurements were compared in prototype. 86
Figure 4.4 Force time-series of 14 repetition tests using the same seed wave time series (upper figure). The maximum force peak per repetition test was indicated with a red marker. A zoom on the impact event around t=2000 s, were most of the maximum force peaks occurred, was provided (lower left figure). Together with a boxplot of deviations from the mean impact force from all 14 repetition tests (lower right figure). 87
Figure 4.5 Beginning of time-series of impact forces for test testID 492 (upper figure), in red the large-scale and in blue the small-scale impact events. Impact force event distribution (lower left figure) and comparison of force indicators (lower right figure). 89

Figure 4.6 Beginning of time-series of impact forces for test testID 500 (upper figure), in red the large-scale and in blue the small-scale impact events. Impact force event distribution (lower left figure) and comparison of force indicators (lower right figure). 91

Figure 5.1 The time series of total impact force [kN/m] for testID 492 (upper graph) and testID 500 (lower graph) and the 30 largest impacts for each tests highlighted with a blue circle. 97
Figure 5.2 Regular bore pattern (A) observed before impact nr.1 from testID 500 and collision bore pattern (B) observed before impact nr.1 in testID 492 (see ANNEX C). Processing of the laser scanner signals was performed and described in Marinov (2017). 99
Figure 5.3 Sequential overtopping bore pattern (A) observed before impact nr.13 of testID 492 and catch-up bore pattern (B) observed for impact nr.2 of testID 492 (see ANNEX C). Processing of the laser scanner signals was performed and described in Marinov (2017). 100
Figure 5.4 Motion tracking method of the bore leading edge in consecutive video images. The video images where recorded by a top mounted (left) and side mounted (middle) GoPro camera with 59.94 frames per second and 0.002 m spatial resolution. The situation at T_i=0.8 s is shown in the two camera images and the resulting time series of instantaneous bore run-up at the wall after the motion tracking was performed for impact nr.7 of testID 492 (see ANNEX C) is displayed (right). 101
Figure 5.5 Bore-induced impact type classification methodology. . . . 103
Figure 5.6 Impact nr.20 of testID 492 (see ANNEX C) at the moment of impulsive impact (t=1.53 s). A sideview image of the situation (left), the non-dimensional impact force (middle) and non-dimensional impact pressures (right) are displayed. 104
Figure 5.7 Impact nr.29 of testID 492 (see ANNEX C) at the moment of dynamic impact (t=1.48 s). A sideview image of the situation (left), the non-dimensional impact force (middle) and non-dimensional impact pressures (right) are displayed. 105
Figure 5.8 Impact nr.7 of testID 492 (see ANNEX C) in different stages of impact. A) Initial impact stage, B) deflection stage and dynamic impact type, C) moment of maximum run-up, D) reflection stage and quasi-static impact and E) hydrostatic stage are displayed. A sideview image of the situation (left), the non-dimensional impact force (middle) and non-dimensional impact pressures (right) are given for each impact stage A-E. 106
Figure 5.9 Distribution of impact types for the 60 largest impacts of testID 492 and testID 500 (30 from each test). The percentage distribution (right graph) and the distribution in dependence of the non non-dimensional impact force (left graph) is shown. 108

Figure 5.10 Link between the five bore interaction patterns (1. Collision bore pattern of an incoming and reflected bore colliding, 2. Catch-up bore pattern with a second bore overtaking a first bore, 3. Regular bore pattern with no significant interactions observed, 4. Sequential overtopping bore pattern of an incoming bore sliding over a residual water layer from previous impacts 5. Plunging bore pattern with breaking of the incoming bore over a reflected bore against the wall) and the three impact types (1. Impulsive impact type, 2. Dynamic impact type and 3. Quasi-static impact type). . 109

Figure 6.1 Derived maximum bore thickness (A), maximum bore velocity (B) and the combined bore thickness η and velocity u (C) related to the 30 highest impacts in testID 492 and 500. All values were upscaled to prototype. 115

Figure 6.2 Empirical prediction formulas for the dynamic force peak F_1, from tsunami related studies and overtopping wave related studies (right). Results for the 30 highest impacts of testID 492 and testID 500 are given in prototype-scale units using Froude similarity and the length scale factor 1-to-4.3. 118

Figure 6.3 Empirical prediction formulas for the quasi-static force peak F_2. Results for 30 highest impacts of testID 492 and testID 500 are given in prototype using Froude similarity and the length scale factor 1-to-4.3. 121

Figure 6.4 Measured force and theoretical total horizontal force estimate for a quasi-static (1), impulsive (2) and dynamic (3) impact type from test Bi_2_6. The theoretical total horizontal force estimate was calculated based on hydrostatic theory (see Equation 6.6) and using the instantaneous run-up of the bore leading edge at the wall. 123

Figure 6.5 Numerical model set-up in OpenFOAM to reproduce the 'DeltaFlume' experiment and test Bi_2_6, using the hydraulic boundary conditions of the realized paddle motion in the 'DeltaFlume' model test (from Gruwez et al. (2019)). The mildly sloping foreshore, dike, promenade and wall were visible from the side-view image. 125

Figure 6.6 Time-series of total horizontal impact force on the wall from pressure integration for the 'DeltaFlume' data-set (black) and the numerical simulation in OpenFOAM (blue). The test Bi_2_6 (see Table 3.2) was chosen for this study. 126

Figure 6.7 A detailed view on the quasi-static (1), impulsive (2) and dynamic (3) impact from test Bi_2_6 (see Table 3.2), comparing the measured and numerically computed total horizontal impact force. 126

Figure 6.8 Time-series of measured force (black) and theoretical hydrostatic force estimate (blue) and theoretical force (red) for a quasi-static (1), impulsive (2) and dynamic (3) impact type. The hydrostatic horizontal force estimate was calculated based on hydrostatic theory (see Equation 6.6) and using the instantaneous run-up of the bore leading edge at the wall. The theoretical force estimated was calculated based on the vertical accelerations of the water mass in front of the wall (see Equation 6.10). 127

Figure 7.1 Relative promenade width G_c/L_t and relative water depth at the dike toe $h_t/H_{m0,o}$ for Chen et al. (2016); Van Doorslaer et al. (2017) plotted together with the measurements from data-set 'UGent1'-'UGent3' and 'DeltaFlume' (see Section 3). 132
Figure 7.2 The calculated maximum bore-induced impact force after Chen et al. (2016) compared to the measured maximum bore-induced impact force for the tests in data-set 'UGent1'-'UGent3' and 'DeltaFlume'. 133
Figure 7.3 The non-dimensional average overtopping discharge q^* plotted against the non-dimensional maximum impact force F^*_{max} for each test of the data-sets 'UGent1'-'UGent3' and 'DeltaFlume' (left figure). The same data points on a logarithmic scale (right figure) introducing the boundaries (vertical black lines) for sample S_1-S_5. The red circle indicates the average value per sample S_1-S_5. . . . 137
Figure 7.4 Sensitivity of shape κ and scale λ parameter in dependence of sample size n. Data sample S_4 was chosen for investigation (Table 7.1). The shape κ and scale λ parameter were plotted together with the 95% confidence interval. 139
Figure 7.5 Calculated κ and scale λ parameter for S_4 in dependence of the high-pass threshold. The coefficient of determination R^2 and standard deviation σ are calculated accordingly. 141
Figure 7.6 Plotting positioning of the impacts and best-fit line (left figure). Fitting of the linearised Weibull extreme value distribution to the upper 15% of impacts (red dots) and derived shape κ and scale λ parameter for sample S_1-S_5 (right figure). 142
Figure 7.7 Scale λ (left figure) and shape κ (right figure) parameter for sample S_1-S_5 were plotted over the non-dimensional average overtopping discharge q^*, together with the best-fit lines. 143
Figure 7.8 Prediction chart with combined empirical (F_{max}) and statistical (F_m with according P_m) result. 145
Figure 7.9 Six-step prediction methodology for overtopped bore-induced impacts on dike mounted walls. 147
Figure 7.10 Example calculation using the prediction chart (see Figure 7.8) and prediction methodology (see Figure 7.9). 149

List of Tables

Table 1.1 Qualitative comparison of tsunami/tidal/dam break flow bore and short duration overtopping bore characteristics resulting from irregular and broken waves. 4

Table 2.1 Classification of foreshore depth based on the ratio of water depth at the dike toe h_t and spectral wave height offshore $H_{m0,o}$ (Hofland et al., 2017). 11
Table 2.2 Experimental studies on overtopping bore-induced loading of vertical walls (values in model scale). 18
Table 2.5 Drag/resistance coefficients C_D, C_r to approximate the maximum tsunami impact force on buildings 23
Table 2.6 Empirical and semi-empirical approaches to calculate the impact force on a vertical wall caused by a bore like flow. 24
Table 2.7 Froude Scaling factors 31
Table 2.8 Uncertainties for bore-induced impact force measurements in laboratory scale models 34

Table 3.1 Investigated parameters for 'UGent1' - 'UGent3' model tests in their range (all values in model scale) 47
Table 3.2 Test programme 'DeltaFlume' bichromatic waves in chronological order (values in model scale using Froude similarity and a length scale factor λ=4.3) 52
Table 3.3 Test programme 'DeltaFlume' for irregular waves in chronological order (values in model scale using Froude similarity and a length scale factor $\lambda = 4.3$) 54
Table 3.4 Location of wave gauges in 'DeltaFlume' model set-up (X=0 at the paddle). 56
Table 3.5 Settings for the synoptic measurement devices in the 'DeltaFlume' model tests 64
Table 3.6 Overview of testIDs for data-set 'UGent1' - 'UGent3' and 'DeltaFlume' 65
Table 3.7 Settings for spectral wave analysis in WaveLab (all values in model scale) 66
Table 3.8 non-dimensional range of wave parameters for the data-sets 'UGent1'-'UGent3' and 'DeltaFlume' 68

Table 3.9 Filter settings for frequency filtering of impact force and pressure in Matlab® (all values in the according model scale) 75

Table 4.1 Comparison of wave flume and model characteristics between large-scale and Small-scale experiment. Values were up-scaled and compared in prototype 81
Table 4.2 Hydraulic boundary conditions test testID 492. The values were up-scaled and compared in prototype 84
Table 4.3 Hydraulic boundary conditions test testID 500. The values were up-scaled and compared in prototype 85
Table 4.4 Statistical parameters showing the differences in measured impact force due to the stochastic impact behaviour. A test with hydraulic boundary conditions comparable to a storm with a 1000 year annual return interval was repeated 14 times in the 'UGent3' model tests. 88
Table 4.5 Force indicators from large-scale and small-scale measurements compared in prototype for test testID 492 90
Table 4.6 Force indicators from large-scale and small-scale measurements compared in prototype for test testID 500 92

Table 5.1 Hydraulic conditions for testID 492 and testID 500 (all values in model scale). 97

Table 6.1 Dynamic impact type F_1 prediction formulas with goodness-of-fit parameters (prototype values). 119
Table 6.2 Quasi-static impact type F_2 prediction formulas with goodness-of-fit parameters (prototype values). 122

Table 7.1 Characteristics of sample S_1-S_5 based on the impacts from the data-sets 'UGent1'-'UGent3' and 'DeltaFlume'. The sample boundaries where determined based on damage criteria related to an average overtopping discharge q (Eurotop, 2016) 138
Table 7.2 Fitting parameters for sample S_1-S_5 144
Table 7.3 Input parameters for the example calculation. Values were given in prototype. 148

Nomenclature

Latin symbols I

A_c	dike crest freeboard	m
a	acceleration	m/s^2
B	flume width	m
C_v	coefficient of variation	m
D_{50}	particle size	m
d	model height	m
d_w	wall height	m
F	force	kN/m
F_{avg}	average force of all impacts	kN/m
F_{dyn}	dynamic impact force	kN/m
F_{hyd}	hydrostatic force	kN/m
F_{imp}	impulsive impact force	kN/m
F_{max}	maximum impact force	kN/m
F_{qs}	quasi-static impact force	kN/m
F_r	Froude number = u/g · L	$-$
$F_{1/250}$	average force from 1 in 250 impacts	kN/m
F_{10}	average force of 10 highest impacts	kN/m
F_{20}	average force of 20 highest impacts	kN/m
f_n	resonance frequency	Hz
G_c	promenade width	m
g	acceleration due to gravity = 9.81	m/s^2
H	wave height	m
H_s	significant wave height	m
H_{m0}	spectral wave height	m
h	water depth	m
h_t/H	relative water depth dike toe	$-$
L	characteristic length	m
L_0	deep water wave length	m
l	model length	m

Latin symbols (II)

m	mass	kg
n	transition slope angle	$-$
P	pressure	kPa
P_f	exceedance probability	$-$
P_{hyd}	hydrostatic pressure	kPa
q	average overtopping	l/sm
R_e	Reynold's number $= \rho \cdot \mathsf{u} \cdot \mathsf{L}/\eta$	$-$
$R_{u2\%}$	run-up at dike	m
R^2	coefficient of determination	$-$
S	sample	$-$
$S_{m-1,0}$	wave steepness $= \mathsf{H}_{m0} \cdot 2 \cdot \pi/\mathsf{g} \cdot \mathsf{T}_{m-1,0}$	$-$
$T_{m-1,0}$	spectral wave period	s
T_p	wave period	s
t	time	s
t_n	resonance period structure	s
t_r	impact rise time	s
u	flow velocity	m/s
W_e	Weber number $= \rho \cdot \mathsf{u}^2 \cdot/\sigma$	$-$
x	space coordinate in main flume direction	$-$
y	space coordinate in cross flume direction	$-$
z	vertical space coordinate	$-$

Greek symbols

α	dike slope angle	$-$
γ	reduction factor overtopping calculation	$-$
Δ	difference	$-$
δ	equivalent slope overtopping calculation	$-$
η	water surface elevation	m
	flow thickness	m
	dynamic viscosity	kg/ms
Θ	foreshore slope angle	$-$
λ	froude length scale factor	$-$
	weibull scale parameter	$-$
μ	mean value	$Unit$
ξ	surf-similarity-parameter $= \tan(\Theta)/\sqrt{H_{m0} \cdot 2 \cdot \pi/g \cdot T_{m-1,0}}$	$-$
π	pi-number $= 3.14159$	$-$
ρ	fresh water density $= 997$	kg/m^3
σ	standard deviation	$Unit$
	surface tension	N/m

Other symbols

$^\circ$	angle	degrees

Subscripts

c	dike crest
i	indice
o	offshore
t	dike toe
SS	Small-Scale
LS	Large-Scale

Abbreviations

BIV	Bubble Image Velocimetry
CI	Confidence Intervall
DWD	Deutscher Wetterdienst
GP	Generalized Pareto
IAT	Impact Analysis Toolbox
MAPE	Mean Averaged Percentage Error
MPS	Maximum Product of Spacing method
PoT	Peak-over-Threshold
RMSE	Root Mean Square Error
RSE	Relative Standard Error
SE	Standard Error
SWL	Still Water level
TAW	Tweede Algemeene Wateranpassing
WALOWA	WAve LOads on WAlls

Samenvatting

Belastingen door golfoverslag op verticale wanden geplaatst op een dijk met een ondiep en licht hellend voorland zijn een recente onderzoeksinteresse geworden. Typisch zijn deze verticale wanden een stormmuur die bovenop de dijk is gebouwd om overstroming van het achterland te vermijden of de muren van een gebouw aan het einde van promenade langs de zee. Deze locatie van de verticale wanden creëert een situatie waarbij de golf verschillende transformatieprocessen ondergaat voordat uiteindelijk de impactbelasting tegen de verticale wand wordt gegenereerd. Deze processen zijn breken in ondiepe wateren, aanloop en overslag over de dijk, een (lopende) hydraulische sprong of turbulente "bore" vorming, propagatie langs de promenade en uiteindelijk bore-geïnduceerde belasting van de verticale wand.

Echter, bestaande benaderingen om de belasting in te schatten werden vaak afgeleid voor een situatie met de verticale wand zonder een ondiep voorland, onder directe golfbelasting. Verder is de gemiddelde golfoverslag uitgebreid bestudeerd om de hoeveelheid water die over de structuur stroomt te beperken. De gemiddelde golfoverslag is echter ongeschikt als (rechtstreeks) invoergegeven voor de structurele stabiliteitsanalyse van een ontwerp tegen bore-geïnduceerde belastingen. Vandaar dat ontwerprichtlijnen, die rekening houden met de impactbelastingen voor de structurele stabiliteitsanalyse van dergelijke verticale wand, schaars zijn. De bore transformatieprocessen voorafgaand aan de impact hebben nog steeds een grondig onderzoek nodig om de belastingen op een meest fysisch zinvolle manier te voorspellen. Parallelle metingen van golfparameters aan de teen van de dijk, gemiddelde golfoverslag, de golfoverslagstroomdikte en -snelheid langs de promenade en de uiteindelijke belastingen op de muur zijn beperkt en de link tussen deze processen moet verder worden onderzocht. Bovendien vereist het door de bore-geïnduceerde belastingproces zelf nader onderzocht te worden om het sterk stochastische gedrag ervan beter te verklaren en er rekening mee te houden.

Daarom was het doel van dit onderzoek de voorbereiding van experimentele proeven voor een bepaalde modelgeometrie met een licht hellend en ondiep voorland, dijk, promenade en muur. De geometrische en hydraulische opstelling leek het meest op een doorsnede langs de Belgische kust. De parameters voorlandshelling cot(θ), dijkhelling cot(α), dijkhoogte d, waterdiepte offshore en aan de dijkteen, evenals de promenadebreedte en hun effect op de gemeten belastingen werden onderzocht. De resulterende golfbreking werd bestudeerd met behulp van de spectrale golfparameters offshore en aan de dijkteen. De gemiddelde golfoverslag q werd gemeten over de dijkkruin en de stromingsvorming en -transformatie

bestudeerd in termen van golfoverslagdikte en snelheid op de promenade. Ten slotte werden de belastingen aan de muur gemeten in termen van kracht en druk. Voor de nabewerking van de druk- en krachtsignalen is een "Impact-Analysis-Toolbox" (IAT) gemaakt in een Matlab-omgeving, met een drie-staps nabewerkingsprocedure. Eerst werden de druk- en krachtsignalen gefilterd in het frequentiedomein, waarbij laagdoorlaat-, hoogdoorlaat- en bandfilters ongewenste ruis verwijderden en een trendlijncorrectie werd toegepast om drift uit de signalen te verwijderen. In een tweede stap werd een totale horizontale kracht per meter breedte berekend door de individuele druksignalen over de hoogte te integreren of de som van de kracht signalen te nemen die op dezelfde meetplaat waren bevestigd. In een derde stap werd een piekdetectiemethode ontwikkeld om de maximale kracht te onderscheiden voor elke afzonderlijke impactgebeurtenis. In totaal werden vier modelproeven uitgevoerd, waarbij 3 kleinschalige (Froude verschaling met een lengteschaal van 1-to-25) en één grootschalige (Froude verschaling met een lengteschaal van 1-to-4.3) modelopbouw. De modellen werden respectievelijk 'UGent1' - 'UGent3' en 'DeltaFlume' genoemd. De gegevens van deze modellen werden verder gebruikt om de bore interactieprocessen voorafgaand aan de impact te bestuderen en om drie verschillende impacttypen te onderscheiden ('Impulsief', 'Dynamisch', 'Quasi-statisch'). Het doel was ook om het voorspellend vermogen van de bestaande semi-empirische formules voor de totale horizontale impactkracht (deels uit Tsunami-gerelateerd onderzoek) verder uit te werken en daarbij een analytische benadering te ontwikkelen om de totale horizontale impactkrachtsignaalvorm van individuele impactgebeurtenissen te beschrijven. Ten slotte leidden de gecombineerde resultaten van de processtudie en beoordeling van bestaande semi-empirische voorspellingsformules tot de ontwikkeling van een statistisch voorspellingsinstrument dat rekening houdt met het stochastische gedrag bij bore-geïnduceerde belastingmetingen. Een onderzoek naar de verwachte onzekerheden die voortkomen uit niet-herhaalbaarheidsproblemen, schaal- en modeleffecten bij metingen van de belasting in het laboratorium, ronden dit onderzoek af.

De complexe interactie van korte duur bores als gevolg van onregelmatig gebroken golven in extreem ondiepe wateren werden bestudeerd met behulp van hoge ruimtelijke resolutie wateroppervlak metingen van een laser profiler, geïnstalleerd 5 m boven de dijkteen. Dit resulteerde in een Field-of-View (FoV) van ongeveer 21 m in de richting van de gootlengteas. Twee hydrodynamische condities met onregelmatige offshore golfparameters vergelijkbaar met stormen met een terugkeerperiode van 1,000 en 17,000 jaar voor de Belgische kust werden gebruikt voor deze studie (Veale et al., 2012; Verwaest et al., 2009). De twee proeven werden uitgevoerd in het grootschalige 'DeltaFlume'-experiment en bestonden elk uit ongeveer 1,000 golven. In totaal was de studie gericht op 30 bores die de 30 grootste belastingen in de twee proeven veroorzaakten, resulterend in 60 onderzochte gebeurtenissen. Vijf bore interactiepatronen werden geïdentificeerd: (1) gewone bore-patroon (EN: regular bore pattern), met een enkele bore overloop en geen zichtbare interactie met eerdere gereflecteerde bores; (2) botsende bore-patroon (EN: collision bore pattern), met botsing van inkomende en gereflecteerde bores. De reflectie vond plaats op de dijk of aan de muur op de promenade; (3) overslaande bore-patroon (EN: plunging bore pattern), waarbij de bore in de buurt van de muur

overslaand breekt, met insluiting van een luchtkussen; (4) opeenvolgende bore-patroon (EN: sequential overtopping bore pattern), waarbij de inkomende bore over een resterende waterlaag bovenop de promenade schuift, met een verminderde wrijving en dus hogere impactsnelheden; (5) inhalende bore-patroon (EN: Catch-up bore pattern), met een snellere tweede bore die een langzamere eerste bore inhaalt en een cumulatieve inslag op de wand genereert. Verder werd het opeenvolgend overslagmechanisme (EN: sequential overtopping mechanism) geïdentificeerd als een belangrijk proces. Wanneer een eerder gebroken golf op de dijk resulteerde in een lokaal verhoogd waterniveau, kon de volgende inkomende bore soepel over de dijk slaan zonder tegen de dijk te breken. Voor dit mechanisme werd verwacht dat dit resulteerde in hogere energetische belastingen. De overgeslagen stroming laagdikte en snelheden bovenop de promenade werden gemeten met behulp van respectievelijk resistieve golfhoogtemeters en schoepenwielen. Deze metingen werden telkens grotendeels vertroebeld door één van de eerder beschreven bore interactiepatronen en er kon geen duidelijke relatie gevonden worden, bijvoorbeeld met de totale horizontale kracht op de muur.

Het belastingproces werd bestudeerd met behulp van het totale horizontale krachtsignaal en de verdeling van de drukken langsheen de muurhoogte, samen met de berekende hydrostatische kracht op basis van de oploophoogte van de bore aan de muur. De oploophoogte van de bore werd verkregen met behulp van videobeelden van voor- en zijaanzichtcamera's aan de wand. Voor elk inslag van een bore tegen de muur werd een dubbele piekvorm waargenomen voor het horizontale krachtsignaal, met vergelijkbare grootte voor de twee pieken. De eerste piek vond plaats bij de eerste inslag van de bore tegen de muur. De stroming werd verder naar boven afgebogen tot het moment van maximale oploop waarbij een daling van het totale inslagkrachtsignaal werd waargenomen. De tweede piek vond plaats na maximale oploop, waarbij de watermassa naar beneden viel en weer naar buiten werd gereflecteerd. Er werd een classificatiemethode ontwikkeld op basis van de verhouding tussen de eerste F_1 en de tweede F_2 krachtspiek en de snelheid van stijging in het krachtsignaal of stijgtijd t_r. Drie belastingstypen werden onderscheiden: (1) impulsieve impact type (EN: impulsive impact type), met een dominante eerste piek ($F_1/F_2 > 1{,}2$) en een stijgtijd kleiner dan 10^{-2} s; (2) Dynamische impact type (EN: dynamic impact type), met een dominante eerste piek ($F_1/F_2 > 1{,}2$) en een stijgtijd groter dan 10^{-2} s; (3) quasi-statische impact type (EN: quasi-static impact type), met een dominante tweede piek ($F_1/F_2 < 1{,}2$). De meeste impacten en de impact met de grootste kracht bestonden uit quasi-statische impact types. Op basis van deze resultaten werd voorgesteld een maximale krachtschatting af te leiden voor de structurele ontwerprichtlijnen voor de quasi-statische impact types. Er werd verwacht dat de opgeschaalde quasi-statische impact types minder werden beïnvloed door schaaleffecten vanwege het bijna hydrostatische gedrag van het water voor de muur op het ogenblik van de tweede piek F_2. Dit was echter alleen strikt mogelijk indien er geen dynamische effecten (voor de eerste dynamische impact F_1) vanwege de resonantieperiode van de structuur tn die binnen het bereik van de snelheid van de stijging t_r lag, in aanmerking moesten genomen worden voor de structurele analyse. Een koppeling tussen de vijf geïdentificeerde bore-patronen en de drie geïdentificeerde impacttypen werd besproken en alleen het overslaande

bore-patroon bleek in ieder geval tot dynamische/impulsieve impact types te leiden. Het botsende bore patroon was het meest voorkomend (46% van alle interacties werd geïdentificeerd als botsende bore patroon) en resulteerde in het merendeel van de gevallen in quasi-statische impact types. Een zeer praktische conclusie was dat de maximaal gemeten horizontale kracht voor een extreem ondiep en licht hellend voorland, samen met golfomstandigheden vergelijkbaar met een storm met een terugkeerperiode van 1,000 jaar aan de Belgische kust, F_{max}=19 kN/m (prototype waarde) bedraagt. Deze gebeurtenis werd voorafgegaan door een gewoon bore patroon zonder efficiënt overslag mechanisme. De gebeurtenis werd geclassificeerd als een quasi-statisch impact type met een gemeten (prototype) stroomlaagdikte η_{max}=0.56 m, maximale stroomsnelheid u_{max}=4.67 m/s en maximale oploop aan de wand R_{max}=2.49 m.

Vervolgens werden dezelfde 60 impactgebeurtenissen en bijbehorende stroomlaagdikten, snelheden en oploop gebruikt om bestaande semi-empirische voorspellingsformules voor de totale horizontale impactkracht toe te passen. Op basis daarvan, werd de voorspellende capaciteit van de bestaande formules beoordeeld. De formules werden onderscheiden of ze eerder de dynamische eerste impact van de bore tegen de muur beschrijven (gerelateerd aan inkomende momentumflux, laagdikten en snelheden) of de bijna hydrostatische situatie na maximale oploop van de watermassa (gerelateerd aan de oploop aan de muur of de laagdikte dichtbij de muur). Slechts een beperkt aantal voorspellingsformules voor individuele bore belastingen op muren, als gevolg van gebroken golven in ondiepe wateren, waren beschikbaar en de studie werd uitgebreid met formules voor voorspelling van Tsunami belastingen. Het belangrijkste verschil is dat Tsunami belastingen van langere duur zijn en vaak als stroming rond de structuur worden beschouwd, aangezien de breedte van de bore kruin tot de breedte van het gebouw erg groot is. De dynamische eerste piek F_1 werd het best beschreven met vergelijking 2.11 (Robertson et al., 2011) (met een standaard afwijking van 8.6 kN/m in prototype en MAPE = 0.9614). De eenvoudige momentumflux theorie (zie vergelijking 6.5) aangepast aan de gegevens toonde een vergelijkbare voorspellingsnauwkeurigheid. De bijna hydrostatische tweede piek F_2 werd het best beschreven met de hydrostatische krachtschatting gepast aan de gegevens (standaard afwijking=3.23kN/m in prototype en MAPE=0.9993) en met gebruik van de maximale oploop van water aan de wand (zie vergelijking 6.8). Bij de passing werd een coëfficiënt C_1=0.32 verkregen, zeer dicht bij de coëfficiënt van C_1=0.33 (gevonden door Chen et al. (2012) in kleinschalige experimenten voor regelmatige golven). Dit leverde de praktische conclusie dat slechts ∼80% van de maximale oploop effectief de kracht op de muur veroorzaakte. Het gevolg voor de berekening van het kantelmoment was, dat de hefboomarm met ∼20% kan worden verminderd voor het ontwerp van deze structuren. Deze waarneming werd verklaard door het lichtere waterlichaam voor de muur als gevolg van opwaartse versnelling, opspattend water en een kleine of losgeraakte oplooptong in het bovenste deel van het water aan de muur. Verder werd een theoretisch model voorgesteld, gebaseerd op de verticale versnelling van de watermassa vóór de muur, om het volledige tijdsverloop van het horizontale krachtsignaal te voorspellen. Omdat het model alleen rekening houdt met de verticale versnelling, en niet met de horizontale versnellingen, werd voornamelijk het

eerste deel van het krachtsignaal niet goed voorspeld. Desalniettemin reduceert het model, nadat de inkomende stroming in verticale richting is gebracht, de overschatting aanzienlijk, als gevolg van de schatting met de hydrostatische kracht. De verticale versnellingen voor de muur werden numeriek afgeleid uit een gevalideerd OpenFOAM-model, dat werd gebruikt om een test uit de 'DeltaFlume' dataset te modelleren.

Voor beiden, de best passende voorspellingsformules voor de dynamische eerste F_1 en quasi-statische tweede piek F_2, was de voorspellingsnauwkeurigheid laag. Er werd geargumenteerd dat bore interactieprocessen voorafgaand aan de impact, niet-uniformiteit van het bore front (3D-effecten), meesleuren van lucht in de bore en zelfs kleine fluctuaties en turbulentie in de bore verschillende bore impactprocessen veroorzaakten, resulterend in het stochastische gedrag van de gemeten totale horizontale kracht. Daarom werd een statistische methode onderzocht om de totale horizontale kracht te voorspellen. Voor dit doel werden de impacten van de datasets 'UGent1'-'UGent3' en 'DeltaFlume' gecombineerd in één grote dataset. Het toepassingsbereik van de dataset 'UGent1'-'UGent3', 'DeltaFlume' lag in het bereik van een eerder afgeleide dataset (Chen et al., 2016), met een uitbreiding naar grotere relatieve promenade-breedten G_c/L_t en extreem ondiep water $h_t/H_{m0,o}$ <0.3 (volgens Hofland et al. (2017)). Met dit groot aantal gegevens werden problemen als gevolg van te weinig gegevenspunten voor een robuuste statistische analyse overwonnen. De onderverdeling in monsters werd gedaan op basis van een nieuw empirisch verband tussen de dimensieloze maximale impact F^*_{max} en de dimensieloze gemiddelde golfoverslag q^*. De grenzen van deze steekproef werden vastgesteld op basis van voorgestelde waarden in Eurotop (2016). Vijf datamonsters S_1-S_5 werden onderscheiden en een gevoeligheidsanalyse naar de steekproefomvang toonde aan dat ongeveer 50 krachtpieken nodig waren voor een robuuste passing van de statistische verdeling aan de krachtpieken. Verder werd een gevoeligheidsanalyse van de passingsdrempel uitgevoerd en werd een waarde van 15% geselecteerd. Alleen krachtpieken boven deze drempelwaarde werden gebruikt om de gelineariseerde Weibull-verdeling aan elk monster te passen en de bijhorende vorm- en schaalparameter werden afgeleid. De vorm- en schaalparameter wordt opgedragen over de dimensieloze gemiddelde golfoverslag q^* voor de vijf steekproeven. De best passende lijn voor vorm- en schaalparameter werd berekend en vertoonde een zeer stabiel gedrag (R^2=0.9873 voor vorm- en R^2=0.925 voor schaalparameter). Ten slotte werd een zes-stappen voorspellingsmethodologie ontwikkeld, die de empirische en statistische methodes combineert: een maximale verwachte impactkracht F_{max} werd empirisch bepaald samen met zijn statistische overschrijdingskans P_m. De overschrijdingskans P_m kan worden geïnterpreteerd als de kans dat F_{max} wordt overschreden gedurende een storm met 13,000 offshore golven en hydraulische randvoorwaarden (h_t, $H_{m0,t}$, $T_{m-1,0,t}$, q) gespecifieerd samen met de geometrische informatie (A_c, G_c) in de invoerparameters .

Ten slotte werden de niet-herhaalbaarheidsproblemen, model- en schaaleffecten voor laboratoriumbelastingmetingen onderzocht, die werden opgewekt door de impact van bores op dijk-gemonteerde muren. Dit werd gedaan om de nauwkeurigheid van de voorspelling van de impactkracht, verkregen uit laboratoriumexperimenten, beter te beoordelen. Eerst werd een basisonzekerheid vastgesteld door eenvoudig-

weg dezelfde tijdreeks van golven 14 keer te reproduceren en de impactkrachten aan de muur te meten. Deze zogenaamde niet-herhaalbaarheid van impactkrachten werd gekwantificeerd met behulp van de variatiecoëfficiënt en lag in de orde van 10% (in extreme gevallen tot 20%) voor F_{max}, $F_{1/250}$. De schaaleffecten werden onderzocht door de proeven te vergelijken van laboratoriumtesten op verschillende schaal met een Froude-lengteschaalverhouding van 1-to-5.81. Een vergelijkbare geometrie en dezelfde tijdreeks van golven werd in beide experimenten gebruikt. Er werd geconcludeerd dat wanneer de minimale waterdiepte aan de dijkteen, evenals de dikte en snelheid van de golfoverslagstroming werden behouden, de schaalgerelateerde fouten in de impactkrachtmeting verdwijnen binnen de onzekerheden met betrekking tot niet-herhaalbaarheid en modeleffecten. Deze bevinding leek in tegenspraak met de algemene veronderstelling dat krachtmetingen in het kleinschalige model significant hoger zijn dan prototypemetingen. Deze tegenstrijdigheid werd voornamelijk verklaard door de kenmerken van de turbulente, beluchte en gebroken bore-inslagen, resulterend in een samendrukbaar en minder gewelddadig impactproces voor de dynamische eerste piek F_1 (merk op dat dit impactgedrag heel anders was in vergelijking met gewelddadige brekende golfimpacten op zeeweringen die in de breekzone waren gebouwd). Eerder werd beschreven dat een meerderheid en de grootste impacts bestonden uit quasi-statische impact types, de tweede piek F_2 in het dubble piek kracht signal, veroorzaakt door een bijna hydrostatische waterlaag vlak voor de muur, kort na de maximale oploop. Voor de quasi-statische impact types werden daarom geen schaalgerelateerde effecten verwacht. Er werd echter een kleine systematische schaalgerelateerde verschuiving naar hogere impactkrachten waargenomen van grootteorde van respectievelijk 4%, 9%, 8%, 13%, 16% voor F_{max}, $F_{1/250}$, F_{10}, F_{20}, F_{30}, in het kleine schaalmodel. Bovendien was het aantal impacten lager in het kleinschalige model (424) in vergelijking met het grootschalige model (549). Verschillen gerelateerd aan modeleffecten werden meestal waargenomen in de golfgeneratie en absorptie in het kleinschalige model en veranderende zand bathymetrie in het grootschalige model. Dit resulteerde gemiddeld in een verschil van 10% in spectrale golfparameters op de locatie van de dijkteen tussen de twee schaalmodellen.

Het wordt verder aanbevolen om de studies van bore transformatieparameters op de promenade te bevorderen, zoals de helling van het bore-front in de buurt van de muur. Dit zou het inzicht vergroten, vooral van de impulsieve en dynamische impact types. Gevalideerde numerieke modellering kan een optie zijn om deze vorm te bestuderen. De vorming van het stromingsveld in termen van bore-dikte en -snelheid op de promenade en de transformatie van het stromingsveld langs de promenade moet verder worden onderzocht om hun verandering langs de promenade te bestuderen.

Voor de voorgestelde combinatie van empirische en statistische impactkrachtvoorspellingsmethodologie wordt een voorbeeldberekening uitgevoerd met behulp van de invoerparameters van een andere laboratoriumschaalmodeltest (Chen et al., 2016). Dit diende als een eerste aanwijzing dat de gepresenteerde voorspellingsmethodiek niet buiten bereik was. Ondanks deze eerste bevestiging is verdere validatie van de voorspellingsmethode vereist, idealiter met prototypemetingen.

Voor toekomstige studies over schaaleffecten in verband met bore belasting

op muren op een dijk met een zeer ondiep voorland, werd het aanbevolen om de golfgeneratie en golfabsorptie in het kleinschalige model aan te passen om de kenmerken van de lange golven beter te reproduceren. Bovendien zouden metingen van de luchtbellen in beide schalen, op een locatie dicht bij de wand waar de kracht optreedt, nuttig zijn om de ongelijkheden van de meegevoerde lucht tussen verschillende schaalmodellen te beoordelen. Het gebruik van druksensoren in beide schaalmodellen wordt aanbevolen om de invloed van de schaal op de piekdruk te bestuderen. Bovendien kunnen extra middelgrote schaalmodellen of prototype metingen gebruikt worden om te beoordelen of de bore inslagen lineair verschalen en om het relatieve schaalverschil te vergroten.

Summary

Overtopping bore-induced loads on dike mounted vertical walls in shallow water and mildly sloping foreshore conditions have recently become an important research topic. Typically, these vertical walls are either a storm wall constructed on top of the dike to prevent flooding of the hinterland or residential building walls constructed at the end of sea-facing promenades. The onshore location of the vertical walls creates a situation where the bore undergoes several processes before finally generating the impact load against the vertical wall. These processes include breaking in shallow waters, run-up and overtopping over the dike crest, bore formation and transformation along the promenade and final bore-induced loading of the vertical wall.

However, approaches to estimate the impact load were often derived for a situation with the vertical wall offshore of the coastline, under direct wave loading. Furthermore, the average overtopping discharge has been extensively studied to design for a limited amount of water flowing over the structure. The average overtopping discharge is unsuitable as input for any structural stability analysis to design against bore-induced loads and design guidance for a vertical wall onshore taking into account the impact loads for structural stability analysis is scarce. The bore transformation processes prior to impact still need thorough investigation to predict the impact loads in a most meaningful way. Parallel measurements of wave parameters at the dike toe, average overtopping discharge, flow thickness and velocity along the promenade and final impact loads at the wall are limited and the link between these processes needs to be further investigated. Additionally, the bore-induced loading process itself requires further investigation, to better explain and account for its highly stochastic behaviour.

Therefore, it was the objective of this research study to prepare laboratory model testing for a particular model geometry with mildly sloping foreshore, shallow waters, dike, promenade and wall. The geometrical and hydraulic set-up was most similar to a cross-section along the Belgian coast. The parameters foreshore slope cot(θ), dike slope cot(α), dike height d, water depth offshore h_o and at the dike toe h_t, as well as the promenade width G_c and their effect on the measured impact loads was investigated. The resulting wave breaking was studied using the spectral wave parameters offshore and at the dike toe. The average overtopping discharge q was measured over the dike crest and the flow formation and transformation studied in terms of overtopping flow thickness and velocity on the promenade. Finally, the impact loads at the wall were measured in terms of impact force F and

pressure p. For the post-processing of the pressure and force signals an Impact-Analysis-Toolbox (IAT) was created in a Matlab environment, involving a 3-step post-processing procedure. First, the pressure and force signals were filtered in frequency domain introducing low-pass, high-pass, bandwidth filters and a trend-line correction to remove drift from the signals. In a second step a total horizontal force per meter width value was obtained by integrating the individual pressure signals over the height or taking the sum of load cell signals attached to the same measurement plate. Finally, a peak detection method was developed to distinguish the maximum force for each individual impact event. In total 4 laboratory model tests were conducted, involving 3 small-scale (Froude similarity and length-scale factor 1-to-25) and one large-scale (Froude similarity and length-scale factor 1-to-4.3) model set-up. The models were termed 'UGent1'-'UGent3' and 'DeltaFlume' respectively. The data from these models was further used to study the bore interaction processes prior to impact and to distinguish 3 different impact types (Impulsive, Dynamic and Quasi-Static). Furthermore, we aimed to elaborate on the predictive capability of existing semi-empirical formulas (partly from Tsunami related research) to predict the total horizontal impact force and to derive an analytical approach to describe the total horizontal impact force signal shape of individual impact events. Finally, the combined evidence from the process study and review of existing semi-empirical prediction formulas led to the development of a statistical prediction tool accounting for the stochastic behaviour in overtopping bore-induced impact load measurements. A study of the expected uncertainties arising from non-repeatability issues, scale- and model effects in laboratory impact load measurements rounded off this study.

The complex interaction of short-duration bores resulting from irregular broken waves in extremely shallow waters was studied using high spatial resolution water surface measurements from a laser profiler installed 5 m above the dike toe location. This resulted in a Field-of-View (FoV) of approximately 21 m in flume length direction. Two tests with irregular offshore wave parameters similar to a storm with an annual recurrence interval of 1,000 and 17,000 years for the Belgian coast were used for this study (Veale et al., 2012; Verwaest et al., 2009). The two tests were conducted in the large-scale 'DeltaFlume' experiment and were comprised of approximately 1,000 waves each. In total the study was focused on 30 bores causing the 30 highest impacts in the two tests, resulting in 60 investigated events. Five bore interaction patterns were identified: (1) regular bore pattern, with a single bore overtopping and no visible interaction with previous reflected bores; (2) collision bore pattern, with collision of incoming and reflected bore. The reflection either occurred at the dike or the wall on top of the promenade; (3) plunging breaking bore pattern, with the bore breaking in the vicinity of the wall, under inclusion of an air pocket; (4) sequential overtopping bore pattern, with the incoming bore sliding on a residual water layer on top of the promenade and subsequent reduced friction and higher impact velocities; (5) catch-up bore pattern, with a faster second bore overtaking a slower first bore and generating a cumulative impact at the wall. Furthermore, a sequential overtopping mechanism was identified as an important process. When a previously broken wave at the dike resulted in a locally high water level the subsequent incoming bore could smoothly

overtop the dike without breaking against the dike. The sequential overtopping mechanism was expected to result in higher energetic impact loads. Overtopping flow thickness and velocities on top of the promenade were measured using resistive type wave gauges and paddle wheels respectively. These results were largely overshadowed by any of the previously described bore interaction patterns and no clear relation, for example to the total horizontal impact force, could be found.

The impact process was studied using the total horizontal impact force signal and the distribution of pressures along the wall height together with the computed hydrostatic force estimate based on the run-up of the bore at the wall. The run-up of the bore was obtained using motion tracking methods from front- and side-view camera images of the bore leading edge at the wall. For the bore impacts, a double peak total horizontal impact force signal shape was observed, with similar magnitudes for the two peaks. The first peak occurred on first impact of the bore with the wall. The flow was further deflected upwards until the moment of maximum run-up and a drop in the total impact force signal was observed. The second peak occurred after maximum run-up, with the water mass falling down and being reflected outwards again. A classification methodology was developed based on the ratio between the first F_1 and second F_2 peak and the impact rise time tr. Three bore impact types were distinguished: (1) Impulsive impact type, with a dominant first peak (F_1/F_2 >1.2) and a rise time smaller than 10^{-2} s; (2) Dynamic impact type, with a dominant first peak (F_1/F_2 >1.2) and a rise time larger than 10^{-2} s; (3) Quasi-static impact type, with a dominant second peak (F_1/F_2 <1.2). The majority of events and the largest impact force were comprised of Quasi-static impact types. Based on these findings it was suggested to derive a maximum force estimate for structural design guidance for the Quasi-static impact types. It was expected that the up-scaled Quasi-static impact types were less affected by scale effects due to the almost hydrostatic behaviour of the water in front of the wall at the moment of the second peak F_2. This was however strictly only possible if no dynamic effects (for the first dynamic impact), due to the resonance period of the structure t_n being in the range of the impact rise time t_r, needed to be considered for structural analysis. A link between the five identified bore patterns and the three identified impact types was discussed and only plunging bore breaking led to dynamic/impulsive impact types in any case. Collision bore pattern was the most frequent (46% of all interactions were identified as collision bore pattern) and resulted in Quasi-static impact types in the majority of the cases. A very practical conclusion was that the maximum measured horizontal impact force for extremely shallow water and mildly sloping foreshore conditions, together with wave conditions similar to a storm with an annual recurrence interval of 1,000 years at the Belgian coast, was F_{max}= 19 kN/m (prototype value). This event was preceded by a regular bore pattern with no efficient overtopping mechanism. The event was classified as Quasi-static impact type and prototype flow layer thickness η_{max}=0.56 m, maximum flow velocity u_{max}=4.67 m/s and maximum run-up at the wall $R_{h,max}$=2.49 m were measured.

Next, the same 60 impact events and related flow thicknesses, velocities and run-up were used to fit existing semi-empirical prediction formulas (to predict the total horizontal impact force) with the data and to judge the predictive capability of

the existing formulas based on the goodness-of-fit parameters. The formulas were distinguished whether they rather described the dynamic first impact of the flow against the wall (related to incoming momentum flux and layer thicknesses and velocities) or the almost hydrostatic situation after maximum run-up and outward reflection of the water mass (related to the run-up at the wall or layer thickness close to the wall). Only limited number of prediction formulas for individual overtopping bore impacts on walls, resulting from broken waves in shallow waters, were available and the study was extended to Tsunami bore impact prediction formulas. The main difference is that Tsunami bore impacts were of longer duration and often considered flow around the structure, with a larger crest width to building width ratio. The dynamic first peak F_1 was best described with Equation 2.11 (σ=8.6 kN/m in prototype and MAPE=0.9614). Simple momentum flux theory (see Equation 6.5) fitted to the data revealed a similar prediction accuracy. The almost hydrostatic second peak F_2 was best described with the fitted hydrostatic force estimate with Equation 6.8 and using the maximum run-up of water at the wall (σ=3.23kN/m in prototype and MAPE=0.9963). A coefficient C_1=0.32 was obtained, very close to the coefficient of C_1=0.33 (found by Chen et al. (2012) in small-scale experiments for regular waves). This resulted in the practical conclusion that only ∼80% of the maximum run-up was effectively causing the force on the wall. The implication on the calculation of the overturning moment was that the lever arm can be reduced by ∼20% for the design of these structures. This observation was explained by the unweighting of the water body in front of the wall due to upward acceleration, splash-up and small or detached run-up tongue in the upper part of the water in front of the wall. Furthermore, a theoretical model based on the vertical accelerations of the water body in front of the wall was proposed to predict the total horizontal impact force signal shape. As the model only takes into account the vertical acceleration, thus does not consider the horizontal accelerations, some features of the total impact force shape, notably the beginning of the signal, were not captured well. Nevertheless, once the incoming flow was turned into vertical direction the model significantly reduces the overestimation resulting from the hydrostatic force estimate. The vertical accelerations in front of the wall were derived numerically from a validated OpenFOAM model, which was used to remodel a short duration test from the 'DeltaFlume' data-set.

For both, the best-fit prediction of the dynamic first F_1 and quasi-static second peak F_2, the prediction accuracy was low. It was argued that bore interaction processes prior to impact, non-uniformity of the bore front (2D-Effects), air-entrainment in the bore, and even small fluctuations and turbulence in the bore caused different bore impact processes resulting in the stochastic behaviour of the measured total horizontal force. Hence, a statistical method was investigated to predict the total horizontal impact force. For this purpose the impacts from the data-sets 'UGent1'-'UGent3' and 'DeltaFlume' were combined into a larger data sample (more than ∼100 impacts per sample). The range of application of the 'UGent1'-'UGent3', 'DeltaFlume' data-set was in the range of a previously derived data-set (Chen et al., 2016), with an extension towards larger relative promenade widths G_c/L_t=0.04-0.5 and extremely shallow waters $h_t/H_{m0,o}$ <0.3 (after Hofland et al. (2017)). With the large sample (more than ∼100 impacts per sam-

ple), issues due to too few data points for robust statistical analysis were minimized. The subdivision into samples was done based on a novel empirical link between the non-dimensional maximum impact F^*_{max} and the non-dimensional average overtopping discharge q^*. The sample boundaries were set based on suggested values from Eurotop (2016). Five data samples S_1-S_5 were distinguished and a sensitivity study on sample size showed that approximately 50 force peaks were required for robust fitting of the statistical distribution to the force peaks. Furthermore, a sensitivity study of the upper fitting threshold was conducted and an upper 15% fitting threshold selected. Only force peaks above this threshold were used to fit the linearised Weibull distribution to each sample and the shape and scale parameter were derived. The shape and scale parameter were plotted over the non-dimensional average overtopping discharge q^* for the five samples. The best-fit line for shape and scale parameter was calculated and showed a very stable behaviour (R^2=0.9873 for shape and R^2=0.9925 for scale parameter). Finally, a 6-step prediction methodology was developed, combining the empirical and statistical prediction capabilities: A maximum expected impact force F_{max} was empirically determined together with its statistical exceedance probability P_m. The exceedance probability P_m can be interpreted as the probability that F_{max} will be exceeded for a storm with 13,000 offshore waves and hydraulic boundary conditions (h_t, $H_{m0,t}$, $T_{m-1,0,t}$, q) specified together with the structural information (A_c, G_c) in the input parameters.

Lastly, the non-repeatability issues, model- and scale effects for laboratory impact load measurements induced by overtopping bores on dike mounted walls were investigated. This was done to better judge the accuracy of any impact force prediction derived from laboratory experiments. First, a base-line uncertainty was established by simply reproducing the same time-series of waves 14 times and measuring the impact forces at the wall. This so called non-repeatability of impact forces was quantified using the coefficient of variation and was in the order of 10% (in extreme cases up to 20%) for F_{max} and $F_{1/250}$. The scale-related effects were investigated by comparing tests from different scale laboratory experiments with the Froude similarity and length scale ratio 1-to-5.81. A similar geometry and the same time-series of waves was used in both experiments. It was concluded that if a minimum water depth at the dike toe, as well as thickness and velocity of the overtopping flow were maintained, the scale-related errors in the impact force measurement disappear within the uncertainties related to non-repeatability and model effects. This finding seemed contradictory to the general assumption that force measurements in the small-scale model are significantly higher than prototype measurements. The contradiction was mainly explained by the characteristics of the turbulent, aerated and broken wave impacts, resulting in compressible and less violent impacts for the first dynamic peak F_1 in the double peak impact force signal. Note this impact behaviour was very different compared to violent breaking wave impacts on seawalls constructed in the breaking zone. Furthermore, the majority and largest measured impacts were of quasi-static nature, the second peak F_2 in the double peak impact force signal, for which no major scale-effects were expected. However, a small systematic scale-related shift to higher impact forces was observed in the order of 4%, 9%, 8%, 13%, 16% for F_{max}, $F_{1/250}$, F_{10}, F_{20}, F_{30} respectively, in the small-scale model. Furthermore, the number of impacts

was lower in the small-scale model (424) compared to the large-scale model (549). Differences related to model effects were mostly observed in the wave generation and absorption in the small-scale model and changing sand bathymetry in the large-scale model. This resulted on average in a 10% difference in spectral wave parameters at the dike toe location between the two scale models.

For future studies on scale effects related to overtopping bore impacts on dike mounted walls, it was recommended to further advance the wave generation and wave absorption in the small-scale model to better represent the long wave characteristics. Additionally, measurements of air entrainment in both scales, at a location close to the wall where the impact force occurs, would be beneficial to judge the dissimilarities of the entrained air between different scale models. The use of pressure sensors in both scale models is recommended to further study the scale influence on peak impact pressures. Furthermore, extra intermediate scale models or fully prototype measurements could be used to judge whether the bore impacts scale linearly and to increase the relative scale difference.

It was further recommended to advance the study of bore transformation parameters on the promenade, such as bore front slope in the vicinity of the wall. This would increase understanding, especially of the impulsive and dynamic impact types. Validated numerical modelling might be an option to reproduce the shape of the bore front slope. The formation of the flow field in terms of bore thickness and bore velocity on the promenade and the transformation of the flow field along the promenade should be investigated further to study their change along the promenade.

For the proposed combination of empirical and statistical impact force prediction methodology an example calculation was performed using the input parameters of another laboratory scale model test (Chen et al., 2016). This served as a first indication that the presented prediction methodology was not out of range. Despite this first confirmation, further validation of the prediction methodology is required, ideally from prototype measurements.

Chapter 1

Introduction

The sea levels are expected to continue to rise in the near future, posing a threat to the coastal communities and assets constructed in the coastal area. As projected in the synthesis report of the Intergovernmental Panel on Climate Change (IPCC, 2014) the global mean sea level rise will exceed the observed rate of 2 mm/year (1971-2010) in the 21st century. This is also the average increase rate (~ 2.7 mm/year) for the local mean high tides at the gauge Cuxhaven between 1840 and 2005 (see red line in left Figure 1.1). The predicted future sea level rise after IPCC (2014) ranges from 0.28 m to 0.98 m in the year 2100 for different climate change scenarios (see right Figure 1.1). Additionally, extreme storms, as observed in the winter season 2013/2014 along Europe's Atlantic and North Sea coasts (see Figure 1.2), were more frequent and of higher intensity (Masselink et al., 2016). At the same time socio-economic changes put further pressure on the coastal area. The coastal area worldwide is comparably more densely populated and in the year 2000 half of all cities with more than 500,000 inhabitants were located within 50 km of a coastline (UNEP, 2006).

In Belgium roughly 400,000 people live within an area at risk of flooding. The attractiveness of the coast, in terms of leisure and economic activities, leads to an increased number of people, buildings and assets close to the coastline. When vulnerability in the coastal area and probability of flooding increases, the risk for inhabitants, accompanying industry and infrastructure also goes up. Hence, the increased need to properly prevent flooding in these areas and to build structures which are designed to withstand wave impact loads. This is especially true for countries with low elevation, such as Belgium, the Netherlands, Germany, parts of the US East coast, Indonesia or the coasts in northern Italy. There is a need for a sufficiently stable coastal structure to prevent flooding and withstand wave impact loads.

However, an absolute safety against coastal flooding is not achievable, e.g. due to long- and short term uncertainties associated with the prediction of the global sea level. The local effects of climate change and rising sea levels are often difficult to predict or of stochastic nature with numerous interacting parameters. Even if the prediction accuracy will improve, the accurate prediction of extreme flooding

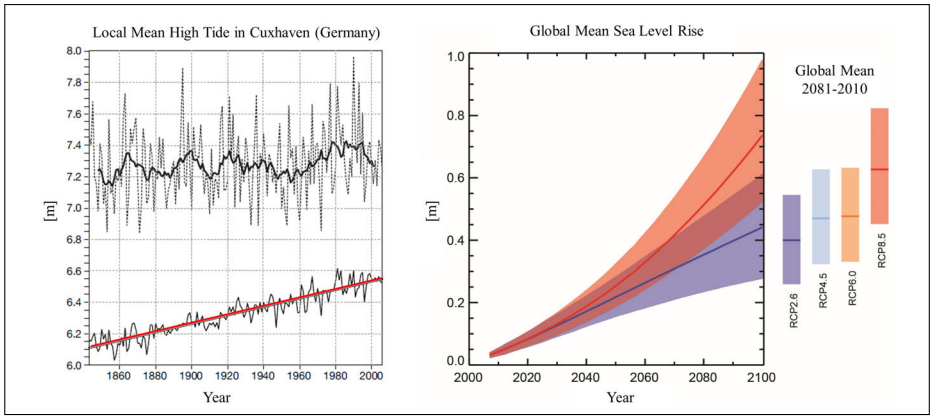

Figure 1.1: Measured mean high tide water level at level Cuxhaven in Germany (red line in the left figure). Sea level rise scenarios as predicted by the IPCC (2014) (right figure).

events will remain a challenge. This uncertainty generates a problem for the design of any coastal structure which has to withstand waves and prevent flooding. A designer might want to build the structure stable enough for a foreseeable future and with the possibility to be adapted or strengthened in case of further sea level rise or increased number of extreme flooding events, instead of providing an overly conservative design, for an uncertain extreme event in the far future. To properly assess the structural stability of any coastal structure, reliable tools to predict the wave-induced impact loads are required. In fact, existing approaches to designing coastal structures are often based on limiting the amount of water overtopping the structure and cannot be used for structural stability analysis.

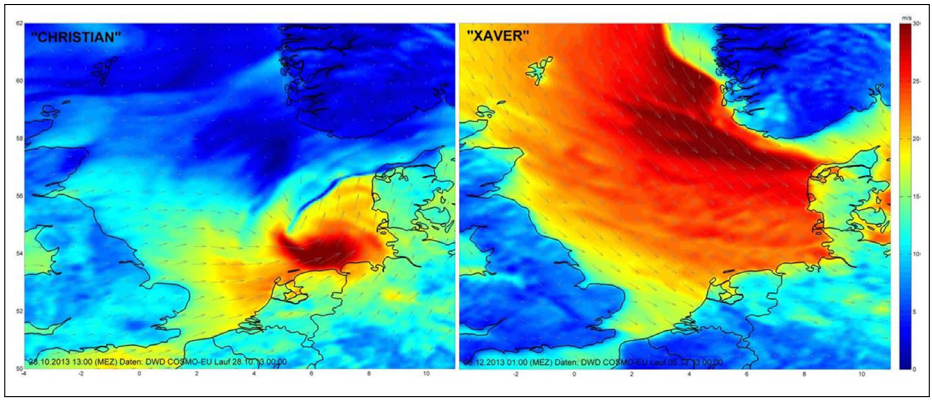

Figure 1.2: Windfield from 'Deutscher Wetterdienst' (DWD) for storm Christian (28.10.2013) and storm Xaver (06.12.2013). Xaver showed the highest measured storm surge water level at Pegel Norderney Riffgat since 1906.

1.1 Background and Motivation

The coastal structures along the shores of low-lying countries are often comprised of a two-component soft- and hard structure (see Figure 1.3). The mildly sloping sand foreshore in shallow waters is referred to as soft structure, and is adaptable to the forces of the waves. In Belgium, the sandy foreshore slopes range between 1-to-20 in Knokke-Heist and 1-to-90 in De Panne. Sandy foreshores are also found along parts of the Dutch and German coastlines. The soft structure is then followed by a hard structure, most often a dike with an attached promenade. On top of the promenade a storm wall or buildings are constructed. It was shown that one third of the Belgian coastline is not properly protected against severe storm surges (Mertens et al., 2009). Furthermore, structural coastal protection measures, such as dikes and storm walls, are commonly designed and assessed based on a reduction in overtopping (Verwaest et al., 2011), not taking into account the hydrodynamic loads induced by overtopped waves. Hence, rethinking the design of storm walls on the dike and buildings constructed at the end of the promenade is key to strengthening the coastal resilience against flooding and overtopping wave impact loads.

If rising sea level or an extreme storm exceeds the limits of the installed coastal protection, additional measures to prevent flooding of the hinterland and direct wave loading are needed (see Figure 1.4). A short term solution can be to add an additional storm wall on top of the dike (either temporarily or as a fixed solution), to raise the crest freeboard. By raising the crest freeboard the amount of overtopping water is limited. The crest freeboard is defined as the distance between the still water level and the point where the water, once overtopped, cannot re-enter the sea again. Usually this point is the top of the wall. In numerous cases along the coasts of low-lying countries, buildings are constructed at the end of a wide-crested dike or promenade, like in Belgium. Taking into account upcoming challenges concerning sea level rise and more frequent and severe storm surges due to climate change, these buildings will experience increased flooding and direct wave loading.

Figure 1.3: Storm water level reaching the dike in Ostend, Belgium (right figure). Before the beach nourishments were carried out starting from 2007 (Van Doorslaer et al., 2017). Typical coastal set-up for the Belgian coastline (left figure). With the soft-structure mild foreshore, followed by the hard-structure dike, promenade and wall (photo by Nicolas Milot).

Typically free surface waves are generated by wind blowing along the water surface. The small pressure fluctuations along disturbances of the water surface

and the horizontal component of it resulting in a mean shear stress will gradually form a fully developed wave. When the wind blows sufficiently long enough over a large enough fetch of sea a fully irregular wave field exist. The wave energy is further transferred as a transversal wave. When the wave approaches the coastline, it starts to transform over the first coastal defence structure, the mildly sloping foreshore, and breaks due to depth limitations in the shallow water (also called surf zone). Finally, a broken turbulent wave of short duration approaches and overtops the second coastal defence structure. Overtopped wave impacts are then the result of the interaction between the overtopped wave with any obstacle situated on the promenade. It was previously described that the overtopped wave shows a bore type behavior (Chen et al., 2014). According to the authors, the only difference to a 'real' bore is that it is induced by stochastic waves and that the bores may hit in groups or even as infragravity waves. Roeber and Bricker (2015) describe similarities of a tsunami bore and a bore generated by surf beat interacting with a coral reef during typhoon conditions. Recently, Lubin and Chanson (2016) proposed using the analogy of a tidal breaking bore to best describe the similarities to a bore resulting from broken waves. They observed that both bores, the tidal bore and the bore resulting from broken waves, are highly aerated and showed a sequence of splash-ups, as well as similarities between bubble plume behaviour. Compared to tidal bores, the bores resulting from broken waves in an irregular wave field are prone to interactions with previously overtopped bores (see Table 1.1). This leads to a complex and turbulent interaction process of the water masses before impact. In order to predict reliably the impact loads at the wall, a good understanding of the bore formation, bore interaction processes and final bore-induced loading of a secondary hard structure or building is required and barely investigated nor completely understood (Allsop et al., 2004). Furthermore, the relationship between the wave conditions at the toe of the dike, the run-up at the dike, the overtopping over the dike crest, the bore transformation along the promenade and the impact loads at the wall are not yet fully understood and engineering design guidance is scarce.

Table 1.1: Qualitative comparison of tsunami/tidal/dam break flow bore and short duration overtopping bore characteristics resulting from irregular and broken waves.

Type	Generation mechanism	Aeration	Bore interaction	Flow around building
Tsunami, Tidal, Dam break bore	Landslide, Earthquake, Tsunami	Turbulent, aerated and foamy bore front/roller	Limited	Yes
Overtopping bore	Wave breaking, Overtopping	Turbulent, aerated and foamy bore front/roller	Yes	No

Overtopped bore loads on storm walls, buildings and people have scarcely been measured, resulting in a lack of generic design guidance (Eurotop, 2016). Overtopping bore-induced loads can be a severe hazard to people and objects exposed. Geeraerts et al. (2005) found overtopped bore loads on a dummy person to be 8.8 kN, with accompanying overtopping of $q = 1\,\mathrm{l/s}$ per m. This is a rather high value compared to a 0.14 kN slipping limit for pedestrians proposed by Endoh and Takahashi (1994). Most of the impact prediction guidelines suffer from the

drawback that they are not designed for a geometrical set-up with dike mounted vertical walls. E.g. impact prediction force formula in U.S. Army Corps of Engineers (2002), based on the works by Camfield (1991), are designed for land based structures on a plane slope not taking into account overtopping over the dike crest in extremely shallow waters.

Figure 1.4: Flooding of the harbor in Norden (Germany) during a storm surge (left figure). Wave overtopping of the dike and impact at coastal structures on the barrier island Norderney (middle figure). Overtopping wave splash at the Belgian coast before the nourishment starting from 2007.

Maximum impact forces are key for a reliable design of coastal structures and often derived from small-scale experiments, up-scaled to prototype. Several small-scale experiments were conducted for the above-described coastal situation, using Froude similarity and a length scale factor between 1-to-20 and 1-to-35. The impact loads on the structure were investigated for irregular waves (Van Doorslaer et al., 2017; Streicher et al., 2016; Chen, 2016; Kortenhaus et al., 2017) and regular waves (Chen et al., 2015). In this way they suffer from scale-effects, mainly due to dissimilarities in the entrained air and the air content of the foamy bores (Blenkinsopp and Chaplin, 2007). Entrained air usually leads to cushioning effects of the impact pressures. Hence, less air entrained in the small-scale experiments will lead to less cushioning of the impact (Bullock et al., 2001). This is expected to lead to an overestimation of the impact loads, when upscaling the results from small-scale to prototype (Cuomo et al., 2010). Prototype tests of overtopped wave loads on a vertical wall were carried out (De Rouck et al., 2012; Ramachandran et al., 2012) in the large wave flume ('Grosser Wellenkanal', GWK) in Hannover, Germany. In their experimental configuration the influence of the mildly sloping foreshore and shallow waters at the dike toe, that results in broken bores approaching the dike, was not taken into account. Ko and Yeh (2018) and Kihara et al. (2015) investigated the slightly different situation tsunami bore impacts on vertical walls. The bore generates a continuous in-stream of water at the wall and no short duration bore interaction processes prior to impact were observed. The derived prediction tools often predict the average impact force (Van Doorslaer et al., 2017; Kortenhaus et al., 2017; Chen et al., 2015) or a maximum impact force but do not account for the underlying physical processes and are of rather empirical nature (summary given in Streicher et al. (2018)).

To summarise, storm walls situated on top of dikes are an appropriate short term measure to cope with rising sea levels or extreme storm events. The overtopping

Figure 1.5: Storm walls on the barrier island Norderney during regular conditions (left figure) and during a storm surge with overtopping bore-induced loads on the wall elements (right figure). The storm fotos were taken 09.11.2007 (source: NLWKN).

bore-induced loads need to be predicted to reliably design these storm walls, or any buildings situated on top of the dike, to withstand bore attack and prevent flooding. However, for an accurate prediction of the bore-induced loads it is important to distinguish the different physical processes during overtopping, bore formation and transformation, until final impact with the vertical wall. Furthermore, it is favourable to derive this knowledge from laboratory experiments featuring irregular waves as they reflect better the bore-bore interaction characteristics also found in reality. Finally, large-scale experiments are preferred to minimize the scale-effects, which are expected to arise from the difference in aeration of the water between a small-scale model and prototype.

1.2 Main objective and methodology

The main objective of this study is to gather more insight into the different physical processes that occur during bore formation in mildly sloping foreshore and shallow water conditions, run-up and overtopping over a dike, bore propagation along the promenade, leading to bore-induced loads on vertical structures such as storm walls or buildings constructed on top of the dike. Better knowledge of the physical processes will lead to the development of semi-empirical equations and statistical prediction tools as a basis for new design guidance in this field. First, a short literature review in order to increase knowledge and understanding of short-duration overtopped bore impacts on dike-mounted vertical walls will be performed. The bores result from irregular broken waves in mild foreshore and shallow water conditions. A better understanding of the processes leading to the impact is required for a reliable and safe design of these structures with respect to sea level rise and increased storminess in the future. In the literature study an overview of existing experimental studies will be established and the prediction formulas derived from these studies presented (see Chapter 2). A review of the non-repeatability, scale- and model effects in laboratory impact force measurements rounds off the litera-

ture study. The research gaps will be identified and result in the specific objectives for this thesis and a more detailed methodology (see Section 2.7 and 2.6). The method of investigation for this thesis is based on the analysis of experimental data derived from small- and large-scale experiments, for overtopping bore-induced loads on dike mounted walls in shallow water and mild foreshore conditions.

Chapter 2

Fundamental processes and scientific state-of-the-art

It was the purpose to summarize the existing knowledge on overtopped bore-induced loading of vertical walls in this Chapter. The specific conditions on which the literature study was focused were walls mounted on top of sea-facing promenades in shallow waters and mildly sloping foreshore conditions (see Figure 2.1). First, the generation of bores resulting from depth generated breaking waves was described in Section 2.1. Then the recent findings on bore interaction and bore impact processes were summarized in Section 2.2 before the existing experimental studies on this topic were summarized in Section 2.3. For some of the studies empirical and statistical prediction tools were derived (see Section 2.4). Finally, the scale- and model effects for laboratory measurements of bore-induced loading of vertical walls was discussed in Section 2.5. Throughout the literature review, the research gaps were identified and resulted in the specific objectives for this thesis (see Section 2.6) and the particular thesis outline (see Section 2.7).

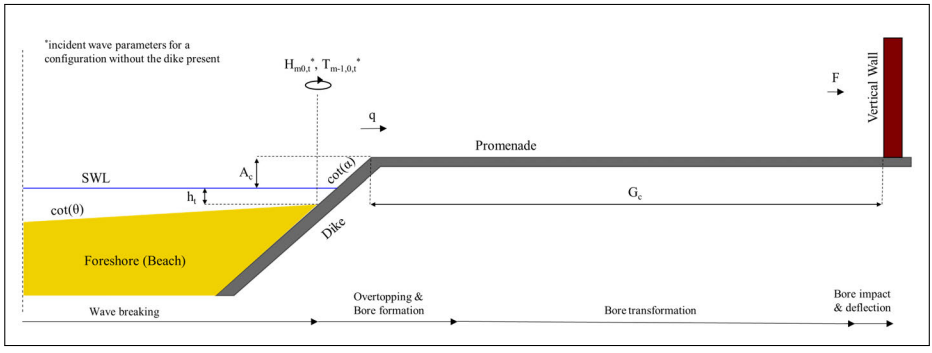

Figure 2.1: Overview of geometrical and hydraulic parameters

2.1 Bores in shallow water and mildly sloping foreshore conditions

Foreshore slopes along the Belgian coast range between 1-to-20, close to Knokke-Heist, and 1-to-90, close to De Panne (Gruwez et al., 2018). Typically a foreshore slope between 1-to-35 and 1-to-40 is considered transitional between a mild and a steep foreshore (Hofland et al., 2017; Ruessink et al., 2013). With the steeper slopes being more representative for a critical post-storm situation at the Belgian coast. In Eurotop (2016) the foreshore slope in front of the coastal structures was defined as having a minimum length of $L_{m-1,0}$, with horizontal to 1-to-10 bottom slope, and discussed in terms of water depth and its effect on the wave characteristics, steepness (see Equation 2.1) and breaker parameter (see Equation 2.2),

$$S_{m-1,0} = \frac{H_{m0}}{L_o}, \tag{2.1}$$

$$\xi_{m-1,0} = \frac{tan(\alpha)}{\sqrt{2 \cdot \pi \cdot H_{m0}/g \cdot T_{m-1,0}^2}}. \tag{2.2}$$

With, H_{m0} and $T_{m-1,0}$ the offshore spectral wave height and period, tan(α) the structure slope, and L_0 the deep water wave length. The breaker parameter reached large values between 4-10 and the wave steepness was often smaller than 0.01 (Eurotop, 2016)). The authors stated that this often indicated a shallow or very shallow foreshore, depth-limited wave breaking, a flattening of the wave spectrum and spilling waves. The transition from shallow to very shallow foreshores was also related to a decrease in wave height H_{m0} from offshore to the toe of the structure by 50%. They further state that for a shallow foreshore the waves were still breaking but the spectral shape was maintained, while for a very shallow foreshore the spectral shape is flattened with increased magnitude in the lower and higher frequency range. This was in line with the observations made by Hofland et al. (2017) and Van Gent (1999a), who found that there was a significant shift towards higher spectral periods $T_{m-1,0}$ along a very shallow foreshore. This was explained by the depth-limited breaking of the waves along the foreshore and release of free long waves from the wave group (Hofland et al., 2017; Chen, 2016; Altomare et al., 2016; Van Gent, 1999a). However, Hofland et al. (2017) pointed out a problem using the breaker parameter and wave steepness for classification. The former classifies a deep foreshore together with non-breaking swell waves formally as shallow foreshore and the latter classifies steep structure slopes as shallow foreshore. The physical relevance, relating a very shallow foreshore to heavy wave breaking, was lost. Hence, Hofland et al. (2017) developed a criterion to classify foreshores into extremely shallow, very shallow, shallow and deep, on the basis of the related wave characteristics. The classification was done based on the criteria $h_t/H_{m0,o}$ (see Table 2.1).

Table 2.1: Classification of foreshore depth based on the ratio of water depth at the dike toe h_t and spectral wave height offshore $H_{m0,o}$ (Hofland et al., 2017).

Offshore	Shallow	Very shallow	Extremely shallow
$h_t/H_{m0,o}$ >4	4> $h_t/H_{m0,o}$ >1	1> $h_t/H_{m0,o}$ >0.3	$h_t/H_{m0,o}$ >0.3

The offshore location was defined as $h_t/H_{m0,o}$ >4, with no depth-induced wave breaking. A shallow foreshore is then defined as 1<$h_t/H_{m0,o}$ >4 where the wave breaking started to get influenced by the water depth but the same single-peak offshore wave spectrum was maintained. For a very shallow foreshore, 0.3< $h_t/H_{m0,o}$ >1, the offshore wave height was reduced, similarly to what was stated in Eurotop (2016), by 50%-60% and a flattening of the wave spectrum and increased low-frequency energy observed. Finally, extremely shallow foreshores were defined as $h_t/H_{m0,o}$ >0.3 with a dominant low frequency component for the wave spectrum.

In case of shallow to extremely shallow foreshores (Hofland et al., 2017) the waves were breaking along the foreshore and the wave spectrum flattened and shifted towards low-frequency components. This resulted in a highly aerated and turbulent bore at the toe of the coastal structure and was best compared to a tidal breaking bore (Lubin and Chanson, 2016). In this conditions the water mass in the bore was transported in the direction of bore propagation. Suzuki et al. (2017) proposed to use the solitary wave model to compute the shallow water wave length in this conditions,

$$L_t = T_{m0-1,0,t} \cdot \sqrt{g \cdot (h_t + H_{m0,t})}. \tag{2.3}$$

Run-up and overtopping of coastal structures were usually defined for deep foreshore conditions (Eurotop, 2016). Average overtopping volumes in mildly sloping foreshore and shallow water conditions, with broken bores as a result, were first predicted by Van Gent (1999b) based on model tests with foreshore slopes 1-to-100 and 1-to-250, as well as smooth dike slopes 1-to-4 and 1-to-2.5 (see Equation 2.4),

$$q = \sqrt{g \cdot H_{m0}^3} \cdot 10^c \cdot exp(-\frac{R_c}{H_{m0} \cdot \gamma_f \cdot \gamma_\beta \cdot (0.33 + 0.022 \cdot \xi_{m-1,0})}). \tag{2.4}$$

Where q was the overtopping discharge per meter width of the structure, R_c was the crest freeboard, γ_f was the reduction coefficient considering the effects of the slope roughness and γ_β was the reduction coefficient considering the effects of wave obliqueness. The c-coefficient in Equation 2.4 was assumed a normally distributed parameter with mean value equal to -0.92 and a standard deviation σ equal to 0.24. The 5% upper and under exceedance limits were calculated as (-0.92)$\pm$1.64σ. Altomare et al. (2016) extended the prediction to foreshore slopes between 1-to-250 to 1-to-20 and for very shallow waters by introducing an

equivalent slope tan(δ) (see Equation 2.5),

$$tan(\delta) = \frac{1.5 \cdot H_{m0} + R_{u2\%}}{L_{Slope}}. \tag{2.5}$$

The equivalent slope tan(δ) was basically an average slope over the equivalent slope length L_{slope}, between the foreshore slope tan(Θ) from the point on the foreshore with a depth of 1.5·H_{m0} and dike slope tan(α) from the run-up level $R_{u2\%}$ (see Equation 2.6). By adding the foreshore slope as part of the structure the effects of heavy wave breaking and change in spectral wave parameters on the foreshore were taken into account,

$$L_{Slope} = \frac{R_{u2\%} + h_t}{tan(\alpha)} + \frac{1.5 \cdot H_{m0} + h_t}{tan(\Theta)}. \tag{2.6}$$

Finally, it should be mentioned that the crest freeboard R_c was typically defined as the distance between the still water level and the height of the coastal structure from where on the water cannot flow back to the sea. In the case of a wall situated on top of a dike this would be the top of the wall. However, if the vertical wall was a building or otherwise non-overtopped this resulted in unphysical or unrealistic predictions, when R_c was used as defined above. Therefore, Van Doorslaer et al. (2017) suggested to use the parameter A_c instead, defined as the distance between the still water level and the dike crest height (see Figure 2.1).

2.2 Bore interaction and bore impact processes

The first study to distinguish and classify different bore interaction patterns prior to impact was done by Chen (2016) with data derived from small-scale laboratory experiments depicting shallow water and mildly sloping foreshore conditions. She investigated three ways in which bore interaction can influence the impact on the wall. For the catch-up pattern (case 1) a first bore is followed by a second and faster bore, they join on the promenade and generate an amplified impact on the wall. The collision pattern (case 2) describes any collision of incoming and reflected bore on the promenade. Depending on the location of the collision this results in an amplified (collision close to wall) or dampened (collision further away from wall) impact. For the wet bed situation (case 3) the incoming bore slides over a residual water layer from a preceding bore. This results in less friction and velocity damping during propagation over the promenade, and subsequently the impact is amplified. Streicher et al. (2016) observed in similar small-scale experiments that bore interaction on the promenade can lead to amplified impacts, for example plunging bore breaking against the wall.

The blocking of the bore due to a wall on the promenade and the resulting impact of the bore against the wall is termed 'wall effect' by Chen et al. (2014). For a single bore overtopping the dike and impacting against the wall, they defined four stages of impact at the wall: In the (S_1) pre-impact stage the bore was

propagating and transforming over the promenade. During the (S_2) initial impact stage a first tiny water jet impacted at the wall followed by the main water wedge impact and squeezing of the initial water jet against the wall. This in turn was followed by the (S_3) deflection stage during which the water flipped through and was deflected upwards along the wall, transferring all kinetic energy into potential energy until maximum run-up at the wall was reached. Finally, during the (S_4) reflection stage the water started to fall downwards again, hitting the remaining incoming water and being reflected offshore again due to partial blocking of the wall.

Kihara et al. (2015) investigated tsunami bore impacts on tide walls. Based on signals from pressure sensors measuring over the wall height, they distinguished four impact phases: (P_1) Impulsive impact phase with a duration of $10^{-3} - 10^{-2}$ s. (P_2) Dynamic impact phase, $0.1 - 1$ s long and during which the flow against the wall was fully developed and the water mass flipped upwards. (P_3) Initial reflection phase during which the water collapsed on the continued incoming flow and pressures on the wall were larger than hydrostatic. (P_4) Quasi-steady/hydrostatic phase from 10s after initial impact onwards during which the pressure distribution on the wall was hydrostatic.

The impact process for tsunamis (Kihara et al., 2015) and overtopping waves (Chen et al., 2014) are classified in various corresponding stages or phases, named differently and taking into account the differences between short duration overtopping waves and long duration tsunami bores.

Bore impacts against a vertical wall resulted in a double peak shape of the measured force impact signal (Ko and Yeh, 2018; Van Doorslaer et al., 2017; Chen et al., 2015, 2014, 2012; Streicher et al., 2016; Kihara et al., 2015; De Rouck et al., 2012; Ramachandran et al., 2012; Ramsden, 1996; Martin et al., 1999). The first peak was typically assigned to a dynamic impact of the moving bore being blocked by the wall. During deflection and reflection of the bore a dominant influence of the second peak was observed. The physical reason for the second peak was debated at length. It was either assigned to a hydrostatic force, due to the water in front of the wall (De Rouck et al., 2012) or to the down-rush of water after run-up and blocking of the wall in one direction (Streicher et al., 2016; Kihara et al., 2015; Chen et al., 2012; Martin et al., 1999; Ramsden, 1996). The latter argued that the second force peak was situated after the maximum run-up in time and therefore cannot be directly assigned to a maximum water layer in front of the wall. Kihara et al. (2015) assumed that the second peak in the impact signal was due to two effects, acceleration of continuous flow against the lower part of the wall and downward accelerated flow by gravity due to collapsing water. The double peak impact signal shape was already described by Kortenhaus and Oumeraci (1998) and Oumeraci et al. (1993) for direct wave loading of structures situated in relatively deep water. Kortenhaus and Oumeraci (1998) defined a criterion to classify the entire impact either as a dynamic (dominant first peak F_1) or quasi-static (dominant second peak F_2) impact type. If the force ratio F_1/F_2 exceeds 2.5, the impact would be considered a dynamic impact type. For the first time, Ko and Yeh (2018) described the double peak impact signal shape theoretically and validated their assumption with measurements obtained from experiments studying tsunami bore

impacts on building walls. Using the laser induced fluorescence method they were able to cut out cross sections of the water body in front of the wall to determine the splash-up height, which is a different term for run-up height, at the wall in small-scale experiments. They observed a two-peaked impact signal with the first peak related to the slamming action and rising water in front of the wall and the second peak related to falling action and the collapsing of water after maximum splash-up. The generated tsunami bores were repeatable enabling a statistical analysis of the parameters. Based on a very short duration observation 2.72 s$<$ t $<$2.8 s, where the impact pressure gradients were very small over the wall height, they made the assumption that the velocity profile in front of the wall can be seen as uniformly distributed over the height. When using the Euler equation to predict the force response of the structure and assuming uniform velocity profiles, the measured force was better approximated than using the hydrostatic approach (which would always overestimate the impact force) based on splash-up height. The slight overestimation using the Euler equation might be due the fact that incompressible fluid is assumed in theory, while in the experiment a two-phase flow of air and water was present. So, the impact forces were reduced. In all cases using a uniformly distributed velocity profile resulted in better force estimates than using a linearly distributed velocity profile. Hence, they made the assumption that the splash-up water body, at least at the tip of the splash-up behaves like a solid body projectile.

Theoretically, the impact at the wall is the result of a deterministic process chain starting with the I) wave breaking in shallow waters, II) wave run-up at the dike, wave overtopping over the dike crest, III) transformation of the bore flow on the promenade and IV) finally impact of the bore at the wall (see Figure 2.2).

Additionally interaction patterns of the bore, such as V) catch- up, VI) sequential overtopping or VII) anticipated collision of a reflected bore with new incoming water were observed (see Chapter 5). Occasionally, several interaction patterns were observed for the same event. If each physical process could be described correctly, a perfect link between the waves in I) and the impact force in IV) would be the result. For each part in the process chain an output parameter would be calculated, which again serves as the input for the next. However, due to small fluctuations in the flow, turbulent processes, air entrainment, bore interaction, this remains a challenge for any approach to predict the impact loads.

2.3 Experimental studies on overtopped bore loading of vertical walls

There were several experimental studies existing featuring overtopping wave-induced loading of vertical walls. They were herein distinguished in 3 categories: (1) experimental studies involving the overtopping discharge (see Section 2.3.1), as key design parameter for coastal structures; (2) experimental studies conducted for shallow water and mildly sloping foreshore conditions similar to the present study (see Section 2.3.2) and (3) other related studies (see Section 2.3.3). An overview of the existing experimental studies was given in Table 2.2.

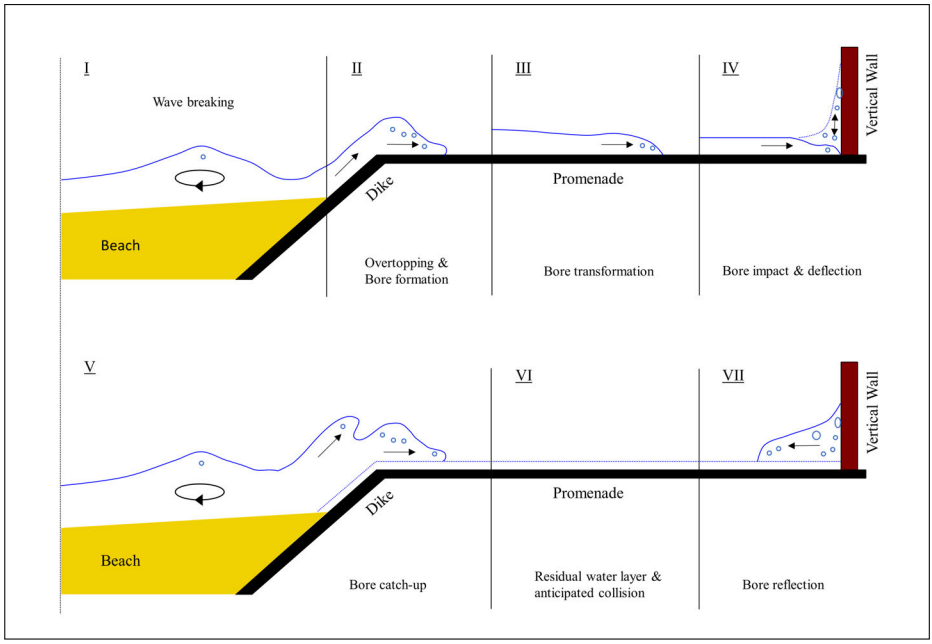

Figure 2.2: Process overview of overtopping bores impacting a vertical wall on top of a promenade. I) wave breaking, II) wave overtopping and formation of overtopping bore, III) transformation of bore along promenade, IV) initial impact at the wall and upward deflection, V) wave catch-up and VI) sequential overtopping, VII) anticipated collision of incoming and reflected bore.

2.3.1 Studies involving the overtopping discharge

Usually storm walls on top of a dike are designed to limit a certain amount of water overtopping the wall, to ensure that the hinterland is not flooded. However, for a structural stability design the bore-induced loads on these structures was required. Only few studies were conducted to investigate the relation between the overtopping water and associated impact loads on the structure. Allsop et al. (2004) provide a tentative relation between the average overtopping discharge and maximum local impact pressures on a sea wall and concludes that with increasing discharge and smaller promenade width the pressure increases. Kortenhaus et al. (2017) discusses the possibility to use the average overtopping discharge and relate it to the bore-induced impact force $F_{1/250}$ for dike mounted walls. The experiments (model scale 1-to-25) on which the discussion was based were conducted at Ghent University wave flume facility on a geometry similar to the Belgian coast. A 1-to-35 foreshore slope was built from concrete and attached to a dike and promenade made from plywood. At the end of the promenade a wooden, non-overtopped vertical wall was constructed, representing a storm wall or sea-facing building wall. The impact forces were then measured by means of load cells attached to a measurement plate integrated into the wall at the end of the promenade. In this study the incident

wave parameters at the dike toe were measured in separate tests by removing the dike and promenade from the set-up. Additionally, the individual and average overtopping over the dike crest was measured in another test series featuring the same irregular time-series of waves. Hence, a relation between average overtopping discharge and the impact forces was enabled. Furthermore, the promenade width, freeboard and dike height were varied during their experiments.

A number of studies used the instantaneous maximum overtopping discharge, as the product of maximum flow thickness and maximum flow velocity on the promenade, to relate it to the measured impact force (Ramachandran et al., 2012; De Rouck et al., 2012). Experiments were conducted in the Große Wellenkanal (GWK) in Hannover, to measure the overtopping bore-induced impact forces on a vertical wall in deep water conditions at the dike toe. A promenade of 10 m was installed with a non-overtopped wall in the end. The wall was partially opened during the experiment to enable fast drainage of water after impact. They noticed that the measurement of flow parameters in alternating wet and dry conditions (on the promenade) remains a challenge. However, they established the link between the instantaneous overtopping discharge and the impact force on the wall, which resulted in a better prediction accuracy than simply using either the layer thickness or velocity. Furthermore, they noticed that for the same layer thickness, a higher velocity would result in a higher impact force as well. Regular (Ramachandran et al., 2012) and irregular (De Rouck et al., 2012) waves were tested. Their analysis was focused always on the first of a series of overtopping bores, to avoid any effect from the complex bore interaction patterns when reflection at the wall would occur. The analysis was summarized in Van Doorslaer et al. (2017). In a different approach the wave overtopping simulator (Van Der Meer et al., 2010) was used to simulate an overtopping bore by releasing a defined volume of water (500 l/m per s up to 5.000 l/m per s) on to a 10 m wide promenade and measure the impact force of the bore flow against two measurements plates installed at the end of the promenade (Van Doorslaer et al., 2012). The layer thicknesses and velocities were measured by means of a potentiometer and paddle wheels attached to a surf board floating on the water at the promenade location. A direct link between the individual overtopping volume, flow thicknesses, flow velocities and impact forces was achieved. The repeatability of these measurements was remarkable, as a defined volume was used and no bore interaction with previously reflected bores occurred. The most recent experiment on overtopping bore-induced impacts and measuring both the overtopping discharge and impact forces was conducted at Ghent University within the CREST project (Gruwez et al., 2018). A variation of foreshore slopes, 1-to-20 until 1-to-90, were investigated together with a variety of promenade widths G_c=10 − 30 m in prototype. The measurement set-up was most similar and a continuation of the experimental set-up described in Kortenhaus et al. (2017). Additionally, the wave parameters were measured in high-resolution along the mildly sloping foreshore to enable a detailed investigation of the wave transformation. The analysis of this data-set was ongoing and no further results available yet.

The above described experimental studies have in common that they all discuss the average or instantaneous overtopping discharge and its relation to an impact

force on the wall. No direct link expressed with a prediction formula between the average overtopping discharge q, as a key design parameter for coastal structures, and the maximum impact force F_{max} could be found.

2.3.2 Studies in shallow waters and mild foreshore conditions

Chen (2011) were the first to derive a set of equations relating the impact force induced by an overtopping bore on a wall on top of a dike to the incoming wave and structural parameters. Tests for irregular and regular waves were conducted. Small-scale experiments (Froude similarity and length scale factor 1-to-30) were conducted in shallow water conditions at the dike toe, mildly sloping foreshores and for promenade widths between $0 - 15$ m in prototype. The studies were continued by the author (Chen et al., 2012, 2014, 2015) based on the same experimental data-set and the regular wave tests. A prediction formula to link the impact force with the incoming wave and structural parameters was underpinned with the physical momentum flux theory described in Hughes (2004a,b). An overall good prediction accuracy was obtained by the derived formula, respecting the physical processes of run-up at the dike and overtopping flow thickness. However, it remains unclear whether the predicted impact force can be seen as a maximum impact force in this conditions and if the results were transferable to irregular wave conditions. Furthermore, the authors used bubble image velocimetry to observe the impacting flow and to better study the impact process itself (Chen et al., 2014). This yields in an advanced impact process description in several stages (see Section 2.2). Also, a link between the impact pressures and the impact rise time was established in the same publication. Chen et al. (2016) continued using the same data-set to arrive at a statistical prediction of a maximum impact force for a certain exceedance value. Only the above described experimental study from Kortenhaus et al. (2017) and Gruwez et al. (2018) included also a set-up with shallow water and mildly sloping foreshore. Other than that, no studies for this specific coastal geometry were found.

2.3.3 Other related studies

Several prediction tools for the impact force exist for geometries different from dike mounted walls in shallow water and mildly sloping foreshore conditions. For example impact prediction force formula in U.S. Army Corps of Engineers (2002), based on the works by Camfield (1991), were designed for land based structures on a plane slope not taking into account overtopping over the dike crest in extremely shallow waters. Den Heijer (1998) investigated experimentally overtopping wave impacts on a quay wall, dike and a dike with berm structure in deep water conditions using irregular wave time-series. A relation between the maximum impact force and wave and structural parameters was established. No mild foreshore and broken bores at the dike toe were considered in his study. Kleidon (2004) and Geeraerts et al. (2005) both investigated overtopping bore-induced impact forces for permeable rubble mound breakwaters. The former investigated the impact forces on a dummy person on top of the breakwater and the latter the impact

Table 2.2: Experimental studies on overtopping bore-induced loading of vertical walls (values in model scale).

Reference	Model scale	Geometry parameter					Hydraulic parameter		Measurement					Relation	Comments
		$\cot(\theta_2)$	$\cot(\alpha)$	A_c	G_c	d_w	h_t	Waves	η	u	F	P	q		
		[-]	[-]	[m]	[m]	[m]	[m]	[-]	[m]	[m/s]	[kN/m]	[kPa]	[l/s·m]		
Gruwez et al. (2018)	1-to-25 1-to-35	20 35 50 80	2	0.04 0.12	0.4 0.8 1.2	non-overtopped	0.012 0.052	Irregular 1,000 waves Bichromatic waves 1^{st} and 2^{nd} order $H_{s,o}$=0.04-0.2m $T_{p,o}$=1.6-2.4s	yes	yes	yes	yes	yes	average overtopping, wave/geometry parameters and $F_{1/250}$	individual overtopping and velocity is still to be analysed
Kortenhaus et al. (2017)	1-to-25	35	2	0.04 0.12	0.4 1.2	0.4	0.01 0.05	Irregular 1,000 waves $H_{m0,o}$=0.08-0.19m $H_{m0,t}$=0.025-0.08m $T_{p,o}$=1.7-2.63s	yes	yes	yes	yes	yes	average overtopping, wave/geometry parameters and $F_{1/250}$	individual overtopping and velocity is still to be analysed
Van Doorslaer et al. (2017)	-	none	2 3	0.19 0.24 0.29	0 1	0.08	0.55 0.73 0.78	Irregular waves $H_{s,o}$=0.08-0.215m $T_{p,o}$=1.8-2.6s	no	no	yes	no	yes	wave/geometry parameters and $F_{1/250}$	no overtopping measured
Chen et al. (2015)	1-to-25	35	3 6	0.012 0.052	0.25 0.5 0.75	0.5	0.05 0.09	Regular waves 10-15 H_t=0.03-0.1m	yes	no	yes	yes	no	wave/geometry parameters and force	regular waves analysed, momentum flux theory based on Hughes (2004a)
Chen et al. (2014)	1-to-25	35	3	0.012	0.5	0.5	0.09	Regular waves H_o=0.2m T_o=4s	yes	yes	yes	yes	no	impact pressures and impact rise time	bubble image velocimetry applied
Bellotti et al. (2014)	1-to-6	none	Quay wall 3	0 0.17 0.33	1.69	0.2	2.39 2.55 2.72	Irregular waves, 1,000 $H_{s,o}$=0.17-0.5m $T_{p,o}$=1.67-4.06s	yes	yes	yes	yes	yes	-	overtopping measured over the storm wall
Ramachandran et al. (2012)	1-to-1	20	3	1.5 2	10	1.5 1.7	4.5 5	Regular waves H_o=1-1.6m T_o=6-12s	yes	yes	yes	yes	no	instantaneous discharge and impact force	analysis of flow thickness and velocity proved to be difficult
De Rouck et al. (2012)	1-to-1	20	3	1.5 2	10	1.5 1.7	4.5 5	Irregular waves $H_{m0,o}$=0.85-1.5m T_o=6-12s	yes	yes	yes	yes	no	instantaneous discharge and impact force	analysis of flow thickness and velocity of first wave in a group
Van Doorslaer et al. (2012)	1-to-1	none	2.35	-	10	0.5 (horiz.) 1.7 (vert.)	-	Bore released from overtopping simulator	yes	yes	yes	no	no	individual volume and impact force	overtopping simulator

Reference	Model scale	Geometry parameter					Hydraulic parameter		Measurement					Relation	Comments
		$\cot(\theta_2)$	$\cot(\alpha)$	A_c	G_c	d_w	h_t	Waves	η	u	F	P	q		
		[-]	[-]	[m]	[m]	[m]	[m]	[-]	[m]	[m/s]	[kN/m]	[kPa]	[l/s·m]		
Verwaest et al. (2011)	-	none	Quay wall 2.25 3	0.12-0.48	0 0.4 2	∼0.4	0.6-0.92	Irregular waves H_s=0.079-0.207m T_p=1.26-2.175s	no	no	no	yes	yes	wave/geometry parameters and impact force	data from Den Heijer (1998)
Chen (2011)	-	none	2.35	0.025-0.075	0-0.5	0.05	0.55-0.6	Irregular waves 1,000 Regular waves 10-15 $H_{m0,t}$=0.03-0.1m $T_{m-1,0,t}$=1.4-1.6s (irr.)	no	no	no	yes	yes	wave/geometry parameters and impact force	four different formulas derived
Geeraerts et al. (2005)	1-to-1	-	1.4	7.08-7.63	5-10	wall pipeline dummy	8.77-9.32	H_{m0}=3.03-3.59m T_p=7.91-8.57s	no	no	yes	yes	yes	-	field measurement at permeable rubble mound breakwater Zeebrugge
Allsop et al. (2004)	1-to-30	none	wall	-	0.23	-	-	$H_{s,o}$=0.07-0.21m T_m=1.22-1.79s	yes	yes	no	yes	yes	average overtopping discharge and impact pressures	load/overtopping measurement at first and second wall
Kleidon (2004)	1-to-30	none	1.4	0.173 0.207 0.24	-	dummy	0.645-0.7	H_{m0}=0.126-0.20m $T_{m-1,0}$=1.56-2.01s	yes	yes	no	yes	yes	-	permeable rubble mound breakwater
Den Heijer (1998)	-	none	wall 2.25 3	0.12-0.48	0 0.4 2	∼0.4	0.6-0.92	Irregular waves H_s=0.079-0.207m T_p=1.26-2.175s	no	no	no	yes	yes	wave/geometry parameters and F_{max}	different formulas derived for quay wall, dike and dike with promenade

forces on a vertical wall, dummy person and a pipeline situated $5 - 10$ m landward from the breakwater crest. While Kleidon (2004) did experimental model studies the results from Geeraerts et al. (2005) were obtained from field measurements at the Zeebrugge breakwater in Belgium. Hence, the measurements by Geeraerts et al. (2005) were taken for a situation with deep water at the breakwater toe. No direct link between the wave parameters, structural parameters and the impact force was established. However, the maximum measured impact forces on the dummy person, pipeline and vertical wall were 8.8 kN, 1.3 kN and 1.43 kN respectively. The wave conditions were H_{m0}=3.59 m, T_p=8.75 s and the average overtopping volume q=0.61 l/s per m. Taking into account the slipping criteria of 0.140 kN derived by Endoh and Takahashi (1994) these are comparably high and potentially dangerous impact forces for people and structures on top of the breakwater. Especially when taking into account that the overtopping discharge was lower than 1 l/s per m, the design criteria for the Belgian coast as of to date. Verwaest et al. (2011) introduced a semi-empirical formula based on the assumption that the hydrodynamic loading equals the momentum rate generated by the water reflected at the wall. The formula includes a reduction factor due to the promenade width and was based on the layer thickness and velocity descriptor developed by Schüttrumpf and Oumeraci (2005). The formula was calibrated based on the experimental data-set from Den Heijer (1998). Hence, the formula is valid for deep water conditions at the dike toe. More recently, Bellotti et al. (2014) presented medium scale experiments on overtopping bore-induced loads on walls conducted in the CIEM wave flume facility in Barcelona. These experiments were conducted in deep water conditions at the dike toe. The experimental data was further used by Van Doorslaer et al. (2017) to establish an empirical relationship between the spectral wave height, crest freeboard and $F_{1/250}$ impact force at the wall. In the same publication Van Doorslaer et al. (2017) presents small-scale experiments conducted in the Ghent University wave flume facility for similar, deep water, conditions at the dike toe.

2.4 Review of existing prediction formulas for bore-induced impact forces

The Belgian coastal geometry is often comprised of a mildly sloping foreshore, dike, promenade and wall or building on top of the promenade. With overtopping bores traversing across the dike crest, an impact is generated on these buildings or walls. To predict the bore-induced impact force empirical (see Section 2.4.1) and statistical (see Section 2.4.1) prediction formulas were previously derived from experimental measurements and theoretical considerations.

2.4.1 Empirical prediction formulas

A comprehensive overview of existing semi-empirical force prediction formulas was established (see Table 2.6). To judge the predictive capability of the formulas for the specific situation, four main criteria were distinguished: (1) which formula input

parameters were used, for example bore velocity of incoming flow, spectral wave parameters, etc.; (2) whether the fitting data was derived from small- or large-scale experiments, with the latter being less distorted by scale effects due to the entrained air; (3) which geometrical set-up was used, for example mild foreshore, shallow water, dike, flat bottom, and (4) which wave conditions, for example tsunami bore, irregular, regular waves were tested in the experiment, to account for realistic wave conditions. Furthermore, it was attempted to conclude whether the formulas rather predicts the first peak (F_1 was related to the dynamic impact of the bore against the wall) or the second peak (F_2 related to the hydrostatic pressure after maximum run-up at the wall) of the double peak impact force signal shape (Streicher et al., 2019b; Van Doorslaer et al., 2017; Chen et al., 2014; De Rouck et al., 2012; Ramachandran et al., 2012; Martin et al., 1999; Ramsden, 1996).

Because the different formulas used varying symbol conventions, the formulas were adapted using the same naming convention.η [m] was the time-varying bore thickness on the promenade, u [m/s] the time-varying bore velocity on the promenade, G_c the promenade width, A_c the crest freeboard between top of the dike and still water level, $H_{m0,t}$ and $T_{m-1,0,t}$ the spectral wave parameters at the dike toe, q the average overtopping discharge, h_t the water depth at the dike toe, the g=9.81m/s^2 the acceleration due to gravity, and ρ_w was the density of water approximated as 1,000kg/m^3.

Previously, the analogy was made between an overtopping wave and a tsunami bore (Chen et al., 2015) or an overtopping wave and a tidal bore (Lubin and Chanson, 2016). The initial impact, first force peak F_1, was expected to follow the same physical process for bores resulting from broken waves and a tsunami bore, since both bore types display a turbulent and foamy bore front with air entrained in the bore. Therefore empirical and semi-empirical approaches to predict tsunami bore impacts were included in this review as well. An early approach to predict the dynamic impact of an overtopped water wedge against a wall was theoretically derived by Cumberbatch (1960) for incompressible, inviscid fluid and irrotational flow without the effects of gravity. Cross (1967) showed that this theoretical approach could be interpreted using laboratory data and by adding a hydrostatic force term (see Equation 2.7). He also introduced the bore front slope θ_0 as a parameter to calculate the impact force F [N] related to the incoming bore flow parameters (see Equation 2.8),

$$F = \frac{1}{2} \cdot \rho_w \cdot g \cdot \eta^2 + C_f \cdot \rho_w \cdot \eta \cdot u^2, \tag{2.7}$$

$$C_f = tan(\Theta_0)^2 + 1. \tag{2.8}$$

Experiments with bores resulting from broken solitary waves on 1-to-50 slope wet bed situations were carried out by Ramsden (1996). He adapted the approach by Cross (1967) for the bore impact force F [N] against a wall (see Equation 2.9),

$$F = \frac{1}{2} \cdot \rho_w \cdot b \cdot (\eta + h)^2 + \rho_w \cdot b \cdot \eta \cdot u^2. \tag{2.9}$$

where b [m] was the building width and h [m] the initial water level before arrival of the bore. The dry bed surge impact force can thus be calculated by simply excluding the variable h. Asakura et al. (2002) developed an empirical formulation for the tsunami impact force derived from experiments on a mild sloping foreshore and a vertical wall (see Equation 2.10). The maximum force F_{max} [N] was only dependent on three times the layer thickness in front of the wall squared,

$$F_{max} = \frac{1}{2} \cdot \rho_w \cdot g \cdot (3 \cdot \eta)^2. \tag{2.10}$$

Based on the findings from Asakura et al. (2002) an experimental test campaign on the same set-up excluding the vertical wall was carried out by Robertson et al. (2011). The incoming and unobstructed bore flow parameters, thickness η [m] and velocity u [m/s], were related to the maximum bore impact force F_{max} [N] and an empirical best-fit equation was derived (see Equation 2.11),

$$F = \frac{1}{2} \cdot \rho_w \cdot g \cdot \eta^2 + \rho_w \cdot \eta \cdot u^2 + \rho_w \cdot g^{\frac{1}{3}} \cdot (\eta + u)^{\frac{4}{3}}. \tag{2.11}$$

Recently, tsunami impacts on storm walls were researched by Kihara et al. (2015). They noticed that the pressure distribution at the wall changes from dynamic to more quasi-steady state (>5 s) over the duration of the impact. In quasi-steady state an almost hydrostatic pressure distribution occurred over the wall height, dependent only on the bore depth in front of the wall (for $\eta > 1.5$ m). The maximum force peak F_{max} [N] was then the hydrostatic force or the integrated pressure over the run-up height (see Equation 2.12),

$$F_{max} = \frac{1}{2} \cdot \rho_w \cdot g \cdot \eta_{max}^2. \tag{2.12}$$

Additionally, a variety of drag-force-based approaches in the field of tsunami impact research existed for dry bed surges and wet bed bores (Wüthrich, 2017; Fujima et al., 2009; Arnason, 2005; FEMA, 2000; Ramsden, 1993). They approximated the maximum bore impact force using a variation of the Morrison equation, neglecting the inertia term, and thus focusing on the drag force F_{max} [N] term of the bore flow (see Equation 2.13),

$$F_{max} = C_d \cdot \rho_w \cdot b \cdot (\eta \cdot u^2)_{max}. \tag{2.13}$$

In Equation 2.13 the density of water ρ_w is approximated as 1.000 kg/m^3, the building width is b [m], the flow thickness is η and depth average bore velocity is u [m/s]. Often flow thickness η and velocity u were measured without the structure present, assuming that a maximum momentum flux would yield in the maximum impact force (Wüthrich, 2017). The use of a drag coefficient C_D in the context of partially submerged structures and not fully developed flow conditions is physically

not entirely correct. The unsteady nature of the flow results in unbalanced hydrostatic forces acting on the structure and 3D effects of the streamlines around the structure (Stolle et al., 2018). Hence, the authors either assumed constant flow conditions and a fully submerged structure (Fujima et al., 2009; Arnason, 2005; FEMA, 2000; Ramsden, 1993) or made use of an equivalent resistance coefficient C_r accounting for the physical differences (Wüthrich, 2017; Arnason et al., 2009). Furthermore, a distinction was made between maximum surge force, related to the initial slamming impact of the flow against the structure, and hydrodynamic force related to the flow field after the initial impact. A coefficient C=3 for the maximum surge force (Arnason, 2005; Ramsden, 1993) and C=2 for the hydrodynamic force was used (Wüthrich, 2017; Arnason et al., 2009; FEMA, 2000).

Table 2.5: Drag/resistance coefficients C_D, C_r to approximate the maximum tsunami impact force on buildings

Wüthrich (2017)	**Arnason et al. (2009)**	**Fujima et al. (2009)**	**Arnason (2005)**	**FEMA (2000)**	**Ramsden (1993)**
C_r	C_r	C_D	C_D	C_D	C_D
2	2	∼1	3	1.2-2	3

While the experiments of Wüthrich (2017) were conducted for dry bed bores travelling on flat horizontal surfaces, the experiments from Fujima et al. (2009) involved a 1-in-3 dike slope and a promenade with a vertical wall at the end. The situation for storm walls, with no flow around the structure, was not entirely the same as for tsunami bore impacts on buildings with small widths. The buildings were relatively narrow compared to the long-crested tsunami bores. Therefore, the empirical impact predictions derived for structures with dry backsides (Kihara et al., 2015; Robertson et al., 2011; Asakura et al., 2002; Cross, 1967) were of major interest due to their geometrical similarity to this study. Furthermore, Tanimoto et al. (1984) predicted the first force peak F_1 as 3.3 times the second force peak F_2. Another upper limit for the first force peak F_1 caused by a tsunami bore was introduced by Ramsden (1996) and Arnason (2005) as 150% of the subsequent hydrodynamic force of the quasi-steady flow F_2. Recently, Chen et al. (2017) proposed to use at least a factor 2.5 to calculate the first dynamic force peak F_1 based on the second quasi-static force peak F_2.

A number of studies were conducted on similar geometries to the geometrical set-up of the present study (mild foreshore, dike). Formulas predicting an individual bore impact force were investigated. For regular waves and a variable wall location, a study was conducted in a small-scale experimental set-up (Chen et al., 2012). Based on momentum flux theory they were able to predict the force F_{max} [N/m] solely dependent on the maximum run-up height $R_{h,max}$ of the water at the wall. The run-up height was measured by a wave gauge installed 1.5 cm in front of the wall. The coefficient C_1=0.33 was defined as a substitute for the unknown bore

Table 2.6: Empirical and semi-empirical approaches to calculate the impact force on a vertical wall caused by a bore like flow.

Reference	Equation	Model scale	Geometry	Waves	Input parameter	Impact type
Cross (1967)	2.7	Small	Flat bottom, wall	Tsunami bore	η, u , Θ	Dynamic
Ramsden (1996)	2.9	Small	Mild foreshore, building	Wet bed bore	η, h, c, b	Dynamic
Asakura et al. (2002)	2.10	Small	Mild foreshore, wall	Tsunami bore	η	Dynamic
Robertson et al. (2011)	2.11	Small	Flat foreshore, wall, no wall	Tsunami bore	η, u	Dynamic
Kihara et al. (2015)	2.12	Large	Flat bottom, wall	Tsunami bore	R_h	Quasi-static
Drag force	2.13	Small	Flat bottom, building	Tsunami wet bore, dry bed surge	η, u	Dynamic
Chen et al. (2012)	2.14	Small	Mild foreshore, dike, promenade, wall	Regular waves	R_h	Quasi-static
Chen et al. (2015)	2.18	Small	Mild foreshore, dike, promenade, wall	Regular waves	η, $H_{m0,t}$, A_c, G_c, L, α	Dynamic/ Quasi-static
Van Doorslaer et al. (2012)	2.15	Large	Overtopping simulator, promenade, wall	Overtopping volume	η, u	Dynamic
Van Doorslaer et al. (2017)	2.16	Large	Dike, promenade, wall	Irregular waves	η, u, R_c	Dynamic
Van Doorslaer et al. (2017)	2.17	Large	Dike, promenade, wall	Irregular waves	$H_{m0,t}$, R_c	Dynamic/ Quasi-static

front angle in the momentum flux theory (Equation 2.14),

$$F_{max} = C_1 \cdot \rho_w \cdot g \cdot R_{h,max}^2. \tag{2.14}$$

In a different approach the wave overtopping simulator (Van Der Meer et al., 2010) was used to simulate an overtopping bore by releasing a defined volume of water (500 l/s per m up to (5.000 l/s per m) on to a 10m wide promenade and measure the impact force F_{max} [N/m] of the bore flow against two measurements plates installed at the end of the promenade (Van Doorslaer et al., 2012). Additionally, bore flow thicknesses η [m] and velocities u [m/s] were measured by means of a potentiometer and paddle wheels attached to a surf board floating on the water. Only the results for a non-overtopped vertical measurement plate were evaluated (Equation 2.15),

$$F_{max} = 1.09 \cdot u + 52.1 \cdot \eta - 9.5. \tag{2.15}$$

Full scale experiments were conducted in the GWK Hannover for a set-up with deeper water at the dike toe, 10 m wide promenade and wall at the end of the promenade (Van Doorslaer et al., 2017). Bore thickness η [m] was measured in the vicinity of the wall by means of wave gauges, and the bore front velocity was estimated as the distance between wave gauge and wall divided by the bore travel time. After applying a selection routine to detect discrete overtopping events, 621 impacts in the lower range were used to derive an empirical equation for the impact force F_{max} [N/m] (Equation 2.16),

$$F_{max} = \rho_w \cdot g \cdot R_c^2 \cdot 0.4 \cdot exp(\frac{(u \cdot \eta)_{max}}{\sqrt{g \cdot R_c^2}})^{1.313}. \tag{2.16}$$

where R_c is the freeboard, defined as the distance between the still water level and the top of the wall at the end of the promenade. They noticed that the instantaneous discharge as the product of bore thickness η and velocity u is a better estimator of the maximum impact force than one of the two parameters studied individually. Also, they stated that the maximum instantaneous discharge decreased by 30% over the 10m width of the promenade

Finally, approaches to predict an average impact force based on the incoming spectral wave and geometrical parameters were derived by Van Doorslaer et al. (2017) and Chen et al. (2015). Average impact force predictions are often preferred as they produce better prediction accuracy of the derived equations and are less effected by the scatter of the maximum impact force. However, with the drawback that the information about maximum impact force and individual impact behaviour is lost. Van Doorslaer et al. (2017) established a prediction formula based on the same GWK experiments described above for the $F_{1/250}$ impact force (see Equation 2.17). $F_{1/250}$ is here defined as an average impact force of the of n highest impact forces. Note, that n is derived from $1/250$ times the number of incident waves at the dike toe,

$$\frac{F_{1/250}}{\rho_w \cdot g \cdot R_c^2} = 7.8 \cdot exp(-2.02 \cdot \frac{R_c}{H_{m0,t}}). \tag{2.17}$$

Where R_c is again the freeboard, defined as the distance between the still water level and the top of the wall at the end of the promenade and $H_{m0,t}$ the spectral incident wave height at the dike toe.

Chen et al. (2015) derived an empirical formula to predict overtopping impact forces based on the momentum flux equations (Hughes, 2004a,b). The empirical formula is a function of the properties of the incoming waves and the dike geometry,

$$F = \rho_w \cdot g \cdot \eta_{a0}^2 \cdot 1.7 \cdot C_{tr}^2 \cdot f(\beta) \cdot exp(-3.08 \cdot f(\beta) \cdot \frac{G_c}{L}). \tag{2.18}$$

With, the unobstructed flow thickness on the promenade $\eta_{a0} = \alpha \cdot H_{m0,t} \cdot [1 - \frac{A_c}{2.25 \cdot H_{m0,t} \cdot tanh(0.5 \cdot \xi)}]$, the correlation coefficient for obstructed and unobstructed flow depth $C_{tr} = 0.33 \cdot \ln(G_c/L) + 1.86$, the dike slope function $f(\beta) = \cot(\beta)$, the dike slope β, the wave length L, the wave height at the toe $H_{m0,t}$, the crest freeboard A_c, the breaker parameter defined as $\xi = \frac{tan(\alpha)}{\sqrt{(H_{m0,t} \cdot L)}}$.

The formula contains several coefficients, such as a dike slope function $f(\beta)$ and a correlation coefficient for unobstructed and obstructed flow depth C_{tr}, and an initial overtopping flow depth coefficient $\alpha = 0.77$, which were quantified using data from experimental model tests. The physical model tests were carried out in the Flanders Hydraulics wave flume facility. The basic geometry consists of a foreshore, a dike, a promenade and a storm wall. The calculated forces using the derived empirical formula match very well with the measured values. No relationship between the average overtopping discharge q and measured forces is provided. For the analysis only regular waves were analysed.

To summarize, existing semi-empirical formulas to predict the impact force were evaluated from related literature. As can be seen from Table 2.6, none of the existing formulas were derived from large-scale experiments, featuring a mild foreshore and shallow water and for irregular wave conditions at the same time. Hence, an impact load prediction based on large-scale experiments to avoid scale related effects, in mild foreshore and shallow water conditions to account for the coastal geometry of low-lying countries and irregular wave conditions for most realistic wave boundary conditions, is still missing. Additionally, there is no impact force prediction available which takes into account the overtopping discharge q, as the currently up-to-date design parameter.

2.4.2 Statistical prediction formulas

It was previously noted that bores resulting from irregular sea states show a stochastic impact behaviour (Chen, 2016; Altomare et al., 2015), thus hindering a deterministic relation between each individual bore and the induced impact load. An alternative way of describing the overtopping bore-induced loads is to look at the distribution of impacts and derive an impact load related to a certain exceedance probability; a statistical prediction of the bore-induced loads.

Statistical analysis of overtopped bore impact loads on dike mounted vertical walls was carried out previously by Van Doorslaer et al. (2017) and Chen et al. (2016). The main difference between both studies can be found in the geometrical set-up. Chen et al. (2016) used a mild foreshore slope 1-to-35, resulting in shallow to extremely shallow water depths (after Hofland et al. (2017)) and broken waves at the dike toe. Van Doorslaer et al. (2017) instead conducted the experiments without mild foreshore in deep to shallow water conditions at the dike toe (after Hofland et al. (2017)), resulting in wave breaking against the dike.

Chen et al. (2016) draw the similarity between individual overtopping (Eurotop, 2016) and impact force distributions and fitted a Generalized Pareto (GP) distribution function to the upper 10% of measured force peaks. Note, before fitting they used the average mean wave power (Goda, 2010) as a high-pass threshold and performed fitting to the 10% highest force peaks above this threshold. Maximum product of spacing's (MPS) fitting method was used. The authors postulate a prediction formulas for the overtopped bore impacts by empirically relating the fitting parameters to the wave conditions at the dike toe, geometrical parameters and duration of the storm (test duration) for each test. A seven step procedure was proposed to predict the maximum overtopped bore impact force. The seven step procedure was used to predict the maximum impact force based on the values from this study and compare it to the measured maximum impacts (see Figure 7.2). Firstly, the overtopping force impact probability P_{im} should be calculated 2.19,

$$P_{im} = -0.06 \cdot ln(\frac{G_c \cdot A_c}{L_t \cdot H_{m0,t}}) - 0.09. \tag{2.19}$$

Where G_c was the promenade width, A_c the crest height between the still water

level and the dike crest, $H_{m0,t}$ the incident spectral wave height at the dike toe location and L_t the shallow water wave length estimated with Equation 2.20,

$$L_t = T_{m0-1,0,t} \cdot \sqrt{g \cdot h_t}. \tag{2.20}$$

Note that the impact probability for plotting positioning of the highest 10% of impacts P_{im}=$N_{f,10\%}/N_{toe} + 1$ was expressed based on the number of waves at the dike toe N_{toe}. The number of waves at the dike toe N_{toe} were estimated using N_{toe}=$D/T_{m-1,0,t}$. With D [s] the duration of the storm or test duration and $T_{m-1,0,t}$ the incident spectral wave period measured at the dike toe. Secondly, the characteristic force F_c was determined (Equation 2.21) based on the physical overtopping processes parameters wave run-up R_u, crest freeboard A_c, spectral wave height at the dike toe $H_{m0,t}$ related to the 10% highest force peaks,

$$F_c = \rho \cdot g \cdot [H_{m0,t} \cdot \frac{A_c}{R_u}]^2. \tag{2.21}$$

The wave run-up which is exceeded by 2% of the run-up tongues R_u was calculated using Equation 4 from Van Gent (2001), the spectral wave parameters at the dike toe and the coefficients from Table 5 (c_0=0, c_1=3.8). The authors argued that the physical processes were accounted for by including the run-up as a parameter. A relationship between individual waves and impacts however was discarded, due to stochastic behaviour. The characteristic force F_c was then used to derive the empirical threshold of the Generalized Pareto distribution F_u in a third step (see Equation 2.22),

$$\frac{F_u}{\rho \cdot g \cdot H_{m0,t} \cdot A_c} = 0.84 \cdot exp(0.36 \cdot \frac{F_c}{\rho \cdot g \cdot H_{m0,t} \cdot A_c}). \tag{2.22}$$

As the fourth and fifth step the scale λ (Equation 2.23) and shape κ (Equation 2.24) parameter were derived respectively based on the empirically established to spectral wave height at the dike toe $H_{m0,t}$, the crest freeboard A_c, the characteristic force F_c and the fresh water density ρ and acceleration due to gravity g;

$$\frac{\lambda}{\rho \cdot g \cdot H_{m0,t} \cdot A_c} = 0.37 \cdot exp(0.37 \cdot \frac{F_c}{\rho \cdot g \cdot H_{m0,t} \cdot A_c}), \tag{2.23}$$

$$\kappa = -0.59 \cdot ln(\frac{\lambda}{\rho \cdot g \cdot H_{m0,t}^2}) - 0.34. \tag{2.24}$$

The expected overtopping bore-induced impact force exceedance probability P_m was calculated based on $P_m = i/(N_{toe}+1)$ as the sixth step. Setting i=1 and substituting the number of waves at the dike toe with N_{toe}=$D/T_{m-1,0,t}$ the

exceedance probability for the maximum overtopping bore-induced impact force and a storm peak duration D might be obtained. Finally, in the seventh step the bore impact force was computed (Equation 2.25),

$$F_m = F_u \cdot \frac{\lambda}{\kappa} \cdot [(\frac{P_{im}}{P_m})^{\kappa} - 1]. \tag{2.25}$$

Van Doorslaer et al. (2017) instead used a Weibull extreme value distribution function (Equation 7.1) and the number of overtopping waves to define the bore impact force exceedance probability $P_m = i/(N_{ow+}1)$. The number of overtopping waves was derived by multiplying the number of waves at the dike toe N_{toe} with the probability of overtopping P_{ov} (after Victor et al. (2012)). Here the number of waves at the dike toe were derived from the analyzed time-series of wave gauge measurement at the dike toe. Furthermore the fitting sample size of force peaks was determined based on 20% of the number of overtopping waves N_{ow}. This is significantly different from Chen et al. (2016) who used 10% of the number of impacts for the fitting. A fixed high-pass threshold to detect force peaks was chosen at 1N/m in model scale.

The non-dimensional force $F*$ was defined as $F^*{=}F/(\rho \cdot g \cdot R_c^2)$. Note that here the freeboard R_c was defined as the distance between the still water level and the top of the wall, where the impacts were measured. Hence, for the purpose of comparing the results to this study (non-overtopped vertical wall for all data-sets 'UGent1'-'UGent3' and 'DeltaFlume') a wall height of d_w=1m was selected and added to the crest freeboard A_c. The equations for scale λ (see Equation 2.26) and shape κ (see Equation 2.27) parameter were empirically established by relating the distribution parameters to the crest freeboard A_c, spectral wave height at the toe $H_{m0,t}$, the freeboard including the wall height R_c and the average impact force for all force peaks F_{mean},

$$\frac{\lambda}{\rho \cdot g \cdot R_c^2} = F_{mean}, \tag{2.26}$$

$$\kappa = 1.061 - 0.374 \cdot \frac{A_c}{H_{m0,t}}. \tag{2.27}$$

The average impact force F_{mean} for was empirically derived (see Equation 2.28). It was expected that a fixed high-pass threshold (selected at 1 N/m) significantly influences the obtained empirical relation for the average force F_{mean},

$$\frac{F_{mean}}{\rho \cdot g \cdot R_c^2} = 1.8 \cdot exp(-2.66 \cdot \frac{R_c}{H_{m0,t}}). \tag{2.28}$$

When rearranging Equation 7.1 for the impact force and assuming that all overtopping bores will cause an impact at the wall (Number of overtopping bores N_{ow} = number of impacts N_i) the maximum impact force can be calculated (see

Equation 2.29). The exceedance probability for the maximum impact force was $P_m = 1/(N_{ow}+1)$, based on the number of overtopping bores and had to be introduced manually,

$$\frac{F_m}{\rho \cdot g \cdot R_c^2} = 10^{(log(\lambda)+\frac{1}{\kappa}\cdot log(-ln(P_m)))}. \tag{2.29}$$

The comparison of methodologies from Chen et al. (2016) and Van Doorslaer et al. (2017) yields useful insights for any statistical prediction of overtopping bore-induced loads on vertical walls and can be summarized as follows:

- Van Doorslaer et al. (2017) used a Weibull distribution function, which was only slightly less accurate according to the comparison made by Chen et al. (2016). Simplicity of the Weibull distribution might be an argument to further develop on this method.

- Two different definitions for the exceedance probability P_m were introduced, which will alter the obtained force prediction significantly. Either the number of overtopping waves (Van Doorslaer et al., 2017) or the number of waves at the dike toe (Chen et al., 2016) were used to define P_m. Both definitions of P_m were affected by the high variability of spectral bore parameters in the case of very shallow to extremely shallow waters. This causes difficulties to accurately define the number of waves at the dike toe, since different analysis methods might influence the results. Furthermore, assuming that there are more waves at the dike toe N_{toe} or overtopping N_{ow} than number of impacts N_I, reduces the exceedance probability P_m of the impact force artificially. Also, the information about the change in number of impacts due to a variable promenade width was not accounted for by both definitions. Besides others this lead to the effect that when selecting an upper percentile for the fitting of the extreme value distribution, the reduced number of impacts for example due to a longer promenade width were not represented.

- The choice for an upper percentile of force peaks to be used for the fitting of the statistical extreme value distribution was made and selected as 20% of the overtopping waves (Van Doorslaer et al., 2017) and 10% of the impacting bores (Chen et al., 2016). Chen et al. (2016) points out that a sensitivity study regarding the upper percentile is still missing. In both studies a scattered distribution of the fitting parameters was noted, probably due to small samples sizes and accumulation of errors when empirically fitting the distribution parameters. This was especially true for tests with a small number of measured impacts.

- Both approaches do not take into account the average overtopping discharge as a variable to describe shape and scale parameter empirically. Hence, there was no direct link between the average overtopping discharge q [m^3/s per m] and the distribution of impact loads.

2.5 Scale- and model effects in laboratory experiments on bore impacts

In coastal engineering practice physical modelling is a widely used method to better understand and solve issues related to wave transformation and wave-structure interaction processes. The physical modelling method was adopted by the field of coastal engineering from the first hydraulic models conducted by Reynolds (1883) and Prandtl (1904). Large and expensive coastal structures are often tested before they are built, to study the fundamental processes and response to wave attack. Due to time constraints, feasibility and economic reasons often a laboratory small-scale model of these coastal structures is tested instead of a prototype version (Heller, 2011; Frostick et al., 2011). Laboratory experiments represent only part of the reality and uncertainties due to the scaled representation of reality are evident. Hence, a good understanding of scale and model effects is essential, to interpret the obtained results correctly. A scaled-down model of the prototype can be considered similar if the appropriate scaling laws are applied (Frostick et al., 2011). Maintaining similarity between the prototype and the model whilst scale distortion, requires that the following conditions are met: 1) geometric similarity to reproduce the same shapes, 2) kinematic similarity to reproduce the same flow velocities and geometrical motion and 3) dynamic similarity to reproduce the same forces in the scale model (Equation 2.31, 2.31, 2.32),

$$L_{ratio} = \frac{(L)p}{(L)_m}, \tag{2.30}$$

$$V_{ratio} = \frac{(V)p}{(V)_m}, \tag{2.31}$$

$$F_{ratio} = \frac{(F_i)p}{(F_i)_m} = \frac{(F_g)p}{(F_g)_m} = \frac{(F_\mu)p}{(F_\mu)_m} = \frac{(F_e)p}{(F_e)_m} = \frac{(F_p)p}{(F_p)_m} = \frac{(F_s)p}{(F_s)_m}. \tag{2.32}$$

The combined geometric and kinematic similarity provides the scale ratios for length, time, velocity, acceleration and discharge. While the first two are often met the third one requires a balance of inertial, gravitational, fluid friction, elastic compression, pressure and surface tension forces. A balance of all force ratios cannot be achieved and therefore scaling bias or scale effects will exist when laboratory scale model tests are conducted (Heller, 2011; Frostick et al., 2011). Furthermore, the scaling bias will increase with increasing scale number. Hence, it is important to consider the dominant forces in order, to apply the correct scaling law. Scaling laws are often based on non-dimensional numbers which are derived from experiments and by intuitively understanding and choosing the correct and sufficient number of variables. A non-dimensional number describes the interaction of physical parameters without knowing the underlying equation or exact process. Several non-dimensional numbers are derived, which are used for scaling purposes, and

maintaining certain characteristics (kinematic, dynamic, geometrical) of the fluid flow and structure. Depending on the process to be studied an appropriate non-dimensional scale number is chosen. If the non-dimensional scale number is the same in both prototype and model representation similarity of the underlying forces is assumed. Most important in laboratory flow conditions are the non-dimensional Froude (inertial over gravity forces), Reynolds (inertial over viscosity forces) and Weber (inertial over surface tension forces) number. Typically, in situations where the dominant restoring force is gravity, inertial forces are dominant and the effect of the remaining forces such as kinematic viscosity is small (such as open channel flows), Froude number (Equation 2.33) or Froude scaling is applied (Bullock et al., 2001). Froude number was developed via experiments by William Froude and served to quantify the resistance of floating objects,

$$F_r = \frac{u_p}{\sqrt{g \cdot L_p}} = \frac{u_m}{\sqrt{g \cdot L_m}}. \tag{2.33}$$

In Froude scaling the balance between inertia, related to flow velocity u [m/s], and gravitational, related to $\sqrt{g \cdot h}$ [m/s] and characteristic length L [m], force between the model and prototype is achieved. All other force balances are neglected. The Froude factors λ for the investigated parameters of this study are given in Table 2.7. Later it was also shown that the Froude number can be linked to general continuum mechanics with the incompressible Navier-Stokes-Equation.

Table 2.7: Froude Scaling factors

Parameter	**Froude scaling factor**
Length [m]	λ
Time [s]	$\sqrt{\lambda}$
Force [kN/m]	λ^2

The non-dimensional Reynolds number (inertial over viscosity forces) is a measure of the turbulence in a system. For pipe flow Reynolds defined numbers lower than 2,000 as laminar flow (smooth flow, disturbance damped by viscous effects), higher than 4,000 as turbulent (irregular, vorticity) and in between as transitional flow. In coastal engineering praxis it is often assumed that the Reynolds number is sufficiently high, meaning the flow is sufficiently turbulent to not be influenced by viscose effects. However, this assumption is questionable when the flow thicknesses become very small or the flow velocities very low. The Reynolds number is given in equation 2.34,

$$R_e = \frac{\rho \cdot u \cdot L}{\eta}. \tag{2.34}$$

With; the density of the fluid ρ [kg/m^3], the flow velocity u [m/s], the characteristic length L [m] and the dynamic viscosity η [Ns/m^2].

The Weber number (inertial over surface tension forces) gains more importance for the study of capillary waves or very small flow thicknesses, when surface tension effects become important. Schüttrumpf (2001) derived a critical Weber number of 10, which should be exceeded in the model to avoid that surface tension influences the process. Besides that, the Weber number (Equation 2.35) is not often used in typical coastal engineering praxis when scaling is applied to determine the model dimensions,

$$W_e = \frac{\rho \cdot u^2 \cdot L}{\sigma}. \tag{2.35}$$

Where; the density of the fluid ρ [kg/m^3], the flow velocity u [m/s], the characteristic length L [m] and the dynamic viscosity σ [N/m]. Again, the assumption that surface tension effects are of minor importance has to be checked considering the scaled dimensions at hand.

Other non-dimensional numbers used for scaling purposes are Euler number (local pressure over kinetic energy) and Mach number (Inertial over elasticity forces). Dimensional analysis (Buckingham, 1914) yields that the fluid properties and physical constants (density of water ρ [(kg/m^3], the dynamic viscosity of water μ [N s/m^2], the surface tension of air and water σ [N/m], the bulk modulus of elasticity of water E_b [Pa], and the acceleration of gravity g [m/s^2].), flume and model geometry (lengths L [m]) and flow properties (velocity v [m/s] and the pressure differences δP [Pa]) can be described with the three dimensions length [L], time [T] and mass [M]. This results in the above-mentioned five non-dimensionalnumbers (Froude-, Reynolds-, Weber-, Euler- and Mach). Each number should be the same in both model and prototype to achieve full dynamic similarity. The simultaneous similarity of the non-dimensional numbers can not be achieved (for example Froude number similarity requires $V_r = \sqrt{L_r}$ and Reynolds number similarity requires $V_r = \frac{1}{L_r}$ at the same time). Hence, in most cases only one non-dimensional number is chosen for scaling purposes, to model the most dominant process/force ratio.

The choice of one non-dimensional number for scaling purposes can become a source for unwanted scaling effects if for example air-water flow is modelled, such as with entrained and entrapped air in turbulent flows. Blenkinsopp and Chaplin (2007) observed that the void ratio scaled geometrically. Blenkinsopp and Chaplin (2011) continued to add that the bubble plume evolution and size distribution of the bubbles remained the same between scales. This further implies that the rise time of the bubbles is the same in both models as it depends on the bubble size. Since the distance towards the water surface is shorter in the small-scale model, the bubbles will escape the water earlier compared to the large-scale model and a larger amount of ambient air bubbles is expected in the latter (Bullock et al., 2001). The dissimilarity in void ratio is expected to change the compressibility of the water and finally the damping characteristics of the dynamic impacts; the so called cushioning effect (Bullock et al., 2001).The dissimilarities in compressibility of the water between the model and prototype is not accounted for with Froude scaling (Blenkinsopp and Chaplin, 2011, 2007; Bullock et al., 2001). This is expected to lead to an overestimation of the impact forces, when upscaling the results from

small-scale to prototype (Cuomo et al., 2010). Van Gelder et al. (2001) proposed to use a mean reduction factor of 0.67 with a variation coefficient of 30% for the up-scaled maximum impact force measured in a scale-model. This counteracted the scaling error caused by dissimilarities in the air entrainment. Additionally surface tension or viscous effects may play a role if the turbulent overtopping flow in the scale model becomes too small, which again is not accounted for scaling with Froude number (Schüttrumpf, 2001). In this case the low Reynolds number would indicate smooth flow and additional friction as a result and the low Weber number indicates the influence of surface tension effects. This would lead to a potential further reduction or stop of the flow in the small-scale model and in turn to a reduction of impact force as well.

Previously, laboratory experiments were conducted for a scaled geometry similar to the Belgian coast, with a mildly sloping foreshore, shallow waters at the dike toe, a dike and attached to the dike a promenade, with a wall at the end (Van Doorslaer et al., 2017; Chen, 2016; Streicher et al., 2016). In the scale-models the overtopping bore-induced impact forces against the wall were measured and up-scaled to prototype using Froude scaling law. According to the theory higher impact forces were expected for the up-scaled small-scale results when compared to prototype or large-scale measurements.

Besides the scale-effects in small-scale laboratory experiments, model effects might also play a role and influence the obtained force measurement. Model and scale effects are often intertwined, such as with salt water in prototype and fresh water in the model. The difference in densities is firstly a model effect but secondly also affecting the compressibility of the water and therefore the dynamic similarity and force balance related to scale effects. Other model effects are related to the wave generation and absorption software and hardware or the measurement techniques in the model (Hughes, 1995). The poor representation of the real sea-states and especially the long waves by using theoretical wave spectra in the model is another source of model effects (Oumeraci et al., 2000). Typically infragravity waves with prototype periods $\sim 100 - 200\,\mathrm{s}$ are difficult to reproduce in the small-scale models. The measurement system itself might influence the measured impact forces. The load cells and measurement system is often less stiff in the small-scale model. Also the use of materials for the bathymetry, topography and load measurement plate in the model influences the resulting force measurement if it does not behave (less or more smooth, erosion, stiffness etc.) similar to the prototype situation.

Another source of uncertainties in impact force measurement is the stochastic behaviour of the bore-induced impact process itself and the resulting non-repeatability of overtopping bore-induced impacts (Chen, 2016; Altomare et al., 2015). Typically, this is explained by 3D effects of the turbulent bore front or small differences in air entrapment and entrainment in the impacting flow, which lead to unpredictable variations and thus measured impact forces. An overview of uncertainties found in bore-induced load measurements in laboratory scale models is given in Table 2.8.

Table 2.8: Uncertainties for bore-induced impact force measurements in laboratory scale models

Non-repeatability	Model effects	Scale effects
3D effecs of turbulent bore front	Wave generation	Compressibility
Air entrainment	Wave absorption	Surface tension
Air entrapment	Load cell choice	Viscosity
	Measurement set-up	Water properties
	Water/Material properties	Scaling laws

2.6 Research gaps and specific objectives

The findings of the literature review pointed to a lack of experimental studies investigating short-duration bore interaction processes, for bores resulting from irregular broken waves in shallow foreshore conditions, prior to impact on any dike mounted structure. The exact generation mechanism of the double peak impact force signal shape was discussed controversially and also asks for a more detailed investigation of the bore-induced impact process. Previously, a number of semi-empirical prediction formulas were derived for overtopping bore-induced loads. Nevertheless, the approaches were either derived for deep water conditions at the dike toe (not accounting for the broken bore due to depth limitations), regular waves (not accounting for a most realistic wave field), small-scale data-sets (eventually influenced by scale related effects due to air entrainment) or focused on the beginning of a wave group (not accounting for the bore interaction between incoming and reflected bores). Additionally, there was no design guidance, expressed as an impact force prediction formula, to relate the average overtopping discharge q to an impact force F. The overtopping discharge q is a key criteria for design of coastal structures and the link was therefore considered important. Existing statistical impact force prediction approaches, derived for overtopping bore-induced loads on dike mounted walls, suffer from the drawback that not sufficient data points were used for the statistical fitting. This had negative implications on the prediction accuracy of these approaches, as the scatter in the prediction of statistical parameters increased. Furthermore, there was a knowledge gap about the uncertainties in force predictions related to the stochastic behaviour of overtopping bore-induced loads on dike mounted walls.

The research gaps are addressed and the main objective (see Section 1.2) of this study pursued with the following specific objectives:

1. To perform small- and large- scale hydraulic model tests in a 2D wave flume, to measure overtopped bore-induced impact loads on vertical walls. Furthermore, to re-analyse existing data-sets which have been performed for similar geometries and measuring bore-induced impact loads. The analysis will be done in terms of physical processes underlying wave run-up, overtopping and short-duration bore-induced impacts on dike-mounted walls. High

resolution measurements of the bore transformation processes in the vicinity of the wall and pressure distribution, as well as total horizontal impact load measurements at the wall are used for this purpose.

2. To review existing empirical formulas for their predictive capability of maximum overtopping bore-induced impact forces. Furthermore, to propose semi-empirical formulas linking the maximum impact force on a vertical wall or building to meaningful parameters, such as the average overtopping discharge, incoming bore thickness, velocity or run-up at the wall. These semi-empirical and theoretical formulas provide the basis for future design guidance.

3. To develop a more generic impact load prediction tool based on statistical analysis of maximum overtopping bore-induced loads. A special focus is on the novel link between overtopping discharges q and impact forces F, as well as to use a sufficient number of data points for the statistical fitting. Furthermore, to investigate the influence of the upper fitting threshold on the prediction.

4. To investigate the uncertainties in laboratory overtopped bore-induced impact measurements due to stochastic non-repeatability, model- and scale effects. This study will be conducted by comparing similar data-sets derived from two different laboratory scale models.

2.7 Thesis outline

Bore-induced loading on and bore overtopping of vertical coastal structures and buildings was identified as a key research challenge for coasts of low-lying countries. Small- and large-scale laboratory modelling of overtopping bore-induced loads was conducted and led to more fundamental physical insight of the involved processes and the development of empirical and statistical design tools.

The thesis outline was given in Figure 2.3 and will be discussed hereafter. Each chapter of this thesis was preceded with a brief overview and the specific objectives. The general introduction, background and motivation as well as general objectives were given in Chapter 1. Continued with the literature review in Chapter 2 to identify the research gaps and formulate the specific objectives for this study. In the following chapter 3, the conducted laboratory model tests in the small-scale (Ghent University) and large-scale (Deltares Delta Flume) facility were described. Besides the variety of geometrical set-ups and hydraulic boundary conditions, the detailed measurement set-up and synchronised data-processing routines were outlined. A study of uncertainties related to non-repeatability issues, model- and scale effects of overtopping bore-induced loads on dike mounted walls was conducted in Chapter 4, to establish a baseline accuracy against any prediction results can be judged. In the subsequent Chapter 5, two tests from the large-scale model test with wave conditions similar to a 1,000 and 17,000 annual recurrence interval at the Belgian coast were depicted for a detailed analysis. The underlying physical processes of bore interaction prior to impact, bore run-up at the wall and bore-induced impact

loads at the wall were dissected for a better understanding of the phenomena. With this knowledge, a review of empirical formulas to predict the impact force at the wall was conducted in Chapter 6. The existing approaches were extended by semi-empirical formulas and a theoretical model. The overall poor predictability of individual overtopping bore-induced impact forces with empirical formulas and the theoretical model led to the development of a novel statistical prediction methodology in Chapter 7. Maximum impacts from several data-sets were combined into one data-set for this purpose. In this way the stochastic uncertainties in predicting an individual event were overcome by the potentially better predictive capability of a larger data-set, statistically more robust. A special focus was put on the novel link between average overtopping discharge q and the bore impact force F. Finally, the key findings were summarised and recommendations for future research were given in the concluding Chapter 8.

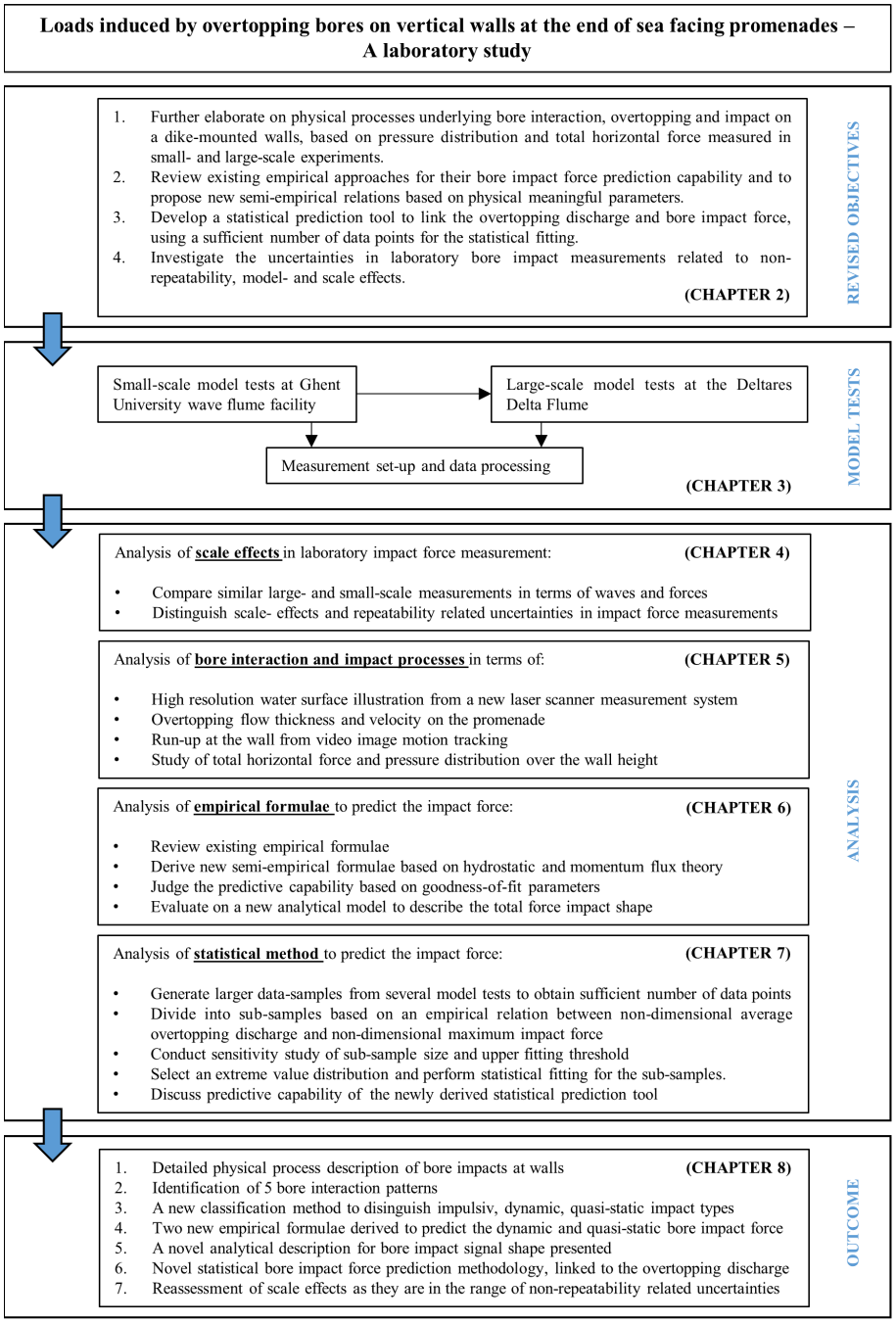

Figure 2.3: Thesis outline

Chapter 3

Experimental set-up

The modelled geometry was a scaled representation of a large part of the bathymetry and topography of coasts from low-lying countries and in particular the Belgium coast. Four representative parts were distinguished (see Figure 3.1): (1) A mild sloping foreshore with a combined slope consisting of a transition slope cot(Θ_1) at the beginning of the foreshore and a main slope cot(Θ_2) seaward of the toe of the dike. (2) Attached to the foreshore a dike with a slope cot(α) and (3) a wide crested promenade of width G_c was built. (4) At the end of the promenade a vertical non-overtopped wall with the height d_w was constructed. The overtopped wave impact loads were measured at the wall location. The model dimensions were down-scaled from prototype dimension using Froude similarity and a length scale factor λ.

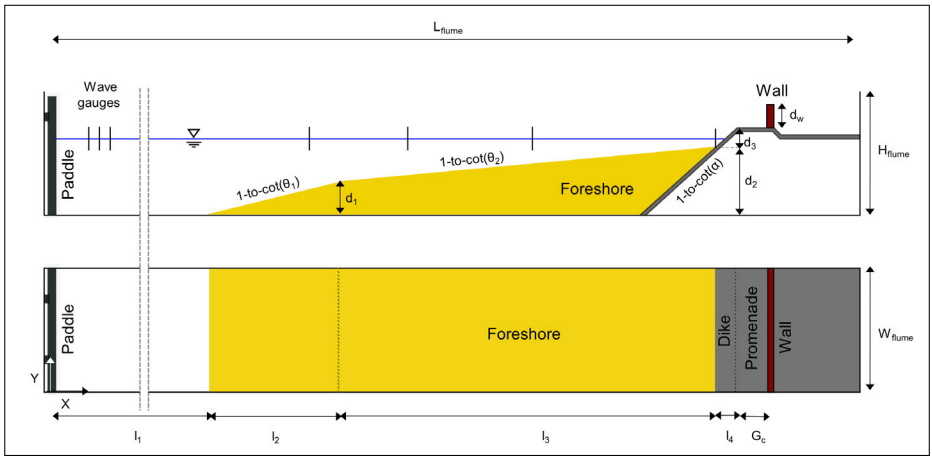

Figure 3.1: Side-view (upper figure) and top-view (lower-figure) sketch of the geometrical model set-up

Three small-scale model tests were conducted in the Ghent University wave flume facility, further referred to as 'UGent1' - 'UGent3' (see Section 3.1). The

model tests were part of the PhD studies and Master Theses projects starting from 2015 to 2018. One large-scale model test was conducted in the Deltares Delta Flume. It was further referred to as 'DeltaFlume' model test (see Section 3.2). The 'DeltaFlume' test was carried out in March 2017 as part of the Hydralab$^+$ project Wave Loads on Walls (WALOWA). Wave conditions similar to a storm with a 1,000 and 17,000 annual recurrence interval were tested during the first small-scale experiment ('UGent1'). In the second small-scale experiment ('UGent2') the range of tested promenade widths G_c was extended, while the third small-scale experiment ('UGent3') was a direct representation of the large-scale experiment from the Delta Flume ('DeltaFlume') and allowed us to study scale-effects related to overtopping wave impacts.

Geometrical (see Section 3.1.1) and hydraulic (see Section 3.1.2) set-up, as well as the test programme (see Section 3.1.3) for the 'UGent1'-'UGent3' model tests was outlined hereafter. A similar documentation was done for the geometrical (Section 3.2.1) and hydraulic (see Section 3.2.2) set-up, as well as the test programme (see Section 3.2.3) for the 'DeltaFlume' model test. Furthermore, the measurement techniques (see Section 3.3) and data processing routines (see Section 3.4) were discussed in this Chapter.

3.1 Ghent University wave flume

The Ghent University wave flume facility is a mid-scale wave flume located at the research campus and coastal engineering research group in Ghent-Zwijnaarde, Belgium (see Figure 3.2). The Ghent University wave flume is operational since 2003 and measures 30 m in length, 1 m in width and 1.2 m in depth. The flume side wall on the opposite end of the wave paddle is made of a 15 m glass wall section, to provide a side-view image on the physical processes during wave transformation and wave-structure interaction. A design water depth of 0.8 m and a maximum wave height of H_{max}=0.35 m can be achieved (Ghent University, 2010). The flume length can be adjusted as it is compartmentalised in four sections. The flume is accessible via the rear end (opposite to the paddle), for easier handling during model construction.

Waves are generated by a piston type wave paddle. The wave paddle is attached to a framework which performs horizontal movements on a linear bearing system and has a maximum stroke length of 1.5 m. The paddle movements are steered by an electro servo motor in step mode and transferred to the paddle via a spindle. The total distance from the wave paddle zero position towards the end of the flume is 3.15 m which yields into 26.85 m flume length which can effectively usable for model testing. The paddle displacements are calculated, transformed into paddle movements using Biésel transfer function (Lykke Andersen and Frigaard, 2010) and allocated to the paddle by an in-house developed wave generation software. The wave generation software is embedded in a LabVIEW^{TM} environment and able to generate both regular and 1^{st} order irregular waves at a paddle steering frequency of 40 Hz. The wave generation software is synchronized with the data acquisition system, such that active wave absorption can be used. The active

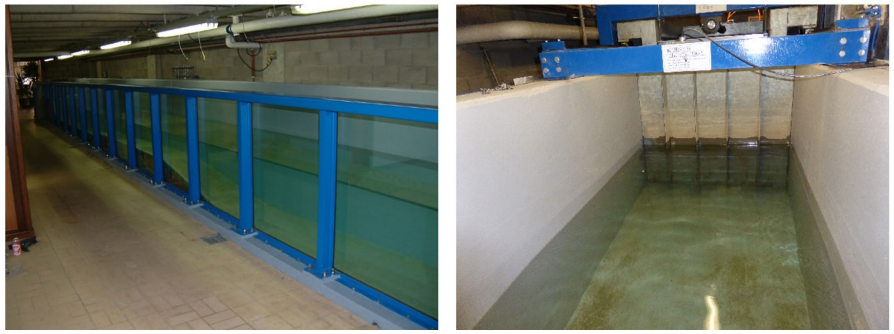

Figure 3.2: Ghent University wave flume facility with glass front along 15m flume width (left figure) and piston type wave paddle (right figure).

wave absorption (AWA) is able to simultaneously absorb the reflected and generate the desired waves (Frigaard and Christensen, 1994; Frigaard and Brorsen, 1995). The set-up for active wave absorption involves two AWA wave gauges in the near wave field from the paddle, approximately 3 water depths (Ghent University, 2010). The distance between the wave gauges is calculated based on the generated wave length. The reflected wave part is incorporated in the newly generated incident water surface elevation steering signal. In this way, the desired incident water surface elevation at the paddle can be achieved.

Two digital filters are used to separate the incident and reflected water surface elevation from the signal of the two AWA wave gauges in real time. The filters are designed to operate in a frequency range which ideally includes all the physical frequencies present in the flume. The according low-pass filter and high-pass filter can be set between $1-1.6\,\text{Hz}$ and $0.25-0.35\,\text{Hz}$ respectively. For a standard experiment, this results in a spectral energy reduction of 5-10% of the peak frequency beyond the limits of the high- and low-cut off frequency. As a result of this set-up it is not possible to absorb frequencies outside the cut-off frequencies. This effects the high frequency capillary waves, but more importantly the low frequency long waves (T_p=$30-300\,\text{s}$ in prototype). The low frequency waves result from the flume seiches, spurious long waves from incorrect bound long wave generation and 1^{st} order wave generation theory that assumes the wave paddle always in zero position to generate the short waves. When not removed by the active wave absorption these additional spurious long waves artificially increase the wave energy in the flume.

3.1.1 Geometrical set-up

The geometrical set-up was chosen as a model representation of a part of the Belgium coast. As stated in Chapter 2 most of the model tests conducted to measure overtopped wave impact loads do not include the mildly sloping foreshore $\cot(\theta_2)$, shallow waters at the dike toe h_t or variable promenade widths G_c. Hence,

a geometrical set-up including a mild foreshore, shallow waters at the dike toe and variable promenade widths was chosen as a similar representation of the reality.

For the 'UGent1' model tests, a cross section with a foreshore slope of cot(θ_2)=35 and a dike slope slope cot(α)=2 was chosen. Foreshore slopes at the Belgian coast varied between 1-to-90 at De Panne in the west and become steeper to about 1-to-20 in Knokke-Heist. The smoother the slope the earlier the wave breaking occurred and more energy was dissipated. Hence, a steep slope was preferred in order to model maximum wave conditions. Furthermore, it was not possible to accurately model the sand properties of the beach material and the morphological changes in a small-scale model. Hence, it was decided to use concrete material to construct the foreshore. This was again considered a worst case scenario, as the energy dissipation within the sand material was not present. Due to length constraints in the Ghent University wave flume the toe of the foreshore was located at approximately -9.25 m TAW in prototype. The water depth at this location was considered deep enough to not effect the wave transformation. According to SWASH calculations on a similar geometry the wave breaking occurred approximately at -4 m TAW in prototype. Anyhow, this means that the foreshore is constructed 271.25m shorter compared to the prototype conditions (Veale et al., 2012) and was continued with a steeper transition slope of cot(θ_1)=2 until the flume bottom (see Figure 3.3). The toe of the dike was set to d_t=6.70 m TAW in prototype and the dike crest location varied between d_c=9 $-$ 10 m TAW in prototype. The resulting dike heights in prototype d_d=2.3 $-$ 3 m were characteristic for the Belgian coast. Attached to the dike was a horizontal promenade with a variable length of either G_c=10 m or 30 m in prototype. The promenade was constructed at a very smooth 1-to-100 slope towards the sea to better drain the water after overtopping. The wall at the end of the flume was not overtopped in order to measure the maximum impacts and to not loose part of the impact energy due to overtopping water. Dike, promenade and wall were constructed of ply-wood in the model, which will result in less friction losses compared to a rough dike or promenade in prototype. Using Froude similarity and a length scale factor λ=25 the model dimensions were derived from prototype to fit the dimensions of the Ghent University wave flume (see Table 3.1).

Additionally, to this 1^{st} geometrical model set-up the wall was removed in the 2^{nd} geometrical model set-up. In this way the incoming flow thickness and velocity on the promenade were measured without the interference from the reflected flow at the wall. The same time-series of waves from the first geometrical model set-up were used. In the 3^{rd} geometrical model set-up the promenade was removed as well to measure the overtopping at the dike crest location for the same time-series of waves used in the 1^{st} and 2^{nd} geometrical model set-up (see Figure 3.4). In a final 4^{th} geometrical model set-up, the dike was removed as well to measure the incident water surface elevations at the dike toe location without the reflections from the dike present. It was opted to not do reflection analysis at the dike toe location to derive the incident waves but to remove the dike, promenade and wall structure to measure the incident waves directly. As long waves are present at the dike toe, a larger distance between wave gauges would have been required for reflection analysis (Mansard and Funke, 1980), which did not fit the flume. Even with more advanced measurement set-ups it remains a challenge to perform

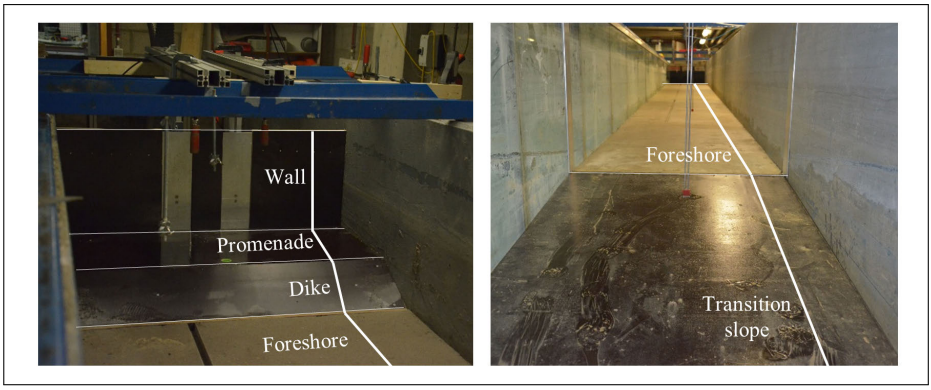

Figure 3.3: Geometrical set-up of 'UGent3' model test with distinct features: transition slope, foreshore, dike, promenade and wall.

reflection analysis on a water surface elevation signal measured in very to extremely shallow waters. No distinct wave shape with a clear trough and crest is present, but a bore like wave propagation, further hindering any reflection analysis to derive the incident wave conditions.

For the 'UGent2' model tests, the same foreshore slope as in the 'UGent1' experiment was chosen as cot(θ_2)=35 (see ANNEX A). To ensure an overlap with the 'UGent1' model tests the dike slope cot(α)=2 was used at first and then varied to cot(θ_2)=3, to investigate the influence of the dike slope on the impact force measurement. Different to the 'UGent1' experiments the dike crest elevation was not varied but kept at d_c=9 m TAW in prototype. As the dike toe elevation was also kept at d_t=6.7 m TAW in prototype, this resulted in a dike height d_d=2.3 m in prototype. The toe of the foreshore was approximately located at $-$9.25 m TAW in prototype. The main advancement of the 'UGent2' experiments compared to the 'UGent1' experiments was that a range of promenade widths G_c=5 m, 10 m, 15 m and 20 m in prototype was tested. The foreshore was again constructed from concrete and the dike, promenade and wall from ply-wood in the model. Using Froude similarity and a length scale factor λ=25 the model dimensions were derived from prototype to fit the dimensions of the Ghent University wave flume (see Table 3.1). For the 'UGent2' experiments the wave flume was split into two sections starting 10m offshore from the dike toe (see Figure 3.5). The split was achieved by installing a thin metal plate in the flume main axis along the foreshore. The metal plate was placed in a pre-fabricated slot in the foreshore, supported towards the side of the flume and divided the entire model set-up starting from 10 m offshore from the dike toe. In the larger 0.7 m wide section the dike, promenade and wall were installed to measure the overtopped wave impacts at the wall. In the smaller 0.3 m section the dike, promenade and wall were removed to measure the incident water surface elevations at the dike toe without the reflections from the dike present. Additionally, to this 1^{st} geometrical set-up the wall was removed in the 2^{nd} geometrical set-up, to measure the incident overtopping flow characteristics on the promenade without the interference from the reflected flow at the wall. In

the 3^{rd} geometrical set-up the promenade was removed as well to measure the overtopping at the dike crest location for the same time-series of waves used in the 1^{st} and 2^{nd} geometrical set-up.

For the 'UGent3' model tests the same foreshore slope as in the 'UGent1' and 'UGent2' model tests was chosen cot(θ_2)=35 (see Figure A). The transition slope cot(θ_1)=10 was constructed as a direct representation of the large-scale 'DeltaFlume' model tests (see Section 3.2.1). A single dike slope cot(α)=2, dike height d_c=9 m TAW in prototype, promenade width G_c=10 m in prototype was used as these experiments served as a small-scale representation of the large-scale 'DeltaFlume' model tests. The dike toe was also kept at d_t=6.7 m TAW in prototype and the toe of the foreshore was approximately located at $-$9.25 m TAW in prototype. The foreshore was again constructed from concrete and the dike, promenade and wall from ply-wood in the 'UGent3' model. Using Froude similarity and a length scale ratio λ_r=5.81 between the 'DeltaFlume' and 'UGent3' model, the geometrical dimensions for the Ghent University wave flume were derived (see Table 3.1). Additionally, to this 1^{st} geometrical set-up the wall, and promenade were removed in the 2^{nd} geometrical set-up to measure the overtopping at the dike crest location for the same time-series of waves used during the 1^{st} geometrical set-up. In the 3^{rd} geometrical set-up, the dike was removed as well to measure the incident water surface elevations at the dike toe location without the reflections from the dike present.

3.1.2 Hydraulic conditions

A storm with 1,000 year annual recurrence interval (ARI) and a '+8.0m Superstorm', which is an extreme storm with an estimated 17,000 year ARI were selected for the investigation (Veale et al., 2012; Verwaest et al., 2009). The Belgian coastal safety Masterplan presents tolerable discharges for these two extreme storms with 1 l/s per m and 100 l/s per m respectively. The discharges were modelled using a 2D SWASH model (Suzuki et al., 2011) and the according wave parameters derived at Flanders Hydraulics Research.

For the 'UGent1' model tests a significant wave height H_s=4 m and a peak period of T_p=12 s were used for the prototype wave conditions, which were very close to the values suggested by (Veale et al., 2012; Verwaest et al., 2009). Two different water levels for this study were rounded from the SWASH model values to h_o=7 m TAW and 8 m TAW in prototype. Together with the dike toe location d_t and dike crest location d_c this yielded in a water depth at the dike toe h_t=0.3 $-$ 1.3 m in prototype and a crest freeboard A_c=1 $-$ 3 m in prototype. The crest freeboard A_c is defined as the distance between the still water level (SWL) and the dike crest location d_c. The values were down-scaled using Froude similarity and a length scale factor λ=25 (Table 3.1). A Jonswap spectrum with peak enhancement factor γ=3.3 was further used to generate the first order irregular time-series of waves based on information of the wave parameters H_s [m] and T_p [s]. The length of the time-series T [s] was equal to approximately 1,000 incoming waves (T=1,000·T_p), which was considered representative for the duration of a typical storm sea. The wave parameters were then varied by simply using 80%,

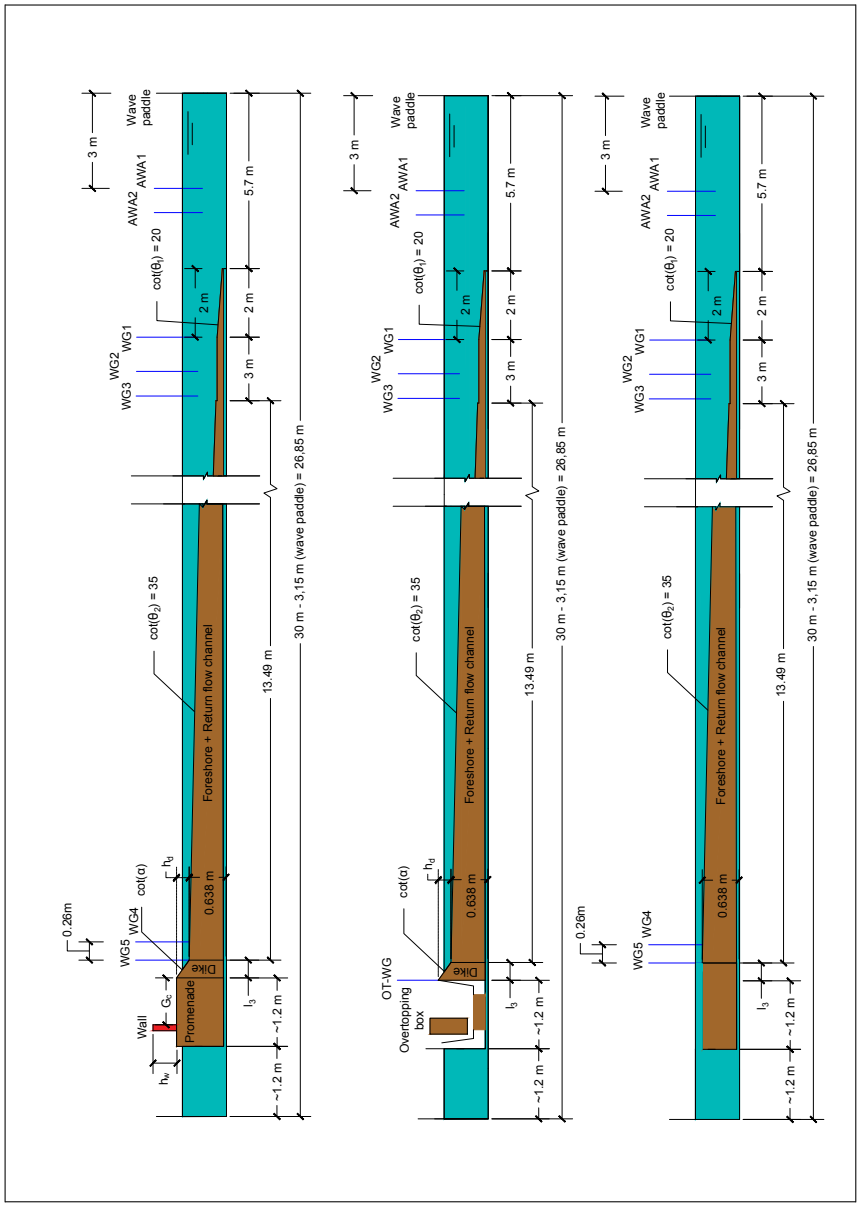

Figure 3.4: Geometrical set-up for 'UGent1' model to measure impact load (upper), overtopping (middle) and incident waves (lower).

90%, 100% and 120% of the H_s and T_p values to generate the time-series. During the experiments the active wave absorption system was switched on at all times.

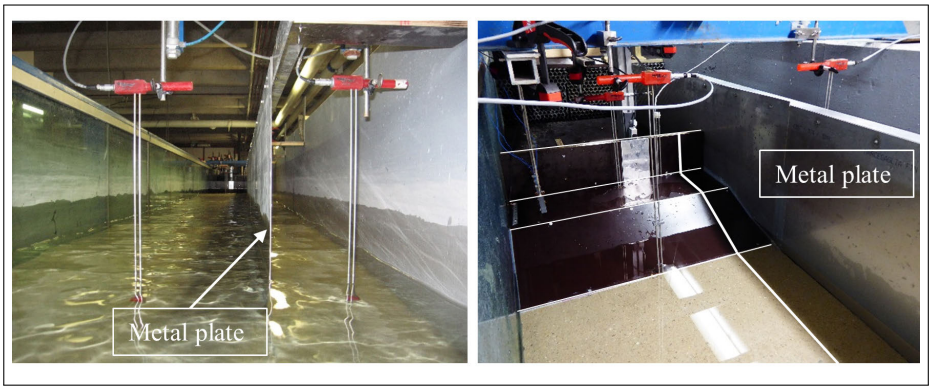

Figure 3.5: Split of wave flume in 'UGent2' model test starting from 10m offshore of the dike toe using a thin metal plate (left figure). Dike, promenade and wall were installed in the 0.7m left section of the split-up (right figure).

For the 'UGent2' model tests, offshore wave heights between H_s=3 − 4 s and peak period T_p=7 − 12 s in prototype were chosen and combined to achieve a range of wave steepness between ξ_o=0.0178-0.0457. These values were in the range of extreme storm wave parameters established for the 'UGent1' model tests. Water levels of h_o=6 m, 7 m and 8 m TAW in prototype were investigated. This resulted in prototype water depths at the dike toe between h_t=−0.7 − 1.3 m and crest freeboards between A_c=1 − 3 m. Note that for negative water depths at the dike toe h_t <0 the dike toe fell dry. The same procedure as for 'UGent1' model tests was followed to down-scale the values and generated the water surface time-series and paddle steering files (see Table 3.1).

A slightly different approach was used to generate the paddle steering files for the 'UGent3' model tests. The realized paddle motion time-series from the 'DeltaFlume' model test was down-scaled, using Froude similarity and a length scale ratio of λ_r=5.81 between the two models. In this way, the exact same paddle motion and desired sequence of waves was used in the two models. The paddle steering signal frequency was 64 Hz in the Delta Flume and 40Hz in the Ghent University wave flume. Hence, interpolation was done to take into account the difference in paddle steering frequencies when down-scaling. With this procedure most similar design wave conditions between the 'UGent3' and 'DeltaFlume' experiment were achieved.

3.1.3 Test programme

All three model tests ('UGent1'-'UGent3') in the Ghent University wave flume were conducted in a similar sequence. In the first stage, the average and individual overtopping q [l/s per m] and V [m^3] over the dike crest was measured by removing the wall and promenade from the geometry. In the second stage, the according

impact forces F [kN/m] on the wall were measured by re-installing the wall and promenade again and by using the same time-series of waves from the first stage. In this stage, most of the repetition tests were included in the test programme. In the third stage, the wall was removed again and only the overtopping flow thicknesses η [m] and velocities u [m/s] on the promenade were measured for the same time-series of waves used in the first and second stage. In the fourth stage, the wall, promenade and dike were removed to measure the incident wave parameters at the dike toe location, without reflections from the dike and wall. Absorption material was installed at the end of the flume to minimise the reflections occurring at the flume end wall. In total this resulted in 379 individual tests comprised of 'UGent1'=109 tests, 'UGent2'=177 tests and 'UGent3'=93 tests for a range of geometric and hydraulic conditions (see Table 3.1).

Table 3.1: Investigated parameters for 'UGent1' - 'UGent3' model tests in their range (all values in model scale)

	'UGent1'	**'UGent2'**	**'UGent3'**
Froude length scale λ [-]	1-to-25	1-to-25	1-to-25
Foreshore slope cot(θ_2) [-]	35	35	35
Transition slope cot(θ_1) [-]	2	10	10
Dike toe location d_t [m]	0.638	0.638	0.638
Dike slope cot(α) [-]	2	2, 3	2
Dike height h_d [m]	0.092, 0.132	0.092	0.092
Crest location d_c [m]	0.73, 0.77	0.73	0.73
Promenade width G_c [m]	0.4, 1.2	0.2, 0.4, 0.6, 0.8	0.4
Wall height h_w [m]	non-overtopped	non-overtopped	non-overtopped
Offshore water depth h_o [m]	0.65, 0.69	0.61, 0.65, 0.69	0.65, 0.69, 0.71
Dike toe water depth h_t [m]	0.012, 0.052	-0.028, 0.012, 0.052	0.012, 0.052, 0.072
Crest freeboard A_c [m]	0.04 - 0.12	0.04, 0.08, 0.12	0.02, 0.04, 0.08
$H_{s,o}$ [m]	0.08 - 0.19	0.12 - 0.16	0.08 - 0.19
$T_{p,o}$ [s]	1.7 - 2.63	1.4 - 2.4	1.7 - 2.68
Rel. water depth $h_t/H_{s,o}$ [-]	0.063 - 0.433	-0.23 - 0.43	0.075 - 0.9
Rel. promenade width G_c/A_c [-]	3.33 - 30	1.66 - 20	5 - 20

3.2 Deltares Delta Flume

The Delta Flume is a large-scale wave flume facility operated by Deltares and located in Delft, The Netherlands (see Figure 3.6). The Delta Flume is operational since 2015 and measures 291 m in length, 5 m in width and 9.5 m in depth (Van Gent, 2015). With its larger dimensions it is possible to conduct large-scale to prototype experiments to study the effect of extreme waves on coastal hard structures or erosive coastal materials. The close to prototype dimensions allow to accurately model parameters such as laminar (porous) flow, clay, sand, grass, impact pressures and forces, which are usually affected by scaling errors in a smaller scale model. 85% of dutch sea dikes can be tested in prototype scale in the Delta Flume (Hofland et al., 2013). Key characteristics of the flume are a design water depth between 2.5 m and 8 m, a maximum wave height of H_{max}=4.5 m, a maximum significant wave height of H_{m0}=2.2 m and corresponding maximum wave period T_p=9.4 s. At this moment, no higher waves are artificially generated anywhere else in the world. Reservoirs with equal dimensions to the flume size and able to store up to 9 million liters of fresh water are installed next to the flume. Three pumping stations with a total capacity of 1.000 l/s are used to fill and empty the flume but also to simulate tide or wind surges. Along the flume sidewalls 2 flume gantry cranes are placed on rails, to install and decommission the models. An additional measurement trolley on the same rails is used to operate different measurement devices from above.

Figure 3.6: Deltares Delta Flume for prototype testing (left figure) and its 9m high blue piston type wave paddle (right figure).

A "dry-back" piston type wave board is used to generate the waves. 4 pistons, moved by hydraulic cylinders, are used to generate regular, 1^{st} and 2^{nd} order irregular and other special (tsunami, bichromatic, etc.) waves. The linear motion of the board is guaranteed using a degree of freedom control on each of the four hydraulic cylinders. The installed electric power for the movement of the wave board is 1.9 MW.The wave board has a maximum stroke length of 7 m, which al-

lows for simultaneous generation of the maximum wave heights and absorption of the reflected waves. The steering signal for the paddle is generated at 64Hz and the wave generation system is not synchronized with the main data acquisition. An active reflection compensation (ARC) is achieved by using 3 wave gauges deployed directly at the wave board and using the measurements of the 3 gauges to distinguish the reflected and incident waves (Wenneker et al., 2013). In this way the steering signal is adopted in real time based on the reflected wave energy. The active reflection compensation was working between the low-cut off 0.02 Hz and high-cut off frequency 1.5 Hz from the wave generation software and most effective towards the lower range. The ARC of the Delta Flume allowed for successful removal of the unwanted seiches and in doing so prevented a build up of unwanted low-frequency wave energy over time.

3.2.1 Geometrical set-up

The sandy foreshore consisted of a transition slope $\cot(\Theta_1)$=10 at the beginning and a main slope $\cot(\Theta_2)$=35 until the dike toe, along l_2=19.5 m and l_3=61.6 m, respectively (see Figure 3.1). The heights d_2–d_3 are a result of the lengths l_1–l_3 together with the slope angles. The total foreshore volume was comprised of $\sim$1000 m^3 of sand. Sand with a grain size D_{50}=320 μm was installed in a minimum 0.4 m deep top layer over the entire foreshore. Below the top layer sand with D_{50}=230 μm was installed. The erosion depth over the entire foreshore never exceeded 0.4 m during the tests, hence a uniform sand distribution of D_{50}=320 μm was assumed. The sand was compacted during the installation process in several stages and the final profile was levelled up to 2cm accuracy before the start of the model tests. Attached to the foreshore a concrete dike with a $\cot(\Theta_1)$=2 slope and a G_c=2.35 m wide promenade with an offshore inclination of 1-to-100 to drain the water was built. At the end of the promenade a vertical h_w=1.6 m high, non-overtopped steel wall was constructed, covering the whole flume width and fixated at the flume side walls (see ANNEX B). The steel wall was comprised of 3 horizontal IPE500 beams and 9 vertical IPE160 beams welded to a 12 mm thick steel plate. The steel plate was prefabricated and openings for the measurement sections were foreseen. The total weight of the wall was approximately 2.3 ton. Simplifying the wall to a clamped single beam structure for the lowest horizontal IPE500 beam and adding the mass of one IPE500 and 9 IPE160 beams, steel plate and added water in front of the wall over 0.66 m height, resulted in a 1^{st} natural frequency of 77 Hz. Furthermore, the natural frequencies were excited using a rubber hammer and manually exerting a short impulse on the wall structure while the measurement was running. This was repeated at least 10 times and a frequency analysis on the tail of the measured signal was performed to obtain the 1^{st} harmonic natural frequency of the wall. No clear peak in the energy density spectrum could be found. The combined evidence lead to the assumption that the natural frequency of the wall was at least 77 Hz or higher and that the wall was constructed sufficiently stiff, to not influence the overtopped wave impact load measurements.

The global coordinate system for the Delta Flume was originated at the lower right corner of the wave paddle when standing with the back to the paddle. The

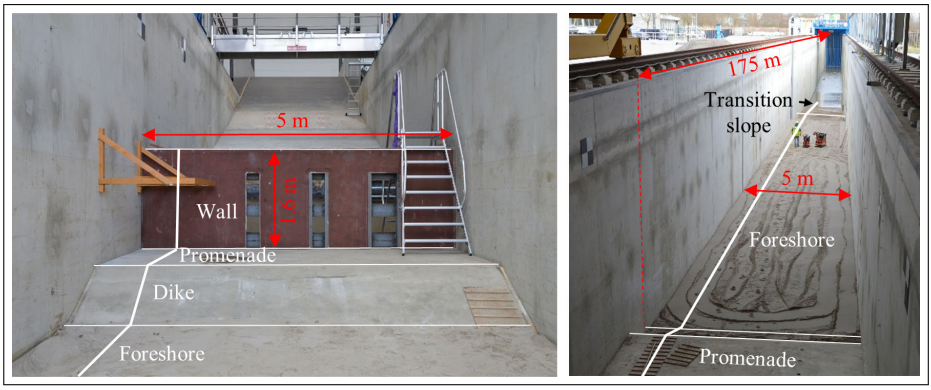

Figure 3.7: Geometrical set-up of 'DeltaFlume' model tests with distinct features: wall, promenade, dike, foreshore and transition slope.

positive X-direction was defined in the main flume axis pointing towards the model. The positive Y-direction was defined in cross flume direction pointing to the left and the positive Z-direction was pointing upwards from the flume bottom. X, Y and Z were written in capital letters. The most prominent locations were the start of the transition foreshore slope at X=93.98 m, the start of the main foreshore slope at X=113.48 m, the dike toe at X=175.08 m, the dike crest at X=176.15 m and the wall at X=178.5 m. Since most measurements were located close to the wall a second, local coordinate system was defined. It was originated at the dike crest location on the same side of the flume as the global coordinate system with positive x-direction in the main flume direction pointing towards the wall, positive y-direction in cross flume direction pointing to the left and positive z-direction pointing upwards. x, y and z of the local coordiante system were written in small letters. The local coordinate system origin corresponded to X=176.15 m, Y=0 m and Z=4.26 m of the global coordinate system. The model dimensions were given in model scale using Froude similarity and a length scale factor λ=4.3.

As the foreshore was comprised of erosive material, the morphological changes were closely monitored by measuring the bed profile along 5 lines in the main flume axis direction. The profiles were obtained with a mechanical bed profiler after each irregular wave test (see Figure 3.8).

At the same time numerical modelling with XBeach was applied to determine the expected morphological behaviour. Combined evidence showed that the erosion at the dike toe location (X=175.08 m) reached a mean value of ∼0.15 m along the flume width and a maximum value of ∼0.3 m during the model tests (Saponieri et al., 2018). A volume of $13 - 23\,m^3$ sand were eroded over a 30 m long section starting at X=147 m until the dike toe (X=175.08 m), while accretion took place over a 40 m long section starting at X=107 m until X=147 m (Saponieri et al., 2018).

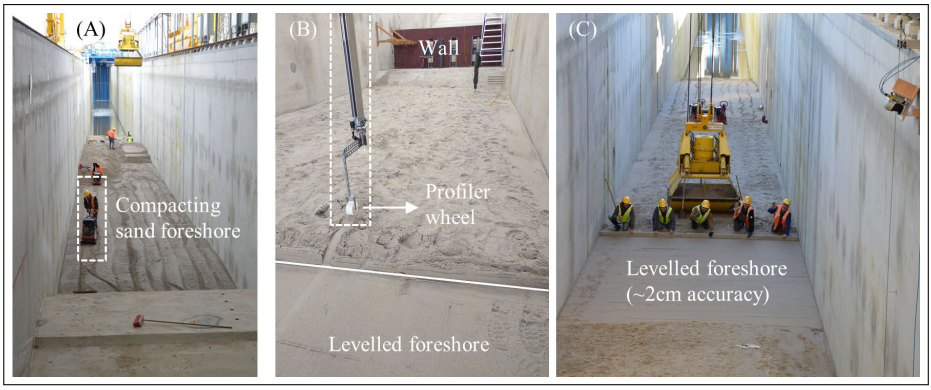

Figure 3.8: $\sim$1.000 m^3 of sand were installed and compacted in layers of 1 m (A). The foreshore evolution was monitored during the experiments with a mechanical bed profiler (B), measuring the total length in main flume axis of the foreshore. The sand was levelled up to 2cm accuracy before the start of the 'DeltaFlume' model tests.

3.2.2 Hydraulic conditions

Most of the time-series of water surface elevation used in the 'DeltaFlume' model tests were up-scaled from the 'UGent1' model tests. Froude similarity and a length scale ratio of λ_r=5.81 between the 'DeltaFlume' and 'UGent1' model was applied. For the design of wave parameters in the 'UGent1' experiment it is referred to Section 3.1.2. The Delta Flume active reflection compensation (ARC) was activated for each model test. Additionally a number of bichromatic waves were generated by the Delta Flume wave generation software, for the purpose of wave interaction studies (see Table 3.2). The bichromatic waves were computed as a set of regular waves (see Equation 3.1),

$$\eta(t) = \sum_{i=1}^{2}(a_i \cdot cos(2 \cdot \pi \cdot f_i \cdot t + \psi_i)). \tag{3.1}$$

The first and second frequency components (f_1 and f_1), phase (ψ_1 and ψ_2) and amplitudes (a_1 and a_2) were specified for the wave generation software (3.2).

Furthermore, long time-series ($\sim$3,000 waves) were generated by the Delta Flume wave generation software, using similar wave parameters H_s [m] and T_p [s] as in the up-scaled time-series from the 'UGent1' experimental campaign. The purpose of a longer time-series of waves was to increase the number of overtopping waves and consequently the number of impact events for statistical analysis. Another long time-series using 2^{nd} order wave generation was used for a single case (testID 493) in order to study the effects of the different wave generation, and possible influence of the long waves (see Table 3.3). The same seed number was used for the generation of the 2^{nd} order wave time-series (testID 494) compared to the equivalent 1^{st} order wave time-series (testID 493). For a selected test (testID 495) the water level was increased by 0.1m, to account for sea level rise.

Table 3.2: Test programme 'DeltaFlume' bichromatic waves in chronological order (values in model scale using Froude similarity and a length scale factor λ=4.3)

testID	$\mathbf{h_o}$	h_t	A_c	f_1	a_1	ψ_1	f_2	a_2	ψ_2
[-]	**[m]**	**[m]**	**[m]**	**[Hz]**	**[m]**	**[°]**	**[Hz]**	**[m]**	**[°]**
Bi_1_4	4.01	0.30	0.25	0.174	0.5	0	0.142	0.4	0
Bi_1_5	4.01	0.30	0.25	0.174	0.5	0	0.142	0.45	0
Bi_1_6	4.01	0.30	0.25	0.174	0.5	0	0.142	0.5	0
Bi_2_4	4.13	0.43	0.12	0.190	0.45	0	0.155	0.36	0
Bi_2_5	4.13	0.43	0.12	0.190	0.45	0	0.155	0.405	0
Bi_2_6	4.13	0.43	0.12	0.190	0.45	0	0.155	0.428	0
Bi_2_6_R	4.13	0.43	0.12	0.190	0.45	0	0.155	0.428	0
Bi_1_6_R	4.01	0.30	0.25	0.174	0.5	0	0.142	0.5	0
Bi_3_6	3.78	0.08	0.47	0.174	0.3	0	0.142	0.3	0
Bi_3_6_1	3.78	0.08	0.47	0.174	0.35	0	0.142	0.35	0
Bi_3_6_2	3.78	0.08	0.47	0.1577	0.35	0	0.129	0.35	270

3.2.3 Test programme

The distinction was made between irregular waves in first, second order form and bichromatic waves. Four tests of the test program were repeated. The tests were given in chronological order in Table 3.3, together with the design wave parameters, water levels h [m] and freeboards A_c [m]. The index 't' and 'o' referred to dike toe and offshore location respectively.

A typical test routine was composed in a threefold sequence. 1) Before the test the measurement devices had to be prepared and checked on their proper working. This involved to start feeding the load measurement equipment with electricity to warm up, to wet the pressure cells in order to avoid temperature shock later in the measurement, to empty the buckets for the wave gauges on the promenade, to check the GoPro memory space, to set the GoPros, the Laser Scanner, Wave radar and ASM (Argus Sand Meter) in measurement mode, to switch on the spotlights, to turn on the data acquisition system and to start the wave paddle. 2) During the tests the proper load measurement was checked in real time and that no damage occurred. This was done from the measurement PC and visually from the observation platform. In this stage usually the logbook was updated and the data from previous experiments copied to a back-up location. 3) After the test, the data acquisition system, Laser Scanner, GoPros, ASM, wave radar and spotlights had to be switched off. The profile measurement was conducted with the mechanical

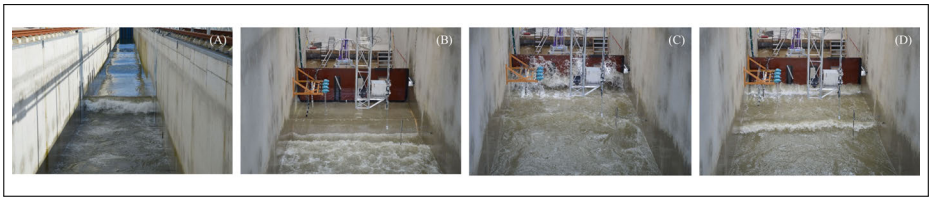

Figure 3.9: a) An incoming wave broke on the shallow and sandy foreshore. b) Two bore crests at the start of the overtopping process over the dike crest and c) consecutive impact of the bores against the vertical wall. d) After the impact process the bores were reflected and travel shoreward again.

profiler and the data from ASM and GoPro cameras was read out. In this stage also a qualitative check of load and wave measurement was performed.

3.3 Measurement techniques

The measurement set-up was divided into 4 main measurement groups, which were again tested in 4 different experimental phases. In each of the phases the same seed wave time series was used. First phase, the water surface elevation measurement and especially the incident water surface elevation measurement at the toe of the dike structure, without the dike present (see Section 3.3.1). The dike was removed, to avoid influence of reflected waves from the dike and to derive the purely incident spectral wave parameters $T_{m-1,0}$ [s] and H_{m0} [m]. The incident wave parameters were typically key parameters for the design of coastal structures. Second phase, the overtopping measurement in which the average q [l/s per m] and individual V [m^3] overtopping over the dike crest was measured (see Section 3.3.2). During the third phase, the overtopping flow thicknesses η [m] and velocities u [m/s] on the promenade were measured without the wall present, to avoid interaction with the reflected flow and derive the incident flow parameters (see Section 3.3.3). The fourth phase, involved the impact measurement of forces F [kN/m] and pressures P [bar] of the overtopped flow against the wall (see Section 3.3.4). Depending on the model test ('DeltaFlume', 'UGent1'–'UGent3') the 4 measurement phases were carried out differently. Additionally, several synoptic measurements were carried out during the different experimental phases (see Section 3.3.5). In all model tests ('DeltaFlume', 'UGent1'-'UGent3') a full synchronisation between the measurement devices was achieved.

3.3.1 Water surface elevation measurement

In all 4 model tests ('DeltaFlume', 'UGent1'-'UGent3') the water surface elevation was measured at least at two locations. A first location was in the flat bottom part of the flume, close to the wave paddle, to measure the deep water surface elevation. This was done in all 4 model tests with 3 wave gauges to allow for reflection analysis of the signal using the method of Mansard and Funke (1980). A

Table 3.3: Test programme 'DeltaFlume' for irregular waves in chronological order (values in model scale using Froude similarity and a length scale factor $\lambda = 4.3$)

testID	h_o	h_t	A_c	$H_{s,o}$	$T_{p,o}$	G_c/A_c	$\frac{h_t}{H_{m0,t}}$
[-]	**[m]**	**[m]**	**[m]**	**[m]**	**[s]**	**[-]**	**[-]**
492	4.01	0.30	0.25	1.10	6.34	9.4	0.273
493	4.01	0.30	0.25	0.93	5.79	9.4	0.323
494	4.01	0.30	0.25	0.93	5.79	9.4	0.323
495	4.13	0.43	0.12	0.93	5.79	19.6	0.462
499	4.13	0.43	0.12	0.46	4.10	19.6	0.935
500	3.78	0.08	0.47	0.93	5.79	5	0.086
501	3.78	0.08	0.47	1.10	6.34	5	0.073
502	4.01	0.30	0.25	1.10	6.34	9.4	0.273
503	4.01	0.30	0.25	0.70	5.02	9.4	0.429
504	4.01	0.30	0.25	0.93	5.79	9.4	0.323
509	3.78	0.08	0.47	0.70	5.02	5	0.114

second location was at the dike toe to measure the incident water surface elevation. At the dike toe location the wave gauge would alternately fall dry and was therefore placed into a plastic foot embedded into the foreshore. To measure the incident water surface elevation at the dike toe accurately and without reflection from the dike different approaches were used in the 4 model tests. For 'UGent1' and 'UGent3' the dike, promenade and wall were removed in this phase and a flat wooden plate attached to the dike toe position (end of foreshore). In this way the waves could travel undisturbed until the end of the flume where they were absorbed by the installed absorption material. For 'UGent2' the wave flume was subdivided in two sections of 0.7 m and 0.3 m width. In the smaller 0.3 m section the incident waves at the dike toe (with the dike and promenade removed) were measured simultaneously with the impact force measurement in the larger 0.7 m part of the flume. Since the large-scale 'DeltaFlume' model tests did not allow for quick removal of the dike, a calibrated SWASH model was used to derive the incident wave parameters at the dike toe for a situation without dike structure in the flume. The SWASH model was operated by the author of Suzuki et al. (2011) and described in Streicher et al. (2019a)). Several additional wave gauges were installed along the foreshore in all 4 model tests ('DeltaFlume', 'UGent1'-'UGent3'). They mainly served to monitor the change in wave parameters, wave breaking and shift in spectral wave energy towards lower frequency components,

due to depth limited breaking and release of long wave components. The exact location of each wave gauge was indicated in Figure 3.4 ('UGent1'-'UGent3') and Table 3.4 ('DeltaFlume'). Water surface elevations were measured by means of resistive type wave gauges DHI 202/50 and DHI 202/30, together with a DHI Wave Amplifier 102E system in the 'UGent1'–'UGent3' model tests. The wave gauges consisted of two thin parallel steel electrodes submerged in the water. The devices measured the conductivity of the instantaneous water volume between the two electrodes in the submerged part. The conductivity changed proportionally to the change of water surface elevation between the steel electrodes. The output in voltage was then converted in a water surface elevation with the linear calibration factors (DHI Water & Environment, 2003). A reference electrode in the foot of the wave gauge, where the two parallel steel electrodes merge was used to compensate for changes in the water conductivity due to salinity or temperature during the experiment. The measurement resolution was <0.001 m.

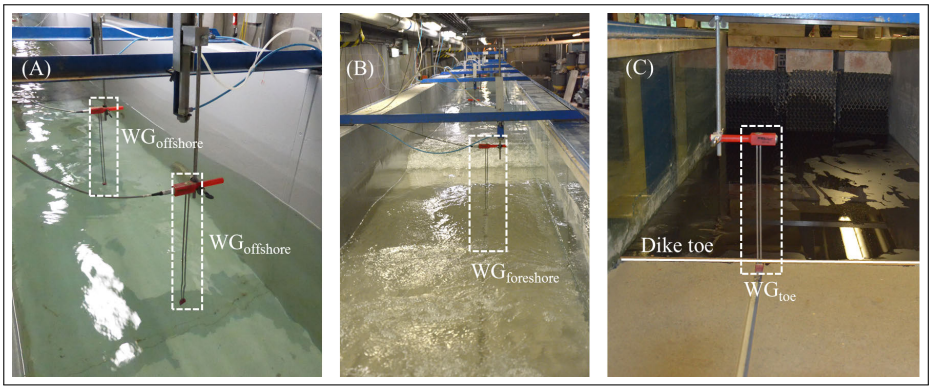

Figure 3.10: Resistive type wave gauges in the Ghent University flume. Offshore wave measurement in the flat bottom part (A) and wave measurement along the foreshore (B) until the incident wave measurement at the dike toe (C).

The water surface elevation in the 'DeltaFlume' model test was measured with in-house made resistive type wave gauges deployed at the right flume wall, when looking towards the paddle. Reference electrodes for these wave gauges were installed at the foot of the wave gauge. Due to the sandy foreshore some of the reference electrodes would have been buried in the sand and were therefore moved further offshore or covered with a permeable box made from wood and geotextiles.

The wave gauges were calibrated before each test ('UGent1'–'UGent3') or after the model test campaign ('DeltaFlume'). The sampling rate was set to 40 Hz ('UGent1'–'UGent3') and 1000 Hz ('DeltaFlume').

3.3.2 Overtopping measurement

Average and individual overtopping were measured only during the 'UGent1' - 'UGent3' model tests. In the 'DeltaFlume' model test no overtopping was measured. By reproducing a similar geometry as was installed in the 'DeltaFlume' in

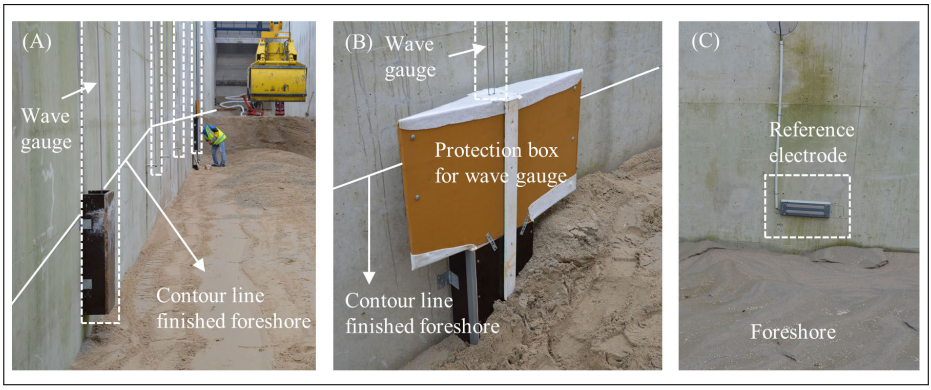

Figure 3.11: Water surface elevation measurement in the Delta Flume with resistive type wave gauges mounted on the flume wall. The foot of the wave gauges was partly covered in a protective box to prevent the finished foreshore layer to interfere with the measurement (A and B). The reference electrode to compensate for changes in water temperature and salinity during the sometimes 4h long experiment (C).

Table 3.4: Location of wave gauges in 'DeltaFlume' model set-up (X=0 at the paddle).

Paddle	WG1	WG2	WG3	WG4	WG5	WG6	WG7	Dike toe
m	m	m	m	m	m	m	m	m
0	43.5	49.5	61.5	107.89	126.42	155.66	174.73	175.08

'UGent3' and using the same time series of realized paddle motion in both models, the overtopping values from 'UGent3' were up-scaled, using Froude similarity and a length scale ratio λ_r=5.81, and assigned to the 'DeltaFlume' as well. Previously, it was observed that up-scaling overtopping discharges measured in small-scale models and comparing it to prototype measurements underestimates the overtopping discharge (De Rouck et al., 2005; Oumeraci et al., 2000). Hence, an underestimation of the up-scaled values was expected. Compared to the 1^{st} measurement phase (water surface elevation) the dike was installed in the flume to measure the overtopping over the dike crest by means of an overtopping box and using the weigh cell technique (Victor et al., 2012). A box was placed on a weigh cell (sampling frequency ~5 Hz) directly behind the dike and connected via a chute (0.1 m or 0.2 m width) to the dike crest (see Figure 3.12).

The overtopping water over the dike crest was transferred via the chute into the box and the weigh cell below the box measures the mass of the overtopped water. This set-up allows for accurate detection of individual volumes even in the presence of sloshing inside the box due to large overtopping volumes. To distinguish individual overtopping events in the post processing a wave gauge was placed on the dike crest with a sampling frequency of 40Hz. The overtopping box had an effective volume of 32l and was emptied during the test via a pump when the volume was ex-

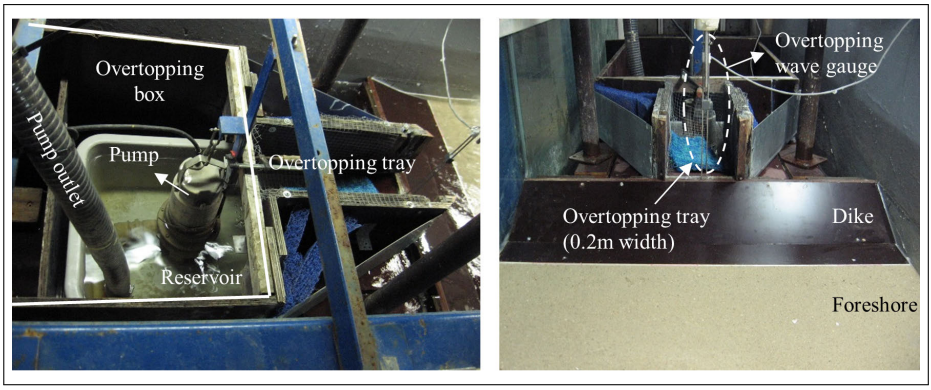

Figure 3.12: Overtopping measurement set-up for the 'UGent1'-'UGent3' data-sets. The overtopping water over the dike crest was guided via the overtopping tray in the overtopping box. The overtopped water was measured by a weigh cell installed below the overtopping box.

ceeded. Both pump and weigh cell were calibrated before the test campaign. For a detailed description of the working of the overtopping measurement it was referred to Gallach Sánchez (2018). The repeatability of average overtopping discharge measurements was discussed controversially and estimated for repetition tests using the same seed number, with a maximum coefficient of variation C_v=12.9% (Kortenhaus et al., 2004) or C_v=1.5% (Gallach Sánchez, 2018). For repetition tests using the same wave parameters but different seed number the maximum coefficient of variation increased to C_v=33% (Kortenhaus et al., 2004) or C_v=4.6% (Gallach Sánchez, 2018). The smaller variability for Gallach Sánchez (2018) was explained by the fact that mostly low crested structures with larger average overtopping discharge q were tested. For larger average overtopping discharge q the variability generally decreases (Romano et al., 2015)

3.3.3 Flow thickness and velocity measurement

Overtopping flow thicknesses η [m] and velocities u [m/s] were measured on top of the promenade. The measurement of overtopping flow thickness and velocity is extremely difficult in alternating wet and dry conditions and for highly turbulent and aerated flows. None of the conventional devices to measure water surface elevations (wave gauges, ultra-sonic distance sensors) or velocities (paddle wheels, micro propellers, acoustic doppler velocimeter, electro-magnetic current meter) was designed to measure in this conditions. Hence, especially the measurement in the small-scale model tests ('UGent1-'UGent3') was a challenge. As a solution the same wave gauges DHI 202/30 and amplifier system DHI Wave Amplifier 102E from the wave measurement were used for the 'UGent1'-'UGent3' model tests (see Figure 3.13). In order to be able to measure also thin layer thicknesses, holes were drilled into the wooden plate of the promenade. Space holders were placed into the drilled holes and the foot of the wave gauges was placed into the space holders.

As a result, the wave gauges were flash mounted with the top of the promenade and recorded the overtopping flow surface elevation which is related to the layer thickness.

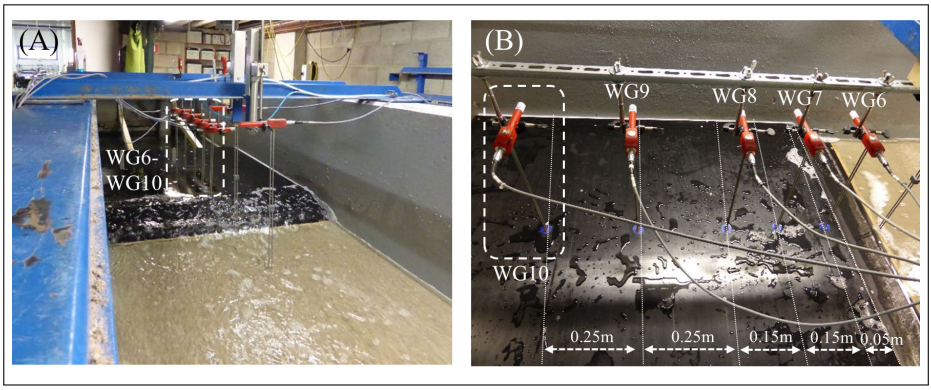

Figure 3.13: The flow thicknesses in the 'UGent1'-'UGent2' data-set was measured with resistive type wave gauges (WG), flash-mounted on the promenade. The flow velocities were derived with transit-time techniques. A frontal image of the wave gauges installed on the promenade (A) and a close up with distances between the wave gauges indicated (B).

The first wave gauge on the promenade was installed 0.05 m, the second one 0.2 m, the third one 0.35 m, the fourth one 0.6 m and the fifth one 0.85 m landwards of the dike crest. The sampling frequency of the gauges was synchronized with the other measurements and set to 40 Hz. The signal of the same wave gauges was used to measure the average velocities between two consecutive wave gauges. To avoid interaction between reflected and incoming flows, the wall at the end of the promenade was removed and absorption material installed at the end of the flume. The so obtained unobstructed flow parameters were measured in a separate experimental phase during the model tests using the same time-series of waves, in order to relate them later to the impact force and overtopping measurements.

For the 'DeltaFlume' data-set the overtopping flow parameters thickness η [m] and velocity u [m/s]] were measured by instruments attached to a wooden frame installed 1m above of the promenade on the right flume side when looking towards the paddle (see Figure 3.14). The flow thickness was obtained by 4 resistance-type wave gauges (WLDM1–WLDM4). The measurement principle is similar to the water surface elevation measurement (see Section 3.3.1), measuring the change in conductivity between two metal electrodes according to the water level. The wave gauge foot with the reference electrode was submerged 5 cm below the elevation of the promenade, in a 12cm deep bucket of water. The flow velocity was obtained by 4 Airmar S300 flow meter paddle wheels (PW1–PW4), measuring only the incoming flow velocity. Two paddles attached to a rotational axis and mounted in a half open housing were rotated by the incoming overtopping flow. Depending on the rotation speed the flow velocity was derived. Originally, these paddle wheels used to be integrated into ship hulls to measure the velocity of the ship. Previously they were

used to measure overtopping flow velocities in comparable set-ups (Van Doorslaer et al., 2012; Van Der Meer et al., 2010). The indicated minimum measurable velocity of this device is 1 m/s. The paddle wheels were measuring at 0.03m above the promenade. Both types of instruments (WLDM and PW) were installed in two lines parallel to the flume wall 0.24 m apart from each other.

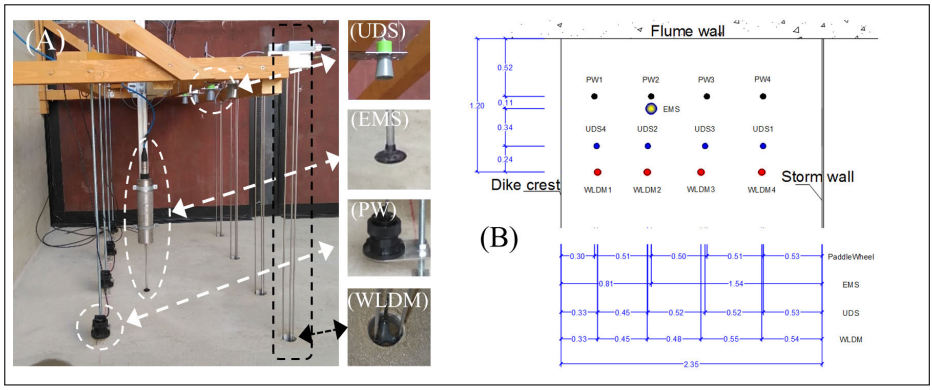

Figure 3.14: The measurement of flow thickness and velocity on the promenade in the 'DeltaFlume' data-set. Ultrasonic distance sensors (UDS) and resistive type wave gauges (WLDM) were used to measure the flow thickness and electro-magnetic current meter (EMS) and paddle wheel (PW) to measure the flow velocities.

Detailed locations of the measurement devices measuring the flow parameters on the promenade can be found in Cappietti et al. (2018). Additionally, an electro-magnetic current (Valeport 802) meter was installed to measure the flow velocity and 4 ultra sonic distance sensors (3 MaxSonar HRXL, 1 Honeywell 943 M18), to obtain a non-intrusive measurement of the flow thickness. These measurements were not further studied in this theses and rather served for redundancy purposes. Furthermore, the ultra-sonic distance sensors often lost the signal, due to spray which would touch the sensor surface.

3.3.4 Impact load measurement

The impact loads at the wall location were measured in all 4 model tests ('UGent1'-'UGent3','DeltaFlume'). For 'UGent1'-'UGent3' a part of the wooden wall was removed and replaced by an aluminium measurement plate (see Figure 3.15). This plate was light enough to react fast to an impacting wave and stiff enough to not deform under impact. The width of the measurement plate was 0.1 m. It should just fit into the gap in the middle part of the wall without contact to the neighboring wall parts, to avoid friction losses. There was a single measurement plate installed in 'UGent1' and 'UGent2' model tests and two measurement plates installed with 10 cm spacing between them in 'UGent3' model test.

The measurement plate was attached to and supported by a 3kg load cell ('UGent1') and 5kg load cell ('UGent2'-'UGent3') from Tedea-Huntleigh. To measure the forces a strain gauge, bonded to the load cell, was used to convert the

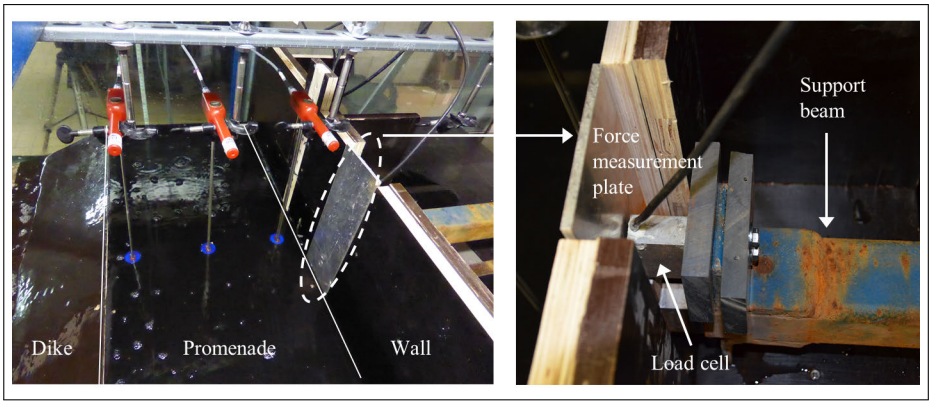

Figure 3.15: Impact force measurement with strain gauge load cells in the Ghent University flume. The strain gauge load cell was attached to a alluminium measurement plate flash mounted in the wall and supported towards the back of the flume with a rigid metal beam

deformation force into an electrical signal. The electrical resistance of the strain gauge changed based on the mechanical deformation. The maximum relative error was stated as 0.02% of the full-scale output. The strain gauge load cell was connected to a 0.1 m-wide aluminum plate, and the plate flush-mounted with the rest of the wall. The other side of the load cell was supported by a steel beam fixed to the end of the flume ('UGent1') or by a scaffolding framework across the flume ('UGent2' and 'UGent3') to provide a stiff structure. This was important to reduce the vibration inside the force measurement system and thus increase the natural frequency f_n of the whole set-up. In this way it was attempted to raise the natural frequency above the excitation frequencies induced by the impacting waves. A static calibration of this measurement was roughly done by placing defined weights on the load cell and measuring the weight response.

In the DeltaFlume model the impact force was measured by 2 compression type HBM U9 load cells with a measurement range of 20kN. The maximum absolute error was 0.007 kN and the maximum relative error 0.363% of the full-scale output. The load cells were vertically spaced above each other and connected the same hollow steel profile to the steel wall. The hollow steel profile was hanging in a prefabricated opening in the steel wall and was attached towards the side to avoid rotational movement. This was done to ensure a force measurement in only one direction. As a result, the hollow steel profile was flush-mounted into the wall. The width of the hollow steel profile was 0.2 m.

Impact pressures were measured by 15 Kulite HKM-379 (M) pressure sensors with a measurement range of 1Bar. The combined error due to non-linearity, hysteresis and repeatability compared to the best-fit straight line (BFSL) was stated to be typically smaller than $\pm$0.1% of the full scale ouptut (FSO). As a maximum it was stated that it never exceeds $\pm$0.1% of the full scale ouptut (FSO). The pressure sensors were spaced vertically and horizontally over a metal plate. The

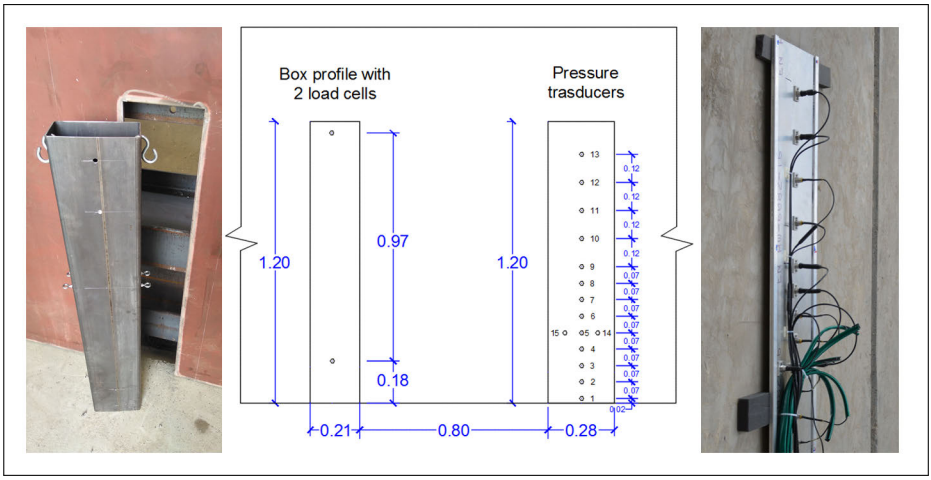

Figure 3.16: Impact force measurement with compression load cells (left) and pressure measurement with piezo-electric pressure sensors (right)

lowest pressure sensor (P1) was installed 0.02 m above the promenade, the next 8 sensors (P2-P9) were installed in distances of 0.07 m and the next 4 sensors (P10-P13) were installed with 0.12 m distance between each other. Pressure sensor P14 and P15 were installed 0.07 m respectively to the right and left of pressure sensor P5. The pressure sensors were mounted on a metal plate. The metal plate fitted into a prefabricated opening and was flash mounted in the middle section of the steel wall as a result.

In all model tests ('UGent1'-'UGent3','DeltaFlume') the impact load measurements were sampled at a frequency of 1000 Hz, known to provide robust enough results and capture even the short duration impulsive impacts (Oumeraci et al., 1993). The impact load measurements were fully synchronized with the other measurements in all model tests.

3.3.5 Synoptic measurement

The water surface elevation in the 'DeltaFlume' model test close to the dike, promenade and wall were monitored in a high-resolution and nonintrusive way. High-resolution profile measurements of the water surface with a SICK LMS511 laser profiler and a GoPro 5 Black overview and sideview camera were obtained. The laser was mounted at the left flume sidewall (when standing with the back to the wave paddle), approximately 5m above the dike toe location (see Figure 3.17). A slant angle of 23° was used to avoid a spiky signal due direct reflection at nadir (Hofland et al., 2015; Blenkinsopp et al., 2012). This resulted in a scanned profile approximately in the middle of the flume (y=∼2.7 m), next to the pressure plate in the steel wall and along the middle of promenade and dike. The measurement frequency was 35 Hz with an angular resolution of 0.25°. The distance between scanned points is a function of the distance the laser beam had to travel and the

angular resolution. On the promenade, the average distance between individual scan points was 2.55 cm. The signal was synchronized with the other recordings via a synchronization pulse received from the main data acquisition system.

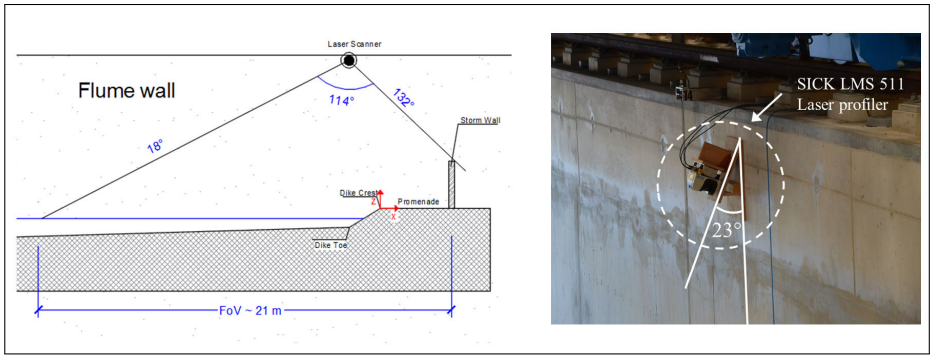

Figure 3.17: The SICK LMS 511 laser profiler was mounted to the left flume wall (when standing with the back to the paddle) approximately at the dike toe location (A). A slant angle of 23 degree was used to prevent oversaturated return signal strength due to reflections in nadir (B).

There were several issues related to the reflection characteristics of the (foamy) water and laser beam characteristics (Hofland et al., 2015). The mostly foamy water surface of the turbulent bores resulted in good reflection characteristics with a sufficiently high received signal strength indicator (RSSI). This indicated that the turbidity of the water did not play a role as the foam was much more reflective and the penetration of the laser beam into the water was minimized. Hence, a better accuracy than the estimated range precision (standard deviation) of $1 - 1.5$ cm found by Streicher et al. (2013) was assumed. The range precision was determined for incidence angles of 15°-90° (angle between incident laser beam and still water surface) in the direction of the laser beam. In parts were there was no foam on the water, the turbidity much lower than 40 NTU (Blenkinsopp et al., 2012) and the distance between water surface and laser profiler too large to provide sufficient reflection strength, no water surface measurement was obtained. Profile measurements covered the water surface at offshore of the dike toe, the dike, promenade until the wall and in total a horizontal length of ∼21 m. This resulted in a field of view of 114°.

A side-mounted and a top-mounted GoPro 5 Black camera were further deployed to obtain an overview picture and eventually allow for motion tracking of the overtopping flow to determine flow velocity on the promenade and run-up at the wall (see Figure 3.18). The GoPro images were recorded at 59.94 fps, a resolution of 2.7 k (2704 px·1520 px) and synchronized with the force and pressure measurement, via a LED pulse visible in the camera images. The spatial resolution in the GoPro images depends on the distance towards and angle of the GoPro with the wall. The resolution was approximately 5.5 mm/px on the steel wall and 9.5 mm/px on the promenade for the overview camera. The resolution for the side-view camera was 2.78 mm/px on the opposite flume wall. Hence, the areas of

interest were covered with a resolution <1 mm/px always.

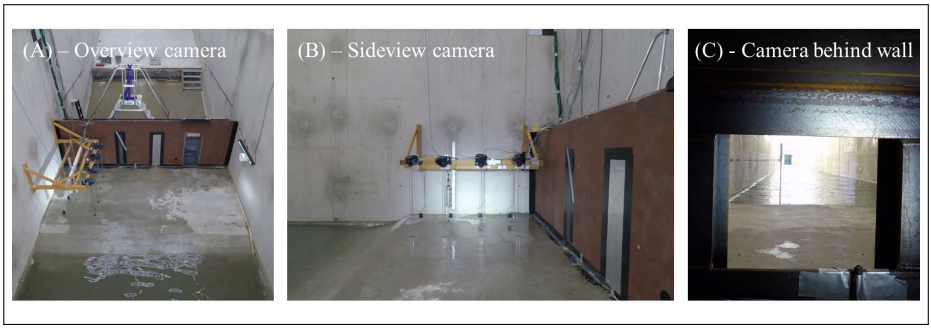

Figure 3.18: Three GoPro 5 Black were deployed during the 'DeltaFlume' experiment. The views from the overview camera (A), the sideview camera (B) and the camera filming through the observation window in the wall (C) were provided.

Issues regarding the storage space and battery capacity of the GoPro cameras were solved by using 128 GB SD cards and portable powerbanks supplying electricity via an USB interface. Artificial, flicker free, lighting consisted of an 200 W LED from an overview flood light installed directly above the overview camera and a more focused LED light from the side to illuminate the area affected by the overtopping flow on the promenade. The GoPro images were synchronized with the other measurements by a LED light within the field of view, which was triggered by the main data acquisition system at the start of the measurement.

In the other model tests ('UGent1'-'UGent3') cameras were installed as well but no further processing was done and they rather served for a quality check in case inconsistencies were found in the data. However, it was attempted to use these camera images as well to determine an overtopping flow velocity by motion tracking of the leading edge against an accentuated background, but no reliable measurements of the flow velocity were obtained.

3.4 Data processing

During the data processing of the different data-sets ('UGent1'-'UGent3' and 'DeltaFlume') synchronisation of the applied analysis methods was a main objective. In this way comparability between the results was assured while minimising the errors resulting from different processing routines (model-effects). Hereafter, the tests from all data-sets were assigned a unique testID (see Section 3.4.1), the wave parameters H_{m0} [m], T_p [s] were derived (see Section 3.4.2), the average overtopping over the dike crest q [l/s per m] calculated (see Section 3.4.3), overtopping flow thickness η [m] and velocity u [m/s] determined (see Section 3.4.4) and the impact forces F [kN/m] and pressures P [kPa] analysed (see Section 3.4.5). Finally, the repeatability of laboratory impact force measurements was studied (see Section 4.3.1).

Table 3.5: Settings for the synoptic measurement devices in the 'DeltaFlume' model tests

	Laser Scanner	**Overview camera**	**Sideview camera**
Location	X = 174.75m Y = 5m Z = 9.26m	X = 172m Y = 2.5m Z = 8m	X = 177.32m Y = 0m Z =5.51m
Sampling frequency	35Hz	59.94 fps	
Angular resolution	0.25°	-	
Field of View (FoV)	∼15m offshore dike toe until wall	dike/promenade/ wall	promenade
Horiz. resolution on dike/promenade/wall	∼0.026 m	<0.01m	<0.003m
Synchronisation	Synchronisation pulse	LED in FOV	
Others	fog filter off first pulse slant angle 23°	Line mode	

3.4.1 Unique test identifier (TestID)

The data-sets 'UGent1'-'UGent3' and 'DeltaFlume' were designed complementary to each other and feature similar geometrical settings. Hence, the data-sets were combined for easier manipulation during the data analysis. To do so, the Matlab® software was used as a tool to combine the geometrical set-ups, wave parameters, overtopping discharges, overtopping flow parameters and impact loads from the four data-sets. Each test from the 'UGent1'-'UGent3' and 'DeltaFlume' data-set was assigned a unique testID in chronological order (see Table 3.6).

As mentioned earlier the separate tests for overtopping, incident waves, flow parameters and impact loads measurements were carried out using the same time-series of waves. These separate tests were assigned individual testIDs and later linked again to each other. For example for the 'UGent1' data-set the overtopping of the first test was measured in testID 001, the according overtopping flow thickness and velocity measured in a test with testID 035, the wave impact load measured in testID 055, the incident waves in testID 097. For testID 001, 035, 055, 097 the same time-series of waves was used. The assumption was that the conditions will be equal in between tests. This was not always the case in practice due to model effects and different reflection characteristics of the different set-ups (see Figure 3.4). All of the tests were linked in this way. For the 'UGent2' data-set the impact loads and incident waves were measured during the same test, in separate channels. Hence, the testID for both measurements was the same. For the 'DeltaFlume' data-set no separate tests were conducted to measure incident waves, overtopping and flow thickness and velocity. These parameters were derived

Table 3.6: Overview of testIDs for data-set 'UGent1' - 'UGent3' and 'DeltaFlume'

Data-set	Measurement	testID
'UGent1'	Overtopping	001-034
	Layer thickness & velocity	035-054
	Impact loads	055-096
	Incident waves	097-112
'UGent2'	Overtopping	113-141
	Impact loads	142-269
	Incident waves	270-397
'UGent3'	Overtopping	398-418
	Impact loads	419-468
	Incident waves	469-487
'DeltaFlume'	Impact loads	488-509

differently (see Section 3.2).

Not all tests could be used for further analysis due to different reasons. Hereby, a list of testIDs which were excluded for further analysis in this theses.

- testID 153, 155, 169, 188-189, 206, 220-221, 236, 248-249, 266 no overtopping measured due to low water level
- testID 067-076, 087-096, 156-160, 169-172, 190-193, 206-209, 222-225, 236-239, 250-253, 255-256, 265-269 no impact measured due to low water level
- testID 077, 146-147, 149-150, 152, 154 errors in the overtopping and impact analysis
- testID 494 second order wave generation used

3.4.2 Wave parameters

As described in Section 3.3.1 the water surface elevation was measured at a deep water location (above the flat part of the flume) and at the dike toe location for a situation with (obstructed) and without (incident) dike present. For the analysis described in this Section the incident wave parameters (without the dike installed in the flume) were investigated as they were key for the design of coastal structures. Wave analysis of the measured water surface elevation was carried out using Wavelab Version 3.7. Spectral wave parameters $H_{m0,o}[m]$ and $T_{m-1,0,o}$ [s] at the WG1-WG3 location were obtained using the method of Mansard and Funke (1980),

to distinguish incident and reflected waves. The amplitude reflection coefficient ranged between 5%-25% with an average of 16%. The low values of amplitude reflection coefficients were explained by the good absorption characteristics of the mild foreshore. The spectral incident wave parameters at the dike toe location $H_{m0,t}$ [m] and $T_{m-1,0,t}$ [s] were obtained by analysing the signal of a single wave gauge installed at the dike toe location. Additionally, the signals from the wave gauges installed along the foreshore were analysed as well and the spectral wave parameters derived.

In the 'DeltaFlume' data-set a spectra independent high-pass filter at 0.03 Hz and a spectra dependent low-pass filter at $3/T_p$ Hz were used (values in model scale). Additionally, the fft block size was selected automatically and the taper width and overlap set to 20%. Furthermore a number of data points were skipped at the beginning and end of each time series to focus the wave analysis on a fully developed wave field.

Table 3.7: Settings for spectral wave analysis in WaveLab (all values in model scale)

	'DeltaFlume'	**'UGent1'**	**'UGent2'**	**'UGent3'**
Froude length scale λ [-]	1-to-4.3	1-to-25	1-to-25	1-to-25
High-pass filter [Hz]	0.03	0.005	0.005	0.005
Low-pass filter [Hz]	$3/T_p$	3	3	3
Taper & Overlap [%]	20	20	20	20
fft block size [-]	auto	auto	auto	auto

In the 'UGent1'-'UGent3' data-sets a spectra independent high-pass filter at 0.005 Hz and low-pass filter at 3 Hz were used (values in model scale). The same fft block size, taper width and overlap settings as for the 'DeltaFlume' data-set were used. The derived wave parameters were very sensitive, especially the incident wave period at the dike toe, to the filter settings of the Wavelab Version 3.7. software and should therefore be treated with care. Waves are usually defined with a wave trough and a wave crest. The wave trough cannot be formed properly due to a limited water depth at the dike toe. Additionally, the shape of the waves compared to the shape of the deep water waves was different. A steep increase and a smoother decrease in the water surface elevation at the dike toe was noticed; similar to the characteristics of a bore.

The derived spectral wave height $H_{m0}[m]$ and period $T_{m-1,0}$ were used to calculate non-dimensional wave parameters. The shallow water wave length L_t was calculated using Equation 2.3. The relative water depth $H_{m0,o}/h_o$ at the WG1-WG3 location was always lower than 0.78 in all tests of the data-sets (see Table 3.8). This served as a first indication that the water depth at this location was sufficiently deep and the waves were non-breaking. The wave steepness for the same location was calculated using Equation 2.1. The obtained steepness's at the location WG1-WG3 were always lower than 0.008 for all tests and the waves were

therefore considered non-breaking swell sea (Eurotop, 2016). Along the 1-in-35 sloped foreshore the waves were breaking due to depth limitations and a broken wave was present at the dike toe. The wave steepness's for the dike toe location were calculated using Equation 2.1 and the incident spectral wave parameters derived for the dike toe location. In these conditions the Eurotop (2016) manual states that steepness's <0.01 often mean that the waves were broken due to depth limitations, as it was the case for all tests of the data-sets.

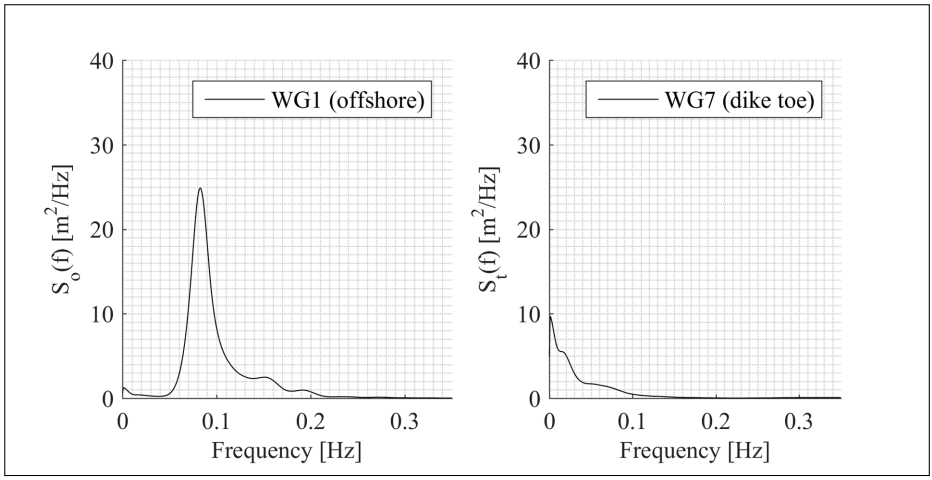

Figure 3.19: Wave spectrum computed based on measured water surface elevation time-series, for testID 500 from 'DeltaFlume' data-set, at WG2 (close to paddle, offshore) and WG7 (close to dike toe). Locations for WG2 and WG7 are given in Table 3.4.

The breaker parameter gave an idea of the kind of wave breaking involved and was calculated using Equation 2.2. The breaker parameter at the toe of the foreshore was calculated using the foreshore slope cot(θ_2)=35 and spectral wave parameters $H_{m0,o}[m]$ and $T_{m-1,0,o}$ [s] from wave gauge WG1-WG3 after reflection analysis. The breaker parameter at the foreshore toe $\xi_{m-1,0,o}$ was mostly <0.227 for the tests. The breaking waves were therefore considered spilling wave breaker, typical for mild foreshores (Eurotop, 2016). The breaker parameter at the dike toe $\xi_{m-1,0,t}$ was calculated using the dike slope cot(α) and the incident spectral wave parameters at the dike toe $H_{m0,t}[m]$ and$T_{m-1,0,t}$ [s]. The breaker parameter at the dike toe was always >5.24 for all tests. Hence, the second breaking of the already broken waves against the dike was considered surging or collapsing wave breaking (Eurotop, 2016).

Based on the criteria $h_t/H_{m0,o}$ developed by Hofland et al. (2017) the foreshore depths at the dike toe were classified as extremely shallow $h_t/H_{m0,o}$<0.3 and very shallow 0.3< $h_t/H_{m0,o}$<1 for the tests of data-set 'UGent1'-'UGent3' and 'DeltaFlume'.

Previously it was described that the waves breaking over a mildly sloping foreshore and in shallow waters were releasing free long waves (Hofland et al., 2017; Chen et al., 2016; Altomare et al., 2016; Van Gent, 1999a). This was also observed

Table 3.8: non-dimensional range of wave parameters for the data-sets 'UGent1'-'UGent3' and 'DeltaFlume'

	'DeltaFlume'	**'UGent1'**	**'UGent2'**	**'UGent3'**
Wave steepnees offshore $S_{m-1,0,o}$ [-]	0.0030 - 0.0033	0.0026 - 0.0030	0.0028 - 0.0078	0.0031 - 0.0035
Breaker parameter offshore $\xi_{m-1,0,o}$ [-]	0.199 - 0.207	0.208 - 0.225	0.129 - 0.215	0.192 - 0.205
Rel. water depth offshore $H_{m-1,0,o}/h_o$ [-]	0.1616 - 0.2767	0.1100 - 0.2889	0.1665 - 0.2946	0.1264 - 0.2780
Wave steepnees dike toe $S_{m-1,0,t}$ [-]	0.00110 - 0.00524	0.00013 - 0.00220	0.00018 - 0.00180	0.00017 - 0.00400
Breaker parameter dike toe $\xi_{m-1,0,t}$ [-]	6.91 - 15.07	10.55 - 44.05	7.91 - 35.13	7.95 - 38.24
Rel. water depth dike toe $h_t/H_{m-1,0,o}$ [-]	0.0669 - 0.4487	0.0532 - 0.6586	0.0745 - 0.4787	0.0664 - 0.8020
Rel. promenade width G_c/L_t [-]	0.0752 - 0.1405	0.0259 - 0.3649	0.0242 - 0.2090	0.0306 - 0.1149

in this study, in a spreading of the spectral wave energy mostly towards lower frequencies for the dike toe location computed for testID 500 from the 'DeltaFlume' data-set (see Figure 3.19). The time-series was transformed into a spectra by Fast Fourier Transform algorithms and using the $pwelch$ functionality in Matlab®. A hamming window of 50 times the sampling frequency was used for the computation.

The shallower the relative water depth at the dike toe, the more flattening of the spectrum would occur resulting in larger spectral wave periods at the dike toe $T_{m-1,0,t}$ (see Figure 3.20). The significant lower values from the 'DeltaFlume' model tests are in two ways. First, the formula was derived mostly based on data derived from experiments with milder slopes (1-to-100 until 1-to-200). Secondly, the active wave absorption in the 'DeltaFlume' model test was able to remove the unwanted seiche frequencies from the flume, resulting in reduced values especially for the wave period at the dike toe. The decrease in spectral wave height $H_{m-1,0}$ from the offshore location, along the mildly sloping foreshore until the dike toe, was in the range of 30%-80%. The average decrease of spectral wave height $H_{m-1,0}$ considering all model tests was 44%. The reduction in spectral wave height $H_{m-1,0}$ was due to wave breaking and loss in energy on the mild foreshore.

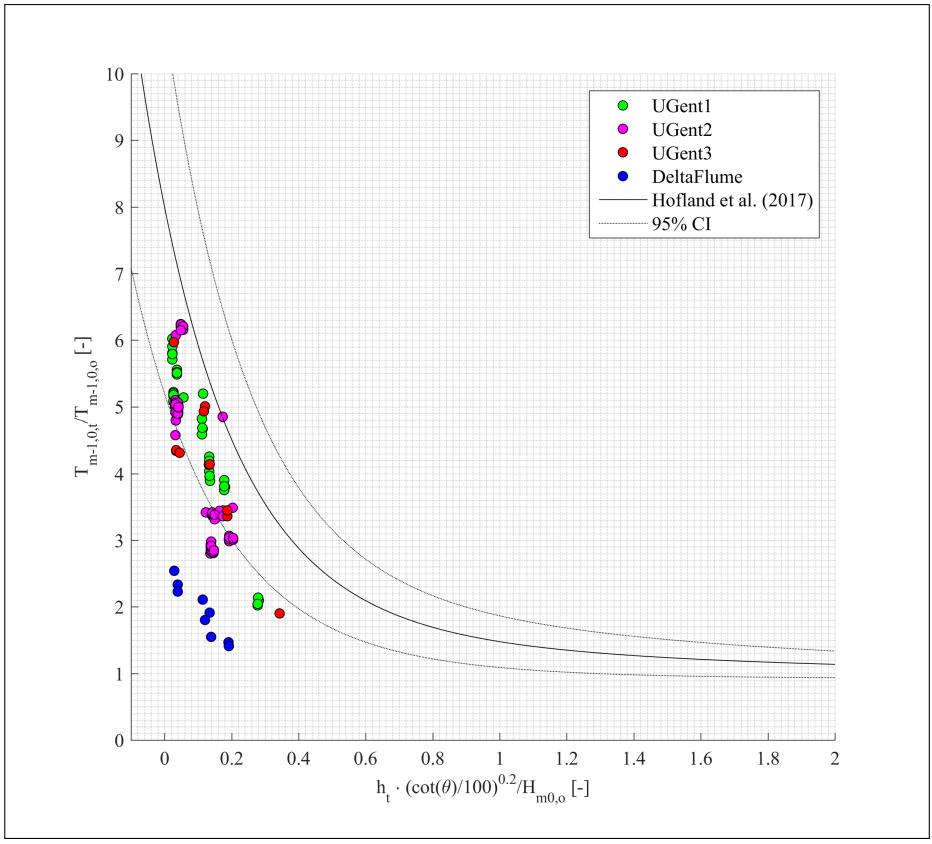

Figure 3.20: Relative water depth at the dike toe (x-axis) and flattening of the spectral wave period from offshore to the dike toe (y-axis) after Hofland et al. (2017). The prediction after Hofland et al. (2017) was given as the black line together with the 95% confidence interval as two times the standard deviation σ.

The increase in spectral wave period $T_{m-1,0}$ from the offshore, along the mildly sloping foreshore, until the dike toe location was in the range of 40-80%. The average increase in spectral wave period $T_{m-1,0}$ considering all model tests was 57%. The increase in spectral wave period $T_{m-1,0}$ was due to the release of the bound long waves in the breaking process on the mild foreshore. It was noted that the active wave absorption in the 'UGent1'-'UGent2' data-sets was not able to sufficiently remove the seiches, associated to the natural frequency of the flume in the order of $0.035 - 0.57$ Hz (depending on geometry and water level). This was partly due to the used 1^{st} order wave generation and partly due to limitations in stroke length of the paddle. As a consequence, a build up of long wave energy in the 'UGent1'-'UGent3' data-sets was observed. However, the contribution of these long frequencies in the energy density spectrum was rather low and it was decided to not apply additional filtering to the data. These low frequencies were also present for the overtopping and force measurements. Hence, removing them

in the wave analysis and relating the waves to the overtopping or impact forces was considered less desirable. The active wave absorption in the 'DeltaFlume' data-set instead was able to remove the flume related natural frequencies during wave generation.

3.4.3 Average overtopping

The average overtopping discharge q [l/m per s] was obtained by analysing the weigh cell measurement described in Section 3.3.2. Post-processing was done in Matlab® using scripts developed by Victor et al. (2012). Basically the weigh cell difference before and after the test gave the absolute mass of overtopped water and divided by the density of the water, width of the overtopping chute and test duration resulted in the average overtopping discharge. The integrated pump curve was used to add the mass of the pumped water to the absolute mass of overtopped water, in case the pump was activated to empty the overtopping box during the test. When the pump inside the overtopping box became submerged, the buoyancy force would increase and thus a lower weight of the pump was measured by the weigh cell. A correction term was introduced based on the fill (submergence of the pump) of the overtopping box, to account for the increase buoyancy force. For details on the analysis method it was referred to Gallach Sánchez (2018). The same time window from the wave analysis (see Section 3.4.2) was used to focus the analysis on a fully developed wave field. Since no overtopping was measured in the 'DeltaFlume' test, the average overtopping discharge from the 'UGent3' data-set were assigned to the 'DeltaFlume' data-set as well (using a similar model geometry and the downscaled realized paddle motion time-series to generate the waves).

The overtopping formula from Van Gent (1999b) was used (see Equation 2.4 with the extension by Altomare et al. (2016) for the equivalent slope (see Equation 2.5). For the prediction using the equivalent slope concept an adjusted c-coefficient 0.791 and standard deviation σ equal to 0.294 were used. The prediction was only applicable for relative water depth at the toe -0.88$< h_t/H_{m0,o}<$2.38, for incident breaker parameter at the toe $\xi_{m-1,0,t}>$7 and for incident wave steepness at the toe $S_{m-1,0,t}<$0.01. Besides the breaker parameter for some tests, all criteria were fulfilled within this study (see Table 3.8)). The computation of average overtopping discharge and comparison to the measured values showed that the measured values were in between 0.1 and 10 times the predicted value and comparable in range for all four data-sets (see Figure 3.21).

3.4.4 Flow thickness and velocity

The analysis of flow thickness and velocity in the 'UGent1'-'UGent3' data-sets remained a challenge. While it was possible to distinguish the maximum flow thicknesses using half-automatic selection tools (Streicher et al., 2016; Hughes, 2015), it was not possible to resolve the flow velocities using transit time techniques in the 'UGent1'-'UGent3' data-sets. Other options to measure the flow velocity were tested: A side-view video camera and motion tracking of the bore front against an accentuated background was used but difficulties in the correct determination of

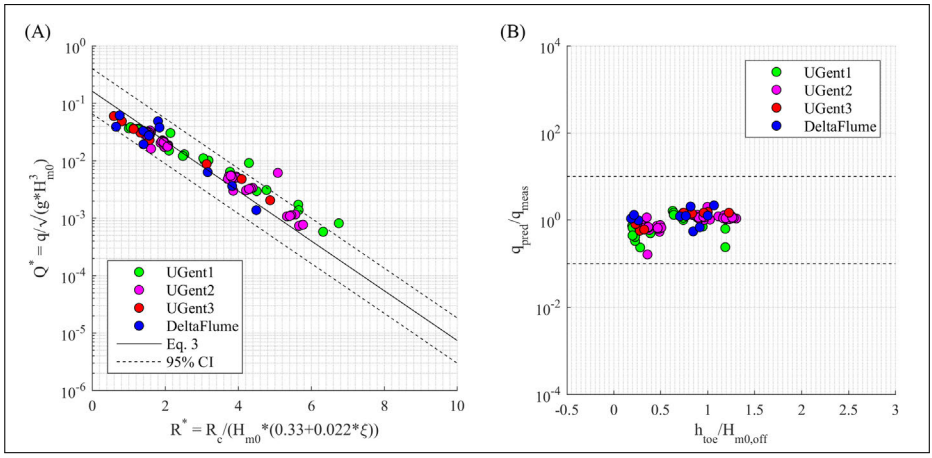

Figure 3.21: Non-dimensional overtopping vs. non-dimensional freeboard (left) and predicted/measured overtopping vs non-dimensional water depth showed that the measured values are within comparable (between data-sets) and predicted (Altomare et al., 2016) range

the bore front from the video images facilitated the analysis. Furthermore, a row of metal pins connected to electric wires was installed with their head just above the promenade. The distance between the pins was defined and a metal plate installed in proximity of the pins, acting as supply electric source. The circuit was closed as soon as water would conduct electricity between any steel pin and the metal plate. When two consecutive steel pins were activated, the average velocity of the water between the pins was obtained. This was done by diving the distance between the pins with the time difference of activation. Droplets of water at the metal pins, erroneous measurements, too small layer thicknesses and non-uniform bore fronts along the promenade proved this method to be not useful.

Therefore, it was decided to limit the analysis of overtopping flow thickness and velocity in this theses to the 'DeltaFlume' data-set as the generally larger thicknesses and velocities enable a reliable measurement. Furthermore, the analysis for layer thickness and velocity was done and described in detail by Hirt (2017), for the flows related to the 30 highest impact forces from test testID 492 and test testID 500 each (see Table 3.3). The time-series of the wave gauges installed on the promenade was used to determine the incoming and reflected flow thicknesses and the time-series of the paddle wheels was used to determine the incoming flow velocity. The time-series were obtained at four locations along the promenade. Only the time-series of the paddle wheels was filtered using a 15Hz low-pass filter to remove the noise from the measurement. The maximum flow thickness η_{max} and maximum flow velocity u_{max} were manually read from the signal (see Figure 3.22). It was further noted that the overtopping flow at location 1 was often affected by the overtopping splash and the flow at location 4 affected by the reflected flow from the wall. Hence, it was decided to use the measurements from location 3, as representative velocity and thickness for the overtopping flow. Location 3 was

situated 1.26 m apart from the dike crest and 1.09m in front of the steel wall. The time-series of flow thickness η [m] and flow velocity u [m/s] for a selected overtopping event from test testID 492 were showcased (see Figure 3.22).

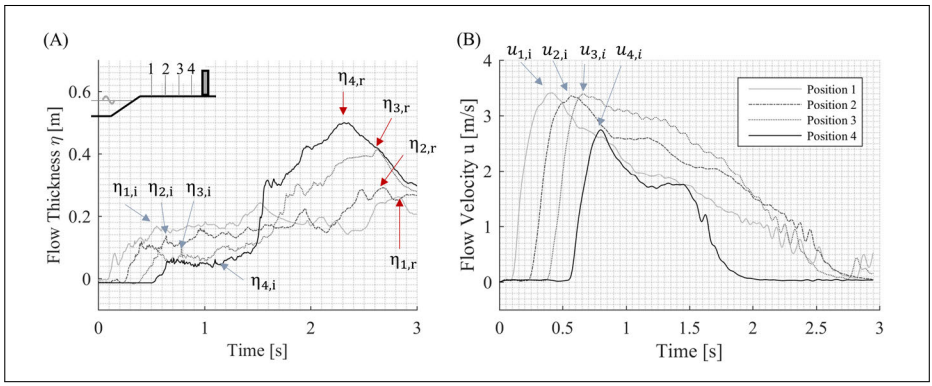

Figure 3.22: Time-series of layer thickness gauges (WLDM1-WLDM4) with incoming η_i and reflected η_r flow thickness measured at location 1-4 (A). Time-series of paddle wheels (PW1-PW4) with incoming bore velocity u_i at location 1-4 (B).

The incoming flow thicknesses slightly decreased along the promenade from WLMD1-WLMD4, the reflected flow was generally higher and the decrease occurred in reversed order from WLMD4-WLMD1 (see Figure 3.22). No reflected flow velocities were observed from the measurement as the paddle wheels were only able to measure in incoming flow direction. The measured maximum bore thicknesses and velocities at location 3 and leading to the 30 highest impacts in test testID 492 and testID 500, ranged between η_{max}=0.02 – 0.42 m and u_{max}=0.62–4.13 m/s (ANNEX C).

3.4.5 Impact force and pressure

Post-processing of measured impact forces and pressures was synchronized between the data-sets ('UGent1'-'UGent3' and 'DeltaFlume') and the same set of analysing routines used. This involved using similar filter settings, to ensure comparability between the data-sets.

The time-series of measured impact force and pressure was recorded with 1.000 Hz sampling frequency in all data-sets. Since the data-sets were derived from different scale models, the sampling frequency should be scaled as well to ensure similarity between the data-sets. It was therefore attempted to upscale the sampling frequency of the 'UGent1'-'UGent3' data-sets to match the sampling frequency of the 'DeltaFlume' data-set, using Froude similarity and the scale ratio λ_r=5.81. In this way the 1.000 Hz signal of the 'UGent1'-'UGent3' data-sets was interpolated and a 415 Hz signal obtained. No significant reduction of the force peaks was observed and it was decided to use the original 1.000 Hz sampling signal in all data-sets instead. The time series for force and pressure measurement was post-processed in three steps for all data-sets. The processing routines were im-

plemented in Matlab® and termed Impact-Analysis-Toolbox (IAT). The Matlab® script was provided in ANNEX E and ANNEX F.

First, any long duration drift was removed from the signal using the 'detrend' functionality in Matlab®. Furthermore an offset correction was applied, by fitting a polynomial best-fit line to the lower values of the time-series (the noise band, not including the force peaks) and subtracting the polynomial best-fit line from the time-series. In this way the entire time-series was shifted towards zero.

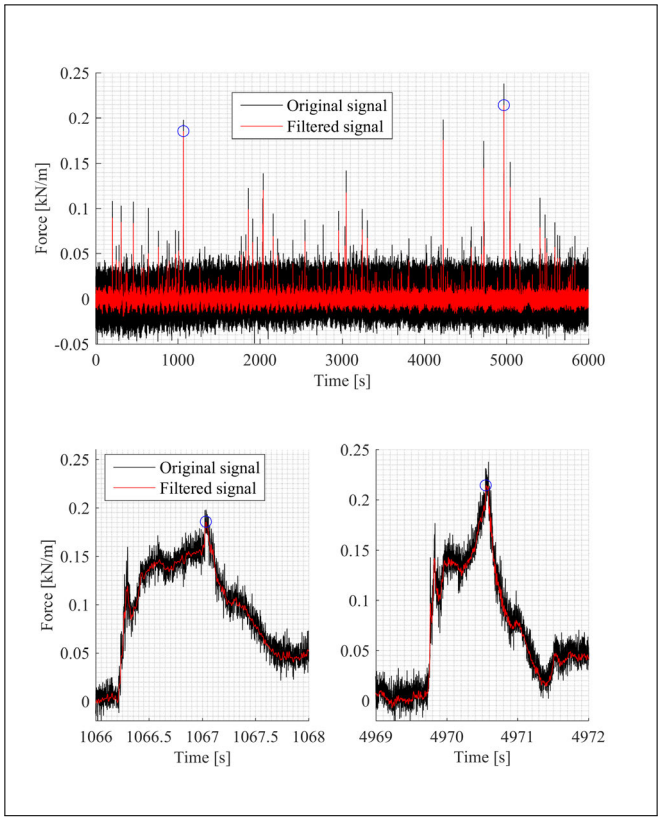

Figure 3.23: Force time-series before (black) and after filtering (red). A zoom on the two highest impacts was provided in the lower figures.The signal from the lower load cell (0.18 m above the promenade) of testID 500 from the 'DeltaFlume' data-set was displayed.

The time-series was then transformed into frequency domain with fast Fourier transformation and a set of frequency components and their according energy density obtained. In frequency domain the filters were set (see Table 3.9), to remove phenomena related to model effects (for example electronic current frequency, natural frequency of the measurement system/wall) from the time-series. Furthermore, low-pass filtering was applied.

The low-pass filter should be chosen as a compromise between removing the

high oscillation noise from the signal and limiting the decrease in peak impact force (typically around 10%-20% for low-pass frequencies around 50 Hz in model scale (Chen, 2016)). Previous studies showed that a 50 Hz low-pass frequency (Chen et al., 2016; Van Doorslaer et al., 2017) showed good results. The force response of any real structure was another aspect to consider. Typical natural periods of $3 - 50$ m high buildings were in the range of $0.1 - 1$ s ($1 - 10$ Hz) in prototype (Chen, 2016) and $0.046 - 0.48$ s ($2 - 22$ Hz) in the scale of the 'DeltaFlume' data-set. Given all these considerations, a low-pass filter for the 'DeltaFlume' data-set of 48 Hz (model scale) was chosen. This was within the range of natural frequencies of coastal buildings and close to the previously applied 50 Hz low-pass filter. Furthermore, the reduction in force peaks was limited (see Figure 3.23 and Figure 3.24). A Butterworth filter design of 4^{th} order was applied.

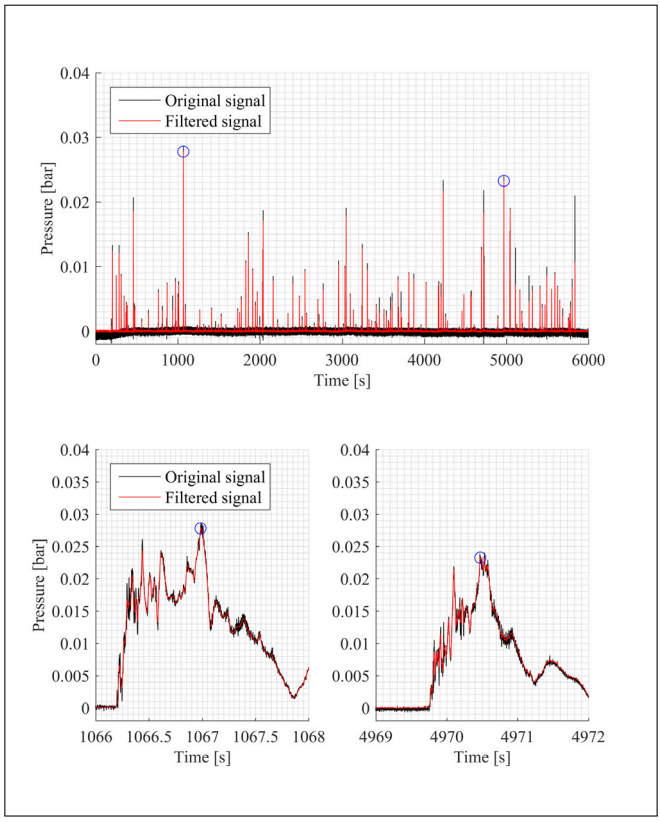

Figure 3.24: Pressure sensor time-series before (black) and after filtering (red). A zoom on the two highest impacts was provided in the lower figures. The signal from pressure sensor P3 (0.16 m above the promenade) of testID 500 from the 'DeltaFlume' data-set was displayed.

A reduction in force peaks after filtering was observed. Anyhow, a zoom on the two largest force peaks showed, that the reduction occurred within the noise band

of the measurement. Generally, the noise bandwidth of the load cell measurement was higher compared to the pressure sensor measurement. Figure 3.24 showed the signal of pressure sensor 3 (installed approximately at the same height as the load cell measurement in Figure 3.23) before and after filtering. A zoom on the two largest pressure peaks showed that also for the pressure sensor signal the reduction in pressure peaks was within the noise bandwidth of the measurement. An average reduction of force peaks of $\sim$26% for the load cell signal and pressure peaks $\sim$6% for the pressure sensor (P_3) signal were found. This was however dependant on individual force/pressure peaks and how much a specific wave impact would excite the resonance vibrations of the measurement system. The reduction of the force/pressure peak due to the filters was higher, when there were more resonance frequencies excited, compared to the reduction of force/pressure peaks where hardly any resonance frequencies were excited. The general conclusion was made that mostly impacts including a large amount of resonance induced vibrations will have a large reduction in magnitude and for the other force peaks the reduction is tolerable, for a 48 Hz low-pass filter.

The low-pass filter was then downscaled to the 'UGent1'-'UGent3' data-set dimensions using Froude similarity and the length scale ratio of λ_r=5.81. This resulted in a similar low-pass filter at 115 Hz for the 'UGent1'-'UGent3' data-sets. Additionally band-stop filters to remove the resonance frequencies of the measurement systems (see Table 3.9) were applied. Furthermore, a band-width filter to remove the noise from the electronic current system (at 50 Hz) was used.

Table 3.9: Filter settings for frequency filtering of impact force and pressure in Matlab® (all values in the according model scale)

	'DeltaFlume'	**'UGent1'**	**'UGent2'**	**'UGent3'**
Froude length scale λ [-]	1-to-4.3	1-to-25	1-to-25	1-to-25
Natural freq. wall [Hz]	> 77	48, 95	70, 75, 90	35, 48, 80
Low-pass filter [Hz]	48	115	115	115
Filtering around [Hz]	-	48, 50, 95	50, 70, 75, 90	35, 48, 50, 80
Order butterworth filter [-]	4	4	4	4

Second, the signals of the two load cells in the 'DeltaFlume' data-set, attached to the same measurement hollow steel profile, were added. The sum was divided by the width 0.2 m of the measurement plate to obtain a horizontal force per meter width value. The pressure sensor signals from the 13 vertically spaced pressure sensors in the 'DeltaFlume' data-set were integrated over the height of the pressure plate in this step. Rectangular pressure integration was applied using half the distance below and above a pressure sensor Δ_i, together with the measured pressure

from this location P_i (see Equation 3.2),

$$F = (P_1 \cdot \frac{\Delta_1}{2}) + (P_{13} \cdot \frac{\Delta_{12}}{2}) + \sum_{i=2}^{12} (P_i \cdot \frac{\Delta_{i-1} + \Delta_i}{2}) \; [N/m]. \tag{3.2}$$

The value from the lowest pressure sensor (P_1) was assumed from the location of P_1 until halfway between P_1 and P_2. The integration for the highest pressure sensor (P_{13}) was done using half the distance between PP_{12} and P_{13}. The result was a horizontal force per meter width value. Comparing the time-series of integrated pressures and force measurement for the 'DeltaFlume' set-up, it was noted that the integrated pressure time-series showed a lower noise bandwidth, which was the effect of the generally lower noise bandwidth in the individual pressure sensor signals (compare Figure 3.23 and Figure 3.24).

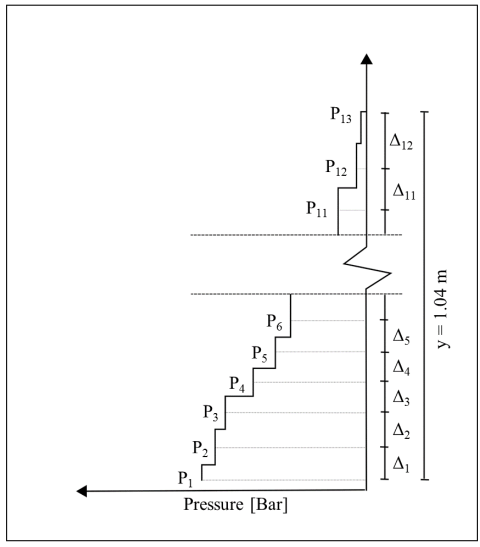

Figure 3.25: A total horizontal force from the pressure sensor signals was obtained by applying rectangular pressure integration (Equation 3.2). The distances Δ_i and pressures P_i were used during the calculation.

For the 'UGent1'-'UGent3' data-sets, the load cell signals were simply divided by the width 0.1 m of the measurement plate to obtain a horizontal force per meter width value.

Third, a half-automatic peak detection method was applied and the key events from the filtered time-series selected. A minimum time between force peaks was set to 2 s in the 'DeltaFlume' data-set and down-scaled, using Froude similarity and length scale ratio λ_r=5.81, to the 'UGent1'-'UGent3' data-sets as 0.83 s accordingly. Previously, (Chen et al., 2016) used the mean wave power as proposed by (Goda, 2010) to define a high-pass threshold for the force peaks. The mean wave power (see Equation 3.3) was used in the present study to define the high-pass

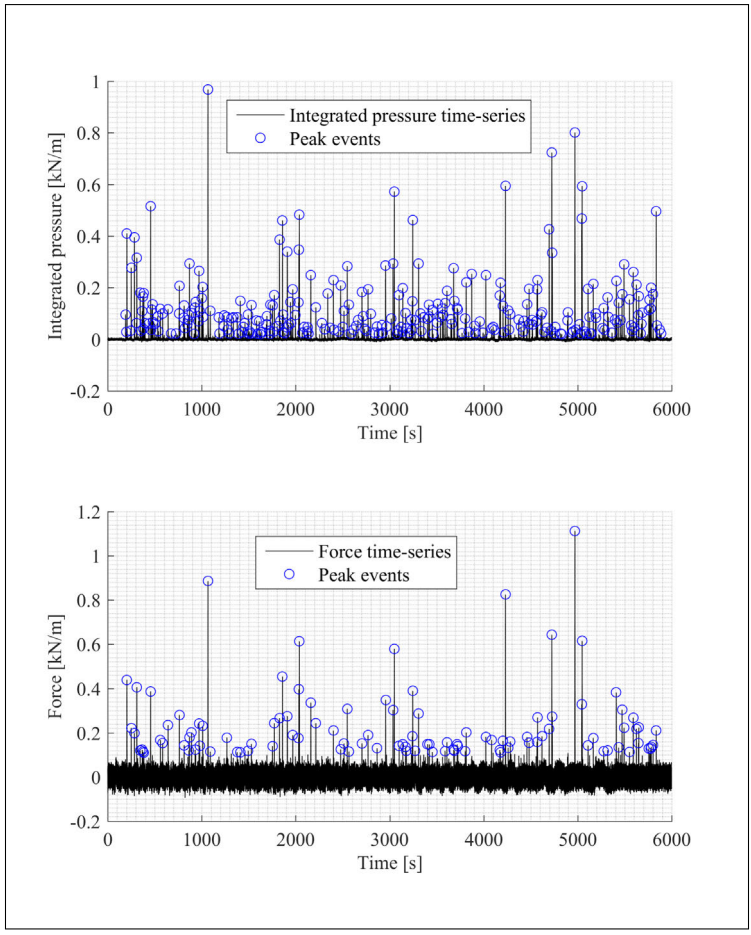

Figure 3.26: Selected peak events for test testID 500 from the 'DeltaFlume' data-set for the integrated pressures (upper figure) and force measurement (lower figure).

threshold for the force peaks in time domain,

$$F_p = 1/8 \cdot \rho \cdot g \cdot H_{m0,t}. \tag{3.3}$$

The high-pass threshold should always be higher than the noise band of the measurement. Hence, the lowest force peaks were checked against video recordings to ensure that a physical impact occurred in the model. Finally, erroneous detected force peaks were manually deleted from the output file.

After post-processing, a total of 39,451 force peaks for the 'DeltaFlume' data-set, 4,528 force peaks for the 'UGent1' data-set, 13,666 force peaks for the 'UGent2' data-set and 21,070 force peaks for the 'UGent3' data-set were obtained (Figure 3.27). The force peaks were up-scaled to prototype for better comparability, using

Froude similarity and the according length scale factor. The exceedance probabilities P_f [%] for the force peaks F [kN/m] were calculated (see Equation 3.4),

$$P_f = \frac{i}{N_i + 1}. \tag{3.4}$$

Where i was the considered force peak and N_i the total number of force peaks ranked from high to low. The obtained force peaks from all 4 data-sets ('UGent1'-'UGent3' and 'DeltaFlume') were plotted as a distribution and showed that the force peaks fell in the same range (see Figure 3.27).

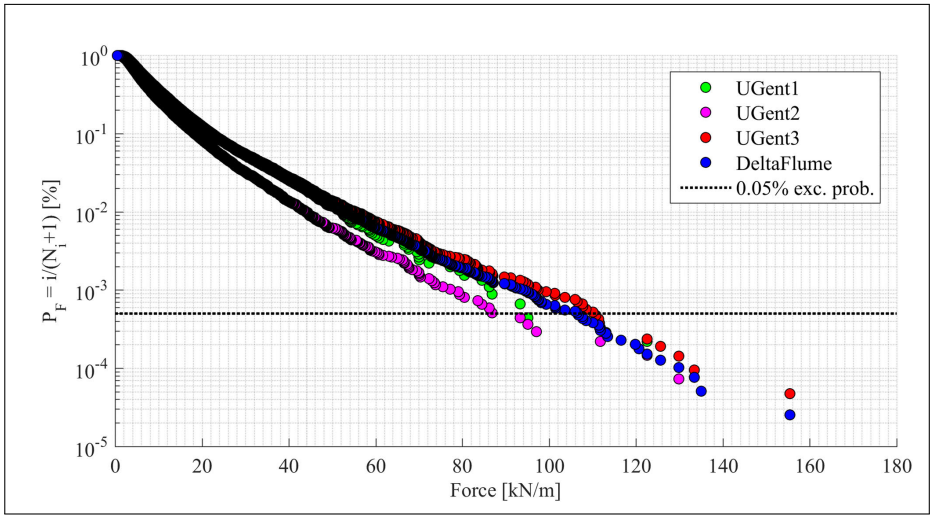

Figure 3.27: Plotting positioning of the force peaks for all impacts from 'UGent1'-'UGent3' and 'DeltaFlume' model tests.

Several force indicators were derived for each test. The most prominent was the maximum impact force F_{max}, often key for the design of coastal structures. The maximum recorded force peaks per model were 122 kN/m, 128 kN/m, 155 kN/m and 155 kN/m for 'UGent1'-'UGent3' and 'DeltaFlume' data-set respectively (values in prototype). Furthermore, the average 1-in-250 impact force $F_{1/250}$ was derived as the average of the 0.4% highest impacts (Goda, 2010). The $F_{1/250}$-value is likely to be more stable over a range of impacts compared to a single maximum event. However, a sufficient number of impacts (>250) need to be measured to distinguish this value from the F_{max} impact force. Other force indicators were the value exceeded by 10% of impacts $F_{10\%}$, the average of the highest 10, 20, 30 impact forces F_{10}, F_{20}, F_{30}, respectively and average of all impact forces F_{avg} per test.

Chapter 4

Analysis of scale effects in laboratory impact force measurement

In this section the non-repeatability related uncertainties, scale- and model effects in laboratory overtopping bore-induced impact load measurements were discussed. After an outline of the specific objectives for this Chapter (see Section 4.1) two scale models were introduced comparatively (see Section 4.2) in terms of model set-up and hydraulic boundary conditions in order to investigate similarity between the scale models. A baseline uncertainty of the impact force measurement was established based on repetition tests and compared to the differences in the measured impact force resulting from scale- and model-effects. The differences in measured force were quantified (see Section 4.3) and summarized in the conclusions (see Section 4.4).

4.1 Specific objectives

In this study the stochastic non-repeatability, model- and scale effects were further investigated by comparing two data-sets derived from similar small- and large-scale experiments. More detailed objectives are:

1. to provide a detailed comparison of small-scale and large-scale model set-up and hydraulic boundary conditions, in order to discuss similarity of the two models.

2. to investigate potential model effects in terms of wave parameters at the dike toe, as they serve as the hydraulic boundary condition for the measured bore-induced impact force.

3. to investigate the non-repeatability of bore-induced impact force measurements using the small-scale model and same time-series of waves, to establish

a baseline uncertainty against which the scale-effects can be judged.

4. to investigate scale effects of bore-induced impact force measurements by comparing the force measurements from the small-scale and large-scale model in prototype and to discuss the absolute and percentage difference of the force indicators F_{max}, $F_{1/250}$, F_{10}, F_{20}, F_{30}, F_{50}, F_{100}, F_{avg}.

4.2 Data analysis and methods

The large-scale (Froude similiarity and a length scale factor 1-to-4.3) experimental campaign was conducted within the research project WALOWA in the Delta Flume. A detailed model set-up was provided in Section 3.2.1. It was further termed the large-scale experiment. The small-scale (Froude similarity and a length scale factor 1-to-25) experimental campaign was conducted at Ghent University. A detailed model set-up was provided in Section 3.1.1. It was further termed the small-scale experiment. The length scale ratio between the two scale models was 1-to-5.81.

4.2.1 Similarities of geometrical model set-up

Hereafter, only a compact overview of the geometry has been summarized with a focus on the main differences (Table 4.1). For better comparability all dimensions were up-scaled to prototype using Froude similarity. The geometrical parameters of the model set-ups are highlighted in Figure 3.1. Most striking differences between the two scale models were found in the distance between the wave paddle and the start of the foreshore. While the prototype distance was 404.1 m for the large-scale model, it was only 274 m in the small-scale model. As a result of the length difference the wave propagation and interaction with reflected waves was altered, leading to a different water surface elevation time series at the toe of the dike.

Furthermore, the applied foreshore material in the large-scale model was sand with a grain size diameter of D_{50}=320 μm. In the small-scale model smooth concrete was used to build the foreshore. It was expected that on the one hand the porosity of the sand is expected to lead to additional wave energy dissipation and on the other hand the erosion of sand at the dike toe will lead to larger water depths h_t and potentially higher wave energy at the toe of the dike (Saponieri et al., 2018). Regardless of the scour hole at the dike toe, which developed for the sand foreshore, the dike toe location and water depth at the dike toe h_t were defined at the connecting point between initial foreshore geometry and dike.

Dike and promenade were constructed from plywood in the small-scale model and concrete in the large-scale model. It was expected that the slightly smoother plywood resulted in lower friction losses of the overtopping water flow in the small-scale model. In both scale models the wall was high enough to not be overtopped by the run-up water.

The impact forces were measured with two HBM U9 compression load cells with a measurement range of 20 kN in the large-scale model (see Figure 4.1, A and B). The maximum absolute error was 0.007 kN and the maximum relative error 0.363% of the full-scale output. The load cells were connected above each other

Table 4.1: Comparison of wave flume and model characteristics between large-scale and Small-scale experiment. Values were up-scaled and compared in prototype

	Model scale	Flume	Foreshore	Dike	Promenade	Wall
Small-scale (Ghent University)	1-to-25	$L = 750$m $H = 30$m $W = 25$m	concrete $\cot(\theta_1) = 10$ $\cot(\theta_2) = 35$ $l_1 = 274$m $l_2 = 83.9$m $l_3 = 264.9$m	plywood $\cot(\alpha) = 2$ $h_3 = 2.3$m	plywood $G_c = 10$m	alluminium plate $h_w = 6.88$m not overtopped
Large-scale (Delta Flume)	1-to-4.3	$L = 1251.3$m $H = 40.85$m $W = 21.5$m	sand $\cot(\theta_1) = 10$ $\cot(\theta_2) = 35$ $l_1 = 404.1$m $l_2 = 83.9$m $l_3 = 264.9$m	concrete $\cot(\alpha) = 2$ $h_3 = 2.3$m	concrete $G_c = 10$m	hollow steel profile $h_w = 6.88$m not overtopped

to the same 0.2 m-wide hollow steel profile. The profile was flush-mounted into the wall (red rectangle). The resonance frequency of the large-scale measurement system was estimated to be approximately at 80 Hz. In the small-scale model the impact forces were measured using a Tedea-Huntleigh strain gauge load cell with a measurement range of 5 kN (see Figure 4.1, C and D). The maximum relative error was stated as 0.02% of the full-scale output. The strain gauge load cell was connected to a 0.1 m-wide aluminum plate, and the plate flush-mounted with the rest of the wall (red rectangle). A static calibration of this instrument was roughly done by placing defined weights on the load cell and measuring the weight response. The first resonance frequencies of the small-scale measurement system were found at 35 Hz, 45 Hz, and 53 Hz.

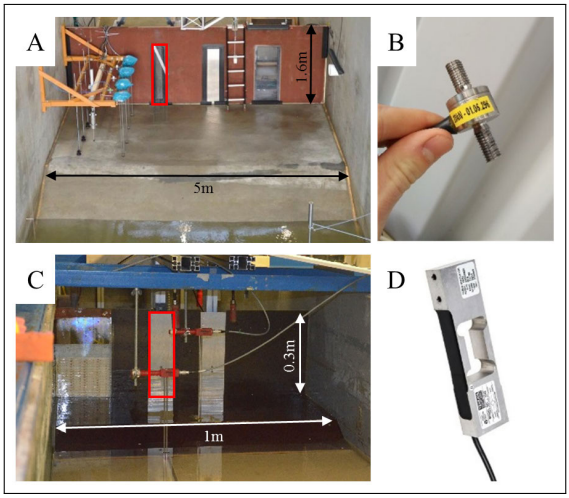

Figure 4.1: Dike, promenade and wall in large-scale (A) and small-scale (C) experiment. The impact forces were measured in the area highlighted in red, with two compression load cells in large-scale (B) and a strain gauge load cell in small-scale.

All other parameters, such as the crest freeboard, A_c, and the offshore water depth, h_o, were kept the same. The comparison of the wave time-series and spectral

parameters at a location close to the paddle and at the dike toe location provided further insight into whether similarity of the hydraulic boundary conditions between the two scale models was achieved.

4.2.2 Similarities of hydraulic boundary condition

Waves were generated in both scale models with a piston type wave paddle. Two tests with wave conditions similar to a storm with an annual recurrence interval of 1,000 (testID 500) and 17,000 years (testID 492) were selected for this study (see Table 3.3).

The steering signal in the small-scale model was the down-scaled measured time-series of waves from the large-scale model. In this way a most similar sequence of waves in both scale models was achieved. The active wave absorption system was activated in both scale model experiments.

The water surface elevation η(t) was measured with resistive type wave gauges deployed at the flume wall for the large-scale model and in the middle of the flume for the small-scale model. The measurement location in flume length direction was the same between scale models and referred to as the offshore location (above the flat bottom part in the flume and before the start of the foreshore) and as the dike toe location. Spectral wave parameters at the offshore location $H_{m0,o}$ [m] and $T_{m-1,0,o}$ [s] and at the dike toe location $H_{m0,t}$ [m] and $T_{m-1,0,t}$ [s] were obtained for test testID 492 (Table 4.2) and test testID 500 (Table 4.3) in both scale models. The spectral analysis was performed using similar analysis settings. Low cut-off and high cut-off frequencies were the scaled equivalent of each other using the length scale ratio 1-to-5.81. This resulted in a low cut-off frequency of 3 Hz (large-scale model) and 7 Hz (small-scale model), as well as a high cut-off frequency of 0.025 Hz (large-scale model) and 0.060 Hz (Small-Scale model).

The ratio for the offshore spectral wave height $H_{m0,o,SS}/H_{m0,o,LS}$ and period $T_{m-1,0,o,SS}/T_{m-1,0,o,LS}$ between large-scale (LS) and small-scale (SS) experiment was in the order of $\sim$1% and $\sim$3% respectively for test testID 492 (Table 4.2). This was considered acceptable and confirmed by the good agreement between the large-scale and small-scale time-series of water surface elevation η (Figure 4.2, upper row). However, the ratio of spectral wave height $H_{m0,t,SS}/H_{m0,t,LS}$ and period $T_{m-1,0,t,SS}/T_{m-1,0,t,LS}$ at the dike toe between large-scale and small-scale experiment was in the range of $\sim$10% for test testID 492. This was confirmed by the slightly worse agreement between large-scale and small-scale time-series of water surface elevation η at the dike toe (Figure 4.2, lower row). There were more shorter waves visible in the large-scale model time-series at the dike toe location.

The same analysis was performed for test testID 500. The ratio for the offshore spectral wave height $H_{m0,o,SS}/H_{m0,o,LS}$ and period $T_{m-1,0,o,SS}/T_{m-1,0,o,LS}$ between large-scale and small-scale model was in the order of $\sim$2% and considered a good agreement (Table 4.3). The ratio of spectral wave height $H_{m0,t,SS}/H_{m0,t,LS}$ and period $T_{m-1,0,t,SS}/T_{m-1,0,t,LS}$ at the dike toe between large-scale and small-scale model was in the order of 7% and 10% respectively. It is striking that the wave height for at the dike toe in the small-scale model was lower than in the large-scale model, for testID500 (see Table **??**). This difference could possibly be

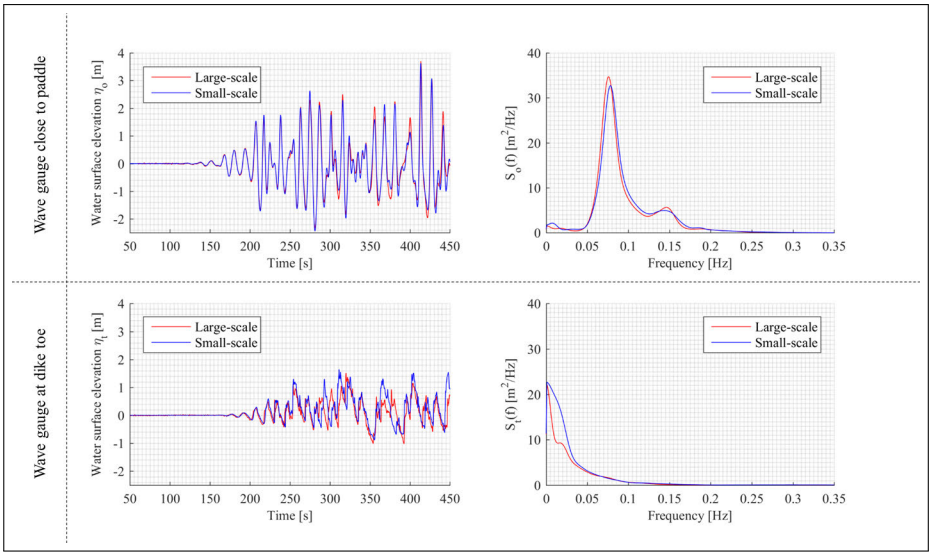

Figure 4.2: Beginning of water surface elevation time-series (left) and wave spectrum calculated for the entire time-series (right) for test testID 492. The measurements in the upper row were obtained at the location close to the paddle and in the lower row at the dike toe location. Small-scale (blue) and large-scale (red) measurements were compared in prototype.

explained by the increased water depth at the dike toe due to the fully developed erosion hole in the large-scale model (∼0.15 m in model scale and 0.65 m in prototype (Saponieri et al., 2018)), because the test was conducted at a later time during the experimental campaign, while testID 492 was conducted in the beginning of the experimental campaign, with less erosion at the dike toe (Streicher et al., 2017). This remains an assumption and further tests with variable erosion depth at the dike toe location need to be analysed. It could also be that the smaller water depth at the dike toe in testID 500, compared to testID492, was causing the difference. For smaller water depths, a larger effect of the dissimilarities in the entrained air and its influence on the transport of spectral energy across the breaking zone between large- and small-scale model was expected.

The agreement of the water surface elevation time-series and spectral distribution between small-scale and large-scale model was considered good at the offshore location (Figure 4.3, upper row). Comparable to test testID 492 the agreement decreases at the dike toe location (Figure 4.3, lower row). Additionally it was noted that the number of small waves was higher for the large-scale model tests and the dike toe location in both tests.

Whereas a difference of ∼1-3% in spectral wave parameters at the offshore location seems negligible, the difference of ∼10% for the dike toe location becomes more significant for both tests and should be considered when interpreting the results of the impact force measurements. The deviation of 10% in the dike toe spectral wave parameters was not unusual and shows that even in the controlled

Table 4.2: Hydraulic boundary conditions test testID 492. The values were up-scaled and compared in prototype

testID 492	Small-scale (SS)	Large-scale (LS)	Ratio (SS/LS)
Model scale	1-to-25	1-to-4.3	1-to-5.81
$H_{m0,o}$ [m]	4.64	4.59	1.011
$T_{m-1,0,o}$ [s]	11.67	12.03	0.970
$H_{m0,t}$ [m]	2.79	2.51	1.112
$T_{m-1,0,t}$ [s]	37.03	33.42	1.108
Duration [s]	$\sim$ 13000	$\sim$ 13000	-
h_o [m]	17.25	17.16	1.005
h_t [m]	1.3	1.21	1.074
A_c [m]	1	1.08	0.926

model environment and most accurate reproduction of the prototype, it was difficult to create similar conditions and differences in the wave kinematics were to be expected (Andersen et al., 2011). Furthermore, the larger number of waves at the dike toe location in the large-scale model will increase the number of impacts at the wall as well. It was assumed that the higher number of impacts will also lead to a higher maximum impact force simply because of the higher probability of an extreme impact

4.3 Results and discussion

Just as for the geometrical model set-up and hydraulic boundary conditions, care was taken to make the data processing of the large-scale and small-scale impact force measurements as similar as possible. In this way additional model effects due to different data processing routines were minimized, and the investigation of scale effects enabled. The post-processing routines described in Section 3.4.5 were used to analyse and filter the data. The filter settings for the signals of the two scale model results were scaled representatives of each other and a high-pass threshold based on the mean wave power used (see Equation 3.3).

The time-series of measured impact force at the wall was recorded at 1000 Hz in both scale models. It was further attempted to down-sample the measurement frequency of the large-scale model, using Froude similarity and the scale ratio 1-to-5.81, to artificially create a similar measurement frequency used in the small-scale model. In this way the 1000 Hz signal of the large-scale model was interpolated and a 415 Hz signal obtained. No significant reduction of the force peaks was observed, and it was decided to use the original 1000 Hz measurement signals.

Table 4.3: Hydraulic boundary conditions test testID 500. The values were up-scaled and compared in prototype

testID 500	Small-scale	Large-scale	Ratio (SS/LS)
Model scale	1-to-25	1-to-4.3	1-to-5.81
$H_{m0,o}$ [m]	3.76	3.81	0.987
$T_{m-1,0,o}$ [s]	10.89	11.11	0.980
$H_{m0,t}$ [m]	1.74	1.87	0.930
$T_{m-1,0,t}$ [s]	32.54	29.70	1.096
Duration [s]	$\sim$ 12000	$\sim$ 12000	-
h_o [m]	16.25	16.30	0.997
h_t [m]	0.30	0.34	0.882
A_c [m]	2	1.94	1.031

4.3.1 Repeatability of laboratory impact force measurements

It is commonly accepted that wave-induced impact measurements are highly stochastic and non-repeatable (Chen, 2016; Altomare et al., 2015). The non-repeatability was mainly attributed to 3D effects of the turbulent bore front, air entrapment during wave impact, and air entrainment in the turbulent bore front. Hence, it was attempted to quantify the non-repeatability of bore-induced impacts in order to establish a baseline uncertainty against which the model and scale related differences in measured impact force can be compared. For this purpose the irregular wave time-series of test testID 500 (see Table 4.4) was repeatedly (14 times) tested in the small-scale model. The results for the bore-induced impact force were up-scaled to prototype scale and the time-series as well as the statistical parameters studied (see Figure 4.4).

The same time-series of waves was used in each repetition test, resulting in an average difference of the spectral wave height $Hm0,t$ [m] and $T_{m-1,0,t}$ [s] at the dike toe of less than 0.5%. Even though the same time-series of waves showed good repeatability, the impact forces varied greatly. The maximum impact force per test was measured at different times in between repetition tests and varied significantly in magnitude (see Figure 4.4, upper figure). A zoom into the impact event which caused the maximum impact force in most of the times (t=$\sim$2000 s) was provided and showed the general shape of this impact event for the 14 repetition tests (see Figure 4.4, lower left figure).

Furthermore, the arithmetic mean value μ (see Equation 4.1), the standard deviation σ (see Equation 4.2) and coefficient of variation C_v (see Equation 4.3)

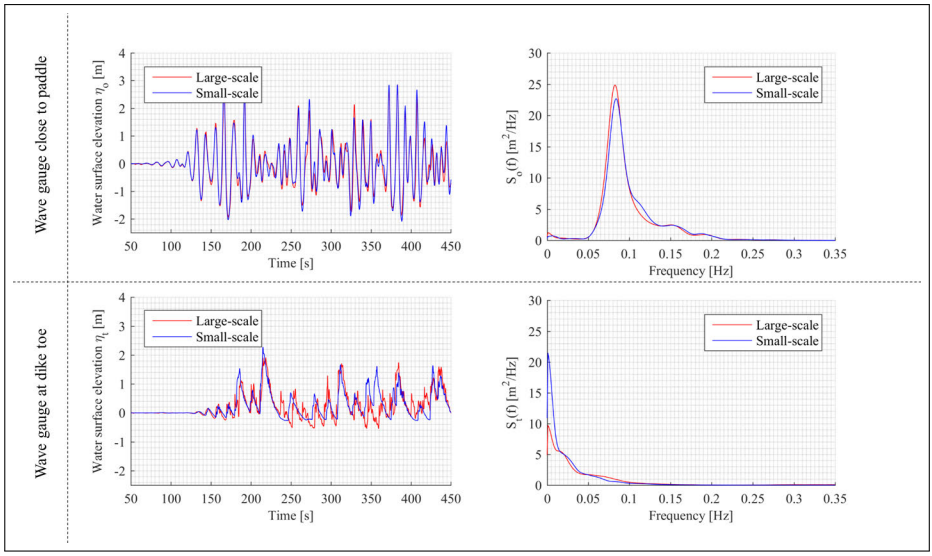

Figure 4.3: Beginning of water surface elevation time-series (left) and wave spectrum calculated for the entire time-series (right) for test testID 500. The measruements in the upper row were obtained at the location close to the paddle and in the lower row at the dike toe location. Small-scale (blue) and large-scale (red) measurements were compared in prototype.

were computed for the 14 repetition tests, to quantify the uncertainty,

$$\mu = \frac{1}{n} \cdot \sum_{i=1}^{n} x_i, \tag{4.1}$$

$$\sigma = \sqrt{\frac{1}{n} \cdot \sum_{i=1}^{n} (x_i - \mu)^2}, \tag{4.2}$$

$$C_v = \frac{\sigma}{\mu}. \tag{4.3}$$

These statistical parameters were derived for the force indicators: maximum impact force F_{max}, average 1-in-250 impact force $F_{1/250}$, average of the highest 10, 20, 30 impact forces F_{10}, F_{20}, F_{30}, respectively and average of all impact forces F_{avg} (see Table 4.4).

The coefficient of variation (or relative standard deviation) C_v was around 10% for the maximum impact force F_{max} (and the same for $F_{1/250}$, since there were only 46 total impact events). The coefficient of variation was in the order of ∼5.5% for

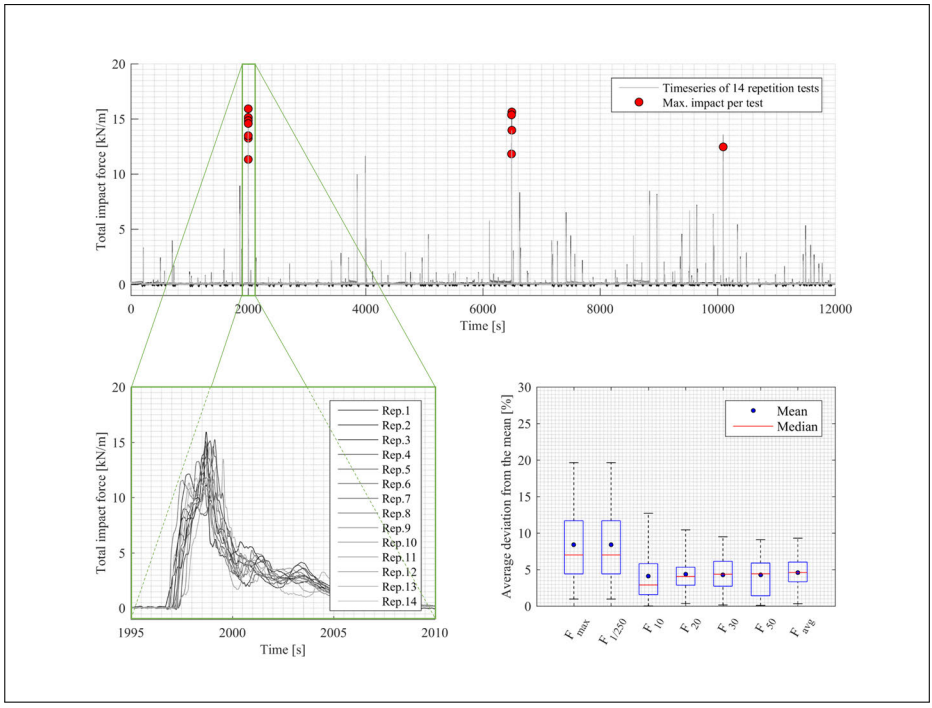

Figure 4.4: Force time-series of 14 repetition tests using the same seed wave time series (upper figure). The maximum force peak per repetition test was indicated with a red marker. A zoom on the impact event around t=2000 s, were most of the maximum force peaks occurred, was provided (lower left figure). Together with a boxplot of deviations from the mean impact force from all 14 repetition tests (lower right figure).

the other force indicators F_{10}, F_{20}, F_{30}, F_{avg}). Additionally, the average deviation from the mean was computed (see Equation 4.4),

$$\bar{D} = \sum_{i=1}^{14} \frac{\mu - F_i}{\mu}. \tag{4.4}$$

The values were in the range of the coefficient of variation C_v with ∼8% for F_{max} and $F_{1/250}$ and ∼4.5% for the other force indicators (see Table 4.4). The deviation of the mean for each of the 14 repetition tests was calculated and a boxplot generated (see Figure 4.4, lower right figure). The boxplot provides the additional information that even though the average deviation from the mean is around 8%, there are single repetition tests with a deviation from the mean in the order of 20% for F_{max} and $F_{1/250}$, as can be seen from the upper outliers in the boxplot. It was therefore concluded that the relative uncertainty related to the non-repeatability of the maximum bore-induced impact force for an irregular wave train was 10% and could go up to 20% in extreme cases. This is in the range of coefficient of variations C_v for quasi-static and dynamic impact forces measured

Table 4.4: Statistical parameters showing the differences in measured impact force due to the stochastic impact behaviour. A test with hydraulic boundary conditions comparable to a storm with a 1000 year annual return interval was repeated 14 times in the 'UGent3' model tests.

	μ [kN/m]	σ [kN/m]	C_v [%]	$\bar{D}$ [%]
F_{max} [kN/m]	14.10	1.44	10.21	8.41
$F_{1/250}$ [kN/m]	14.10	1.44	10.21	8.41
F_{10} [kN/m]	8.57	0.48	5.60	4.10
F_{20} [kN/m]	6.20	0.32	5.16	4.36
F_{30} [kN/m]	4.97	0.26	5.23	4.27
F_{avg} [kN/m]	2.48	0.13	5.24	4.58

with load cells, for a regular wave train and estimated as 10% and 14%, respectively by Chen (2016).

4.3.2 Scale effects in laboratory impact force measurements

To study the small-scale and large-scale impact force measurement for test testID 492 (Table 4.2) the time-series of bore-induced impact force were up-scaled and compared in prototype scale. Froude similarity and a length scale factors of 1-to-4.3 (large-scale) and 1-to-25 (small-scale) were used. First, the time-series were synchronized by shifting one time series relative to the other to obtain the visual best-fit overlay. This allowed qualitative study of the number of occurrences and magnitude of impact events (Figure 4.5, upper figure).

It was noted that there were less impact events recorded in small-scale (424 impact events) than in large-scale (549 impact events). Also, in terms of magnitude it was observed that the same event in time differed significantly in between both scale models. Furthermore, the maximum impact was not recorded at the same time in the two scale models. The distribution of the impact events showed that the small-scale model results were higher in magnitude compared to the large-scale model results (Figure 4.5, lower left figure). On the x-axis the total impact force for each impact event was plotted in force per meter width, and the y-axis shows the corresponding exceedance probability. As described earlier, the mean wave power after Goda (2010) was used to define the high-pass threshold. The same force indicators as in the non-repeatability study were used: maximum impact force F_{max}, average 1-in-250 impact force $F_{1/250}$, average of the highest 10, 20, 30, 50 impact forces F_{10}, F_{20}, F_{30}, F_{50} respectively and average of all impact forces F$_{a}vg$ (Figure 4.5, lower right figure). In all cases, the small-scale model force indicator was higher than the according large-scale model force indicator (Table 4.5).

The relative difference between small-scale and large-scale model force indicator

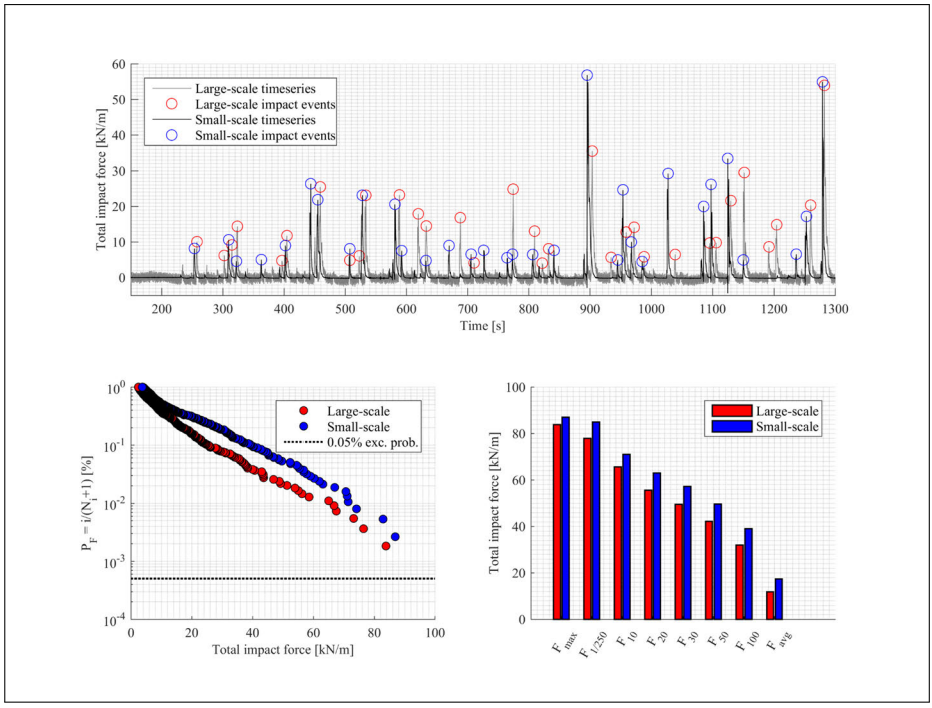

Figure 4.5: Beginning of time-series of impact forces for test testID 492 (upper figure), in red the large-scale and in blue the small-scale impact events. Impact force event distribution (lower left figure) and comparison of force indicators (lower right figure).

was calculated. The maximum impact force F_{max} was ∼4% higher in the small-scale model, the average impact force $F_{1/250}$ was ∼9% higher in the small-scale model (Table 4.5). The other force indicators were ∼8%-34% higher in the small-scale model.

The same analysis was repeated for test testID 500 (Table **??**). For the time-series of impact force (Figure 4.6, upper figure) it was noted that relative difference in the number of impact events between small-scale (46 impact events) and large-scale (103 impact events) was higher compared to test testID 492. The distribution of the impact events showed that the small-scale model results were only higher in between P_F=5·10^{-2}–3·10^{-1} exceedance probability and that the large-scale model results showed the highest impact force. The maximum impact forces were lower compared to test testID 492 due to the less severe wave conditions. A study of the force indicators showed that all of them, contrary to the findings for test testID 492, were higher in the large-scale model (Figure 4.6, lower right figure). The relative difference for F_{max} and $F_{1/250}$ was 19%, with higher in the large-scale model (Table 4.6). Note that the result for F_{max} and $F_{1/250}$ were the same because only 46 or 103 impact events were recorded. Furthermore, the large-scale results were 3%-30% higher for the other force indicators. The F_{50} and F_{100} force indicators could not be compared due to the insufficient number of impact events.

Table 4.5: Force indicators from large-scale and small-scale measurements compared in prototype for test testID 492

testID 492	Small-scale (SS)	Large-scale (LS)	Ratio (SS/LS)
Nr. of impacts [-]	424	549	0.772
F_{max} [kN/m]	86.97	83.87	1.037
$F_{1/250}$ [kN/m]	84.96	77.88	1.091
F_{10} [kN/m]	70.97	65.70	1.080
F_{20} [kN/m]	62.98	55.55	1.134
F_{30} [kN/m]	57.30	49.56	1.156
F_{50} [kN/m]	49.69	42.22	1.177
F_{100} [kN/m]	39.08	32.01	1.221
F_{avg} [kN/m]	15.78	11.79	1.338

Whereas the results for test testID 492 were in line with the widely accepted narrative of an overestimation of wave impacts in small-scale models, the results for test testID 500 were contradictory. On the one hand it was assumed that this was the result of the larger spectral wave height $H_{m0,t}$ at the dike toe (10% higher in large-scale) due to the formation of the erosion hole (0.15 m in model scale and 0.65 m in prototype (Saponieri et al., 2018)); and consequently larger water depth at the dike toe. Higher energy waves transform up to the dike toe leading to more overtopping, and finally more and potentially higher impact events at the wall. Furthermore, the water depths at the dike toe in test testID 500 were h_t <0.02 m in the small-scale, which means that effects of surface tension are not negligible any longer in the wave transformation (Schüttrumpf, 2001). On the other hand the overtopping flow thicknesses and velocities on the promenade were rather small for test testID 500. Consequently, effects due to viscosity and surface tension, neglected in the Froude up-scaling, might influence the results. It was previously stated that for flow depths η_{crit} <0.0035 m (Kolkman, 1984), Reynolds number Re_{crit} <1,000 and Weber number We_{crit}<10 (Schüttrumpf, 2001) the flow becomes hydraulic smooth and the resistance due to viscosity and surface tension will further decrease or stop the flow. This would finally lead to lower values in the small-scale model compared to the large-scale model and was expected to be another source for scale effects of bore-induced impacts. This driving process for scale effects and under-prediction in the small-scale model was previously also observed for small overtopping discharges (Andersen et al., 2011; Burcharth and Andersen, 2009; De Rouck et al., 2005). Measurements of the flow thickness η [m] and velocity v [m/s] on the promenade were obtained for the 30 highest impacts of test testID 500 in the large-scale model (Streicher et al., 2018).

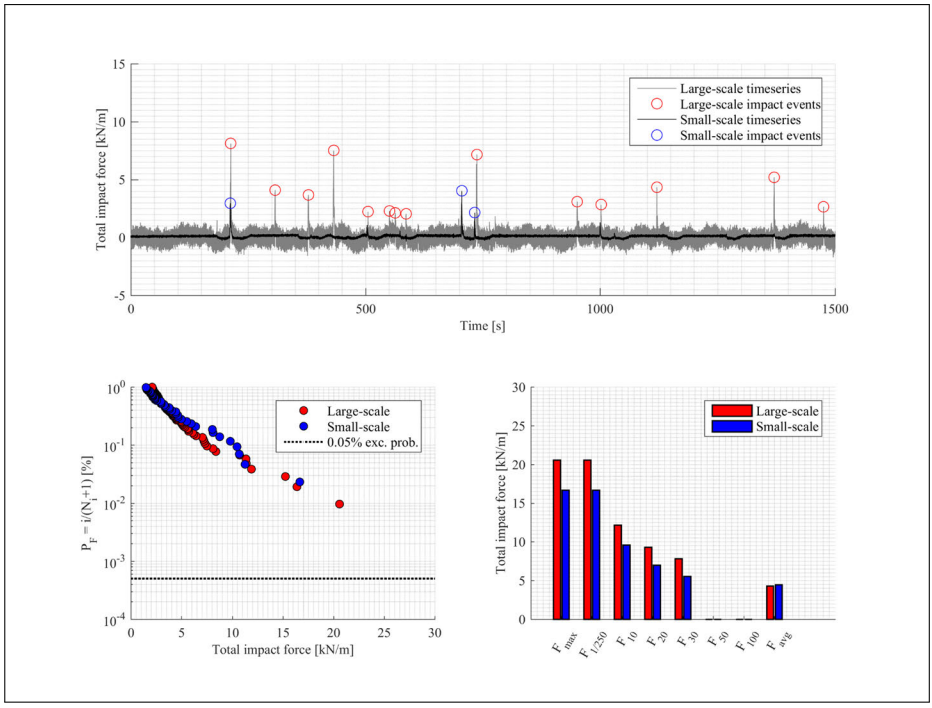

Figure 4.6: Beginning of time-series of impact forces for test testID 500 (upper figure), in red the large-scale and in blue the small-scale impact events. Impact force event distribution (lower left figure) and comparison of force indicators (lower right figure).

No flow thickness and velocity could be obtained from the small-scale model. As a first estimate for the flow thickness η [m] and velocity v [m/s] in the small-scale model the large-scale results were down-scaled using Froude similarity and a length scale and the scale ratio 1-to-5.81. While the Reynolds numbers Re in the so obtained small-scale results were in the range Re=4221-27724 and above the critical Re_{crit}=1,000, the Weber numbers were in the range of We=22-310 and closer to the critical We_{crit}=10. However, this comparison is very tentative and the analysis of measured flow thickness η [m] and velocity v [m/s] in the small-scale model need to be further investigated. Due to the combination of model effects (erosion hole at dike toe in large-scale) leading to higher wave energy at the dike toe and unresolved scale effects due to the size of the flow thicknesses and velocities in the small-scale model test testID 500, no further study of scale related effects for the bore-induced impact force was conducted based on test testID 500.

For test testID 492 the small-scale model showed a small systematic shift towards higher force impacts compared to the large-scale model. Also the force indicators F_{max}, $F_{1/250}$, etc. were systematically higher (3%-34%). The overestimation of forces in the small-scale model was not remarkably high, especially for F_{max} and $F_{1/250}$. The Reynolds and Weber number of the overtopping flow related to the 30 highest events were well above the critical Reynolds and Weber number.

Table 4.6: Force indicators from large-scale and small-scale measurements compared in prototype for test testID 500

testID 500	Small-scale (SS)	Large-scale (LS)	Ratio (SS/LS)
Nr. of impacts [-]	46	103	0.447
F_{max} [kN/m]	16.66	20.57	0.810
$F_{1/250}$ [kN/m]	16.66	20.57	0.810
F_{10} [kN/m]	9.61	12.15	0.791
F_{20} [kN/m]	6.99	9.30	0.752
F_{30} [kN/m]	5.53	7.83	0.706
F_{50} [kN/m]	-	-	-
F_{100} [kN/m]	-	-	-
F_{avg} [kN/m]	4.19	4.31	0.972

Hence, scale effects related to viscosity and surface tension of the overtopping flow were considered negligible. Typically, the overestimation of impact force in smaller scale models was explained by the lower amount of entrained air and the resulting lower cushioning effect during the impact process. In the case of overtopping bore-induced impacts, the bores reaching and impacting the dike-mounted wall were all broken and no violent plunging breaking, in contrast to plunging wave breaking on seawalls constructed in the breaking zone (Bredmose et al., 2015, 2009; Bullock et al., 2007). Hence, the cushioning effect was less effective because the bore-induced impacts were less violent and of rather quasi-static nature (Streicher et al., 2019b). Therefore, the error induced due to Froude scaling was expected to be rather small (Kortenhaus and Oumeraci, 1999). Nevertheless, no such air entrainment was measured during the experiments and it remains an assumption that the small systematic shift to higher forces in the small-scale model was a result of the lower amount of entrained air.

The difference in bore-induced impact force between the scale models could also be explained by the difference in spectral wave parameters at the dike toe, which were 10% higher in the small-scale model. The long waves were less efficiently absorbed in the small-scale model and resulted in this increase in spectral wave parameters at the dike toe. The underlying assumption here would be that 10% higher spectral wave parameters will result in a systematical shift of 3%-34% higher impact forces.

In any case the observed higher bore-induced impact forces in the small-scale model, especially for F_{max}, $F_{1/250}$, F_{10}, F_{20}, F_{30} were in the range of 3%, 9%, 8%, 13%, 16% respectively. Compared to the results from the non-repeatability study, which showed an average deviation of 10% and in extreme cases of 20% for

the maximum bore-induced impact force F_{max}, the scale-effect related deviation, possibly due to air entrainment, was considered subordinated. Adding also the average reduction of 10%-20% (Chen et al., 2016) due to filtering of the impact forces, the scale related error disappears within the uncertainties caused by the non-repeatability and model effects.

4.4 Conclusions

In this study the non-repeatability, model- and scale effect for laboratory bore-induced impact force measurements on a dike mounted wall were investigated. The main conclusions of this study were:

- If a minimum water depth at the dike toe, as well as thickness and velocity of the overtopping flow was maintained (η¿0.0035 m, R_e¿1000, W_e¿10 after Schüttrumpf (2001); Kolkman (1984)), the scale-related errors in the impact force measurements disappeared within the uncertainties related to non-repeatability and model effects.

- This new finding was at first contradictory to the common assumption that force measurements in the small-scale model are significantly higher than prototype measurements. The contradiction was mainly explained by the characteristics of the turbulent, aerated and broken wave impacts in both scale models, resulting in compressible and less violent impacts. Note this impact behaviour was very different compared to violent breaking wave impacts on seawalls constructed in the breaking zone. Also, the relative scale ratio between the two models was rather low with 1-to-5.81.

- However, a small systematic scale-related shift to higher impact forces was still observed in the order of 4%, 9%, 8%, 13%, 16% for F_{max}, $F_{1/250}$, F_{10}, F_{20}, F_{30} respectively, in the small-scale model. Furthermore, the number of impacts was lower in the small-scale model (424) compared to the large-scale model (549).

- Uncertainties related to the stochastic non-repeatability of bore-induced impact forces were quantified using the coefficient of variation C_v and were in the order of 10% (in extreme cases up to 20%) for F_{max}, $F_{1/250}$.

- Differences related to model effects were mostly observed in the wave generation and absorption in the small-scale model and changing sand bathymetry in the large-scale model. On average this resulted in a 10% difference in spectral wave parameters at the dike toe location between the two scale models.

For future studies on scale effects related to overtopping bore-induced loads on dike mounted walls, it was recommended to further advance the wave generation and wave absorption in the small-scale model to better represent the long wave characteristics. Additionally, measurements of air entrainment in both scales, at

a location close to the wall where the impact force occurs, would be beneficial to judge the difference in flow aeration between different scale models. The use of pressure sensors in both scale models is recommended to further study the scale influence on peak impact pressures. The use of pressure sensors in both scale models is recommended to further study the scale influence on peak impact pressures. Furthermore, extra intermediate scale models or fully prototype-scale measurements could be used to judge whether the bore-induced impact forces scale linearly and to increase the relative scale difference. Finally, the salinity of the sea water, resulting in different water density compared to the fresh water used in the model tests, will alter the way air is entrained and therefore influence the loading of the wall. Future research to investigate the effects of using sea water instead of fresh water for wave impact load measurements is therefore recommended.

Chapter 5

Analysis of bore interaction and bore-induced impact process

Short duration bores in the coastal zone are generated by wave breaking in shallow water and mild foreshore conditions. In storm weather situations and for sea level rise scenarios these bores approach the dike and interact with previously overtopped or reflected bores. This results in a complex and turbulent interaction process of the water masses before impact on any structure on top of the dike. The specific objectives for this Chapter were outlined in Section 5.1. Combined laser scanner and video measurements were used to study the bore interaction processes (see Section 5.2.1). Five bore interaction patterns were distinguished as 1) regular bore pattern; 2) collision bore pattern; 3) plunging breaking bore pattern; 4) sequential overtopping bore pattern and 5) catch-up bore pattern. Video images of the bore running up the wall and motion tracking of the leading edge were used to obtain a time series of the run-up water at the wall (see Section 5.2.2). The impact loads of the bore hitting the wall on the promenade were studied based on the signal of a vertical array of 13 pressure sensors installed over the wall height. Three impact types were distinguished (see Section 5.2.3) and classified as 1) impulsive impact type in Section 5.3.1; 2) dynamic impact type in Section 5.3.2 and 3) quasi-static impact type in Section 5.3.3. The majority of $\sim 2/3$ of the total number of impacts were comprised of the quasi-static impact type (see Section 5.3.4). Links between the bore patterns and impact types were discussed (see Section 5.3.5) and its implication on force prediction under consideration of possible scale effects highlighted (see Section 5.3.6). As summary of the research findings in Section 5.4 concludes this Chapter.

5.1 Specific objectives

It is the aim of this Chapter to extend the knowledge about overtopped bores impacting a dike-mounted vertical wall in shallow water and mildly sloping foreshore conditions. An identification of bore interaction patterns will be obtained based on the observed physical processes from laser scanner and video image data. This study also aims to further elaborate on the physical processes underlying short-duration bore-induced loads on a dike-mounted wall, based on pressure distribution and total horizontal impact force. A final goal is to develop a thorough methodology to classify the different impact types. More detailed objectives are:

1. To increase the knowledge and understanding of short-duration overtopping bore-induced loads on dike-mounted vertical walls required for a reliable and safe design of these structures with respect to sea level rise and increased storminess in the future.

2. To study overtopping bore interactions of multiple bores in the vicinity of a dike, promenade and dike-mounted vertical wall in shallow water and mildly sloping foreshore conditions. The complexity of these processes and difficulty of measurement due to alternating dry and wet conditions on the promenade requires innovative measurement techniques.

3. To investigate bore impact processes on dike-mounted vertical walls in order to classify bore impact types.

4. To discuss links between bore patterns and bore impact types and to elaborate on the implications on any prediction tools and scale effects.

5.2 Data analysis and methods

This section comprises the methods to analyse the acquired data and an outline and discussion of results for bore interaction patterns, bore run-up at the wall and bore impact proccesses and a classification of bore impact types. For this purpose testID 492 and 500 were depicted from the 'DeltaFlume' data-set (see Section 3.2). Both tests were comprised of 1,000 irregular waves each. The range of wave parameters was similar to a design storm with 1,000 (testID 500) and 17,000 (testID 492) annual recurrence interval for the Belgian coast (Veale et al., 2012; Verwaest et al., 2009). The spectral wave parameters at the dike toe were determined with validated SWASH model calculations (see Section 3.4.2). The offshore spectral wave parameters were obtained from reflection analysis. As expected, the wave height decreased by a factor of 3.5-4.0 (see Table 5.1) due to wave breaking and loss in energy on the mild foreshore; and the spectral wave period increased by a factor of 2.1-2.2 due to the release of the bound long waves in the breaking process on the mild foreshore (Hofland et al., 2017).

For both selected tests the 30 highest impacts after post-processing of the integrated pressure signals (see Section 3.4.5), were selected for the analysis (see Figure 5.1). This resulted in 60 analysed individual impacts. With a total number

Table 5.1: Hydraulic conditions for testID 492 and testID 500 (all values in model scale).

testID	Waves	h_o	h_t	A_c	$H_{m-1,0,o}$	$H_{m-1,0,t}$	$T_{m-1,0,o}$	$T_{m-1,0,t}$	$S_{m-1,0,t}$	$\xi_{m-1,0,o}$	$\frac{h_t}{H_{m0,t}}$
[-]	[-]	[m]	[m]	[m]	[m]	[m]	[s]	[s]	[-]	[-]	[-]
492	∼1000	3.99	0.28	0.27	1.05	0.3	5.80	12.30	0.0014	0.2	0.27
500	∼1000	3.79	0.08	0.47	0.87	0.22	5.41	12.05	0.0012	0.2	0.09

of 760 (testID 492) and 251 (testID 500) detected impacts, the analysed impacts represent a relative sample size of 4% and 12% of the total number of impacts, respectively for testID 492 and 500. The 30 highest force impacts were numbered in descending order based on the maximum peak of the measured force signals (see ANNEX C).

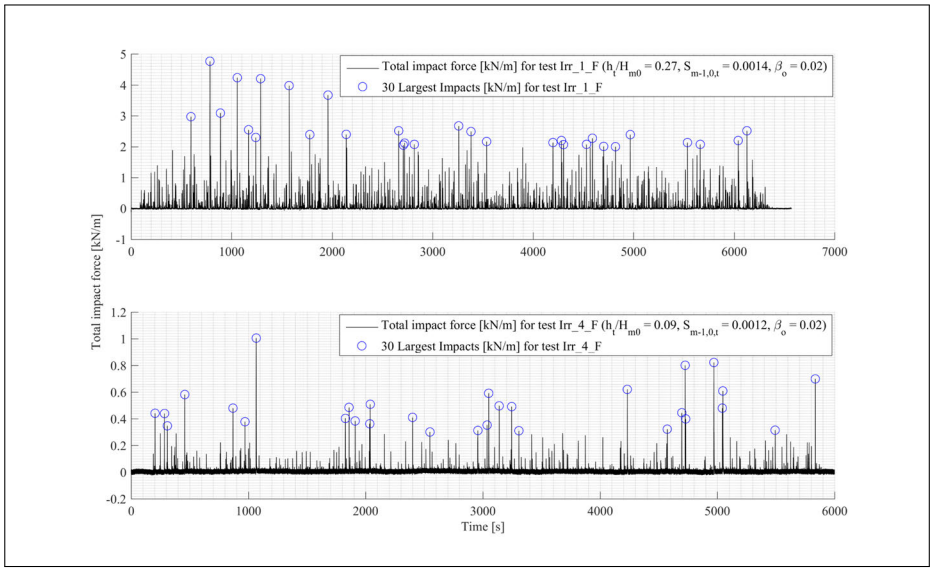

Figure 5.1: The time series of total impact force [kN/m] for testID 492 (upper graph) and testID 500 (lower graph) and the 30 largest impacts for each tests highlighted with a blue circle.

The maximum total horizontal impact force for testID 492 was found to be 4.77 kN/m in model scale (88.2 kN/m in prototype using Froude similarity and a scale factor 1-to-4.3). The maximum total impact force for testID 500 was found to be 1.01 kN/m in model scale (18.7 kN/m in prototype using Froude similarity and a scale factor 1-to-4.3).

On one hand this was a relatively small sample (60 impact events) to be representative for all measured impacts, on the other hand this allowed us to focus more on individual analysis of the highest impacts. The author preferred to focus the analysis to the extreme events with the purpose of formulating practical and reliable design guidance. Inherent to this selection procedure was that the

obtained 60 impacts were of rather random nature in terms of bore impact process and bore formation process prior to impact. The large variation of incoming bore parameters, for example bore interaction patterns, required an individual analysis and process description for each individual impact event. The measurement files were cut to 3-s-long clips for all 60 impacts to facilitate the analysis. In all cases, the range extending from 1.5 s before to 1.5 s after the maximum impact force was considered for further analysis.

5.2.1 Bore interaction patterns

During wave breaking on the foreshore, run-up on the dike, overtopping over the dike crest and travelling across the promenade, until impact against the wall, waves experience several transformation processes. This results in broken waves, which propagate as "short-duration bores" (in contrast to the long- duration bores induced by tidal and tsunami bores) with different patterns and characteristics affecting the final impact loading of the wall. Due to the irregular nature of random sea waves, the short-duration bores overtake each other, collide with reflected bores, and exhibit a number of further interaction patterns over the entire length of the bore transformation area. To study the bore interaction processes in a nonintrusive way and in alternating wet and dry conditions on the promenade, the high resolution profile measurements of the water surface with the SICK LMS511 laser profiler were used (see Section 3.3.5).

To distinguish the different bore formation patterns, the high spatial and temporal laser scanner measurement related to each impact event were analysed together with the video side- and overview images. Processing of the signals was performed and described in Marinov (2017). This resulted in five observed bore patterns: (1) regular bore pattern, (2) collision bore pattern, (3) plunging breaking bore pattern, (4) sequential overtopping bore pattern, and (5) catch-up bore pattern.

The regular bore pattern (1) consists of a single turbulent bore travelling over the foreshore and approaching the dike. This bore overtopped the dike, travelled along the promenade and impacted on the wall without interaction with previous bores (see Figure 5.2, A). These types of bore patterns mostly occurred in testID 500 with the less energetic wave conditions.

The collision bore pattern (2) refers to the situation of an incoming bore which collided with a previously reflected bore (see Figure 5.2, B). The reflection of the previous bore took place at the dike or at the wall. The next incoming bore collided with the reflected bore and broke again. This resulted in a loss of bore front uniformity, as well as air and turbulence induced due to the breaking process. The subsequent overtopping and impact at the wall was expected to be lower than for the regular bore pattern. If the collision occurred on the promenade, usually the incoming bore jumped over the reflected bore. If the collision took place in vicinity of the wall, this resulted in plunging breaking bore pattern (3). Breaking against the wall and inclusion of an air pocket between breaking bore and wall are the characteristics of this bore type. Entrapped air due to plunging breaking against a wall was also observed by Oumeraci et al. (1993) for breaking wave impacts in deep water conditions, and this introduces a problematic issue related to scaling of

impact forces.

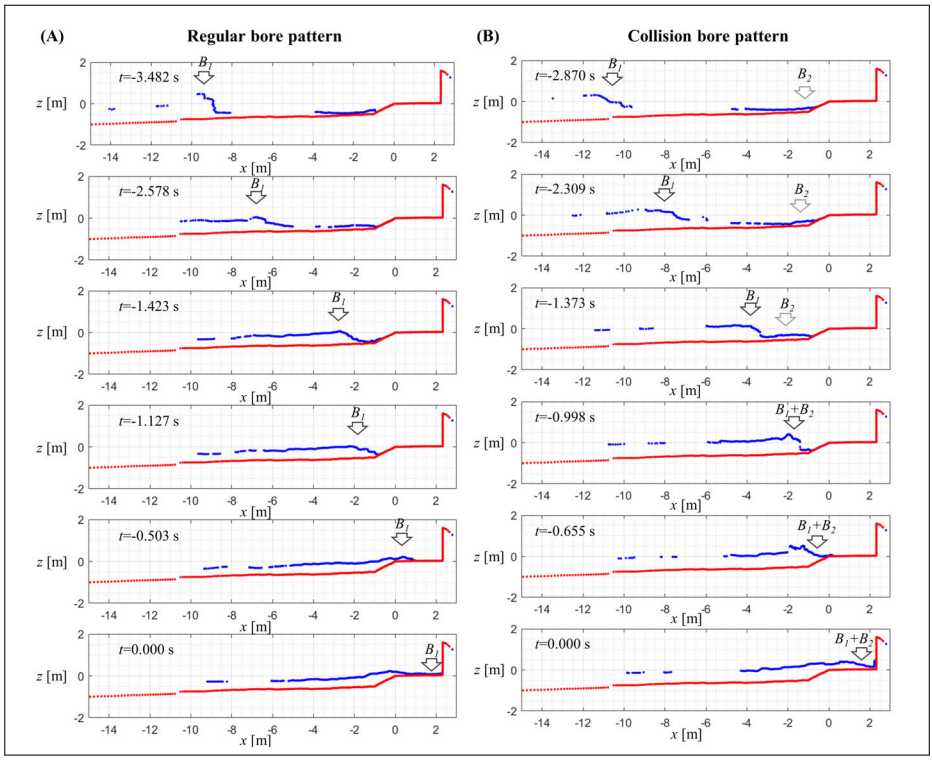

Figure 5.2: Regular bore pattern (A) observed before impact nr.1 from testID 500 and collision bore pattern (B) observed before impact nr.1 in testID 492 (see ANNEX C). Processing of the laser scanner signals was performed and described in Marinov (2017).

The sequential overtopping bore pattern (4) was an overtopping bore which slides on a residual water layer on top of the promenade, remaining from previous overtopping events (see Figure 5.3, A). There was no collision with reflected bores observed, but instead delayed breaking of the incoming bore on the residual water layer on the promenade and a highly turbulent bore front which slid on top of the residual water layer was observed until the bore impacted the wall. The friction between incoming bore and promenade was reduced due to the residual water layer and the impact at the wall was expected to be of higher magnitude.

The catch-up bore pattern (5) was observed for two successive bore crests with different velocities travelling over the foreshore and approaching the wall (see Figure 5.3, B). While travelling on the foreshore and overtopping the dike, the second bore crest travelled faster and overtook the slower first bore crest. If the first bore broke against the dike, it further facilitated the catch-up of the second bore. Also, this resulted in an enhanced overtopping mechanism because the first bore would cushion the breaking against the dike of the incoming second bore and less energy was lost during the overtopping process of the second bore. The

relatively higher velocity of the second bore accelerated the water mass in the first bore along the promenade and higher energy impacts occurred.

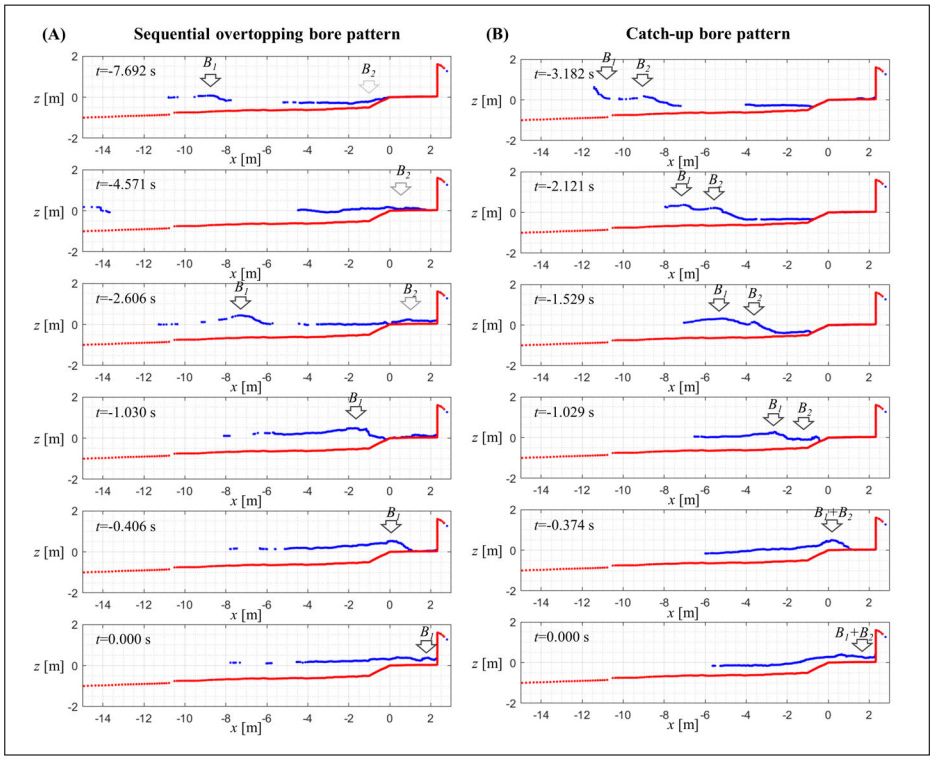

Figure 5.3: Sequential overtopping bore pattern (A) observed before impact nr.13 of testID 492 and catch-up bore pattern (B) observed for impact nr.2 of testID 492 (see ANNEX C). Processing of the laser scanner signals was performed and described in Marinov (2017).

As can be seen from the catch-up pattern, all bore patterns are often influenced by another mechanism, termed efficient overtopping mechanism. Efficient overtopping mechanism was observed when there was a sufficiently high water level in front of the dike due to previous waves and wave set-up. During efficient overtopping mechanism the incoming wave would not break against the dike but instead approaches at the same height as the dike crest and overtops the dike very smoothly. With efficient overtopping mechanism there was no energy lost due to breaking of the incoming bore against the dike; therefore, it was expected that the efficient overtopping mechanism also increases the impact force on the wall. This is in contrast to an emerged dike against which the incoming bore breaks and loses part of its energy due to the breaking process. A series of bore patterns were sometimes visible prior to one impact event. For this study, it was decided to identify only one bore pattern which was visually more distinct. Also, complex 2D effects (non-uniform flow in cross flume direction), foamy bore fronts and air

entrainment during breaking, were observed and are expected to change the impact characteristics of the bore against the wall.

5.2.2 Bore run-up at wall

In addition to the measured pressures and total impact forces (see Section 3.3.4), a hydrostatic pressure estimate was derived based on the instantaneous run-up of the bore at the wall. The instantaneous hydrostatic pressure estimate P_{hyd}(t,y) [kPa] was calculated for each pressure sensor location y [m] based on the instantaneous run-up R_h(t) [m] using Equation 5.1,

$$P_{hyd}(t, y) = \rho \cdot g \cdot [R_h(t) - y]. \tag{5.1}$$

The instantaneous run-up R_h(t) of the impacting bore at the wall was determined using two GoPro Hero5 video images from a side mounted and top mounted camera (see Section 3.3.5) and motion tracking of the leading edge of the run-up water body. The images from the overview camera (see Figure 5.4, left) were used to track the leading edge of the run-up bore at the wall and the images from the side view camera (see Figure 5.4, middle) to judge whether the run-up water was in visible contact with the wall and where it separated because of reflection from the wall. Therefore, only the area which was in visible contact with the wall was used to determine the instantaneous run-up height. A length scale was introduced to the images by measuring the length of defined objects in the images, such as the 1.6m wall height, and converting the obtained pixels into meters.

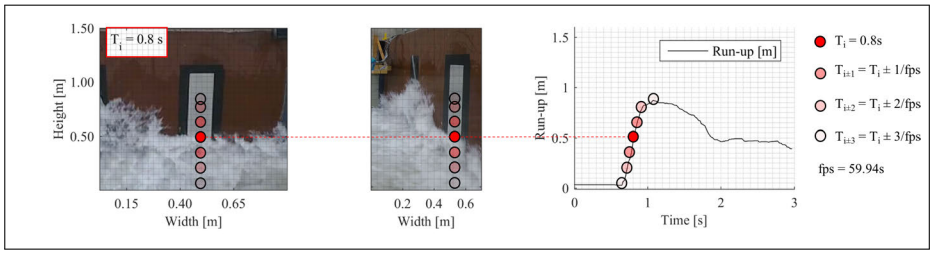

Figure 5.4: Motion tracking method of the bore leading edge in consecutive video images. The video images where recorded by a top mounted (left) and side mounted (middle) GoPro camera with 59.94 frames per second and 0.002 m spatial resolution. The situation at T_i=0.8 s is shown in the two camera images and the resulting time series of instantaneous bore run-up at the wall after the motion tracking was performed for impact nr.7 of testID 492 (see ANNEX C) is displayed (right).

The red circles (see Figure 5.4, right) correspond to the same time stamps shown in the overview (see Figure 5.4, left) and sideview (see Figure 5.4, middle) image. The run-up was obtained on a line parallel to the pressure sensor array on the silver metal plate (see Figure 5.4, middle). According to the coordinate system in the Delta Flume (see Section 3.2.1), this corresponded to y=2.15 m from the right flume wall (when standing with the back to the paddle). It was important

to determine pressure and run-up measurement at the same location to take into account that the bore front was not always uniform along the flume width (for example cross waves, 2D effects along the flume width). Then the leading edge of the bore during the entire image sequence of impact and run-up was manually tracked in the video images and in this way the run-up at the wall was obtained. The measured maximum run-up heights ranged between $R_{h,max}$=0.20–1.59 m in model scale (see ANNEX C).

The method of tracking the run-up leading edge in combined overview and side-view video images was preferred over obtaining the run-up, for example by using the highest pressure sensor that was showing an impact pressure in the wall, due to higher spatial resolution. Theoretically the accuracy of this method is determined by the spatial (2 mm resolution) and temporal (59.94 frames per second) resolution of the camera images. Nevertheless, the foamy and non-uniform bore front made it difficult to always identify the leading edge of the run-up bore. Hence, errors due to flow separation from the wall and fuzzy run-up front, are expected. A standard deviation for the maximum run-up $\sigma_{R_{h,max}}$=0.33 m was obtained by repeated tracking of the same event. This was equivalent to a relative error of 3% in terms of maximum run-up height $R_{h,max}$. The camera viewed the wall in an angle (as it was not mounted on the same height as the wall), which resulted in an error due to the projection of the image onto the wall surface. The maximum error in vertical direction due to the projection was in the same order as the standard deviation of the maximum run-up. Hence, a minimum error of twice the standard deviation can be expected.

5.2.3 Bore impact type classification

Based on the measured total impact force and pressure distribution over the wall height, the characteristics of the impact signal were discussed. The combined evidence of visual process observations, total impact force and pressure distribution, were used to classify impact types. Typically, the total horizontal impact force signal showed a double peak shape for each impact event. While the first peak (F_1) was related to the dynamic impact of the bore against the wall, the second peak (F_2) was related to the down-rush of the bore after maximum run-up. For the investigated impacts in the present study, the ratio of F_1/F_2 was in the range of 0.48–2.38. Using the classification from Kortenhaus and Oumeraci (1998) for church roof impact profiles none of the studied impacts were considered dynamic. Hence, the term Twin Peaks would be more accurate in this situation, accounting for the fact that the magnitude difference of first (F_1) and second (F_2) peak was smaller. For the present study the ratio F_1/F_2=1.2 was used to distinguish dynamic ($F_1 > 1.2 \cdot F_2$) and quasi-static impact types ($F_1 < 1.2 \cdot F_2$).

The factor 1.2 was selected based on a comparison of the 30 highest impacts from testID 492 with the 30 highest impacts from a repetition test (testID 502) using the same time-series of waves and geometrical set-up. The average difference between the 30 highest impacts was 0.39 kN/m. This was equal to an average difference in horizontal impact force of 16%. In order to establish a robust distinction between first (F_1) and second (F_2) impact, the 1.2 threshold, accounting

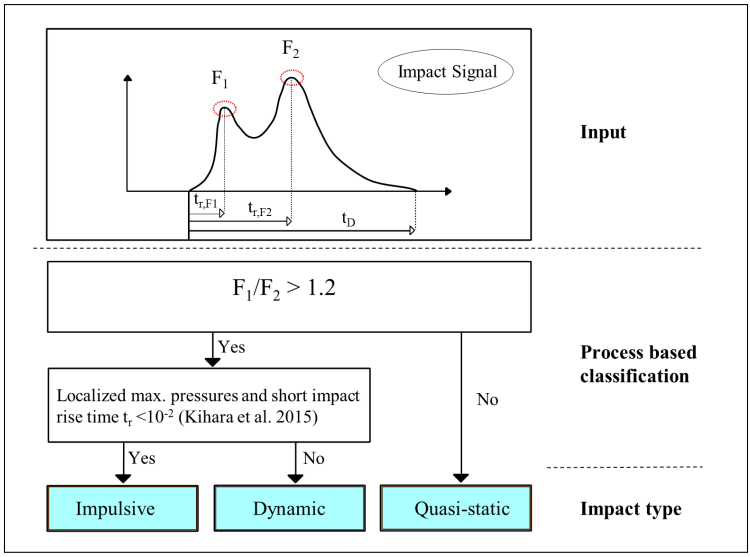

Figure 5.5: Bore-induced impact type classification methodology.

for 20% variability in maximum impact force, was chosen as a safe choice well above the measured 16%. In several cases, the rise time t_{r,F_1} of the dynamic first (F_1) impact was very short (t_{r,F_1}=$3 \cdot 10^{-3}$–$1.2 \cdot 10^{-2}$ s), comparable to impulsive impact phase duration $10^{-3} - 10^{-2}$ s observed by Kihara et al. (2015). The rise time in this study was defined as the time between the start of the impact until the maximum recorded force. Hence, a second criterion was introduced based on the rise time t_{r,F_1} of the first peak (F_1) to account for the possibility of very short duration impulsive impact types. If the rise time of the first impact (F_1) was shorter than $t_{r,F_1} = 10^{-2}$ s the impact was considered impulsive impact type. Furthermore, the impulsive impact types showed a very localized maximum pressure in the lower part of the wall. The classification of impact types does not consider the resonance period of the wall, since this is a very structure dependent parameter. In this study only the loading conditions were investigated but not the structural response and the criteria to determine the impact types were summarized in the methodology chart (see Figure 5.5).

5.3 Results and discussion

5.3.1 Impulsive impact type

For 9 of the studied 60 impacts a high magnitude and short duration (t_r=$3{\cdot}10^{-3}$-$1.2{\cdot}10^{-2}$ s peak in the beginning of the impact signal occurred (see Figure 5.6, middle), resulting from the initial impact of the bore tip with the wall. It can be seen from the sideview image (see Figure 5.6, left), that the upward deflection of the main water body had not begun at this moment. From the pressure distribution

(see Figure 5.6, right) it is evident that the peak pressure was almost solely recorded at the second lowest pressure sensor, indicating a highly localized phenomenon in the lower part of the wall.

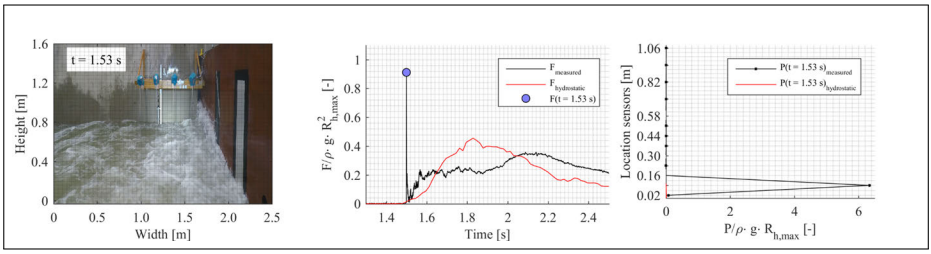

Figure 5.6: Impact nr.20 of testID 492 (see ANNEX C) at the moment of impulsive impact (t=1.53 s). A sideview image of the situation (left), the non-dimensional impact force (middle) and non-dimensional impact pressures (right) are displayed.

A possible generation mechanism was either a very steep bore front which impacted at the wall or when an incoming bore collided with a previously reflected bore (tip) in vicinity of the wall under inclusion of an entrapped air pocket (for example Impact nr.2 of testID 500). The latter resulted in plunging type bore breaking against the wall and led to significantly higher impulsive impacts and an oscillating force signal due to the oscillating entrapped air bubble (Bullock et al., 2007). Hence, they were referred to as impulsive impact types and occurred over the entire spectrum of investigated impacts with the second largest impact (F=4.25 kN/m) classified as impulsive impact type (see ANNEX C).

5.3.2 Dynamic impact type

After the initial impulsive impact type or in the absence of an impulsive impact type, the continuous instream of water against the wall led to upward deflection of the water at the wall and an increase in measured total force and pressures over the wall height (see Figure 5.7). Usually this resulted in the first peak (F_1) in the measured double peak total horizontal force signal. The measured pressures over the wall height were of larger magnitude than the hydrostatic pressure based on the run-up at the wall. The pressure distribution was not linear but rather uniform from the bottom up to about the 0.16 m wall height. Above 0.16 m wall height the drop of pressures was more rapid with increasing height (see Figure 5.7). It was assumed that the formation of two rollers in the impacting flow result in this particular pressure distribution (Kihara et al., 2015). An outward directed roller above 0.16 m in counterclockwise direction (in reference to the sideview frame shown in Figure 5.7), resulted in the rapid pressure drop. Conversely, the flow formed a clockwise roller below 0.16 m wall height, resulting in downward acceleration in the lower part of the wall and the expected hydrostatic decrease was compensated by this downward accelerated water body. This led to the assumption that the dynamic effects based on incoming bore velocities and their change in direction were dominant over the hydrostatic effects at this moment. Hence, the first impact (F_1), in

the absence of an impulsive impact type, was termed dynamic impact type. At first it seems difficult to distinguish impulsive and dynamic impact types and there were usually components of both impact types present. However, while the rise time of the impulsive impact types was of very short duration (t_r=·10^{-3}–$1.2 \cdot 10^{-2}$ s) and highly localized in terms of pressure distribution on the wall (see Figure 5.6), the dynamic impact types showed longer rise times t_r of the maximum total impact force (0.1–0.6 s). Also, the high impact pressures were distributed over a larger area at the wall. Dynamic impact types were found over the entire magnitude spectrum of the studied impacts. Approaches to predict the dynamic impact force F_1 were outlined in Section 6.3.1.

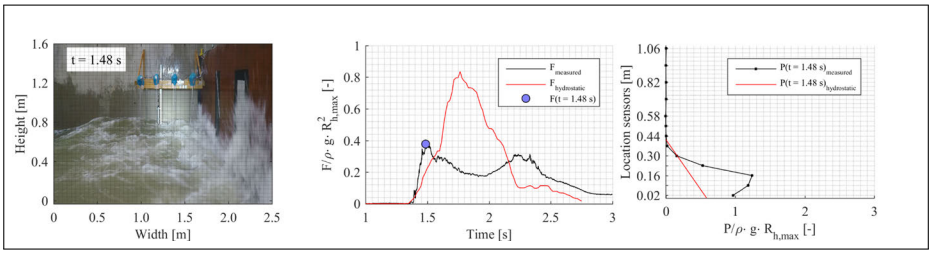

Figure 5.7: Impact nr.29 of testID 492 (see ANNEX C) at the moment of dynamic impact (t=1.48 s). A sideview image of the situation (left), the non-dimensional impact force (middle) and non-dimensional impact pressures (right) are displayed.

After the peak of the dynamic impact force, the water was continuously deflected upwards until it reached the elevation of maximum run-up at the wall (see Figure 5.8, B).

At the same time the measured pressures over the entire wall height were smaller than the hydrostatic pressure estimate. Still, a small uniform pressure distribution in the lower part of the wall below y=0.16 m could be observed. It was assumed that a small portion of the clockwise roller is still present in this lower region at the wall. The original expectation would be that the measured pressures and total force were close to the hydrostatic force and pressure estimate at the moment of maximum run-up. This was not observed and the measured pressure distribution and total force over the wall height showed lower values (see Figure 5.8, C). It was assumed that this difference arose from the different vertical accelerations in the run-up water body. As the rising water velocity decreased to zero, an upward-directed acceleration made it appear as if the water mass had less than its actual weight. Thus, the measured force was reduced from what the hydrostatic force would be because the 'apparent weight' of the water was less than the actual water weight. We hypothesize that the change in pressure over a small length of the vertical wall at the moment of maximum run-up consists of the hydrostatic pressure due to gravity minus the pressure due to the positive upward acceleration of the run-up. The theoretical prediction of the impact signal shape resulting from this hypothesis was further investigated in Section 6.3.3.

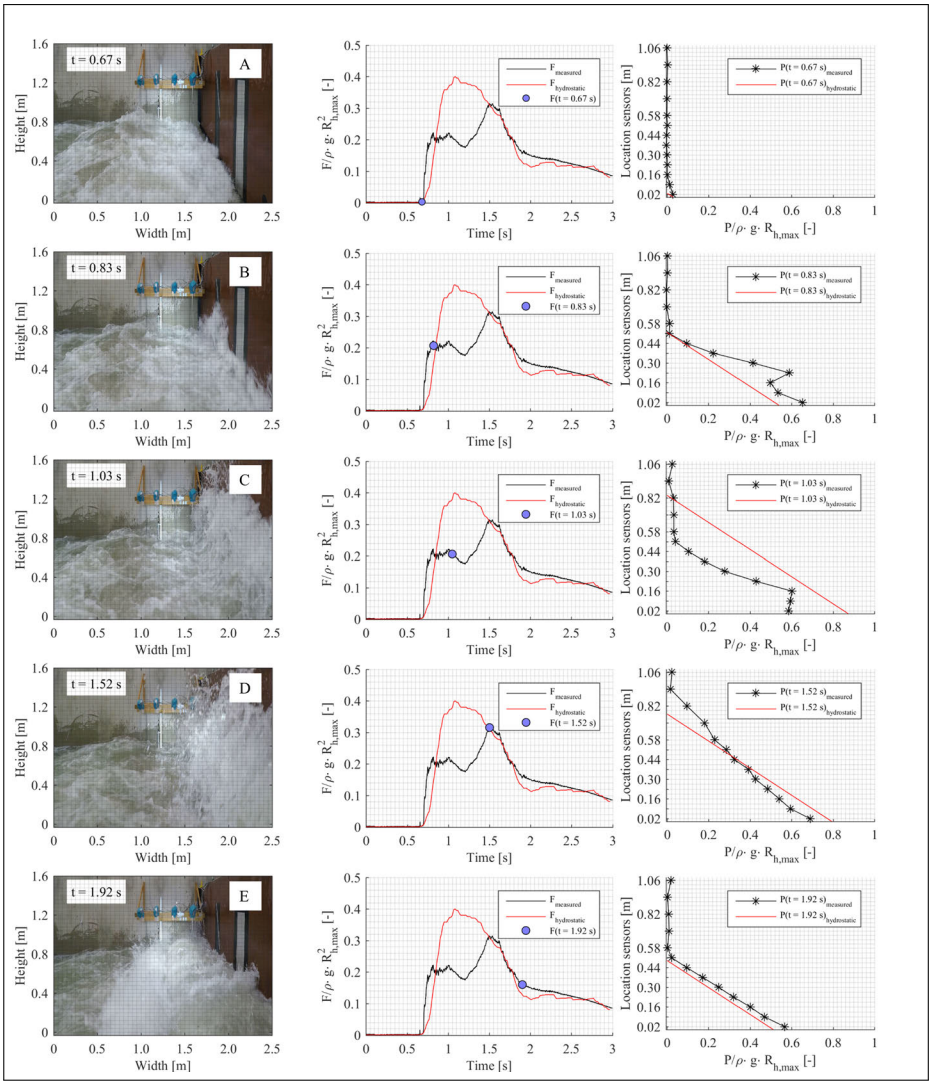

Figure 5.8: Impact nr.7 of testID 492 (see ANNEX C) in different stages of impact. A) Initial impact stage, B) deflection stage and dynamic impact type, C) moment of maximum run-up, D) reflection stage and quasi-static impact and E) hydrostatic stage are displayed. A sideview image of the situation (left), the non-dimensional impact force (middle) and non-dimensional impact pressures (right) are given for each impact stage A-E.

5.3.3 Quasi-static impact type

After maximum run-up of the water body at the wall, the upper part of the water body collapsed; and due to blocking of the wall, outward reflection of the water body occurred. A short time after the maximum run-up, the pressures in the upper

part of the water body were larger than estimated hydrostatic pressures based on the instantaneous run-up (see Figure 5.8, D). It was hypothesized that this difference was also related to the vertical accelerations of the water body in front of the wall. The falling water velocity approached zero, and a downward-directed acceleration added to the effect of gravitational acceleration giving an apparent water weight greater than the actual weight. The magnitude of the downward acceleration was dependent on the time and spatial variation of vertical velocity. Despite the small additional dynamic component, the pressure distribution resembled a hydrostatic distribution and the measured total force almost fell together with the hydrostatic force estimate based on the instantaneous run-up of the water at the wall (see Figure 5.8, D). Hence, the authors decided to use the term quasi-static impact type to refer to the second peak (F_2) in the impact signal because of the dominant hydrostatic effects. The small dynamic component is sufficiently considered by using the term 'quasi' in the impact type name. Quasi-static impact types comprised the majority, as well as the largest (F=4.77 kN/m), investigated impacts (see ANNEX C). Approaches to predict the quasi-static impact force F_1 were outlined in Section 6.3.2.

Unlike tsunami bore impacts, which reach a quasi-steady state a few seconds after the main impact (Kihara et al., 2015), this was never really the case for the short duration bore impacts examined in the present study. However, the total horizontal force converged with the hydrostatic force estimates and the estimated hydrostatic pressure line with the measured pressures towards the tail of the impact time series (see Figure 5.8, E).

5.3.4 Distribution of impact types

As a summary, the combined impacts from testID 492 and testID 500 were classified as impulsive in fifteen percent and in dynamic impact types in fifteen percent of the impacts as well. The quasi-static impact types were found in seventy percent or $\sim$2/3 of the impact events (see Figure 5.9, right). There were fewer dynamic impact types for testID 500 compared to 492. At the same time the number of impulsive impact types increased for testID 500, while the quasi-static impact types remain almost constant in number. This is attributed to the fact that the overtopped water volumes were of smaller thickness and duration for testID 500, such that a full dynamic impact with continuous instream of water and formation of rollers could not develop. Given the fact that the majority of impacts ($\sim$2/3) and the largest impacts were of quasi-static impact types, they were considered as the most relevant impact type to be further investigated. This assumes that the failure mechanism of the structure is not initialized by the short duration impulsive pressure peaks.

The non-dimensionalized impact force showed that below F/ρ·R$_{h,max2}$=0.5 all the quasi-static impact types were found (see Figure 5.9, left). The best-fit line through this part of the data was at $F/\rho \cdot R_{h,max2}$=0.32, which indicated that a prediction for these impacts could be achieved using hydrostatic theory, the maximum run-up Rh,max and a coefficient 0.32. In between 0.5$<$ $F/\rho \cdot R_{h,max2}$ $<$0.9 only dynamic and impulsive impact types were found and above

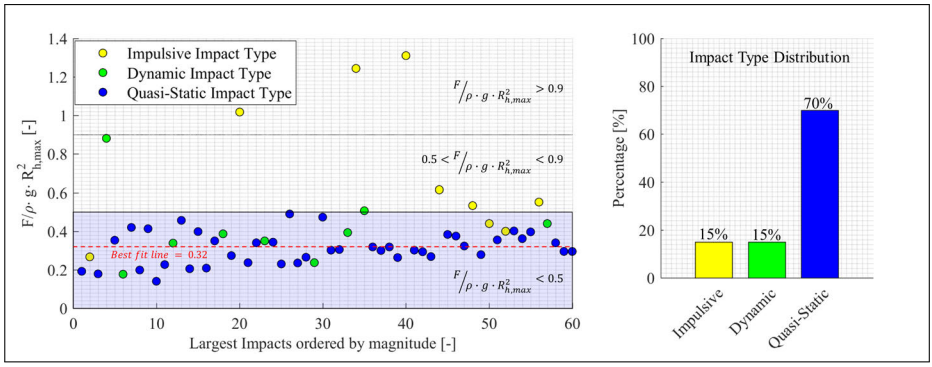

Figure 5.9: Distribution of impact types for the 60 largest impacts of testID 492 and testID 500 (30 from each test). The percentage distribution (right graph) and the distribution in dependence of the non non-dimensional impact force (left graph) is shown.

$F/\rho \cdot R_{h,max2}$ >0.9 only impulsive impact types were found.

5.3.5 Link between bore impact type and bore interaction pattern

Only the plunging bore pattern, collision of incoming with reflected bore in vicinity of the wall and breaking under entrapped air against the wall, resulted in dynamic/impulsive impact types at all times (see Figure 5.10). Similar findings are reported for plunging type wave breaking against a vertical sea wall (Oumeraci et al., 1993). For the other bore patterns (regular, catch-up, collision and sequential bore pattern) the link between the pattern and impact type at the wall was not as apparent as for the plunging breaking bore pattern. Most of the bore patterns (46% of events or 28 in total), were comprised of collision bore patterns. From which the majority of events (23 out of 28 events) resulted in quasi-static impact types. The same trend was observed for catch-up (16% of events or 10 in total), sequential (13% of events or 8 in total), regular bore interaction pattern (17% of events or 10 in total), with most of them resulting in quasi-static impact types (see Figure 5.10).

When considering efficient overtopping mechanism, i.e. when the water at the dike was sufficiently high for the next incoming bore to just pass over the dike crest without breaking against the dike, it was observed that the bores were more likely to generate a dynamic or impulsive impact type; for example taking into account efficient overtopping mechanism for the collision bore pattern, 80% of the bores generated a dynamic/ impulsive impact type. On the contrary, without efficient overtopping mechanism the collision bore pattern generated a quasi-static impact type in 95% of the cases. This yields to the conclusion that with efficient overtopping mechanism sufficient energy in the overtopping bore is maintained, and not dissipated during wave breaking against the dike, resulting in larger dynamic impacts (F_1) on initial impact compared to the quasi-static impacts (F_2). Only for

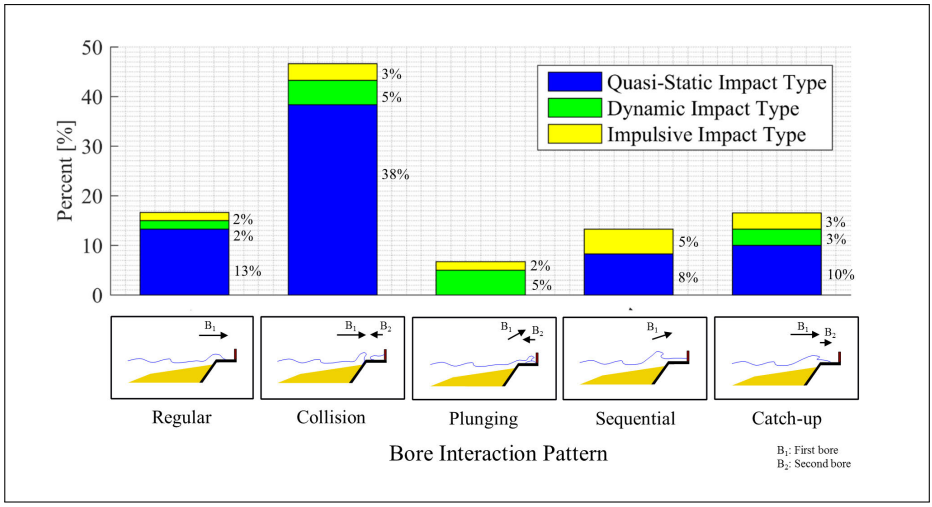

Figure 5.10: Link between the five bore interaction patterns (1. Collision bore pattern of an incoming and reflected bore colliding, 2. Catch-up bore pattern with a second bore overtaking a first bore, 3. Regular bore pattern with no significant interactions observed, 4. Sequential overtopping bore pattern of an incoming bore sliding over a residual water layer from previous impacts 5. Plunging bore pattern with breaking of the incoming bore over a reflected bore against the wall) and the three impact types (1. Impulsive impact type, 2. Dynamic impact type and 3. Quasi-static impact type).

testID 500 (see ANNEX C), with less energetic hydrodynamic conditions, regular bore patterns were observed. For this bore pattern, the absence of interaction, leading to bore breaking, with other bores was the key criterion. No interaction mainly resulted from the fact that the overtopped bores were less in total number and shorter in duration for testID 500 with lower overtopping discharge compared to test testID 492 (see ANNEX C).

The findings are an extension of the results from Chen (2016), who identified catch- up, collision and plunging bore pattern as well as single wave pattern, equivalent to the regular bore pattern in the present study. However, the sequential bore pattern and efficient overtopping mechanism are introduced for the first time in the present study, collision and catch-up bore pattern already observed before the dike, the probability of occurrence discussed and a first attempt to link the bore interaction patterns to the impact types attempted.

5.3.6 Implications on force predictions

Bore interaction patterns resulting from broken irregular waves were observed to increase the turbulence, aeration and flow complexity of the incoming flow. Furthermore, bore thickness and velocity changed dramatically along the promenade, for example when the catch-up bore pattern, plunging bore breaking or collision bore pattern occurred. Hence, it was concluded that for maximum impacts the

flow parameters bore thickness and velocity are a less reliable predictor of impact forces. Any prediction tool derived from measurements of bore thickness and velocity on the promenade and used for the prediction of maximum impact forces should therefore be treated carefully. It was concluded that a deterministic prediction of the maximum impact force based on the process parameters run-up at the dike, overtopping of the dike, bore thickness and velocity on the promenade can hardly be achieved due to the presented bore interaction patterns. Furthermore, small variations during bore transformation along the promenade, bore front uniformity (3D effects), air entrainment and the turbulent flow processes in vicinity of the wall complicate any deterministic prediction of maximum impact forces. The variations in the bore impact process along the flume width direction may result in different loading conditions at the wall. Furthermore, 3D effects due to oblique wave attack should be considered as natural sea state and need further investigation. Additionally, most of the impact prediction tools suffer from the drawback that they are not designed for a geometrical set-up with dike mounted vertical walls. For example impact prediction force formula in U.S. Army Corps of Engineers (2002), based on the works by Camfield (1991), are designed for land based structures on a plane slope not taking into account overtopping over the dike crest in extremely shallow waters. If they are designed to predict impact forces on dike mounted walls in extremely shallow waters, they often predict average impact forces (Van Doorslaer et al., 2017; Kortenhaus et al., 2017; Chen et al., 2015) or a maximum impact force but do not account for the different physical processes resulting in the different impact types (summary given in Streicher et al. (2018)). Maximum impact forces are key for a reliable design of coastal structures and often derived from small-scale experiments and up-scaled to prototype (see Section 4). In this way they suffer from scale-effects, mainly due to dissimilarities in the entrained air and the air content of the foamy bores (Blenkinsopp and Chaplin, 2007). Entrained air usually leads to cushioning effects of the impact pressures. Hence, less air entrained in the small-scale experiments will lead to less cushioning of the impact (Bullock et al., 2001). This is expected to lead to an overestimation of the impact loads, when upscaling the results from small-scale to prototype (Cuomo et al., 2010). Here, the classification into impact types gives useful insights. Mainly the very short duration and localized impulsive and also the dynamic impact types are expected to suffer from scale-effects when up-scaled to prototype due to the not properly scaled air properties and cushioning effects in the impacting flow. On the contrary quasi-static impact types are expected to be less affected by scale-effects, due to the almost hydrostatic situation of the water in front of the wall after maximum run-up. Since the total impact force signal showed a double shape, with similar magnitudes of dynamic (F_1) and quasi-static impact type (F_2), the majority of impacts ($\sim$2/3) and largest impact force (see ANNEX C) were considered quasi-static impact type, it might be worthwhile to consider only quasi-static impact types for the structural design. This is strictly only possible if no dynamic effects, due to the natural period of the structure tn being in the range of impact rise times t_r, need to be considered (see Figure 5.5)). Typically natural periods of 3-50m high buildings are in the range of $0.1 - 1$ s (Chen et al., 2016). The studied rise times for impulsive impact types ($t_{r,F1}$=$3 \cdot 10^{-3}$–$1.2 \cdot 10^{-2}$ s) did not fall within this range.

This becomes different if there are for example glass structures with higher natural periods. Anyhow, the rise times of the dynamic impact types (0.1–0.6 s) where in the critical range and dynamic structural analysis most likely has to be carried out.

5.4 Conclusions

The complex interaction of short-duration bores resulting from irregular broken waves in extremely shallow waters were studied, and the types of bore interaction patterns were identified. The impacts the bore generated at the vertical wall were classified into three impact types, and a link between bore patterns and impact types was discussed. This study focused on the 60 highest bore impacts on a vertical wall for 2 tests (30 impacts from each test) with wave steepness's at the dike toe of 0.0012 and 0.0014 as well as an offshore breaker parameter of 0.2 (similar to design storm conditions at the Belgian coast with a 1,000 and 17,000 annual recurrence interval, see Section 3.1.2). The results and conclusions can be summarised as followed.

- Five bore interaction patterns prior to impact were identified: (1) regular bore pattern, (2) collision bore pattern, (3) plunging breaking bore pattern, (4) sequential overtopping bore pattern and (5) catch-up bore pattern. The bore interaction process complicates a deterministic prediction of impact forces based on bore properties, for example thickness and velocity.

- For the bore impacts at a dike-mounted vertical wall a double peak impact signal shape was observed, with similar magnitudes for the two peaks. A new classification methodology was developed and three bore impact types were distinguished: (1) impulsive impact type, (2) dynamic impact type, (3) quasi- static impact type.

- The majority of impacts ($\sim$2/3 of all impacts) and the largest impact force was considered quasi-static impact type. Based on these findings it was suggested to use the quasi-static impact types to derive a maximum force estimate for structural design guidance. This would have the advantage that the up-scaled results are less affected by scale effects due to the almost hydrostatic behaviour of the water in front of the wall for this impact type. This is strictly only possible if no dynamic effects, due to the resonance period of the structure tn being in the range of the impact rise time t_r, need to be considered for structural analysis.

- A tentative link between the five identified bore patterns and the three identified impact types was discussed. Only plunging bore pattern lead to dynamic/impulsive impact types in any case. Collision bore pattern was the most frequent (46% of all interaction patterns were identified as collision bore pattern) and resulted in quasi-static impacts type in the majority of cases. The other bore patterns were equally frequent and most of them resulted in quasi-static impact type.

- A more practical conclusion was that the maximum measured impact force for extremely shallow foreshore conditions, wave steepness at the dike toe $S_{m-1,0,t}$=0.0012 and breaker parameter offshore β_o=0.02 (similar to a design storm condition with a 1,000 year annual recurrence interval at the Belgian coast) showed a maximum expected impact force of $\sim$19 kN/m (prototype value).

Though experiments were conducted on a rather large scale (Froude similarity and a length scale factor 1-to-4.3), scale effects are still expected, mainly due to dissimilarities in the entrained air and the air content of the foamy bores, when upscaling the obtained results to prototype, especially for the measured impact pressures and the resulting impact forces of the dynamic and impulsive impact types. A further investigation of the entrained air in the overtopping bores and consequent scale effects for overtopped wave impacts in extremely shallow water conditions is therefore required. Additionally, an advanced study of bore transformation parameters, such as bore front slope, bore thickness and velocity in vicinity of the wall for single impact events related to regular bore interaction patterns would increase understanding of the impulsive and dynamic impact types. A statistical analysis to predict the maximum impact force of overtopped bores on a dike- mounted vertical wall might be more beneficial to account for the stochastic behaviour of the measured impacts.

Chapter 6

Analysis of empirical & theoretical impact force prediction

A double peak total horizontal impact force signal shape was observed with two distinct peaks during every impact (see Chapter 5). The two peaks were assigned consecutively to the dynamic components (thickness and velocity) or hydrostatic components (time-varying run-up and run-down of water at the wall) of the impacting bore. The two peaks were termed dynamic F_1 and quasi-static F_2 impact respectively. In this Chapter it was aimed to describe and predict the double peak impact signal shape with its two distinct peaks F_1 and F_2. First, the specific objectives for this Chapter were given (see Section 6.1). The prediction accuracy of the reviewed empirical formulas (see Section 2.4) was evaluated using horizontal bore flow property measurements on the promenade (see Section 6.2.1) to predict the total horizontal bore-induced impact force from the large-scale 'DeltaFlume' data-set in Section 6.2. The prediction accuracy was judged based on the error estimators MAPE, coefficient of variaton R^2 and standard deviation (see Section 6.2.2). The prediction accuracy of the quasi-static impact F_2 was increased based on fitting the hydrostatic theory to the maximum run-up measurement at the wall (see Section 6.3.2). Additionally, it was attempted to theoretically predict the double peak impact force signal shape based on the vertical accelerations of the water mass in front of the wall (see Section 6.3.3). After deconstructing the process chain preceding an impact, using the physically most meaningful parameters to predict the impact force, evaluating on a range of existing approaches, and observing the scattered prediction results, it was concluded that the impact behaviour is highly stochastic and statistical analysis would be more beneficial (see Section 6.4).

6.1 Specific objectives

Existing empirical prediction formulas for bore-induced impact forces on dike mounted walls were reviewed in the literature study (see Chapter 2). The presented formulas were used to achieve the specific objectives of this Chapter:

1. To study how well existing empirical prediction formulas capture the underlying physical process which lead to the first dynamic F_1 and second quasi-static F_2 force peak from the double peak, bore-induced and total horizontal impact force signal shape.
2. To adapt existing and derive new semi-empirical formulas to predict the maximum dynamic F_1 and quasi-static F_2 force peak, in agreement with the underlying physics and based on the large-scale 'DeltaFlume' data-set.
3. To elaborate on a theoretical model to predict the total horizontal impact force based on the instantaneous accelerations of the water masses in front of the wall.

6.2 Data analysis and methods

For the purpose of this study the impact process leading to the first dynamic F_1 and second quasi-static F_2 force peak was investigated using large-scale experimental data (testID 492 and 500 from the 'DeltaFlume' data-set). The model set-up was described in Chapter 3 and the details of the two selected tests were highlighted previously in Table 5.1. The two selected tests featured wave conditions similar to a storm with a 1,000 and 17,000 annual recurrence interval at the Belgian coast. The 30 highest force peaks from each of the two tests were selected, resulting in 60 events used for the further study. The 60 impact force events were up-scaled to prototype using Froude similarity and length scale factor 1-to-4.3. The existing prediction formulas were tested using these 60 force peaks. Additionally, the momentum flux and hydrostatic theory were fitted to the data for the first F_1 and second F_2 force peaks respectively.

6.2.1 Horizontal bore properties on promenade

The horizontal bore properties mainly consisted of the incoming flow thickness η [m] and incoming flow velocity u [m/s]. The measured time-series of bore thicknesses and velocities as described in Section 3.3.3 were used to derive the maximum bore thickness and velocity related to the 30 highest impact events, based on the processing routines described in Section 3.4.4. The measurements were obtained at location number three, half way along the promenade and 1.09m in front of the wall. It was previously observed that the maximum thickness did not necessarily coincides with the maximum velocity of the overtopping bore flow (Hughes et al., 2012; Schüttrumpf and Oumeraci, 2005). Also, the authors noticed that maximum velocities are measured at the front of the overtopping flow. This was supported by Van Der Meer et al. (2010), stating that the front velocities represented well

the maximum velocity averaged over the depth. However, for the purpose of this study it was decided to use the maximum measured bore thickness and maximum measured bore velocity to empirically relate them to the maximum impact force (see Figure 6.1).

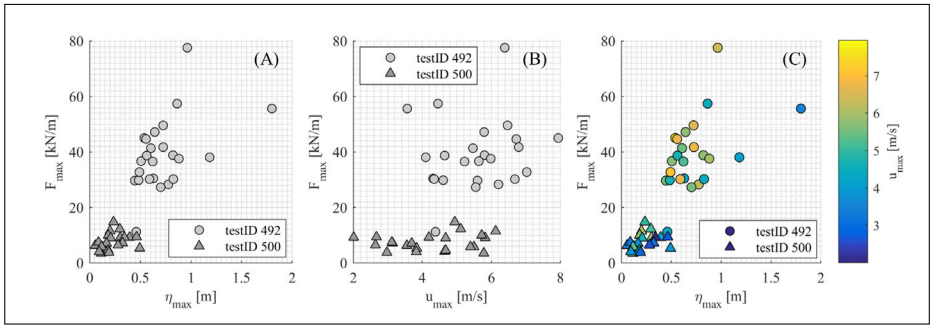

Figure 6.1: Derived maximum bore thickness (A), maximum bore velocity (B) and the combined bore thickness η and velocity u (C) related to the 30 highest impacts in testID 492 and 500. All values were upscaled to prototype.

The peak forces for the 30 highest impacts of testID 492 and 500 showed an increasing trend with increasing maximum bore thicknesses (see Figure 6.1 (A)). For the maximum bore velocities this trend was not so obvious. The higher wave energy and water level in testID 492 lead in general to higher velocities but no increasing trend was observed for events with the same testID (see Figure 6.1 (B)). Anyhow, when plotting maximum impact force, thicknesses and velocities in the same figure (see Figure 6.1 (C)), it was observed that keeping the same thickness, a higher velocity tends to result in a higher maximum impact force (as the lighter colours associated with higher velocities were found in the upper range of data points). The same trend was observed previously by Van Doorslaer et al. (2017). The implication of Figure 6.1 (C) would be that any impact force prediction formula including both the maximum flow thickness η [m] and incoming flow velocity u [m/s] should result in a better prediction accuracy.

6.2.2 Statistical error estimator

The predicted impact forces F_{pre} were plotted together with the measured impact forces F_{obs} for the 60 events, for the different formulas outlined in Table 6.2 and Table 6.1. A figure with the predicted values on the x-axis and observed values on the y-axis was generated and a 45°-line introduced in the plot. If a perfect prediction was achieved the data points would fall on the 45°-line. To assess the accuracy of the prediction formulas, a number of statistical error estimators was used. The standard deviation (see Equation 6.1) was a dimensional measure of a data-set variation and described how close the observations were distributed around

the mean value (see Equation 6.2),

$$\sigma = \sqrt{\frac{1}{n-1}\sum_{i=1}^{n}(|F_i - F_{mean}|)}, \tag{6.1}$$

$$F_{mean} = \frac{1}{n} \cdot \sum_{i=1}^{n} F_i. \tag{6.2}$$

Hence, a lower standard deviation generally meant that the prediction was more precise. However, the accuracy had to be judged by observing how close the values were situated around the 45°-line. Furthermore, the goodness-of-fit of the predictions was also evaluated using the coefficient of determination R^2 as it was typically applied to assess whether a prediction followed closely the 'regression line' (see Equation 6.3),

$$R^2 = 1 - \frac{\sum_{i=1}^{n}(F_{obs,i} - F_{pre,i})^2}{\sum_{i=2}^{n}(F_{obs,i} - F_{mean})^2}. \tag{6.3}$$

In this case the 'regression line' was the 45° line. The squared residuals were calculated, meaning that with larger distances to the 'regression line' the error was relatively larger compared to smaller distances to the 'regression line'. This may yield in unwanted effects, that the larger deviations in impact force prediction for the higher impact forces, will outweigh the better prediction accuracy for the lower impact forces. Furthermore, it was not entirely correct to use R^2 for a goodness-of-fit correlation when the 'regression line' was not calculated based on the available data (as in this case, where the 45°-line was the artificial 'regression line') and may yield in negative values, due to a biased over- or under prediction. Anyhow, due to its wide spread popularity and comprehensible outcome it was given as another estimator to assess the prediction accuracy. In theory, the closer the coefficient of determination R^2 was to 1, the better the prediction accuracy.

The mean absolute percentage error (MAPE) was chosen as another statistical error estimator (see Equation 6.4), to overcome the bias towards extreme outliers in the coefficient of determination R^2 estimation. Furthermore, MAPE estimates directly the error between the predicted and measured valued without referring to the mean or regression line. Hence, it was considered the best error estimator to evaluate the prediction accuracy of the formulas in this study. A MAPE value closer to one can be interpreted as a better prediction,

$$MAPE = \frac{1}{n} \cdot \sum_{i=1}^{n} \left|\frac{F_{obs} - F_{pre}}{F_{obs}}\right|. \tag{6.4}$$

In the equations 6.1-6.4, F_{mean} stand for the predicted mean force value [kN/m], F_{obs} [kN/m] the measured impact force, F_{pre} the predicted impact force [kN/m], n the number of impact force events, i the counter over each impact force event and F_i the impact force [kN/m] related to event i. Anyhow, there were drawbacks with this method as well, regarding a biased data-set and that it systematically selected the method with lower forecasts. Hence, the combination of the proposed statistical error estimators will be used to judge the accuracy of the impact force prediction formulas, taking into account the major drawbacks of each estimator.

6.3 Results and discussion

In this Section the formulas to predict the dynamic F_1 (see Section 6.3.1) and the quasi-static (see Section 6.3.2) bore-induced impact forces were selected and tested with the 60 highest force peaks from testID 492 and 500. Furthermore, a theoretical model to predict the impact force signal shape was proposed in Section **??**. This was done to assess the prediction accuracy of these approaches and derive at a conclusion whether they could be used to predict the impact load in the case of overtopping bore loads in shallow water and mildly sloping foreshore conditions.

6.3.1 Semi-empirical prediction of dynamic impact type

As described in the previous Section the bore thickness η and velocity u were important during the impact parameters leading to the dynamic force peak F_1. Hence, any existing formulas (see Table 2.6) taking into account the incoming bore thickness η and bore velocity u prior to impact were considered physically most correct. Equation 2.7 (Cross, 1967), Equation 2.9 (Ramsden, 1996), Equation 2.10 (Asakura et al., 2002), Equation 2.11 (Robertson et al., 2011), Equation 2.13 (see Table 2.5) were evaluated from the tsunami-related research; and Equation 2.15 (Van Doorslaer et al., 2012), Equation 2.16 (Van Doorslaer et al., 2017), Equation 6.8 (derived from hydrostatic theory) were evaluated from the overtopping wave-related research studies. The dynamic force peak F_1 for each of the proposed formulas was calculated based on the maximum bore thickness η_{max} and maximum bore velocity u_{max} immediately prior to the dynamic force peaks F_1 for each of the 60 highest impacts. The bore thickness η and velocity u was measured at instrument location WLDM2 and PW2 respectively (see Section 3.3.3). The bore front slope in Equation 2.8 was determined based on a sensitivity study of theoretical bore front slopes and optimizing the goodness-of-fit parameters of the prediction. The optimum bore front slope used in this study was 51°. Additionally, linear regression and fitting of the force peaks to the momentum flux theory (see Equation 6.5) by minimizing the MAPE error was done,

$$F_{mflux} = 2 \cdot \rho_w \cdot \eta_{max} \cdot u_{max}^2. \tag{6.5}$$

Cappietti et al. (2018) suggested that the incoming momentum flux is perfectly reflected 180° at the wall, and therefore, added the coefficient 2 to the momentum

flux theory. The calculated and measured force peaks for the different equations were compared in Figure 6.2.

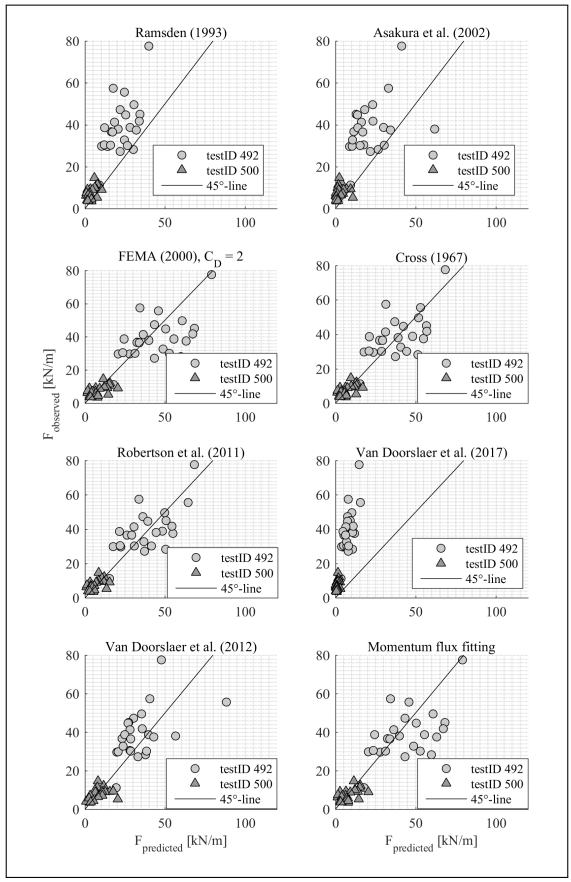

Figure 6.2: Empirical prediction formulas for the dynamic force peak F_1, from tsunami related studies and overtopping wave related studies (right). Results for the 30 highest impacts of testID 492 and testID 500 are given in prototype-scale units using Froude similarity and the length scale factor 1-to-4.3.

The standard deviation σ ($8.66 - 19.32\,\mathrm{kN/m}$) and the mean absolute percentage error MAPE (0.1980–0.9995) for the predictions were calculated and are presented in Table 6.1. The values given in brackets have to be treated carefully because these specific prediction results show a bias. Equation 2.11 (Robertson et al., 2011) yielded in the best goodness-of-fit parameters, using the maximum bore thickness η_{max} and maximum bore velocity u_{max} as input parameters. It was visually observed and confirmed by the goodness-of-fit parameters that neither the tsunami related nor the overtopping wave related approaches performed exceptionally well in predicting the dynamic force peaks F_1 . Equation 2.9 (Ramsden, 1996), Equation 2.10 (Asakura et al., 2002) and Equation 2.16 (Van Doorslaer

et al., 2017) under predict the dynamic force peaks F_1. For the latter this may result from a different wall height in their studies, as this height was included in calculating the freeboard R_c, or that only non-broken waves and discrete overtopping bores in the lower range were used for the fitting with computed average velocities over the promenade. Conversely, Equation 2.13 (Arnason, 2005) using C_D=3 over predicts the dynamic force peaks F_1 . Even the drag force formulas with C_D=2 (see Equation 2.13) with a different physical meaning (impact force generated by fully developed flow around submerged structure as opposed to impact forces on the building or storm wall with dry back sides by unsteady flow) showed similar prediction accuracies compared to formulas derived for a situation with short duration overtopping bores (see Equation 2.16 (Van Doorslaer et al., 2017)) or a wall with a dry back (see Equation 2.11 (Robertson et al., 2011), Equation 2.10 (Asakura et al., 2002), Equation 2.7) (Cross, 1967). An over- or underestimation of the maximum force peak up to a factor of ∼2.2 was observed.

Table 6.1: Dynamic impact type F_1 prediction formulas with goodness-of-fit parameters (prototype values).

Reference	**Equation**	σ	R^2	**MAPE**
[-]	**[-]**	**[kN/m]**	**[-]**	**[-]**
Cross (1967)	2.7	9.04	0.7615	0.9995
Ramsden (1993)	2.9	10.35	(0.3760)	(0.5875)
Asakura et al. (2002)	2.10	18.58	(0.2200)	(0.5418)
Arnason (2005)	2.13 (C_D=3)	19.32	(0.9083)	(0.2560)
Fujima et al. (2009)	2.13 (C_D=1)	10.96	0.6214	0.8373
FEMA (2000)	2.13 (C_D=2)	10.50	0.3563	0.5813
Robertson et al. (2011)	2.11	8.66	0.7800	0.96146e
Van Doorslaer et al. (2012)	2.15	10.80	0.6394	0.9254
Van Doorslaer et al. (2017)	2.16	14.84	(0.7163)	(0.1980)
Momentum flux fitting	6.5	10.81	0.6214	0.8373

The scattered prediction of the dynamic force peaks F_1 shown in Figure 6.2 was assumed to be the result from a highly turbulent bore, bore interaction processes prior to impact, and different impact mechanisms. Even small fluctuations in the bore near the wall resulted in a different impact process (for example wave interaction in front of the wall might lead to plunging wave breaking against the wall). Two-dimensional effects, such as a non-uniform bore front and the fact that certain parameters (for example the bore front slope) were not studied might also contribute to lower prediction accuracy of the dynamic force peak F_1. Additionally,

the bore thickness η and bore velocity u were measured at different locations in the presented experiments from which the prediction formulas were derived, introducing further uncertainty when comparing their predictive capabilities. Nevertheless it seemed more likely that the dynamic force peaks F_1 were of stochastic nature, thus hindering a semi-empirical or deterministic prediction. Similar stochastic behaviour for overtopping bore-induced impact loads was also observed by Chen et al. (2016) and Altomare et al. (2015).

6.3.2 Semi-empirical prediction of quasi-static impact type

As described in the previous Section the hydrostatic force, a mass of water statically subjected on the structure, was dominant in generating the quasi-static force peaks F_2. Hence, any existing formulas (see Table 6.2) taking into account the bore thickness directly in front of the wall, or run-up height of the bore at the wall were physically most correct (see Equation 2.12 (Kihara et al., 2015), Equation 2.14 (Chen et al., 2012), Equation 6.8 (derived from hydrostatic theory)). These formulas were used to predict the quasi-static force F_2 using the maximum run-up height $R_{h,max}$ related to the 60 selected maximum impacts. The calculated result was compared to the according measured quasi-static F_2 force peak (see Figure 6.3). Froude similarity and a length scale factor 1-to-4.3 were used to compare calculated and measured impact force in prototype-scale units. The goodness-of-fit parameters, standard deviation σ ($3.21 - 6.31\,\mathrm{kN/m}$) and the mean absolute percentage error MAPE (0.4432–0.9963) were calculated (see Table 6.2). The values given in brackets had to be treated carefully because these specific prediction results show a bias. Equation 2.12 (Kihara et al., 2015) tends to always over predict the impact force. This was expected because the formula was derived for a situation with developed tsunami overflow over the wall and a sufficiently large water body in front of the entire wall height. Conversely, the run-up events in this study were derived for short duration overtopped bores with thin run-up tongues.

For force peaks above $25\,\mathrm{kN/m}$ all formulas over-predict the impact force. The over prediction was caused by the quadratic influence of the maximum run-up height $R_{h,max}$ in front of the wall, leading to the conclusion that not the entire run-up height, especially for larger run-up values, was effectively contributing to the quasi-static impact force. This was in line with previous studies stating that not all of the total run-up height was effectively contributing to the hydrostatic impact force (Klammer et al., 1996). It was also argued that the maximum run-up height had no direct physical connection to the quasi-static force peak F_2 as the maximum run-up occurred slightly before the quasi-static force peak F_2. This is why the reflected water mass (water body in front of wall after the collapse of maximum run-up) might be an even better approximation of the quasi-static force peak F_2.

Contrary to the assumption in the hydrostatic theory, the maximum run-up water body did not arise from a horizontal water surface in front of the wall, but rather a triangular shape of run-up flow and a thin run-up tongue in the upper part. Linear regression and fitting of the force peaks to the hydrostatic theory was done using the maximum run-up height $R_{h,max}$ obtained from motion tracking of

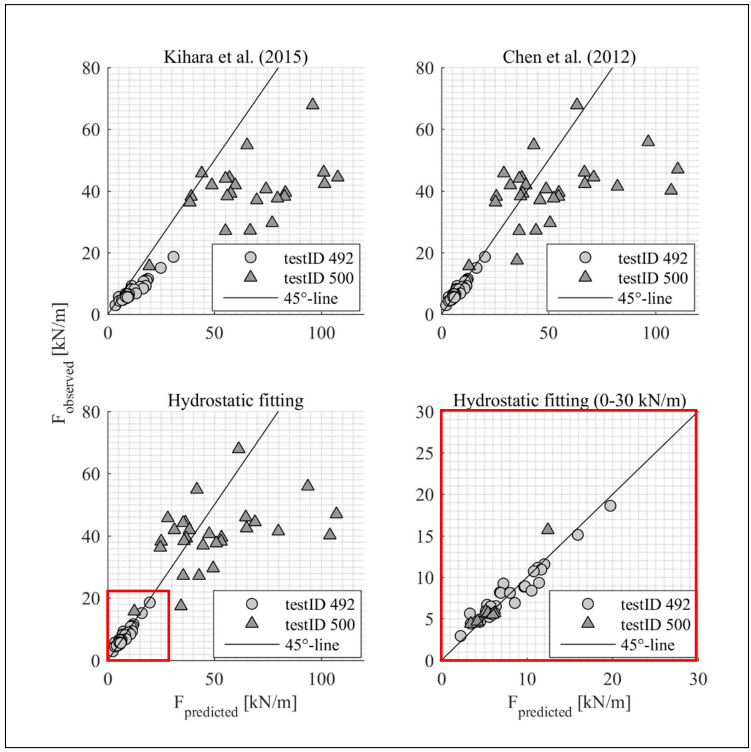

Figure 6.3: Empirical prediction formulas for the quasi-static force peak F_2. Results for 30 highest impacts of testID 492 and testID 500 are given in prototype using Froude similarity and the length scale factor 1-to-4.3.

the bore front at the wall. The fitting was done for force peaks up to 25 kN/m and by minimizing the MAPE error and a best-fit equation obtained (Equation 6.8),

$$F_{Best-fit} = \frac{1}{2} \cdot \rho_w \cdot g \cdot (C \cdot R_{Rh,max})^2, \tag{6.6}$$

$$C = 0.8, \tag{6.7}$$

$$F_{Best-fit} = 0.32 \cdot \rho_w \cdot g \cdot R_{Rh,max}^2. \tag{6.8}$$

Based on these findings it was stated that only a 80% of the maximum run-up $R_{h,max}$ was effectively contributing to the impact force on the wall. Substituting Equation 6.7 into Equation 6.6 yields in a coefficient of 0.32, which was very close to what was found earlier as C_1=0.33 by adapting the momentum flux theory and using regular waves (Chen et al., 2012). Hence, this finding served as a large-scale

confirmation that the prediction of quasi-static force peaks F_2 using 80% of the maximum run-up height was also valid for irregular waves. For practical design guidance and determining the overturning moment of sea-walls, Equation 6.8 can also be used inversely to calculate the 80% maximum run-up height based on any given force.

Table 6.2: Quasi-static impact type F_2 prediction formulas with goodness-of-fit parameters (prototype values).

Author	**Equation**	σ	R^2	**MAPE**
[-]	**[-]**	**[kN/m]**	**[-]**	**[-]**
Kihara et al. (2015)	2.12	6.31	(3.6059)	(0.4432)
Chen et al. (2012)	2.14	3.38	0.2061	0.9725
Hydrostatic fitting	6.8	3.23	0.2943	0.9963

6.3.3 Theoretical prediction of impact signal shape

As the most base line prediction of any horizontal force imposed by a water body on a vertical structure is the hydrostatic theory (see Equation 6.9),

$$F_{hyd}(y,t) = \frac{1}{2} \cdot \rho_w \cdot g \cdot (R_h(y,t))^2. \tag{6.9}$$

The hydrostatic force estimate based on hydrostatic theory is dependant on the height of the water column in front of the structure R_h; the run-up at the wall. The theory is however valid for a static water body of sufficient thickness in front of the wall. In Section 5.3.2 the observation was made that the measured total horizontal force over the wall height showed lower values than the hydrostatic force estimate based on the run-up at te wall (see Figure 6.4 shaded area). It was further stated that the instance of maximum run-up occurred slightly before the measured maximum hydrostatic force and pressure estimate. This was also observed by other researchers who found that the moment of maximum run-up does not coincide with the maximum force on the wall (Cross, 1967; Ramsden, 1996; Kihara et al., 2015; Chen, 2016; Ko and Yeh, 2018).

It was assumed that this difference arose from the different vertical accelerations in the run-up water body. As the rising water velocity decreased to zero, an upward-directed acceleration made it appear as if the water mass had less than its actual weight. Thus, the measured force was reduced from what the hydrostatic force would be because the 'apparent weight' of the water was less than the actual water weight. The measured pressure gradients over the wall height were rather large in this study, thus leading to the assumption that velocities were indeed not uniform over the wall height. Hence, the water body experiences acceleration in vertical

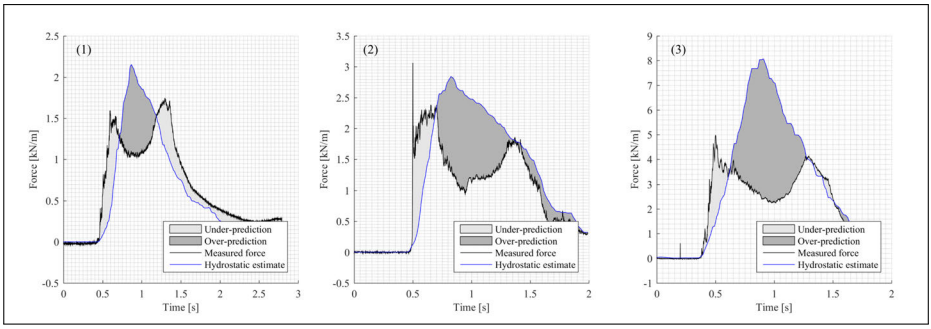

Figure 6.4: Measured force and theoretical total horizontal force estimate for a quasi-static (1), impulsive (2) and dynamic (3) impact type from test Bi_2_6. The theoretical total horizontal force estimate was calculated based on hydrostatic theory (see Equation 6.6) and using the instantaneous run-up of the bore leading edge at the wall.

direction. This theory was further encouraged due to the clockwise and counter-clockwise roller which formed at the wall (see Section 5.3.2), resulting in opposite directed acceleration vectors. The magnitude of the upward acceleration depends on the temporal and spatial variation of vertical velocity of the run-up flow. A short time after the maximum run-up, the pressures in the upper part of the water body were larger than estimated hydrostatic pressures based on the instantaneous run-up. It was hypothesized that this difference was also related to the vertical accelerations of the water body in front of the wall. The falling water velocity approached zero, and a downward-directed acceleration added to the effect of gravitational acceleration giving an apparent water weight greater than the actual weight. The magnitude of the downward acceleration was dependent on the time and spatial variation of vertical velocity. Despite the small additional dynamic component, the pressure distribution resembled a hydrostatic distribution and the measured total force almost fell together with the hydrostatic force estimate based on the instantaneous run-up of the water at the wall.

We hypothesize that the change in pressure over the length of the vertical wall at the moment of maximum run-up consisted of the hydrostatic pressure due to gravity minus the pressure due to the positive upward acceleration of the run-up i.e.,

$$\Delta P(y,t) = \rho \cdot (g - a(y,t)) \cdot \Delta[R_h(t) - y]. \tag{6.10}$$

where P is instantaneous pressure at elevation y [m], time t [s], instantaneous vertical run-up R_h [m] and instantaneous time-dependent acceleration of the run-up water a [m/s^2], that can also vary in the vertical. In Equation 6.10 the first term on the right-hand-side of the equals sign is the hydrostatic pressure, and the second term is the dynamic pressure associated with the wave run-up. Solving

Equation 6.10 for a yields the expression:

$$a(y,t) = g \cdot [1 - \frac{\Delta P(y,t)}{g \cdot \rho \cdot \Delta[R_h(t) - y]}]. \tag{6.11}$$

The ratio in the right-hand side of Equation 6.11 is the ratio of measured pressure to the theoretical hydrostatic pressure based on the height of the run-up. When this ratio is less than unity, the dynamic acceleration is positive (upward), and when the ratio is greater than unity, the dynamic acceleration acts in the same direction as gravity (When the ratio is equal to unity, there is no dynamic acceleration and the pressure distribution is hydrostatic). Equation 6.11 is strictly only valid when $R_h > y$ and $P >$0 (i.e., when the pressure sensor was submerged). Also, it was assumed that this approach is only valid after the dynamic impact occurred, and the water in front of the wall is simplified as a vertical moving body without any significant air entrainment and continuous contact of the run-up water body over the wall height. Accelerations were calculated using the pressure difference $\Delta P(y,t)$ of pressures measured between two consecutive pressure sensors along the wall height (see Section 3.3.4 for the detailed distances between consecutive pressure sensors),

$$\Delta P(y,t) = P(y = i,t) - P(y = i+1,t). \tag{6.12}$$

The assumption showed similarities to the solid-body projectile assumption by Ko and Yeh (2018), who studied the splash-up of tsunami bore impacts on walls. They also observed that the measured forces were lower than the theoretical hydrostatic force based on the run-up at the wall. Ko and Yeh (2018) measured small pressure gradients over the wall height which lead to the assumption that there is a uniform vertical velocity profile of the water in front of the wall. The small pressure gradients were not observed in this study, thus leading to the assumption that velocities were not uniform over the wall height. Hence, the water body experiences acceleration in vertical direction. The magnitude of the upward acceleration depended on the temporal and spatial variation of vertical velocity, and the acceleration also varied over the height of the water column at each moment in time.

In order to prove this assumption a measurement of the time-varying vertical accelerations of the water body in front of the wall, together with the pressure recordings along the wall, were required. Only pressure but no vertical accelerations were measured in the 'DeltaFlume' data-set. Hence, the numerical model OpenFOAM was set-up for the 'DeltaFlume' data-set by Gruwez et al. (2019) and a description provided in Streicher et al. (2019a). OpenFOAM (Weller et al., 1998) is a library of applications and solvers including interFoam, a Navier-Stokes equations solver following an Eulerian mesh-based method for two incompressible, isothermal immiscible fluids using a Volume-of-Fluid (VOF) phase-fraction based interface capturing approach. In this work OpenFOAM v6 was applied, using the solver interFoam (for a detailed description it is referred to Larsen et al. (2019)) with the boundary conditions for wave generation and absorption provided by olaFlow

(Higuera, 2017), hereafter simply referred to as OpenFOAM. Turbulence was modelled by the Reynolds-Averaged Navier-Stokes equations (RANS) coupled with the turbulence closure model $k-\epsilon$ SST (k is the turbulent kinetic energy density, ϵ is the specific dissipation rate). The $k-\epsilon$ SST model that was stabilized in nearly potential flow regions by Larsen and Fuhrman (2018) was used. The OpenFOAM model domain started at the wave paddle zero position, and included the foreshore and dike geometry as measured in the experiment up to the vertical wall. The model was run in a vertical two-dimensional (2DV) configuration (cross-shore section of the wave flume). To optimise the computational time, a variable grid resolution was applied. The structured mesh had a grid resolution of 0.18 m in the air phase and 0.9 m in the water phase. The mesh was further refined in the zone of the surface elevation up to the dike toe (dx=dz=0.045 m) and on the dike up to the wall (dx=dz=0.0225 m). Waves were generated by applying a Dirichlet-type boundary condition: the experimental wave paddle displacement was first converted to a wave paddle velocity, which was then applied to the water phase at the stationary boundary (x=0 m). Active wave absorption (as implemented in olaFlow) was activated to prevent re-reflection of reflected waves. The same geometry of the 'DeltaFlume' model tests and hydraulic boundary conditions of the realized paddle motion from the physical model were used. A side-view image of the numerical model at the moment of bore impact at the wall was shown in Figure 6.5. Distinct features like the mildly sloping foreshore, the dike, the promenade and wall were visible in the validated numerical model set-up. A detailed description of the numerical model set-up can be found in Streicher et al. (2019a).

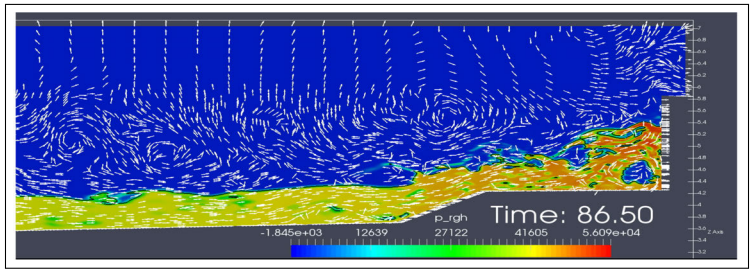

Figure 6.5: Numerical model set-up in OpenFOAM to reproduce the 'DeltaFlume' experiment and test Bi_2_6, using the hydraulic boundary conditions of the realized paddle motion in the 'DeltaFlume' model test (from Gruwez et al. (2019)). The mildly sloping foreshore, dike, promenade and wall were visible from the side-view image.

As the computational demand to remodel an entire test length including 1000 irregular waves was too high, it was decided to choose the short duration Bichromatic wave test Bi_2_6 for this study (see Table 3.2). The time-series was about 200 s long and included ∼10 bore-induced impact events (see Figure 6.6). The measured pressures at the wall were read out from the numerical model at the same locations as they were measured in the 'DeltaFlume' data-set. Furthermore, similar post-processing routines and pressure integration was applied as for the measured pressures in the 'DeltaFlume' data-set (see Section 3.4.5). In this way

a total horizontal force per meter width was obtained from the numerical model, which could be compared to the measured horizontal force per meter width from the 'DeltaFlume' data-set (see Figure 6.6).

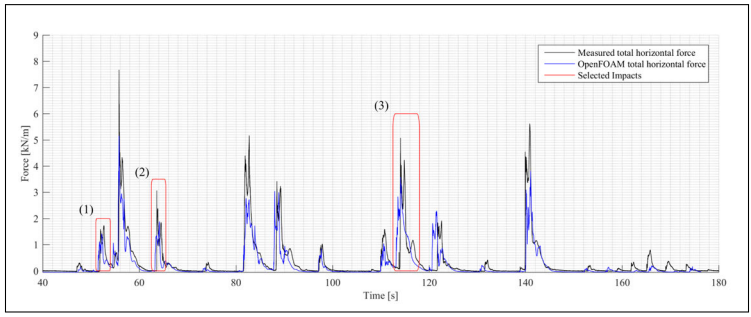

Figure 6.6: Time-series of total horizontal impact force on the wall from pressure integration for the 'DeltaFlume' data-set (black) and the numerical simulation in OpenFOAM (blue). The test Bi_2_6 (see Table 3.2) was chosen for this study.

Three peaks from Figure 6.6 were chosen, representative for a quasi-static (1), impulsive (2) and dynamic (3) impact type, and were highlighted with a red rectangle. These three impacts were depicted for a detailed view in Figure 6.7. In general a good agreement of the total horizontal impact force between measurements and numerical model was observed. However, small difference in the impact signal shape and a general lower numerically computed horizontal impact force were noted.

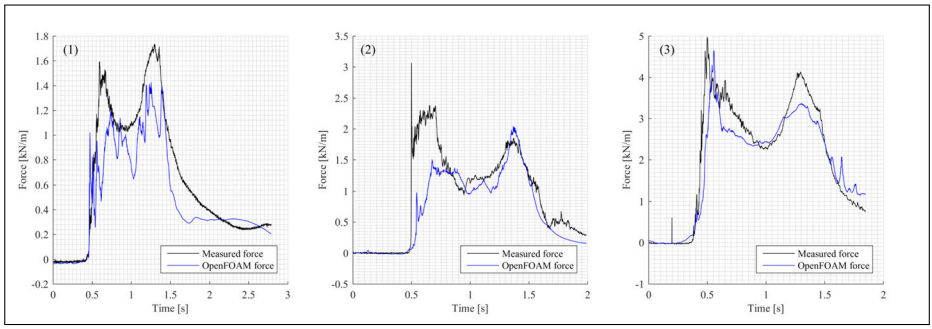

Figure 6.7: A detailed view on the quasi-static (1), impulsive (2) and dynamic (3) impact from test Bi_2_6 (see Table 3.2), comparing the measured and numerically computed total horizontal impact force.

As a next step the vertical velocities 0.02 m in front of the wall were read out from the numerical model, at the same location of the pressure sensors. A distinction was made between air and water flow and the velocities associated with water flow selected. The time-series of the velocities was then smoothed using local regression and weighted linear least squares with a factor 0.2. As a next step the derivative of the smoothed velocity time-series was calculated to derive

the vertical accelerations of the water body in front of the wall. The so obtained vertical accelerations were used to calculate the time-varying pressures along the height of the wall (see Equation 6.10). The time-varying pressures along the wall height were again integrated over the height and a total horizontal force per meter width value obtained. Additionally, the time-varying run-up of the leading edge in front of the wall, as determined in Section 5.2.2, was used to calculate the hydrostatic force estimate with Equation 6.6.

The hydrostatic horizontal force estimate (see Equation 6.6) and the theoretical force based on the change in vertical acceleration (see Equation 6.10) were computed and compared to the measured total horizontal impact force (see Figure 6.8). This was done for the three impacts shown in Figure 6.6.

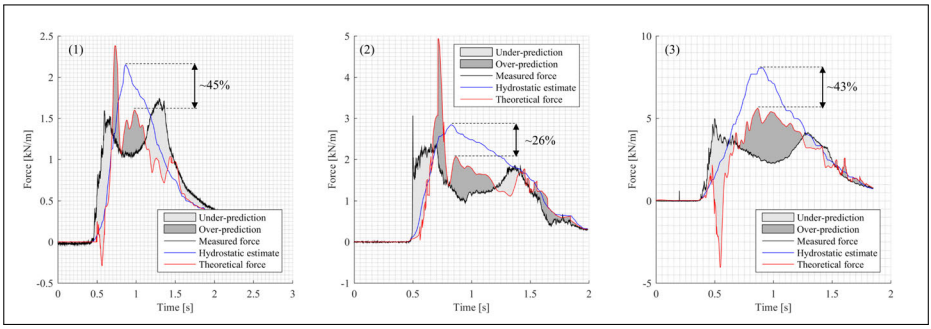

Figure 6.8: Time-series of measured force (black) and theoretical hydrostatic force estimate (blue) and theoretical force (red) for a quasi-static (1), impulsive (2) and dynamic (3) impact type. The hydrostatic horizontal force estimate was calculated based on hydrostatic theory (see Equation 6.6) and using the instantaneous run-up of the bore leading edge at the wall. The theoretical force estimated was calculated based on the vertical accelerations of the water mass in front of the wall (see Equation 6.10).

As indicated in Figure 6.8 the maximum error between the hydrostatic force estimate and the measured impact force could be reduced by 26%-45% with the theoretical model based on the accelerations of the water body in front of the wall. However, a mismatch between the theoretically calculated total horizontal impact force and the measured total impact force remained, especially for the dynamic first peak F_1 of the double peak shape impact force signal. It was most likely due to the fact that no horizontal accelerations were accounted for by the theoretical model. This was especially apparent during the time of the first dynamic peak (F_1) in the impact force signal shape. During the time of the dynamic impact the total force was largely dependant on the horizontal momentum of the incoming bore flow (see Section 5.3.2). Only when the flow was turned 90° and deflected upwards along the wall, the theoretical model based on the vertical accelerations along the wall, became more accurate. The theoretical model was also not able to account for the continuous horizontal in-stream of water in the lower part of the wall, after the dynamic first impact. As a result an overestimation by the theoretical model compared to the measured total horizontal impact force was expected even for the time after the dynamic first peak F_1.

More reasons why the proposed theory was not fully capable of reproducing the total horizontal impact force signal shape were first deducted from the fact that accelerations and measurements of impact pressures were obtained from a different numerical model and a physical model respectively. Small variations (turbulence or entrained air) in the impacting flow, differences in the distribution of velocities and accelerations along the wall might have resulted in deviations which were not due to a failing theory but due to the fact that measurements were obtained from different models. Only simultaneous and high resolution measurements of impact pressures, run-up and accelerations at the wall could help to resolve this issue. Furthermore, the run-up determination using motion tracking might have influenced the result as well, for example the thin run-up tongue which did not develop full hydrostatic force, or detached water due to outward reflection at the wall.

6.4 Conclusions

Overtopping bore-induced impact loads on vertical walls were investigated using large-scale experimental data obtained for a geometrical set-up with mildly sloping foreshore, dike, promenade and wall, in extremely shallow water conditions. The bore impact pressures at the wall were measured together with the bore thickness η [m], bore velocity u [m/s] and run-up at the wall R_h. A process-based investigation of the impact at the wall was conducted, and dynamic force peaks F_1 and quasi-static force peaks F_2 for a double peak impact signal shape were distinguished (see Chapter 5). In the majority of impact events ($\sim$2/3) the quasi-static force peaks F_2 were larger than the dynamic force peaks F_1. The highest force peak (4.76kN/m in model scale) was of quasi-static nature. In this Chapter, an ad-hoc review and comparison of existing formulas to predict the dynamic F_1 and quasi-static F_2 force peak was conducted based on data related to 60 maximum impacts. The 60 maximum impacts were derived from two tests (testID 492 and 500 from the 'DeltaFlume' data-set). In both tests approximately $\sim$1000 irregular waves were generated, with wave conditions similar to storms with a 1,000 and 17,000 annual recurrence interval for the Belgian coast. The first dynamic force peak F_1 was related to the incoming bore thickness and velocity. The second quasi-static force peak F_2 was mostly related to the bore thickness in front of the wall or the instantaneous run-up at the wall. Hence, specific conclusions can be given as:

- Simple momentum flux theory (see Equation 6.5) was adapted as a new approach to predict the dynamic first peak F_1 in the double peak horizontal force impact signal shape. The adapted momentum flux theory was within the range of prediction accuracy of previously proposed formulas. The scatter in all formulas was rather high suggesting a stochastic behaviour of the dynamic overtopping bore-induced impacts on vertical walls. Equation 2.11 (Robertson et al., 2011) resulted in the most accurate prediction (σ=8.6 kN/m in Prototype, MAPE=0.9614).

- Also for the quasi-static force peaks F_2 it was observed that the scatter in the previously proposed prediction formulas, especially for the larger force

peaks, was rather high. Hydrostatic theory was adapted (see Equation 6.8) and a coefficient C_1=0.32 derived to predict the maximum quasi-static force peak F_2 based on the maximum run-up at the wall $R_{h,max}$. The adapted hydrostatic theory resulted in the most accurate prediction (σ=3.23 kN/m in prototype, MAPE=0.9963) in comparison to previously derived prediction formulas.

- A more practical insight was that only 80% of the maximum run-up $R_{h,max}$ was effectively causing the force on the wall in case of the quasi-static impact F_2. This observation was explained by the unweighing of the water body in front of the wall due to upward acceleration, splash up and small or detached run-up tongue of the water in front of the wall.

- A theoretical model based on the vertical accelerations of the water body in front of the wall was proposed to predict the total horizontal impact force signal shape. The vertical accelerations were derived from a numerically OpenFOAM model, which was used to remodel a short duration test from the 'DeltaFlume' data-set. As the model only took into account the vertical acceleration, thus does not consider the horizontal accelerations some features of the total impact force shape, notably the beginning of the signal, were not captured well. Nevertheless, once the incoming flow was turned into vertical direction the model significantly reduces the overestimation, resulting from the hydrostatic force estimate.

It was noted, that even after examining the physical process, distinguishing impact types related to different physical processes (dynamic F_1 and quasi-static F_2 force peaks) and using the most meaningful process parameters (either incoming bore thickness and velocity or run-up height in front of the wall), the prediction accuracy for each of the approaches was low. It was argued that bore interaction processes prior to impact (Streicher et al., 2019b; Chen, 2016), non-uniformity of the bore front (2D-Effects), air-entrainment in the bore (Chen, 2016), and even small fluctuations and turbulence in the bore caused different bore impact processes resulting in the stochastic behaviour of the measured force. Statistical analysis was therefore recommended to further predict force peaks for irregular and broken waves in shallow water and mild foreshore conditions. Additionally, the development of bore thickness and bore velocity along the promenade should be studied further to find a more reliable measurement location of these parameters and study their change along the promenade width. Also, parameters such as the bore front slope and its effect on the impact process should be further investigated. To study the effect of the bore front slope and at the same time ensure repeatability, validated numerical modelling might be an option. Specifically, the impulsive impacts of very short duration at the first impact of the bore tip with the wall were expected to be largely dependent on the bore front slope and need to be further investigated.

Chapter 7

Analysis of statistical impact force prediction

Waves breaking in shallow water with mildly sloping foreshores and overtopping sea dikes generate turbulent bores. These bores show complex patterns (see Section 5), especially if they interact with each other during the storm event. When these turbulent bores meet any structure while travelling over the dike an impact load is generated inducing a maximum force F_{max} on this structure. In Belgium and other low-lying countries, these dike-mounted structures can be a sea wall or building. For the design of these structures it is important to predict the maximum expected impact force. Due to the turbulent and complex interaction patterns of the bore, a deterministic prediction of the impact force is difficult (see Section 6). Hence, a statistical analysis of the stochastic bore-induced force peaks was carried out in this chapter. First a comparison of the data-sets obtained in this study with existing data-sets and statistical prediction methods was attemped in Section 7.1. This review resulted in the specific objectives for this chapter (see Section 7.2). In the following Section 7.3 an appropriate extreme value distribution function was chosen and the force peaks from individual tests in the 'UGent1'-'UGent3' and 'DeltaFlume' data-sets (see Section 7.3.2) were combined into larger samples (more than $\sim$100 impacts per sample). Five samples S_1-S_5 based on the non-dimensional average overtopping discharge q^* were created and a Weibull distribution fitted to the force peaks in the sample. A sensitivity study regarding the sample size (see Section 7.3.3) and fitting threshold (see Section 7.3.4) was carried out to arrive at a robust calculation of shape κ and scale λ parameter (see Section 7.3.5). A statistical relation between the exceedance probability P_m, based on the number of impacts, and the impact force F_m was presented (see Section 7.4). A novel prediction methodology was described involving the empirical prediction of the expected maximum impact force F_{max}, together with an estimated exceedance probability P_m (see Section 7.4.1). An example calculation was carried out in Section 7.4.2. Finally, the derived conclusions were presented (see Section 7.5).

7.1 Review of existing approaches

Statistical analysis of overtopping bore-induced loads on dike mounted vertical walls was carried out previously by Van Doorslaer et al. (2017) and Chen et al. (2016). The ranges of the investigated relative promenade widths G_c/L_t and relative water depths at the dike toe $h_t/H_{m0,o}$ in their studies was shown in Figure 7.1 together with the measurements from the 'UGent1'-'UGent3' and 'DeltaFlume' data-sets of this study (see Section 3). The shallow water wave length L_t was calculated with Equation 2.3.

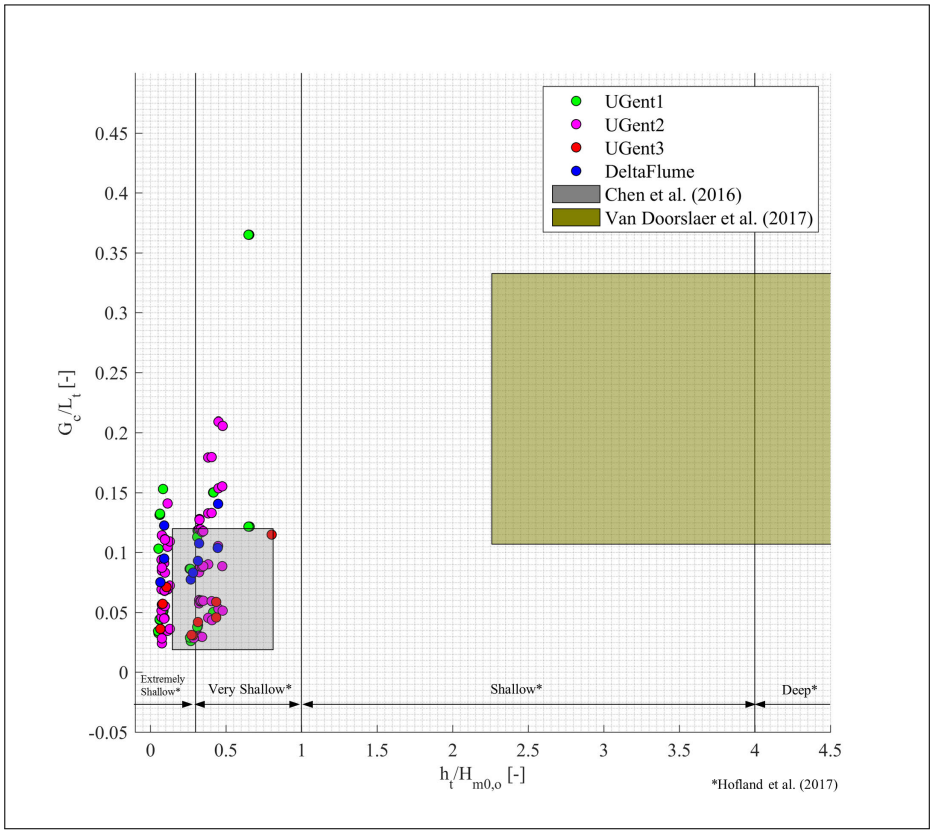

Figure 7.1: Relative promenade width G_c/L_t and relative water depth at the dike toe $h_t/H_{m0,o}$ for Chen et al. (2016); Van Doorslaer et al. (2017) plotted together with the measurements from data-set 'UGent1'-'UGent3' and 'DeltaFlume' (see Section 3).

As expected the ranges of relative water depths for which the Van Doorslaer et al. (2017) data-set is valid varies significantly from the relative water depths obtained for this study. Furthermore there is an overlap between the range of relative water depth and non-dimensional promenade width between the Chen et al. (2016) data-set and the data-sets used in this study ('UGent1'-'UGent3' and 'DeltaFlume'). The data-sets from the present study were obtained for relative

water depths at the dike toe between $h_t/H_{m0,o}$=0.05-0.80 and non-dimensional promenade widths between G_c/L_t=0.02-0.36 (see Table 3.8). Which is an extension of the Chen et al. (2016) data-set towards shallower relative water depths and larger non-dimensional promenade widths. Additionally, a second dike slope cot(α)=2 and a variable promenade width G_c=5 − 30 m in prototype was investigated for the data-sets of the present study ('UGent1'-'UGent3' and 'DeltaFlume').

The seven-step procedure introduced by Chen et al. (2016) was used (see Equation 2.19 to Equation 2.25) to calculate the maximum expected impact force based on the parameters of the data-set 'UGent1'-'UGent3' and 'DeltaFlume' and compare the result to the measured maximum impact force of the tests in data-set 'UGent1'-'UGent3' and 'DeltaFlume' (see Figure 7.2).

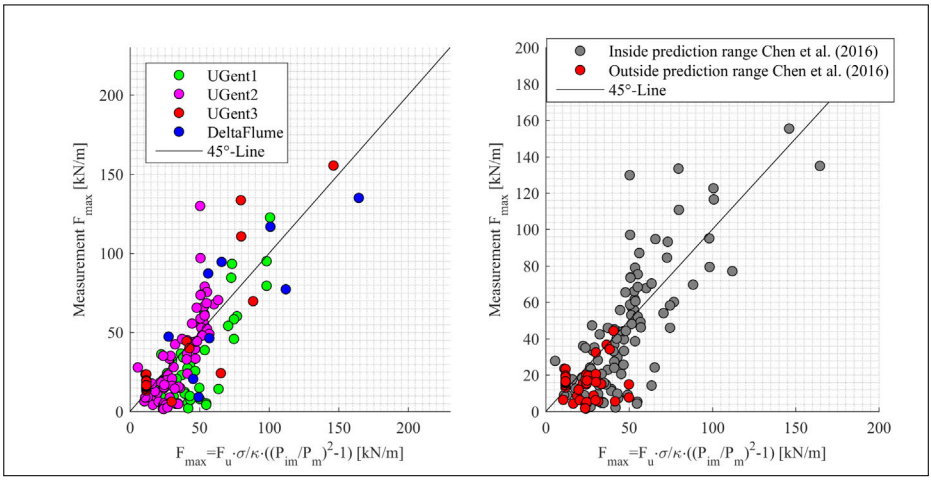

Figure 7.2: The calculated maximum bore-induced impact force after Chen et al. (2016) compared to the measured maximum bore-induced impact force for the tests in data-set 'UGent1'-'UGent3' and 'DeltaFlume'.

Based on this comparison it was concluded that the prediction after Chen et al. (2016) works especially well for the larger maximum force peaks. Below approximately 50 kN/m the predicted values were larger compared to the measured maximum force peaks. Hence, an improved prediction accuracy in this range, as well as reducing the general scatter, was aimed for.

As shown in Figure 7.1 the range of tested parameters with the Van Doorslaer et al. (2017) statistical methodology was outside the range of tested parameters of the data-sets 'UGent1'-'UGent3' and 'DeltaFlume'. It was also noted that the calculated values were significantly under-predicted, probably due to the fact that the mean impact force F_{mean}, which again is highly dependent on the threshold above which force peaks were selected for analysis, was used to compute the empirical relation for the scale parameter. Furthermore, the parameter R_c, distance between still water level and the top of the wall, is not apparent for a non-overtopped wall as investigated for this study. Hence, no direct comparison was attempted. Nevertheless, the comparison of methodologies of Chen et al. (2016) and Van Doorslaer

et al. (2017) yields useful insights (see Section 2.4.2) for the prediction methodology attempted in this study.

7.2 Specific objectives

The overall aim of this study was to establish a statistical relation between the average overtopping discharge q [m^3/s per m] and the distribution of impact loads induced by an overtopped bore on a dike mounted vertical structure, in order to predict F_{max} together with its exceedance probability P_m. The bores were generated by irregular breaking waves in mildly sloping foreshore conditions and for relative water depths a the dike toe ranging from very to extremely shallow (after Hofland et al. (2017)). The detailed objectives were:

1. To increase the test range compared to Chen et al. (2016) towards larger relative promenade widths (G_c/L_t=0.04-0.50) and extremely shallow water depths at the dike toe ($h_t/H_{m0,o}$=0.05-0.80).
2. To establish the link between average overtopping discharge q [m^3/s per m] and distribution of bore-induced force peaks, by using the average overtopping discharge q [m^3/s per m] as a key variable in the derived prediction methodology.
3. To perform the statistical fitting on sufficiently large samples of force peaks, in order to ensure a robust analysis. A sensitivity study of the sample size and fitting threshold should be conducted as part of the analysis.
4. To select an extreme value distribution and determine the statistical parameters for each sample. The scatter in the statistical parameter should now be minimized due to the large enough sample size.
5. To develop a statistical prediction methodology for maximum overtopped bore-induced loads on dike mounted walls.
6. To discuss the predictive capability of the proposed methodology based on data obtained from a different experimental data-set.

7.3 Data analysis and methods

An appropriate extreme value distribution function was chosen (see Section 7.3.1), the bore-induced force peaks from 'UGent1'-'UGent3' and 'DeltaFlume' data-sets (see Section 7.3.2) combined into a larger sample (more than $\sim$100 force peaks per sample). Five samples S_1-S_5 based on the non-dimensional average overtopping discharge q^* were distinguished and a Weibull distribution fitted to the force peaks in each sample. A sensitivity study regarding the sample size (see Section 7.3.3) and fitting threshold (see Section 7.3.4) was carried out to arrive at a robust calculation of shape κ and scale λ parameter (see Section 7.3.5).

7.3.1 Choice of statistical distribution function

Previously the applicability of several statistical extreme value distributions for the statistical analysis of maximum overtopping bore-induced loads on vertical walls was investigated by Chen et al. (2016), leading to the best-fit for a Generalized Pareto distribution. Nevertheless, the mean RMSE was in a similar range for a Weibull distribution in their studies. The good performance of a Weibull distribution for the statistical study of overtopping bore-induced loads on vertical walls was confirmed in another study (Van Doorslaer et al., 2017). Both, Weibull and Generalized Pareto distribution were considered extreme value distributions. The Weibull distribution is based on two parameters while the Generalized Pareto distribution is based on three, adding more complexity for similar accuracy in the outcome (Chen et al., 2016). Hence, the Weibull distribution was chosen for this study. The exceedance probability P_m [%] of the non-dimensional overtopping bore-induced force F^* [-] for a Weibull distribution was given in Equation 7.1 with the shape κ and scale λ parameter,

$$P_m = exp(-[\frac{F^*}{\lambda}]^{\kappa}). \tag{7.1}$$

The non-dimensional overtopped bore impact force F^* [-] as defined in Equation 7.4 was used. The linearised Weibull distribution (see Equation 7.2) was used for the fitting of shape κ and scale λ parameter to the force peaks of the samples S_1-S_5 (see Section 7.3.5),

$$log(\lambda) + \frac{1}{\kappa} \cdot log(-ln(P_m)) = log(F^*). \tag{7.2}$$

For plotting positioning of the data points Equation 7.3 was used for the exceedance probability P_m. Where m was the considered force peak and N_I the total number of force peaks per sample ranked from high to low,

$$P_m = \frac{m}{N_I + 1}. \tag{7.3}$$

7.3.2 Generation of data-samples for statistical analysis

For statistical analysis homogeneity of the processes in the data-sets 'UGent1'-'UGent3' and 'DeltaFlume' was required. The homogeneity for the data-sets was demonstrated (see Section 3 and Figure 3.21) with the average overtopping discharge q being comparable and in the same predicted range for all data-sets ('UGent1'-'UGent3' and 'DeltaFlume'). Furthermore, the recorded force peaks followed a similar distribution for all model tests (see Section 3 and Figure 3.27). It is therefore assumed that the physical processes between model tests 'UGent1'-'UGent3' and 'DeltaFlume' were sufficiently homogeneous. It could be argued that the impact type quasi-static, dynamic or impulsive (see Section 5) was non-homogeneous. Hence, it was first attempted in this study to select only force peaks

from quasi-static impact types. No significant statistical difference to a case where also the dynamic and impulsive impact types were included was found. Hence, it was decided to include force peaks from all impact types for statistical analysis. Additionally, the force peaks from repetition tests and parallel measurement of two load cells as well as integrated pressures were included. This automatically improves the second key criteria for a robust statistical analysis; a sufficient number of data points available for the fitting of the extreme value distribution. The data points were comprised from bore-induced force peaks recorded in the data-sets ('UGent1'-'UGent3' and 'DeltaFlume'). For a detailed description on how the force peaks for each data-set were detected it is referred to section 3. In total 145 tests with different geometrical and hydraulic parameters were selected (see Table 7.1). 139 of the 145 selected tests had a duration of approximately 1,000 offshore waves. Only 6 (testID: 493 494 495 504 424 425) of the selected 145 tests had a duration of approximately 3,000 offshore waves. For each test the non-dimensional average overtopping discharge q^* [-] and the non-dimensional maximum Force F^*_{max} [-] were calculated based on Equation 7.4 and Equation 7.5 respectively,

$$F^*_{max} = \frac{F_{max}}{\rho \cdot g \cdot A_c \cdot H_{m0,t}}, \tag{7.4}$$

$$q^* = \frac{q}{\sqrt{g \cdot h_t \cdot L_t \cdot G_c}}. \tag{7.5}$$

Where, F_{max} [N/m] was the measured maximum force per test, q [$m^3/s \cdot m$] the average overtopping discharge, ρ the salt water density with 1029 kg/m^3, g the gravitational acceleration with 9.81 m/s^2, A_c [m] the crest freeboard, $H_{m0,t}$ [m] the incident spectral wave height at the dike toe, $T_{m-1,0,t}$ [s] the spectral wave period at the dike toe, h_t [m] the water depth dike toe and the promenade width G_c [m]. The shallow water wave length was calculated with Equation 2.3.

The non-dimensional average overtopping discharge q^* [-] was then plotted against the non-dimensional maximum Force F^*_{max} [-] in Figure 7.3 for the individual tests of each data-set ('UGent1'-'UGent3' and 'DeltaFlume').

A linear best-fit line was derived, using linear least square fitting method, for the non-dimensional average overtopping discharge q^* against the non-dimensional maximum force F^*_{max} (see Equation 7.6). The according coefficient of determination was R^2=0.79,

$$F^*_{max} = 3827.4 \cdot q^*. \tag{7.6}$$

It was noted that for tests, especially for low non-dimensional maximum impact forces F^*_{max} and average overtopping discharges q^* the number of selected force peaks was low as well. For example in a test with hydrodynamic conditions similar to a storm with an annual recurrence interval of 1,000 years at the Belgian coast (testID 430-439 and testID 500), there were only $\sim$80 force peaks available. Any analysis on the extreme force peaks, for example the upper 10% would result in

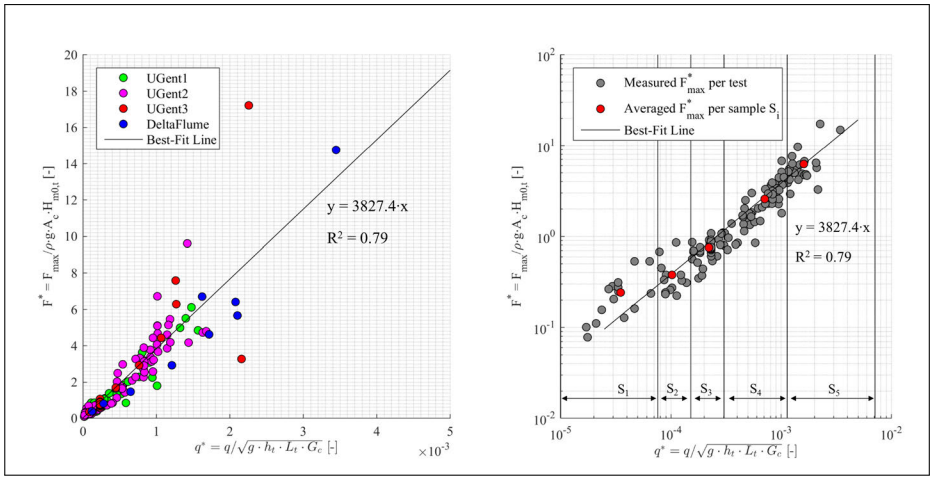

Figure 7.3: The non-dimensional average overtopping discharge q^* plotted against the non-dimensional maximum impact force F^*_{max} for each test of the data-sets 'UGent1'-'UGent3' and 'DeltaFlume' (left figure). The same data points on a logarithmic scale (right figure) introducing the boundaries (vertical black lines) for sample S_1-S_5. The red circle indicates the average value per sample S_1-S_5.

8 force peaks for statistical analysis. A statistical analysis on 8 force peaks does not seem to be very reliable. A storm with an annual recurrence interval of 1,000 years is already a severe event and should be reliably accounted for by any prediction tool. Hence, it was decided to group several tests into samples based on the non-dimensional average overtopping discharge q^* [-]. Five samples S_1-S_5 were generated. The boundaries for the five samples were derived based on suggested average overtopping limits for vehicles and people on the promenade or yachts behind the coastal defense structure (Eurotop, 2016). In Eurotop (2016) five average overtopping regimes (q=0 − 5 l/s per m, q=5 − 10 l/s per m, q=10 − 20 l/s per m, q=20 − 75 l/s per m, q> 75 l/s per m in prototype) were distinguished with according damage criteria (see Table 7.1). The other parameters were kept constant: G_c=10 m, A_c=2.5 m, h_t=0.5 m, $T_{m-1,0,t}$=20 s, $H_{m0,t}$=1.5 m in prototype. The geometrical parameters are one example for a Belgian coastal cross section and hydraulic conditions in the range of a storm with an annual recurrence interval of 1,000 years. The non-dimensional overtopping discharge q^* was used to determine the sample boundaries (see Figure 7.3, right). The x-axis is plotted in logarithmic scale to better show the region of lower non-dimensional overtopping discharges q^* for the samples. All tests and according force peaks were gathered into the samples S_1-S_5 based on the non-dimensional overtopping discharge q^* (see Table 7.1). In total 145 individual tests were used in this study, resulting in 36,756 force peaks for statistical analysis.

For the low non-dimensional overtopping discharges (sample S_1 and S_2) the number of force peaks was still rather low (93 and 314 respectively). This was simply because of the fact that lower non-dimensional average overtopping dis-

Table 7.1: Characteristics of sample S_1-S_5 based on the impacts from the data-sets 'UGent1'-'UGent3' and 'DeltaFlume'. The sample boundaries where determined based on damage criteria related to an average overtopping discharge q (Eurotop, 2016)

Data sample	Average overtopping q [l/s per m]	q^* [-] (Eq. 7.5)	Total nr. of tests [-]	Total nr. of impacts [-]	Eurotop (2016)
S_0	0-443	0 - $7.1210 \cdot 10^{-3}$	145	37090	-
S_1	0-5	0 - $7.5851 \cdot 10^{-5}$	15	93	safe for cars (H_{m0} <3m), people (H_{m0} <1) and larger yachts (H_{m0} >1)
S_2	5-10	$7.5851 \cdot 10^{-5}$ - $1.5170 \cdot 10^{-4}$	13	304	safe for cars (H_{m0} <2), people (H_{m0} <1), sinking small boats (G_c=5-10m), damage large yachts (H_{m0}=3-5)
S_3	10-20	$1.5170 \cdot 10^{-4}$ - $3.0340 \cdot 10^{-4}$	38	2,327	safe for cars (H_{m0}==2), people (H_{m0}=<1), significant damage or sinking larger yachts (H_{m0}=>5)
S_4	20-75	$3.0340 \cdot 10^{-4}$ - $1.1377 \cdot 10^{-3}$	56	11,190	safe for cars (H_{m0} <1, h <0.3m), not safe for people, significant damage or sinking larger yachts (H_{m0}=3-5)
S_5	>75	$1.1377 \cdot 10^{-3}$ - $7.1210 \cdot 10^{-3}$	23	23,176	not safe for cars, people and yachts

charges also led to fewer overtopping volumes and consequently less bore-induced impacts measured at the wall. In the following Section 7.3.3 it was investigated whether the number of force peaks per sample was sufficient for statistical analysis. The underlying assumption, when using the average overtopping to determine the sample boundaries, was that increased average overtopping discharge q resulted in larger individual overtopping volumes (Eurotop, 2016) and finally lead to larger forces measured on the wall. At the same time (Eurotop, 2016) states that a similar average overtopping discharge q can be caused by small waves and low-crested freeboards (many small individual overtopping volumes) or by large waves together with larger freeboards (few large individual overtopping volumes). Depending which scenario was tested this would also effect the loading of the wall. Despite this controversy, it was only considered significant if the statistical analysis for two tests in the same range of average overtopping q would have shown inconsistencies. Another supporting argument to use the average overtopping discharge q over the maximum individual overtopping volumes V_{max} was of practical nature; unlike for the maximum individual volumes, the average overtoppind discharge has been extensively investigated and there are existing empirical (Altomare et al., 2016; Van Gent, 1999b) and numerical (Suzuki et al., 2017) approaches to calculate the average overtopping discharge q in mildly sloping foreshores and shallow water conditions.

7.3.3 Sensitivity of sample size for statistical analysis

The sample size, number of force peaks used for fitting, determines the Weibull parameter estimation accuracy. To study the sensitivity of the sample size a bootstrap-kind approach was used (James et al., 2013). The samples S_1-S_5 were used for this sensitivity analysis. For each sample a sub-sample with n randomly selected force peaks was created. For this sub-sample the Weibull distribution parameters (κ and λ) were estimated using Equation 7.2 and an upper 15% fitting threshold (see Section 7.3.4). This was repeated 1,000 times for each sample size n and the mean parameter and standard deviation calculated (Equation 4.1 and Equation 4.2 respectively). Where, n is the sub-sample size, A the investigated parameter (κ and λ) and σ the standard deviation. Then the sub-sample size n was varied ranging from 10-200 samples and the same process was repeated. One subsequently studies the sample size effect on the parameters (κ and λ) together with its standard deviation. For a visual comparison the evolution of the parameter (κ and λ) as a function of the sample size n, together with the 95% confidence interval (CI) as 1.96 times the standard error was computed. The result for sample S_4 was displayed (see Figure 7.4).

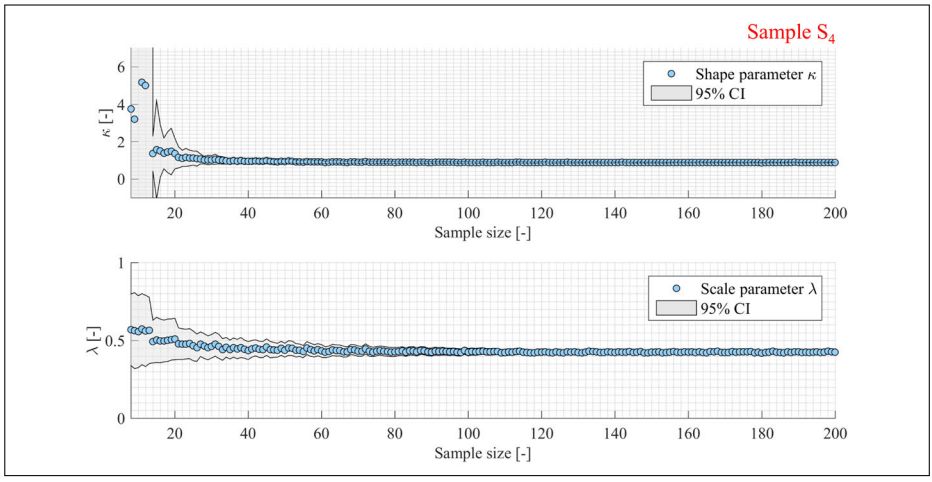

Figure 7.4: Sensitivity of shape κ and scale λ parameter in dependence of sample size n. Data sample S_4 was chosen for investigation (Table 7.1). The shape κ and scale λ parameter were plotted together with the 95% confidence interval.

While the shape parameter κ converged fast towards a constant value already for a sample size of 40, the scale parameter λ required a larger sample size to converge to a rather constant value. A sample size of 100 was indicated as a safe sample size but already for a sample size 50–100 the scale parameter was considered a rather constant value. The findings for S_4 can be applied to the sub-samples S_1, S_2, S_3 and S_5 as well (see ANNEX D).

7.3.4 Sensitivity of the fitting threshold for statistical analysis

In previous studies the upper 20% (Van Doorslaer et al., 2017) and the upper 10% (Chen et al., 2016) of force peaks were defined as fitting thresholds for an extreme value distribution. This upper fitting thresholds were based on the findings from statistical analysis of individual overtopping volumes, where a 10% upper threshold (Hughes et al., 2012) or all values above the mean value (Victor et al., 2012) were used. Especially the 10% upper fitting threshold yield in a better representation of the extreme tail of the overtopping volume distribution, while sacrificing accuracy in the lower volume range of the distribution. It was recommended to further elaborate on the upper fitting threshold in the case of extreme force peak samples (Chen et al., 2016). For this purpose the data sample S_4 (see Table 7.1) was used and change in shape κ and scale λ parameter depending on the fitting threshold investigated (see Figure 7.5). The goodness-of-fit was evaluated using the coefficient of determination R_2 and standard deviation σ of the residuals as given in Equation 6.7 and Equation 4.2 respectively.

For the sensitivity study the fitting threshold was varied between 7% to 100%. This means that 7% to 100% of the non-dimensional force peaks from the sample were used for fitting the statistical distribution. The goodness-of-fit parameters R^2 and standard deviation σ of the residuals were evaluated together with the shape κ and scale λ parameter of the Weibull distribution (see Figure 7.5).

The shape parameter κ was rather stable and showed only slight increase with increasing fitting threshold. The scale parameter λ increased linearly with increasing fitting threshold 10%. This was partly expected, as the scale parameter λ was expected to change when an increasing number of smaller non-dimensional force peaks were included in the fitting. Hence, an engineering choice for a fitting threshold taking into account a sufficient number of extreme events, while minimizing the standard deviation σ and maximizing the coefficient of determination R^2 for the fitted curve, had to be made. Ideally the threshold was chosen as high as possible to fit to the extreme non-dimensional force peaks but as low as necessary to have enough events for the fitting (see Section 7.3.3). Together with the information of the goodness-of-fit parameters, a fitting threshold for further analysis at 15% was finally chosen. This means only the upper 15% of the ranked non-dimensional force peaks per sample were chosen for the fitting of the Weibull distribution to the force peaks in Section 7.3.5. For sample S_1 this resulted in only 10 force peaks for further analysis (see Table 7.2). Nevertheless, it was decided to not further increase the fitting threshold in order to focus the analysis on the extreme non-dimensional force peaks.

7.3.5 Statistical fitting of Weibull distribution to the samples

The linearized Weibull distribution (see Equation 7.2) was fitted to the upper 15% of non-dimensional force peaks for the samples S_1–S_5. Least squares method was used for the fitting and shape κ and scale λ parameter derived for each sample. With shape κ and scale λ parameter parameter the best-fit line for the upper 15% non-dimensional force peaks was derived and plotted together with all non-

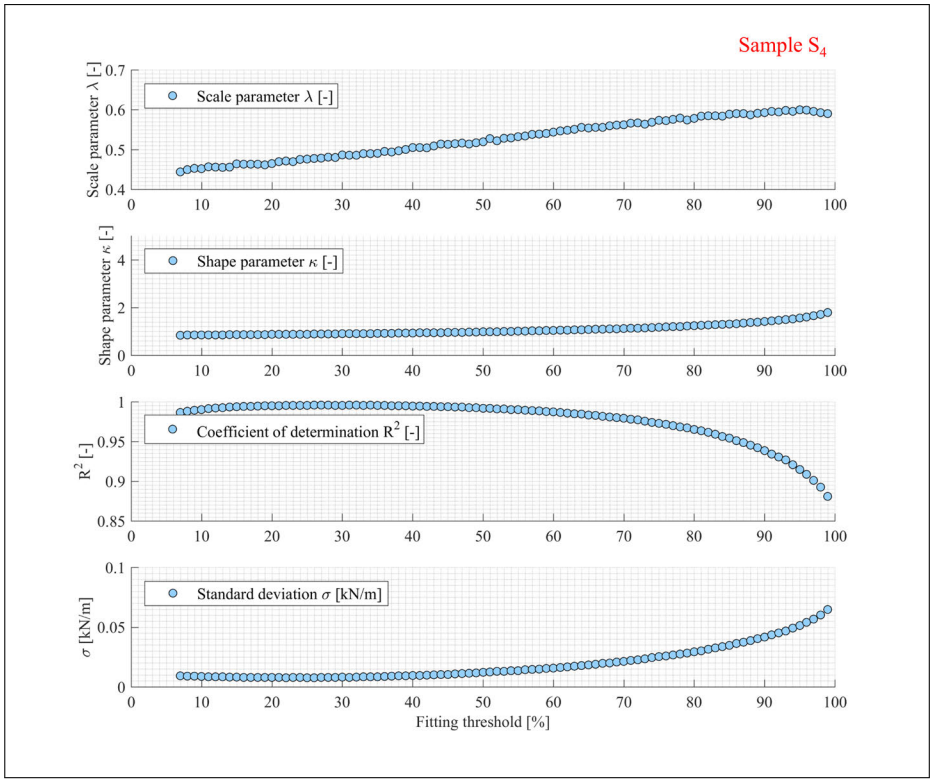

Figure 7.5: Calculated κ and scale λ parameter for S_4 in dependence of the high-pass threshold. The coefficient of determination R^2 and standard deviation σ are calculated accordingly.

dimensional force peaks (blue) and the upper 15% of non-dimensional force peaks (red) in Figure 7.6.

Visually, it was concluded that the linearized best-fit line (see Figure 7.6, graphics on the right hand sided) fits well the upper 15% of non-dimensional force peaks and that the shape of the distributions was similar for the samples S_1-S_5. To make the result of the statistical analysis more comparable between the samples S_1-S_5, it was decided to select randomly 13 tests per sample and perform the fitting on the according non-dimensional force peaks. As one test usually consisted of ∼1,000 offshore waves (only in few cases ∼3,000 offshore waves were tested), in total ∼13,000 offshore waves were considered per sub-sample. Shape κ and scale λ parameter were then determined for the 13,000-offshore-wave-sub-sample. This procedure was repeated 1,000 times, each time selecting randomly 13 tests per sample, and the shape κ and scale λ parameter derived. The averaged sub-sample size, shape κ and scale λ parameter together with their standard deviation were calculated for each sample S_1-S_5 (see Table 7.2) Only for sample S_1 and S_2 the average number of non-dimensional force peaks used for the fitting was

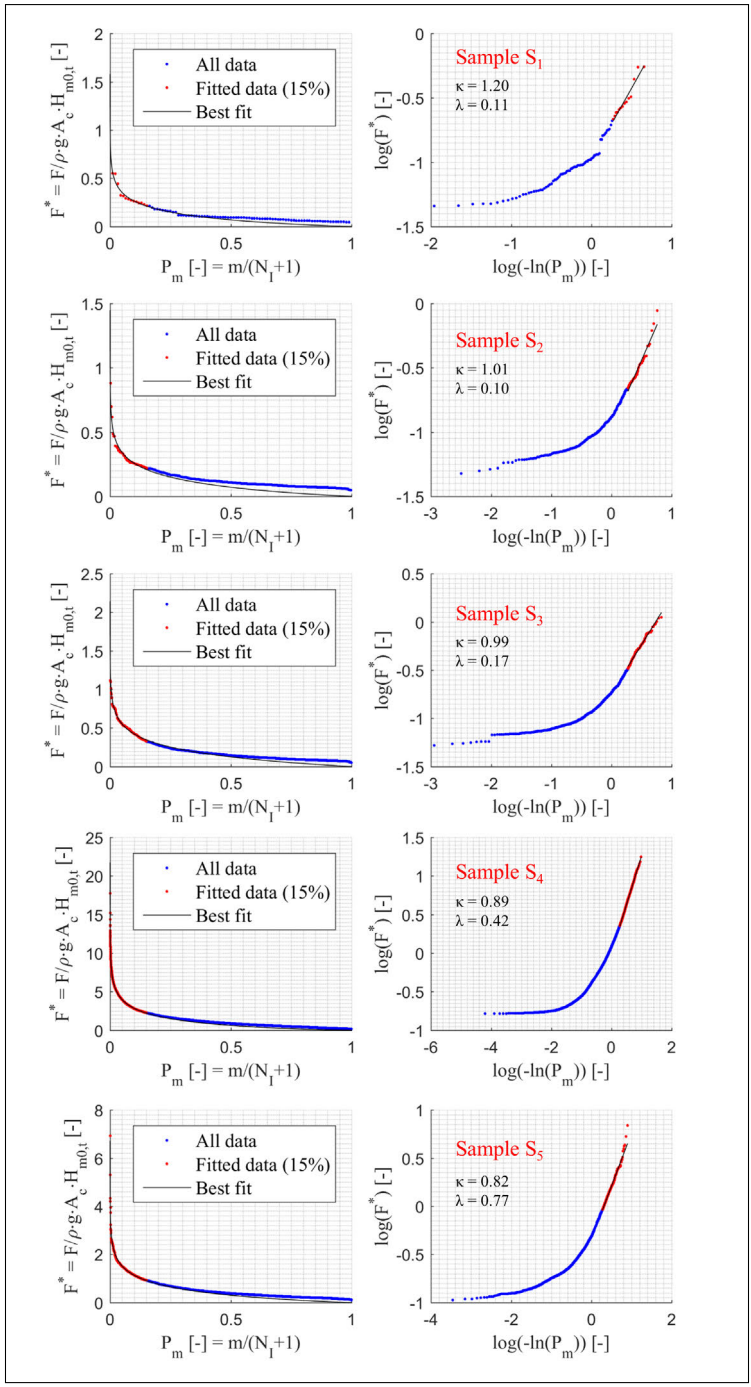

Figure 7.6: Plotting positioning of the impacts and best-fit line (left figure). Fitting of the linearised Weibull extreme value distribution to the upper 15% of impacts (red dots) and derived shape κ and scale λ parameter for sample S_1-S_5 (right figure).

below the critical number of 50 non-dimensional force peaks (see Section 7.3.3). Despite this, the κ and scale λ parameter derived were following the trend of the other samples (except from S_2 showing slightly lower values) and it was carefully concluded that the result for S_1 and S_2 was reliable as well. As a next step, the average shape κ and scale λ parameter for sample S_1-S_5 were plotted against the mean non-dimensional average overtopping discharge (q^*) for each sample S_1-S_5 (see Figure 7.7).

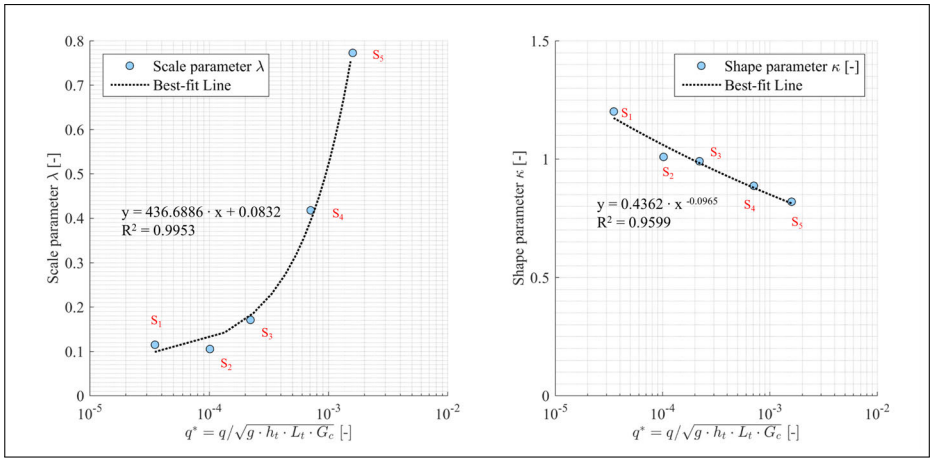

Figure 7.7: Scale λ (left figure) and shape κ (right figure) parameter for sample S_1-S_5 were plotted over the non-dimensional average overtopping discharge q^*, together with the best-fit lines.

It was noted that the scale λ parameter showed a linear trend and the shape κ parameter an exponential decay trend over the non-dimensional average overtopping discharge q^* (note that the x-axis in Figure 7.7 was plotted in logarithmic scale for better visualization of the lower q^*). Hence, a linear best-fit and exponential best-fit line were derived for shape κ and scale λ parameter respectively (see Equation 7.8 and Equation 7.7),

$$\lambda = 436.69 \cdot q^* + 0.0832, \tag{7.7}$$

$$\kappa = 0.4362 \cdot q^{*(-0.0965)}. \tag{7.8}$$

The fitting was done using linear least squares method. The standard deviation of the best-fit lines was larger for the shape parameter and the samples S_1 and S_2 (see Table 7.2). This was explained by the average number of non-dimensional force peaks used for the fitting, which was below the critical number of 50 for S_1 and S_2. However, even shape κ and scale λ for sample S_1 and S_2 followed closely the best-fit line.

Table 7.2: Fitting parameters for sample S_1-S_5

Data sample	Average overtopping q [l/s per m]	Nr. of waves [-]	Nr. of force peaks F^* [-]	Shape (κ) parameter [-]	σ Eq. 4.2	Scale (λ) parameter [-]	σ Eq. 4.2
S_1	0-5	∼13,000	∼10	1.2008	0.8494	0.1147	0.0394
S_2	5-10	∼13,000	∼35	1.0089	0.2914	0.1048	0.0212
S_3	10-20	∼13,000	∼92	0.9898	0.0609	0.1709	0.0178
S_4	20-75	∼13,000	∼302	0.8863	0.0529	0.4173	0.0649
S_5	>75	∼13,000	∼1,481	0.8182	0.0707	0.7725	0.2435

7.4 Results and discussion

The results of the empirical study to predict the maximum expected impact force F_{max} and the statistical study to predict the force F_m related to an exceedance probability P_m will be presented and discussed in Section 7.4.1. The novel methodology to combine the findings from empirical and statistical analysis is given in this Section and an example calculation executed in Section 7.4.2.

7.4.1 Prediction method for maximum overtopped bore loads

In Section 7.3.5 the shape κ and scale λ parameter for a Weibull distribution were derived as a function of the mean non-dimensional average overtopping discharge q^* for each sample S_1-S_5. This resulted in Equation 7.8 for the shape κ and Equation 7.7 for the scale λ parameter. Substituting them into Equation 7.2 the non-dimensional force F^* can be calculated as a function of the return period P_m. For varying return periods P_m this exercise was repeated and displayed as the curved lines in Figure 7.8. The bold curved lines represent the area where data was available to derive the best-fit line for shape κ and scale λ parameter and the thinner outer part of the curved line were the extrapolated areas. The red dots in Figure 7.8 represent the mean value of the individual tests in each sample S_1-S_5. The boundaries of the samples S_1-S_5 were indicated with black vertical lines in Figure 7.8.

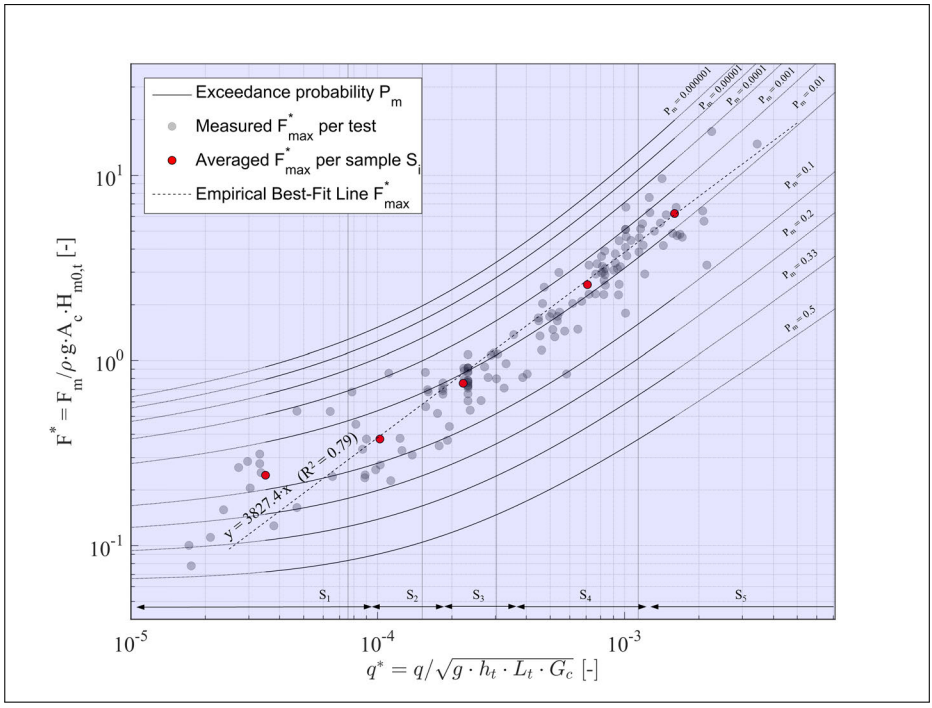

Figure 7.8: Prediction chart with combined empirical (F_{max}) and statistical (F_m with according P_m) result.

Following, the non-dimensional average overtopping discharge q^* was plotted against the non-dimensional force F^* in for each test in this study (grey circles in Figure 7.8). Furthermore, the previously established empirical relation between non-dimensional average overtopping discharge q^* and the maximum non-dimensional force F^*_{max} was introduced as a dotted black line in Figure 7.8). This was possible as the same parameters on x-axis (non-dimensional average overtopping discharge q^*) and y-axis (non-dimensional force F^*) were used for both, the statistical and empirical analysis. As a result, one achieved an overlay of statistical (curved lines with exceedance probabilities P_m) and empirical (dotted line for F^*_{max}) prediction tools. To further elaborate on the use of such overlay a prediction methodology was developed in 6 steps, to showcase the benefits of a combined statistical and empirical prediction of maximum overtopped bore loads on dike mounted vertical walls (see Figure 7.9).

The input parameters for the calculation were the average overtopping discharge q [m^3/s per m], the crest freeboard A_c [m], the promenade width G_c [m], the water depth at the dike toe h_t [m], the incident spectral wave height $H_{m0,t}$ [m] and period $T_{m-1,0,t}$ [s] at the dike toe location. Note, that the incident spectral wave conditions were derived for a situation without the dike present, to avoid influence from reflected waves and focus the analysis on purely incident waves.

1. Based on the input parameters the shallow water wave length L_t was calcu-

lated with Equation 2.3, as well as the non-dimensional average overtopping discharge q^* with Equation 7.5.

2. The empirical relation in Equation 7.6 (see Section 7.3.2) was used to derive the non-dimensional maximum expected impact force F^*_{max}. Alternatively, Figure 7.8 can also be used to derive the non-dimensional maximum expected impact force F^*_{max} in this step. With F^*_{max}, the dimensional maximum expected impact force F_{max} can be calculated with Equation 7.4.

3. Shape κ and scale λ parameter were computed by making use of Equation 7.8 and Equation 7.7. Alternatively, shape κ and scale λ can also be read from Figure 7.8.

4. Equation 7.1 can be used together with the maximum expected impact force F_{max} from step 2) to calculate the exceedance probability P_m. Note, that the exceedance probability P_m was derived for the number of impacts in a storm with 13,000 offshore waves. Alternatively, Figure 7.8 can be used for a visual interpretation in this step, with the non-dimensional average overtopping discharge q^* [x-axis] and non-dimensional maximum expected impact force F^* (y-axis) as input parameters. If the obtained exceedance probability P_m is considered too high/low or the storm duration of 13,000 offshore waves is considered too long, an engineering choice can be made to derive a new exceedance probability P_{m-new} as outlined in Section 7.4.2.

5. The force F_m related to the adapted exceedance probability P_{m-new} can now be calculated by solving Equation 7.1 for the impact force F_m and substituting Equation 7.8 and Equation 7.7 for the shape κ and scale λ parameter. Finally, one may consider ∼20% variability in impact force due to stochastic non-repeatability, scale- and model effects (see Section 4).

The output is a design force F_D in Newton per meter, together with an exceedance probability P_m. The exceedance probability P_m can be interpreted as the probability that the design force F_D will be exceeded for a storm with 13,000 offshore waves and for a geometry (A_c, G_c) and storm conditions (h_t, $H_{m0,t}$, $T_{m-1,0,t}$, q) specified in the input parameters.

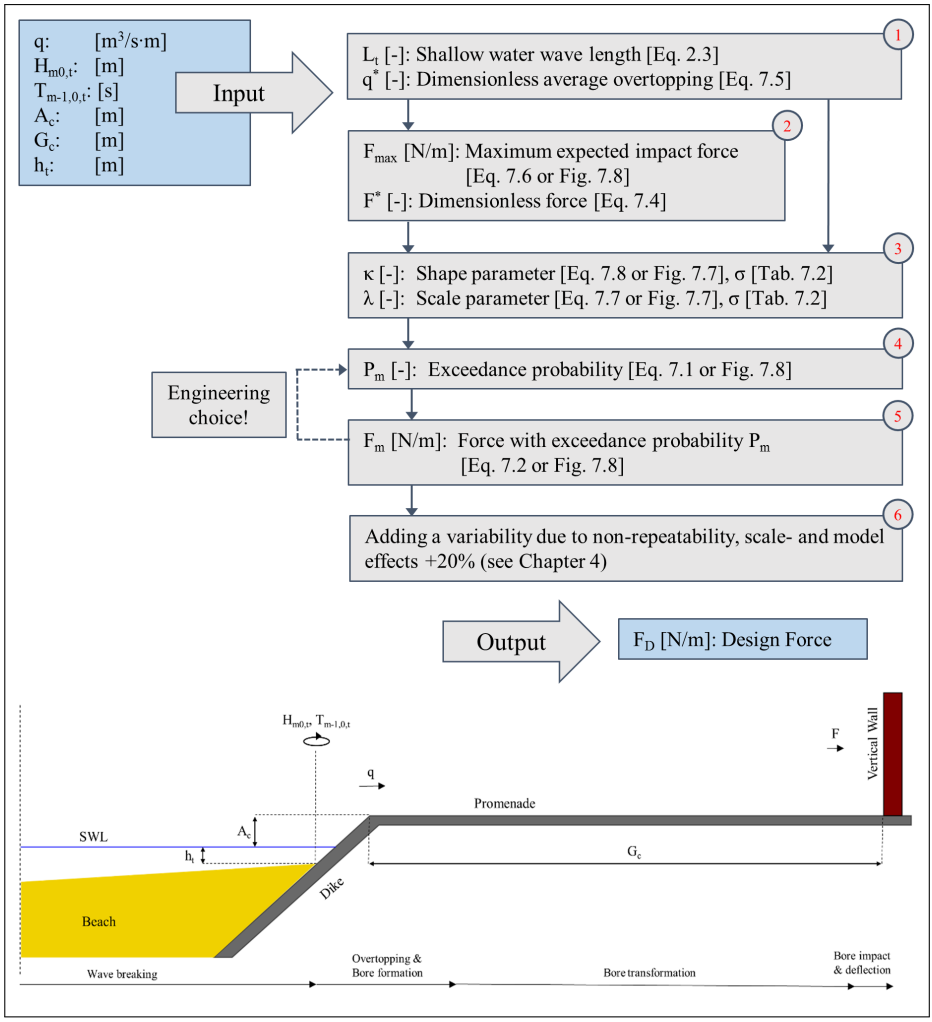

Figure 7.9: Six-step prediction methodology for overtopped bore-induced impacts on dike mounted walls.

7.4.2 Example calculation for prediction methodology

To provide an example of the described combined empirical and statistical prediction methodology (see previous Section 7.4) a test from a similar test campaign was selected (Chen et al., 2016). As shown in Figure 7.1 the range of test parameters in the study from Chen et al. (2016) overlaps with the range of test parameters in this study. A single test was chosen to showcase the new prediction methodology (see Table 7.3).

The selected test featured a 1-tot-35 foreshore slope, a 1-to-3 dike slope, comparable to a typography for countries with low lying coastlines. Values are given

Table 7.3: Input parameters for the example calculation. Values were given in prototype.

q	A_c	G_c	h_t	$H_{m0,t}$	$T_{m-1,0,t}$	ρ	g
[m³/s · m]	**[m]**	**[m]**	**[m]**	**[m]**	**[s]**	**[kg/m³]**	**[m/s²]**
0.12204	1.3	12.5	1.275	0.725	55.9	1029	9.81

in prototype using Froude similarity and a length-scale factor 1-to-25. In case the average overtopping discharge or incident spectral wave parameters at the dike toe were not measured, existing prediction tools can be used. It was previously shown that the average overtopping discharge q in shallow water and mild foreshore conditions can be empirically (Altomare et al., 2016) and numerically with SWASH (Suzuki et al., 2017) derived. The incident spectral wave period at the dike toe was empirically derived by Hofland et al. (2017). For a more detailed analysis SWASH has also proven to be capable to reproduce the spectral wave parameters for the dike toe location including directional spreading (Suzuki et al., 2015). The six-step prediction methodology described in Section 7.4.2 was followed to derive the maximum F_{max} and design F_D impact force for an exceedance probability P_m:

1. The shallow water wave length L_t (see Equation 2.3) and non-dimensional average overtopping discharge q^* (see Equation 7.5) are calculated,

$$L_t = T_{m-1,0,t} \cdot \sqrt{g \cdot (h_t \cdot H_{m0,t})} = 55.9 \cdot \sqrt{9.81 \cdot (1.275 + 0.725} = 247.61 [m],$$

$$q^* = \frac{q}{\sqrt{g \cdot h_t \cdot L_t \cdot G_c}} = \frac{0.12204}{\sqrt{9.81 \cdot 1.275 \cdot 247.61 \cdot 12.5}} = 6.2026 \cdot 10^{-4} [-].$$

2. The maximum expected impact force F_{max} (see Equation 7.6) will be calculated in the next step,

$$F^*_{max} = 3827.4 \cdot q^*.$$

Substituting Equation 7.4 and Equation 7.5 into Equation 7.6 the following expression is derived and solved for F_{max},

$$\frac{F_{max}}{\rho \cdot g \cdot A_c \cdot H_{m0,t}} = 3827.4 \cdot \frac{q}{\sqrt{g \cdot h_t \cdot L_t \cdot G_c}},$$

$$F_{max} = 1029 \cdot 9.81 \cdot 1.3 \cdot 0.725 \cdot 3827.4 \cdot \frac{0.12204}{\sqrt{9.81 \cdot 1.275 \cdot 247.61 \cdot 12.5}},$$

$$F_{max} = 22586.20\ [N/m].$$

Having calculated F_{max}, the non-dimensional maximum expected impact force F^*_{max} can be computed with Equation 7.4,

$$F^*_{max} = \frac{F_{max}}{\rho \cdot g \cdot A_c \cdot H_{m0,t}} = \frac{22586.20}{1029 \cdot 9.81 \cdot 1.3 \cdot 0.725} = 2.559\ [-].$$

The yellow star in Figure 7.10 shows the result of non-dimensional average overtopping discharge q^* plotted against the non-dimensional maximum expected impact force F^*_{max}.

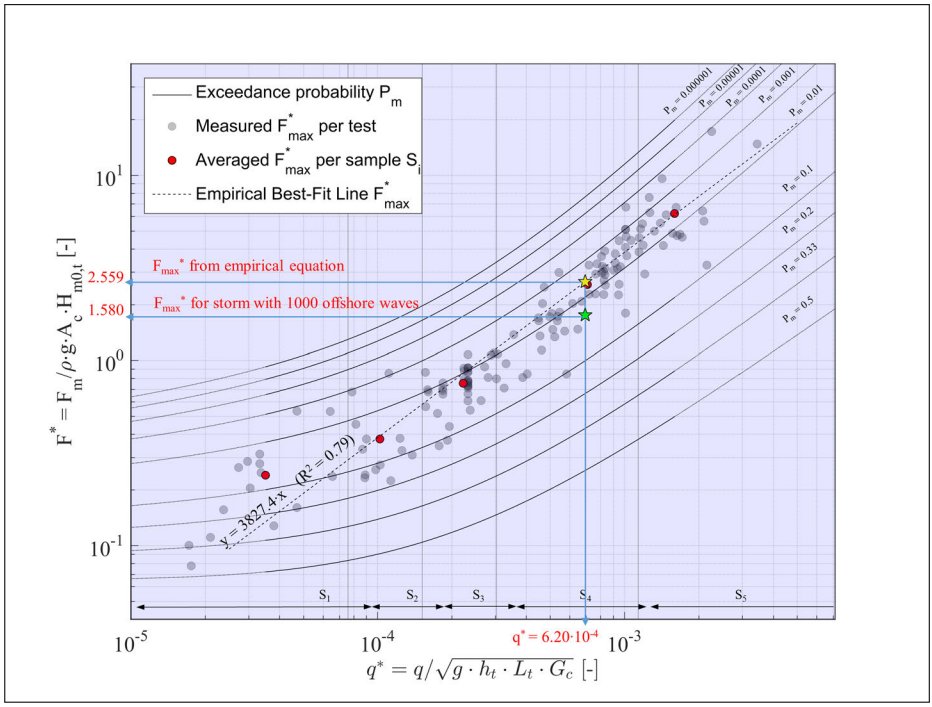

Figure 7.10: Example calculation using the prediction chart (see Figure 7.8) and prediction methodology (see Figure 7.9).

The non-dimensional average overtopping discharge q^* for this test is located in Sample S_4 in Figure 7.10. After Eurotop (2016) this is related to the overtopping damage criteria: 'safe for cars (H_{m0} <1 m, h <0.3 m), not safe for people and significant damage or sinking of larger yachts (H_{m0}=3 − 5 m)' (see Table 7.1).

3. Shape κ and scale λ parameter are computed using Equation 7.8 and Equation 7.7,

$$\lambda = 436.6886 \cdot q^* + 0.0832 = 436.6886 \cdot 6.2026 \cdot 10^{-4} + 0.0832 = 0.3276\ [-],$$

$$\kappa = 0.4362 \cdot q^{*(-0.0965)} = 0.4362 \cdot (6.2026 \cdot 10^{-4})^{(-0.0965)} = 0.8896\ [-].$$

4. The exceedance probability P_m is derived using Equation 7.1 and the calculated shape κ and scale λ parameter as well as the non-dimensional maximum expected impact force F^*_{max},

$$P_m = exp(-[\frac{F^*}{\lambda}]^{\kappa}) = exp(-[\frac{2.559}{0.3276}]^{0.8896}) = 0.0029998.$$

Alternatively this result can also be read from Figure 7.10, indicated with the yellow star.

5. In this step the 'engineering choice' was made to change the exceedance probability P_m to match a storm with 1,000 offshore waves. The exceedance probabilities in Figure 7.8 were derived for impacts resulting from a storm with ∼13,000 offshore waves. The number of impacts for sample S_4 and a storm with 13,000 offshore waves is N_I=358 (see Table 7.2). Note, that the value 302 are the 15% highest impacts used for the fitting. By multiplying 302 with a factor 1.85 (to arrive at 100% of the impacts again) and further multiplying by a factor 1,000/13,000=0.0769 (to reduce the 13,000 to 1,000 offshore waves), a new number of impacts is derived N_{I-new} for a similar storm with 1,000 offshore waves. The underlying assumption is here that the number of impacts reduces proportional to a reduction in the number of offshore waves. Based on N_{I-new} and setting i=1 (for the maximum impact) a new exceedance probability P_{m-new} is calculated, representing the exceedance probability for the maximum impact force during a storm with 1,000 offshore waves,

$$P_{m-new} = \frac{i}{N_I \cdot 1.85 \cdot 0.0769 + 1} = \frac{1}{302 \cdot 1.85 \cdot 0.0769 + 1} = 0.022745.$$

Hence the impact force F_m for the new exceedance probability P_{m-new} is calculated by solving Equation 7.1 for the impact force and substituting P_m with P_{m-new}. The previously computed shape κ and scale λ parameter are used (they are statistically robust),

$$\frac{F_m}{\rho \cdot g \cdot A_c \cdot H_{m0,t}} = 10^{(log(\lambda) + \frac{1}{\kappa} \cdot log(-ln(P_{m-new})))},$$

$$\frac{F_m}{\rho \cdot g \cdot A_c \cdot H_{m0,t}} = 10^{(log(0.3276)+\frac{1}{0.8896} \cdot log(-ln(0.022745)))} = 1.580,$$

$$F_m = 1029 \cdot 9.81 \cdot 1.3 \cdot 0.725 \cdot 10^{(log(0.3276)+\frac{1}{0.8896} \cdot log(-ln(0.022745)))},$$

$$F_m = 15034.56\ [N/m].$$

The newly computed force F_m was non-dimensionalized using Equation 7.4 and plotted together with the exceedance probability P_{m-new}=0.001 in Figure 7.10 as a green star.

6. In this step 20% of F_m were added to F_m in order to derive the design force, accounting for stochastic non-repeatability, scale- and model-effects,

$$F_D = F_m + F_m \cdot 0.2 = 15034.56 + 15034.56 \cdot 0.2,$$

$$F_D = 18041.47\ [N/m].$$

F_D is now the maximum design force for a storm with the duration of ∼1,000 offshore waves and including an uncertainty factor of 20% to account for stochastic effects.

7.5 Conclusions

In this Section a new statistical analysis methodology to predict maximum overtopping bore-induced loads on dike mounted vertical walls in shallow water and mild foreshore conditions was presented. Tests from several experimental data-sets ('UGent1'-'UGent3', 'DeltaFlume') were combined in samples, to overcome the issue of too little data points for robust statistical analysis. The subdivision into samples was done based on an empirical relation between non-dimensional average overtopping discharge q^* and non-dimensional maximum impact force F^*_{max} and the boundaries of the samples were set based on suggested values from Eurotop (2016). A sensitivity study on sample size and fitting threshold was conducted and the shape κ and scale λ parameter for the samples derived. The best-fit line for the distribution parameters was computed to enable a statistical prediction. Finally, the novel prediction methodology was presented in a 6-step approach to arrive at a design force F_D for a given overtopping condition, hydraulic and structural parameters. More detailed conclusions were:

- The range of application of the 'UGent1'-'UGent3', 'DeltaFlume' data-set was in the range of previously derived data-sets (Chen et al., 2016), with an extension towards larger relative promenade widths G_c/L_t=0.04-0.5 and extremely shallow waters $h_t/H_{m0,o}$ <0.3 (after Hofland et al. (2017)).

- A new empirical link between the non-dimensional maximum measured impact force F^*_{max} and the non-dimensional average overtopping discharge q^* for the tests from 'UGent1'-'UGent3', 'DeltaFlume' was established, to predict the maximum impact force F_{max}.

- Five data samples S_1-S_5 were generated for robust statistical analysis from the force peaks of the data-sets 'UGent1'-'UGent3'and 'DeltaFlume'. The sample boundaries were set based on the non-dimensional average overtopping discharge q^* and suggested values from Eurotop (2016).

- A sensitivity study revealed that approximately 50 force peaks were required for robust fitting of the statistical distribution to the force peaks. Furthermore, a sensitivity study of the upper fitting threshold was conducted and an upper 15% fitting threshold selected. Only force peaks above this threshold were further used for the fitting of a Weibull distribution to the data.

- Statistical distribution parameters, shape κ and scale λ parameter, were derived for a Weibull distribution and for each sample S_1-S_5. The best-fit line for shape κ and scale λ parameter over the non-dimensional average overtopping discharge q^* for the five samples was calculated and showed a very stable behaviour (R^2=0.9873 for shape κ and R^2=0.9925 for scale λ parameter).

- Finally, a novel prediction methodology was developed, combining the empirical and statistical prediction presented in this section. A maximum expected impact force F_m can be calculated together with its exceedance probability P_m. The exceedance probability P_m can be interpreted as the probability that F_m will be exceeded for a storm with 13,000 offshore waves and hydraulic boundary conditions (h_t, $H_{m0,t}$, $T_{m-1,0,t}$, q) specified together with the structural information (A_c, G_c) in the input parameters.

- A new 6-step approach was presented to arrive at the design force F_D including the possibility to adjust the exceedance probability (engineering choice) by changing the number of considered offshore waves for the prediction.

An example calculation was performed to showcase the newly derived prediction methodology for a test from the Chen et al. (2016) data-set. This served as a first indication that the presented prediction methodology was not out of range. Despite this first confirmation, further validation of the prediction methodology is required, ideally from prototype measurements. Furthermore, the practicability can be improved by further investigating the relation between exceedance probability P_m and storm duration.

Chapter 8

Summary of key findings and recommendations for future research

A good conclusion should unveil the obvious, go back to why the study was conducted in the first place and zoom out in the end, leading towards recommendations for future research. This was attempted in this Chapter by summarising the main research findings in Section 8.1 and discussing the challenges for future studies in Section 8.2.

8.1 Summary of key findings

The coastal structures of low-lying countries such as Belgium, the Netherlands or Germany are often comprised of a mildly sloping sand foreshore and shallow waters in front of a dike. Often the dike is followed by a promenade. On top of the promenade a storm wall or buildings are constructed. Storm walls situated on top of dikes are a short-term measure to cope with rising sea levels or extreme storm events. These storm walls are commonly designed and assessed based on a reduction in overtopping to prevent flooding, not taking into account the hydrodynamic loads induced by overtopped bore attack. Hence, the overtopping bore-induced loads need to be predicted to enable a reliable structural design of these storm walls, or any buildings situated on top of the dike.

In this study overtopping bore-induced loads on dike mounted vertical walls, in shallow water and in mild foreshore conditions, were investigated from laboratory scale-model tests. The overtopping bores, resulting from breaking waves in an irregular wave field, were of short duration and showed interactions with previous overtopped bores. This yielded in complex and turbulent behaviour of the water masses prior to impact. For an accurate prediction of the impact loads it was considered a key research challenge to investigate and distinguish the different physical processes during bore overtopping, bore formation and transformation,

until final bore impact with the wall.

To summarize, a detailed physical process description of bore-induced loading of dike mounted vertical walls was given. Five bore interaction patterns were identified from laser profiler measurements. A new classification method developed to distinguish impulsiv, dynamic and quasi-static impact types was developed. The majority ($\sim$3/4) and the largest impact force were considered a quasi-static impact type. Two new empirical formulas were derived to predict the dynamic first peak F_1 and the quasi-static second peak F_2 from the double peak impact force signal shape. Furthermore, a theoretical approach to describe the double peak impact force signal shape, involving the vertical accelerations of the bore in front of the wall, was presented. Both, the empirical formulas and analytical description showed high variability in the prediction. To account for the scattered force prediction a novel statistical impact force prediction methodology was developed for F_{max} and linked to the average overtopping discharge q. Finally, a reassessment of scale-effects in laboratory small-scale impact force measurements was done, as they were in the range of non-repeatability related uncertainties. More detailed conclusions were:

- Prior to bore impact on the wall five bore interaction patterns were identified: (1) regular bore pattern, (2) collision bore pattern, (3) plunging breaking bore pattern, (4) sequential overtopping bore pattern and (5) catch-up bore pattern. Collision bore pattern was the most frequent (46% of all interaction patterns were identified as collision bore pattern) and resulted in quasi-static impacts type in a majority of cases (see Chapter 5).

- A double peak impact force signal shape was observed, with similar magnitudes for the two peaks F_1 and F_2. A new classification methodology was developed and three bore impact types were distinguished: (1) impulsive impact type, (2) dynamic impact type, (3) quasi- static impact type. The majority of impacts ($\sim$2/3 of all impacts) and the largest impact force was considered quasi-static impact type (see Chapter 5).

- From a detailed process study in terms of impact pressures, forces and camera images it was concluded that the first dynamic force peak F_1 was related to the momentum of the incoming bore thickness and velocity, while the second quasi-static force peak F_2 was related to the bore thickness in front of the wall after maximum run-up (see Chapter 5).

- For wave conditions similar to a design storm with a 1,000 year annual recurrence interval for the Belgian coast (Veale et al., 2012; Verwaest et al., 2011) and a model geometry comparable to the Belgian coast (shallow water and mild foreshore conditions), the maximum measured impact force in prototype was $\sim$19 kN/m (see Chapter 5).

- Reviewing existing semi-empirical approaches and using the large-scale impact force measurements revealed a scattered prediction of F_1 based on the incoming bore thickness η and velocity u. A most accurate prediction was achieved with Equation 2.11 (Robertson et al., 2011). A prediction for F_2

was derived from hydrostatic theory, using the maximum run-up $R_{h,max}$ of the bore at the wall. After fitting the coefficient 0.5 from hydrostatic theory was changed to 0.32 in Equation 6.8. This also means that only 80% of the maximum run-up $R_{h,max}$ was effectively causing the force on the wall, which has practical implications on the calculation of the overturning moment (see Chapter 6).

- A new six-step statistical prediction methodology was developed. A maximum expected impact force F_m was calculated together with its exceedance probability P_m. The exceedance probability P_m can be interpreted as the probability that F_m will be exceeded for a storm with the hydraulic boundary conditions (h_t, $H_{m0,t}$, $T_{m-1,0,t}$, q) specified together with the structural information (A_c, G_c) in the input parameters (see Chapter 7).

- The shortcomings from previous statistical studies due to small sample sizes were overcome by grouping individual tests into 5 larger samples (S_1-S_5). A sample size of >50 samples resulted in robust statistical analysis. The extreme value Weibull distribution was fitted to the 15% largest impacts of the 5 data-samples S_1-S_5 (see Chapter 6).

- As a part of the new statistical method, a novel empirical link between the maximum impact force F_{max} measured at the dike mounted vertical wall and the average overtopping discharge q over the dike crest was established (see Chapter 6).

- Non-repeatability of maximum overtopping bore-induced impact forces F_{max} and $F_{1/250}$ were estimated from small-scale experiments with a coefficient of variation in the order of 10%. In individual extreme cases a deviation up to 20% for F_{max}, $F_{1/250}$ was observed (see Chapter 4).

- The study of scale-effects revealed a small systematic scale-related shift to higher impact forces in the order of 4%, 9% for F_{max}, $F_{1/250}$ respectively, in the small-scale model. This means, that if a minimum water depth at the dike toe, as well as thickness and velocity of the overtopping flow were maintained, the scale-related uncertainties in the impact force measurements disappeared within the uncertainties related to non-repeatability and model effects (see Chapter 4).

- A number of new measurement approaches and data processing routines were tested. A laser scanner was successfully applied for the first time to monitor bore interaction processes in shallow foreshore conditions. A new method to perform motion tracking was developed to obtain run-up measurements at the wall by tracking the bore leading edge from camera images. A new tool called Impact-Analysis-Toolbox (IAT) was developed for the post-processing of the load cell and pressure sensor signals (see ANNEX E, ANNEX F and Chapter 3).

This concludes the main findings of this thesis. There are still issues to be tackled in order to arrive at a coherent story regarding overtopped bore-induced

impacts on dike mounted vertical walls, in shallow water and mild foreshore conditions. These issues are presented in the following Section as recommendations for future research.

8.2 Recommendations for future research

As the measurement of laboratory impact forces and pressures is highly stochastic further uncertainty studies are recommended to enhance the understanding of the non-repeatability of measured impact loads. Here, a study of repeated 1,000 irregular wave tests for different seed numbers and a range of wave parameters is proposed. Furthermore, to advance the wave generation and wave absorption software to better represent the long wave characteristics in the small-scale model.

The experimental study could be extended to different geometries, such as varying foreshore slopes, to determine its effect on the wave parameters at the dike toe. Furthermore, it is expected that 3D effects of waves attacking from an angle will reduce the measured impact loads, compared to perpendicular 2D wave loading in this study. 3D basin tests could be carried out to prove this.

The measurement and post processing of bore thickness η and velocity u in alternating dry and wet conditions remains a challenge. An advanced study of bore thickness and bore velocity along the promenade should be enabled to further investigate a most reliable measurement location of this parameters and to study their behaviour along the promenade width. Also, parameters such as the bore front slope and its effect on the impact process should be further investigated. Specifically, the impulsive impacts of very short duration at the first impact of the bore tip with the wall are expected to be largely dependent on the bore front slope and need to be further investigated. In order to study the effect of the bore front slope and the bore thickness η and velocity u along the promenade high resolution numerical modelling might be an appropriate tool.

The applicability of the statistical prediction tool presented in this work (see Chapter 7) still needs to be validated, ideally with measurements from a prototype situation. Furthermore, by adding more tests with a small non-dimensional overtopping discharge q^* (around $\sim$1 l/s per m) to the samples S_1 and S_1, the number of data points could be raised to the recommended $\sim$50 for these samples, to arrive at an even more robust fitting. Furthermore, the practicability can be improved by further investigating the relation between exceedance probability P_m and storm duration.

For future studies on scale effects the measurements of air entrainment in both scales, at a location close to the wall where the impact occurs, would be beneficial to judge the difference in flow aeration between different scale models and to further evaluate whether air compression plays a significant role (see Bogaert et al. (2010)). The use of pressure sensors in both scale models is recommended to further study the scale influence on peak impact pressures. Extra intermediate scale models or fully prototype measurements could be used to judge whether the wave impact forces scale linearly and to increase the relative scale difference.

An issue not often discussed but important is the filtering of impact forces and

the reduction of measured impacts due to the filters. Here, a detailed study is proposed to study the effects of the filter settings on the reduction of force peaks, to show which frequencies are responsible for certain parts in the impact force time-series.

Appendix A

Model Geometry 'UGent2' - 'UGent3'

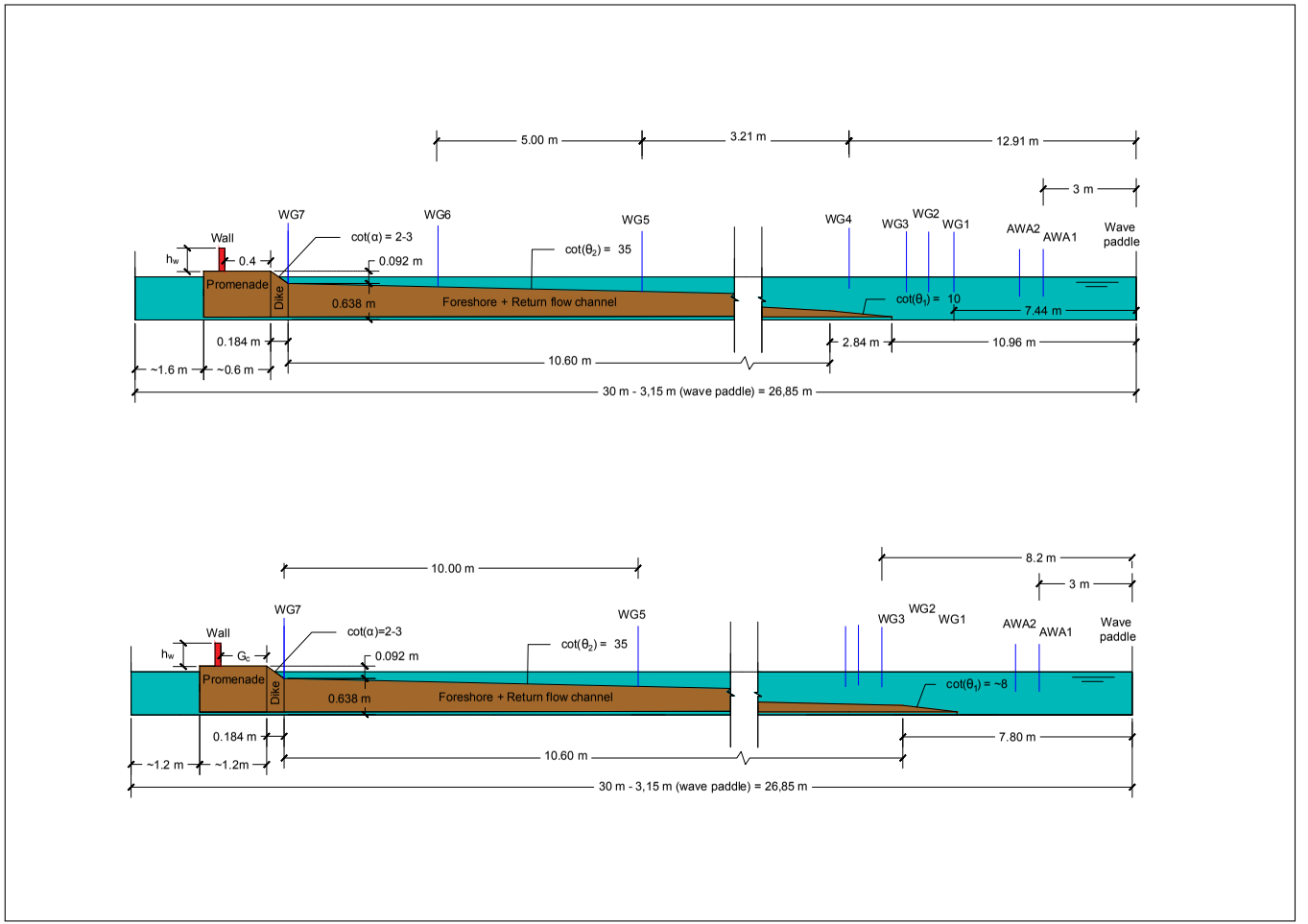

Figure A.1: Geometrical set-up for 'UGent2' (upper figure) and 'UGent3' (lower figure) model to measure impact loads

Appendix B

Wall set-up 'DeltaFlume'

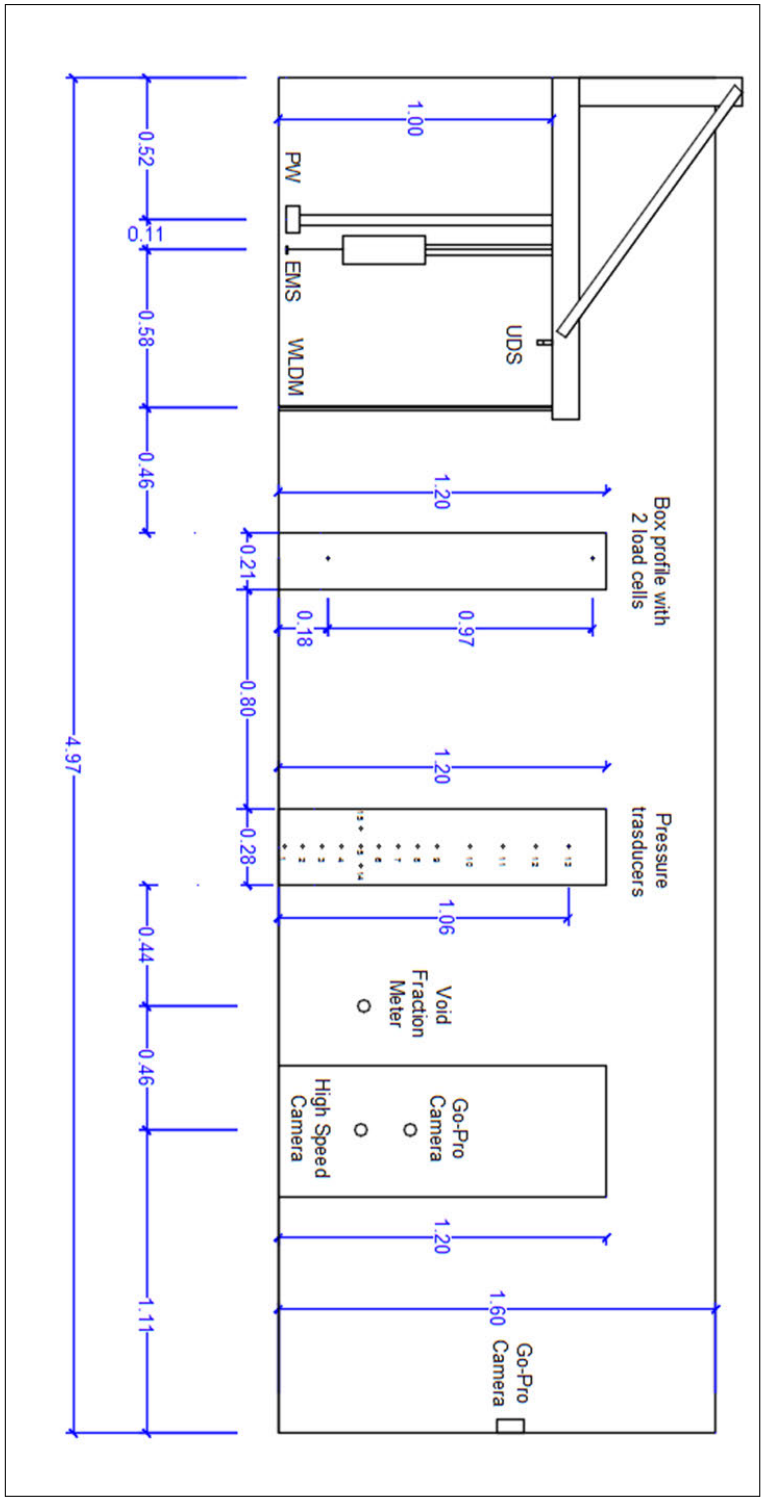

Figure B.1: Wall set-up with measurement devices for the 'DeltaFlume' model tests.

Appendix C

Parameters for testID 492 and testID 500

Table C.1: Details of the 30 highest impacts for testID 492 of the 'DeltaFlume' data-set. Values are in model scale (Froude similarity and length scale factor 1-to-4.3). The bore velocity and thickness were measured at Location 3 (see Section 3.3.3).

Impact nr.	Impact type	Impact force	Bore pattern	Efficient overtopping	Max. thickness	Max. velocity	Max. run-up
[-]	[-]	[kN/m]	[-]	[-]	[m]	[m/s]	[m]
1	quasi-static	4.77	collision	no	0.30	3.43	1.59
2	impulsive	4.25	catch-up	yes	0.31	2.29	1.27
3	quasi-static	4.22	catch-up	yes	0.33	1.53	1.56
4	dynamic	4.20	plunging	yes	0.26	2.46	0.70
5	quasi-static	3.66	collision	no	0.31	1.79	1.03
6	dynamic	3.10	collision	yes	0.26	2.01	1.34
7	quasi-static	2.97	collision	no	0.26	2.68	0.85
8	quasi-static	2.22	collision	no	0.23	3.18	1.17
9	quasi-static	2.39	seq. overtopping	no	0.23	2.45	0.79
10	quasi-static	2.53	collision	yes	0.25	3.50	1.36
11	quasi-static	2.49	collision	no	0.23	1.80	1.06
12	dynamic	2.44	plunging	yes	0.24	3.21	0.86
13	quasi-static	???	catch-up	no	0.23	3.03	0.73
14	quasi-static	2.40	cacth-up	yes	0.46	1.84	1.09
15	quasi-static	2.38	collision	no	0.30	1.25	0.78
16	quasi-static	2.29	collision	no	0.18	3.62	1.06
17	quasi-static	2.26	seq. overtopping	yes	0.20	2.65	0.81
18	dynamic	2.22	catch-up	yes	0.25	2.17	0.77
19	quasi-static	2.20	catch-up	yes	0.16	2.13	0.90
20	impulsive	2.15	seq. overtopping	no	0.21	1.51	0.46
21	quasi-static	2.13	seq. overtopping	no	0.21	2.66	0.96
22	quasi-static	2.12	collision	no	0.11	2.47	0.80
23	dynamic	2.10	plunging	yes	0.21	2.18	0.78
24	quasi-static	2.07	collision	no	0.20	3.35	0.79
25	quasi-static	2.06	collision	no	0.29	1.68	0.96
26	quasi-static	2.06	seq. overtopping	no	0.17	2.02	0.66
27	quasi-static	2.02	catch-up	yes	0.18	3.41	0.94
28	quasi-static	2.00	catch-up	no	0.27	2.62	0.88
29	dynamic	1.97	collision	yes	0.21	2.32	0.92
30	quasi-static	1.96	collision	no	0.22	3.54	0.65

Table C.2: Details of the 30 highest impacts for testID 500 of the 'DeltaFlume' data-set. Values are in model scale (Froude similarity and length scale factor 1-to-4.3). The bore velocity and thickness were measured at Location 3 (see Section 3.3.3).

Impact nr.	Impact type	Impact force	Bore pattern	Efficient overtopping	Max. thickness	Max. velocity	Max. run-up
[-]	[-]	[kN/m]	[-]	[-]	[m]	[m/s]	[m]
1	quasi-static	1.01	regular	no	0.13	2.25	0.58
2	quasi-static	0.82	collision	no	0.17	1.97	0.53
3	dynamic	0.80	catch-up	yes	0.13	2.18	0.46
4	impulsive	0.70	plunging	no	0.05	1.66	0.30
5	dynamic	0.62	collision	yes	0.08	2.03	0.35
6	quasi-static	0.61	seq. overtopping	no	0.19	1.10	0.44
7	quasi-static	0.59	collision	no	0.08	2.23	0.45
8	quasi-static	0.58	collision	no	0.05	1.88	0.43
9	quasi-static	0.51	collision	no	0.18	0.51	0.44
10	impulsive	0.50	collision	no	0.03	1.70	0.20
11	quasi-static	0.49	collision	no	0.12	0.70	0.41
12	quasi-static	0.48	collision	no	0.07	1.74	0.41
13	quasi-static	0.48	regular	no	0.08	2.01	0.43
14	impulsive	0.48	collision	yes	0.09	1.01	0.28
15	quasi-static	0.44	regular	no	0.06	1.92	0.34
16	quasi-static	0.44	collision	no	0.10	1.41	0.35
17	quasi-static	0.44	regular	no	0.04	1.67	0.37
18	impulsive	0.41	catch-up	yes	0.04	1.48	0.30
19	quasi-static	0.40	regular	no	0.04	1.65	0.38
20	impulsive	0.40	seq. overtopping	yes	0.12	n.a.	0.30
21	quasi-static	0.38	collision	no	0.06	2.11	0.33
22	impulsive	0.38	regular	no	0.04	1.71	0.31
23	quasi-static	0.36	collision	no	0.08	2.68	0.30
24	quasi-static	0.35	regular	no	0.06	1.66	0.32
25	quasi-static	0.35	collision	no	0.07	1.25	0.30
26	impulsive	0.32	seq. overtopping	no	0.08	1.33	0.24
27	dynamic	0.32	regular	no	0.06	1.46	0.27
28	quasi-static	0.31	collision	no	0.10	1.65	0.31
29	quasi-static	0.31	regular	no	0.05	1.65	0.33
30	quasi-static	0.30	collision	no	0.06	1.65	0.32

Appendix D

Sensitivity Sample Size S_1, S_2, S_3, S_5

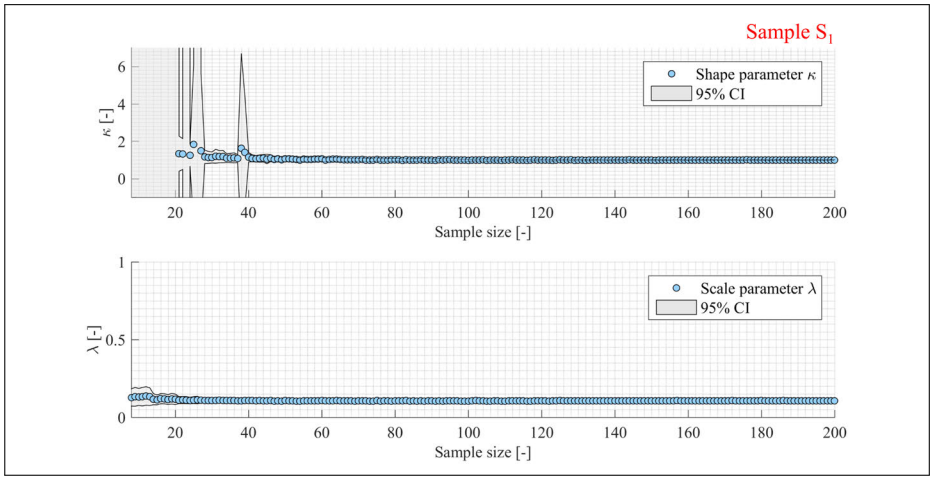

Figure D.1: Sensitivity of shape κ and scale λ parameter in dependence of sample size n. Data sample S_1 was chosen for investigation (Table 7.1). The shape κ and scale λ parameter were plotted together with the 95% confidence interval.

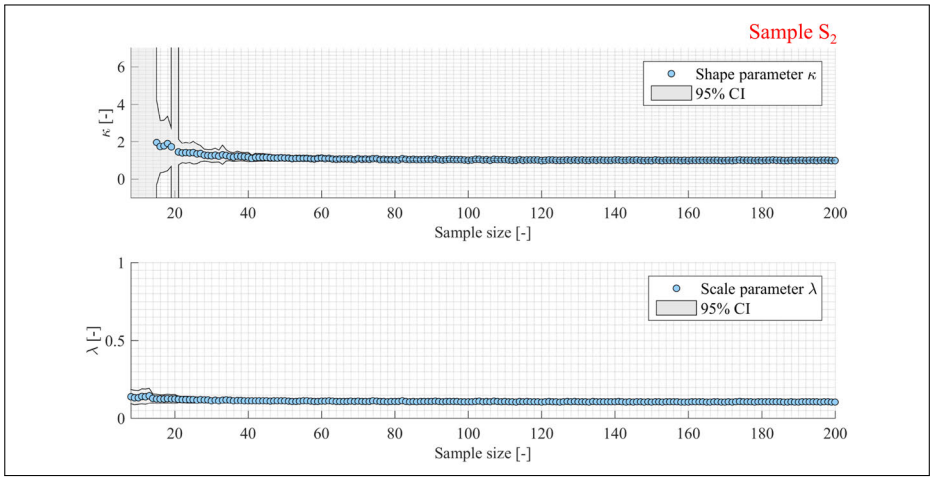

Figure D.2: Sensitivity of shape κ and scale λ parameter in dependence of sample size n. Data sample S_2 was chosen for investigation (Table 7.1). The shape κ and scale λ parameter were plotted together with the 95% confidence interval.

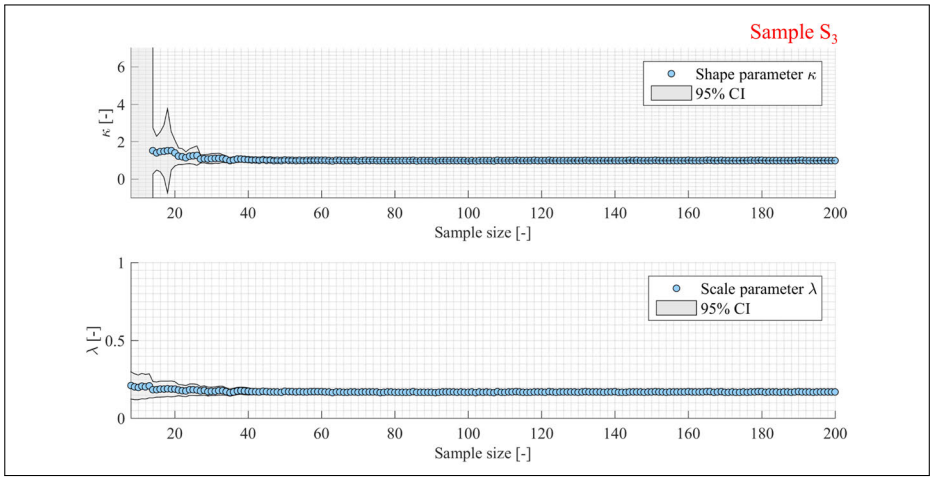

Figure D.3: Sensitivity of shape κ and scale λ parameter in dependence of sample size n. Data sample S_3 was chosen for investigation (Table 7.1). The shape κ and scale λ parameter were plotted together with the 95% confidence interval.

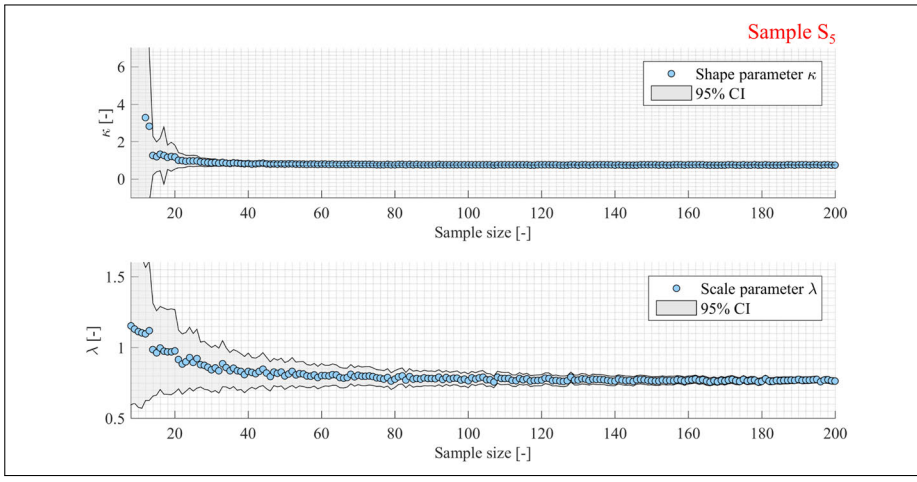

Figure D.4: Sensitivity of shape κ and scale λ parameter in dependence of sample size n. Data sample S_5 was chosen for investigation (Table 7.1). The shape κ and scale λ parameter were plotted together with the 95% confidence interval.

Appendix E

Impact-Analysis-Toolbox (IAT) - Load cell

First script: Load cell signal filtering

```
%%%%%%%%%%%%%%%%%%%%%%%%%%%%%%%%%%%%%%%%%%%%%%%%%%%%%%%%%%%%%%%%%%%%%%%%%%%%%%%
% Date: 11/05/2017
% Author: Maximilian Streicher, Phd student Ghent University.
% Email: Maximilian.Streicher@UGent.be (str.max1@gmx.de)
%
% Script: Filtering of force signals obtained with load cells
%%%%%%%%%%%%%%%%%%%%%%%%%%%%%%%%%%%%%%%%%%%%%%%%%%%%%%%%%%%%%%%%%%%%%%%%%%%%%%%
%
%
%
%% MANUAL USER INPUT

clc; close all; clear all;

dir = '.\Input\Force\';  % input directory
file = '040A_008A.lvm';  % input .txt file with load cell signals (nr. of
% colums equals the number of load cells)
file = char(file);
skiprows = 23; % rows to skip at the beginning of the input file
skipcol = 1; % colums to skip at the beginning of input file
del =  '\t'; % delimiter in input file. space: ' ', tab: 't'
fs = 1000; % sampling frequency of load cell signals [Hz]
hpf = 0; % high pass filter [Hz]. Set to 0 if no high pass filter is used
lpf = 70; % low pass filter [Hz]. Set to 0 if no low pass filter is used
lbpf = [35 80]; % lower boundaries of bandpass filters [Hz].
% Set to 0 if no bandwidth filter is used
ubpf = [70 100]; % upper boundaries of bandpass filters [Hz].
% Set to 0 if no bandwidth filter is used
noise = [0.15 0.15]; % upper noise boundary for each load cell signal.
% All values below the upper noise boundary will be used to calculate the
% polynomial fit through the data in order to do the zero correction of the signal
bf = 4; % order of butterworth filter

%% LOAD DATA

in = dlmread([dir file],del,skiprows,skipcol); % read in data from file
time = (0:1/fs:(length(in)-1)/fs)';  % generate time vector
```

```
%% FILTERING

for i = 1:size(in,2) % go over each load cell individually

% REMOVE DRIFT WITH DETREND
detrY = detrend(in(:,i)); % removes the best straight-line fit from the signal

% REMOVE DRIFT WITH POLYNOMIAL BEST-FIT
idx = find(detrY<=noise(i)); % find values below the upper noise level to generat
% polynomial best-fit line, in order to correct for non-linear drift in the signal
yint = interp1(time(idx),detrY(idx),time);
[p,s,mu] = polyfit(time(idx),detrY(idx),20); % fit polynomial best-fit line
% through selected data
f_y = polyval(p,time,[],mu); % calculate values for best-fit line
noDrift = detrY-f_y; % remove the polynomia best-fit line from the signal

% COMPUTE SPECTRUM FOR COMPARISON
[P,F] = pwelch(noDrift,fs*100,(fs/2)*100,fs*500,fs); % compute spectrum using
% pwelch function in Matlab for visualisation purposes

% FILTERING IN FREQUENCY DOMAIN
X_mags = fft(noDrift); % Fourier transformation
num_bins = length(X_mags); % number of bins

bin_vals = 0 : num_bins-1; % x-vector
fax_Hz = (bin_vals*fs/num_bins); % convert bins into frequencies
N = floor(num_bins/2); % half of the spectrum only

psdx = (1/(fs*num_bins)) * abs(X_mags).^2; % caculate power spectral density
NY = fs/2; % nyquist frequency, half the sampling frequency


% FILTERING
FIL = noDrift;

% low pass filter
if lpf ~= 0
[b a] = butter(bf,lpf/NY,'low'); % low pass butterworth filter design
R1 = freqz(b,a,N); % frequency response butterworth filter
FIL = filtfilt(b,a,FIL); % filtering
clear a b
end

% high pass filter
if hpf ~= 0
[b a] = butter(bf,hpf/NY,'high'); % high pass butterworth filter design
R2 = freqz(b,a,N); % frequency response butterworth filter
FIL = filtfilt(b,a,FIL); % filtering
clear a b
end

% bandwidth filter
R3 = [];
if ubpf ~= 0
for cnt = 1:length(ubpf)
[b a] = butter(bf,[lbpf(cnt) ubpf(cnt)]/NY,'stop'); % bandwidth butterworth
% filter design
tmp = freqz(b,a,N); % frequency response butterworth filter
FIL = filtfilt(b,a,FIL); % filtering
R3 = cat(2,R3,tmp);
clear a b tmp
end
end


%% VISUALIZE OUTPUT

% plot of time series from measured pressure sensor signal
f1 = figure('units','normalized','outerposition',[0 0 1 1]);
```

```
hold on; grid on;
plot(time,in(:,i),'-k');
set(gca,'FontSize',24);
xlabel('Time [s]');ylabel('Force [kN]');
title('Raw data: Force signal');
legend('Time series measured force','FontSize',24);
hold off;

% plot of frequency spectrum
f2 = figure('units','normalized','outerposition',[0 0 1 1]);
hold on; grid on;
leg(1) = plot(fax_Hz(3:N),psdx(3:N)./max(psdx(3:N)),'-b');m% plot spectrum
% computed with fft function
txt{1} = 'FFT spectrum';
leg(2) = plot(F(3:end),P(3:end)./max(P(3:end)),'-r'); % plot spectrum
% computed with Pwelch function
txt{2} = 'PWelch spectrum';
ct = 3;  % initialise counter
if lpf ~= 0  % low pass filter
leg(ct) = plot(fax_Hz(1:N),abs(R1),'-k'); % plot frequency response
txt{ct} = 'Low-pass filter';
ct = ct + 1;
end
if hpf ~= 0   % high pass filter
leg(ct) = plot(fax_Hz(1:N),abs(R2),'.-k');  % plot frequency response
txt{ct} = 'High-pass filter';
ct = ct + 1;
end
if ubpf ~= 0
for cnt = 1:length(ubpf)
leg(ct) = plot(fax_Hz(1:N),abs(R3(:,cnt)),':k'); % plot frequency response
txt{ct} = 'Bandwidth filter';
end
end
set(gca,'FontSize',24);
xlabel('Frequency [Hz]');ylabel('Normalized magnitude [-]');
title('Frequency domain');
legend(leg,txt,'FontSize',24);
axis([0 200 0 1.2]);
hold off;

% plot of time series of signal after each filter step
f3 = figure('units','normalized','outerposition',[0 0 1 1]);
hold on; grid minor;
plot(time,in(:,i),'-','Color',[0.5 0.5 0.5]); % original signal
plot(time,detrY,'-','Color',[1 0 0]);  % after applying Matlab detrend function
plot(time,noDrift,'-','Color',[0 1 0]); % after removing polynomial best-fit ine
plot(time,f_y,'-','Color',[0.5 0 0]); % best-fit polynom
plot(time,FIL,'-','Color',[0 0 1]); % after FFT filtering
set(gca,'FontSize',24);
xlabel('Time [s]'); ylabel('Force [kN]');
title(file);
legend('1. Measured signal', '2. After removing best-fit straight line',...
'3. After removing polynomial best-fit line', '4. Polynomia best-fit line',...
'5. After FFT-filtering','After time average','FontSize',24);
hold off;

%% SAVE OUTPUT

fileID = fopen([savename 'Loadcell_' num2str(i)...
'_filtered.txt'],'w'); % save filtered time series
fprintf(fileID,'%s\t%s\n','Time [s]',['Loadcell_' num2str(i) ' [kN]']);
fprintf(fileID,'%.8f\t%.8f\n',cat(1,time',FIL'));
fclose(fileID);

fileID = fopen([savename 'Loadcell_' num2str(i)...
'_Metadata.txt'],'w');  % save meta data
fprintf(fileID,'%s\t%s\n','original file:',file);
fprintf(fileID,'%s\t%s\n','sample frequency [Hz]:',num2str(fs));
```

```
fprintf(fileID,'%s\t%s\n','high-pass filter [Hz]:',num2str(hpf));
fprintf(fileID,'%s\t%s\n','low-pass filter [Hz]:',num2str(lpf));
fprintf(fileID,'%s\t%s\n','bandwidth filter [Hz]:',...
[num2str(lbpf) '-' num2str(ubpf)]);
fprintf(fileID,'%s\t%s\n','noise [Hz]:',...
[num2str(noise(1)) ',' num2str(noise(2))]);
fprintf(fileID,'%s\t%s\n','filter design:',['butterworth = ' num2str(bf)]);
fprintf(fileID,'%s\t%s\n','force unit:','kN');
fclose(fileID);

savefig(f1,['.\Output\Force\Loadcell_' num2str(i) '_measured.fig']); % save figures
savefig(f2,['.\Output\Force\Loadcell_' num2str(i) '_spectrum.fig']);
savefig(f3,['.\Output\Force\Loadcell_' num2str(i)...
'_postprocessing steps.fig']);

close all;
end
```

Second script: Load cell signal summation

```
%%%%%%%%%%%%%%%%%%%%%%%%%%%%%%%%%%%%%%%%%%%%%%%%%%%%%%%%%%%%%%%%%%%%%%%%%%%%%%%
% Date: 09/05/2017
% Author: Maximilian Streicher, Phd student Ghent University.
% Email: Maximilian.Streicher@UGent.be (str.max1@gmx.de)
%
% Script: calculate the sum of load cells and force per unit width
%%%%%%%%%%%%%%%%%%%%%%%%%%%%%%%%%%%%%%%%%%%%%%%%%%%%%%%%%%%%%%%%%%%%%%%%%%%%%%%
%
%
%
%% MANUAL USER INPUT

clc; clear all; close all;

dir = '.\Output\Force\'; % input directory
skiprows = 1; % rows to skip at the beginning of the input file
skipcol = 1; % colums to skip at the beginning of input file
del = '\t'; % delimiter in input file. space: ' ', tab: 't'
width = 0.1; % width of the force unit measurement plate for each load cell [m]
fs = 1000; % sample frequency
nr = 1; % number of load cells attached to the same measurement plate

%% LOAD DATA

for i = 1:1

nr = i;

Sens = dlmread([savename 'Loadcell_' num2str(nr) '_filtered.txt'],del,...
skiprows,skipcol);
% preallocation of matrix

time = (0:1/fs:(length(Sens)-1)/fs)'; % generate time vector

%% CALCULATION

Sens_sum = sum(Sens,2)./width./1000; % calculate the sum of all load
% cell measurements and convert number to meter unit width [kN/m]

%% VISUALISATION

f1 = figure('units','normalized','outerposition',[0 0 1 1]);
grid minor; hold on;
plot(time,Sens_sum,'-k');
set(gca,'FontSize',24);
```

```
xlabel('Time [s]'); ylabel('Force [kN/m]');
legend('Total force','FontSize',24);
hold off;


%% SAVE OUTPUT

fileID = fopen([savename 'Total_force_Loadcell_' num2str(nr) '.txt'],'w');
% save time series of total impact force
fprintf(fileID,'%s\t%s\n','Time [s]','Total force [kN/m]');
fprintf(fileID,'%.8f\t%.8f\n',cat(1,time',Sens_sum'));
fclose(fileID);

savefig(f1,[dir 'Total_force_Loadcell_' num2str(nr) '.fig']);  % save figure


end
```

Third script: Load cell signal peak detection

```
%%%%%%%%%%%%%%%%%%%%%%%%%%%%%%%%%%%%%%%%%%%%%%%%%%%%%%%%%%%%%%%%%%%%%%%%%%%%%%%
% Date: 09/05/2017
% Author: Maximilian Streicher, Phd student Ghent University.
% Email: Maximilian.Streicher@UGent.be (str.max1@gmx.de)
%
% Script: Peak detection method for total force from loadcells
%%%%%%%%%%%%%%%%%%%%%%%%%%%%%%%%%%%%%%%%%%%%%%%%%%%%%%%%%%%%%%%%%%%%%%%%%%%%%%%
%
%
%
%% MANUAL USER INPUT

% clc; clear all;
close all;

dir = '.\Output\Force\';  % input directory
skiprows = 1; % rows to skip at the beginning of the input file
skipcol = 0; % colums to skip at the beginning of input file
del =  '\t'; % delimiter in input file. space: ' ', tab: 't'
fs = 1000; % sampling frequency of load cell signals [Hz]
sel = 0.00037; % minimum magnitude difference between two consecutive
% detected peaks [kN/m]
hpt = 0.00037; % high pass threshold [kN/m]
dt = 0.83; % minimum time between impacts [s]
addpath('C:\Program Files\Matlab\ResearchR2015b\toolbox\peakfinder');
% add toolboxpath
nr = 1;

%% LOAD DATA

for k = 1:1


nr = k;

Sens = dlmread([savename '\Total_force_Loadcell_' num2str(nr) '.txt'],del,...
skiprows,skipcol); % read in force data from file

%% PEAK DETECTION

[peakLoc peakMag] = peakfinder(Sens(:,2), sel, hpt, 1, 1);
% use Matlab peakfinder toolbox to find peaks.
% 1 stands for maxima and second 1 for including the endpoints

cnt = 1;
```

```
X = zeros(length(peakLoc),1);
Y = zeros(length(peakLoc),1);

for i = 1:length(peakLoc)

window = peakLoc(i)-dt*1000:1:peakLoc(i); % filter values which are
% too close in time
n = find(ismember(peakLoc,window)==1);

if length(n) == 1 % check if only 1 peak was detected in the range of dt
X(cnt,1)=peakLoc(n);
Y(cnt,1)=peakMag(n);
cnt = cnt+1;

else
[mx I] = max(peakMag(n));  % check backwards if the last entrance in
% X and Y is part of the same impact and maybe overwrite

if peakMag(n(I)) >= Y(cnt-1)
X(cnt-1,1)=peakLoc(n(I));
Y(cnt-1,1)=peakMag(n(I));
else
end
end

end

Sens_events = [Sens(X(Y>=hpt),1) Y(Y>=hpt)]; % high pass threshold


%% VISUALISATION

f1 = figure('units','normalized','outerposition',[0 0 1 1]);
hold on; grid minor;
plot(Sens(:,1),Sens(:,2),'-','Color',[0 0 0]);
plot(Sens_events(:,1),Sens_events(:,2),'ob','MarkerSize',15);
set(gca,'FontSize',24);
xlabel('Time [s]'); ylabel('Force [kN/m]');
title(file);
legend({'Total force','Peak event'},...
'FontSize',24,'Location','NorthWest');


%% SAVE OUTPUT

fileID = fopen([savename 'Events_Loadcell_' num2str(nr) '.txt'],'w');
% save peak events
fprintf(fileID,'%s\t%s\n','Time [s]','Events [kN/m]');
fprintf(fileID,'%.8f\t%.8f\n',cat(1,Sens_events(:,1)',Sens_events(:,2)'));
fclose(fileID);

fileID = fopen([savename 'Metadata_Loadcell_' num2str(nr) '.txt'],'w');
% save meta data
fprintf(fileID,'%s\t%s\n','high pass threshold [kN]:',num2str(hpt));
fprintf(fileID,'%s\t%s\n','min. difference in magnitude between 2...
consecutive impacts [kN/m]:',num2str(sel));
fprintf(fileID,'%s\t%s\n','min. time difference between 2...
detected impacts [s]:', num2str(dt));
fprintf(fileID,'%s\t%s\n','force unit:','kN/m');
fclose(fileID);

savefig(f1,[dir 'Events_Loadcell_' num2str(nr) '.fig']);  % save figure

end
```

Appendix F

Impact-Analysis-Toolbox (IAT) - Pressure sensor

First script: Pressure sensor signal filtering

```
%%%%%%%%%%%%%%%%%%%%%%%%%%%%%%%%%%%%%%%%%%%%%%%%%%%%%%%%%%%%%%%%%%%%%%%%%%%%%%%
% Date: 11/05/2017
% Author: Maximilian Streicher, Phd student Ghent University.
% Email: Maximilian.Streicher@UGent.be (str.max1@gmx.de)
%
% Script: Filtering of pressure sensor signals
%%%%%%%%%%%%%%%%%%%%%%%%%%%%%%%%%%%%%%%%%%%%%%%%%%%%%%%%%%%%%%%%%%%%%%%%%%%%%%%
%
%
%
%% MANUAL USER INPUT

clc; clear all; close all;

dir = '.\Input\Pressure\'; % input directory
file = '#Bi_02_6_DR00x15-1kHz.asc'; % input .txt file with pressure sensor signals
% (nr. of colums equals the number of pressure sensors)
skiprows = 1; % rows to skip at the beginning of the input file
skipcol = 0; % colums to skip at the beginning of input file
del = '␣'; % delimiter in input file. space: ' ', tab: 't'
fs = 1000; % sampling frequency of pressure sensor signals [Hz]
hpf = 0; % high pass filter [Hz]. Set to 0 if no high pass filter is used
lpf = 48; % low pass filter [Hz]. Set to 0 if no low pass filter is used
lbpf = []; % lower boundaries of bandpass filters [Hz].
% Set to 0 if no bandwidth filter is used
ubpf = []; % upper boundaries of bandpass filters [Hz].
% Set to 0 if no bandwidth filter is used
noise = [-0.009 -0.004 -0.002 -0.0007 0.0015 0.0005 0.0005 0.0005 0.001...
0.001 0.0005 0.0005 0.001 0.0002 0.0003];
% upper noise boundary for each pressure sensor signal. All values below the
% upper noise boundary will be used to calculate the polynomial fit through
% the data in order to do the zero correction of the signal

bf = 4; % order of butterworth filter

%% LOAD DATA

in = dlmread([dir file],del,skiprows,skipcol); % read in pressure data from file
time = (0:1/fs:(length(in)-1)/fs)'; % generate time vector
```

```
%% FILTERING

for i = 1:size(in,2) % go over each pressure sensor individually

% REMOVE DRIFT
detrY = detrend(in(:,i)); % removes the best straight-line fit from
% the signal

idx = find(detrY<=noise(i)); % find values below the upper noise
% level to generat polynomial best-fit line, in order to correct
% for non-linear drift in the signal
[p,s,mu] = polyfit(time(idx),detrY(idx),22);
% fit polynomial best-fit line through selected data
f_y = polyval(p,time,[],mu); % calculate values for best-fit line
noDrift = detrY-f_y; % remove the polynomia best-fit line from the signal

% COMPUTE SPECTRUM FOR COMPARISON
[P,F] = pwelch(noDrift,fs*100,(fs/2)*100,fs*100,fs); % compute spectrum using
% pwelch function in Matlab for visualisation purposes

% FILTERING IN FREQUENCY DOMAIN
X_mags = fft(noDrift); % Fourier transformation
num_bins = length(X_mags); % number of bins

bin_vals = 0 : num_bins-1; % x-vector
fax_Hz = (bin_vals*fs/num_bins); % convert bins into frequencies
N = floor(num_bins/2); % half of the spectrum only

psdx = (1/(fs*num_bins)) * abs(X_mags).^2; % caculate power spectral density
NY = fs/2; % nyquist frequency, half the sampling frequency


% FILTERING
FIL = noDrift;

% low pass filter
if lpf ~= 0
[b a] = butter(bf,lpf/NY,'low'); % low pass butterworth filter design
R1 = freqz(b,a,N); % frequency response butterworth filter
FIL = filtfilt(b,a,FIL); % filtering
clear a b
end

% high pass filter
if hpf ~= 0
[b a] = butter(bf,hpf/NY,'high'); % high pass butterworth filter design
R2 = freqz(b,a,N); % frequency response butterworth filter
FIL = filtfilt(b,a,FIL); % filtering
clear a b
end

% bandwidth filter
R3 = [];
if ubpf ~= 0
for cnt = 1:length(ubpf)
[b a] = butter(bf,[lbpf(cnt) ubpf(cnt)]/NY,'stop');
% bandwidth butterworth filter design
tmp = freqz(b,a,N); % frequency response butterworth filter
FIL = filtfilt(b,a,FIL); % filtering
R3 = cat(2,R3,tmp);
clear a b tmp
end
end


%% VISUALIZE OUTPUT

% plot of time series from measured pressure sensor signal
```

```
f1 = figure('units','normalized','outerposition',[0 0 1 1]);
hold on; grid on;
plot(time,in(:,i),'-k');  % plot raw data signal
set(gca,'FontSize',24);
xlabel('Time [s]');ylabel('Pressure [bar]');
title('Raw data: Pressure signal');
legend('Time series measured pressure','FontSize',24);
hold off;

% plot of frequency spectrum
f2 = figure('units','normalized','outerposition',[0 0 1 1]);
hold on; grid on;
leg(1) = plot(fax_Hz(3:N),psdx(3:N)./max(psdx(3:N)),'-b');
% plot spectrum computed with fft function
txt{1} = 'FFT spectrum';
leg(2) = plot(F(3:end),P(3:end)./max(P(3:end)),'-r');
% plot spectrum computed with Pwelch function
txt{2} = 'PWelch spectrum';
ct = 3;  % initialise counter
if lpf ~= 0 % low pass filter
leg(ct) = plot(fax_Hz(1:N),abs(R1),'-k'); % plot frequency response
txt{ct} = 'Low-pass filter';
ct = ct + 1;
end
if hpf ~= 0  % high pass filter
leg(ct) = plot(fax_Hz(1:N),abs(R2),'.-k'); % plot frequency response
txt{ct} = 'High-pass filter';
ct = ct + 1;
end
if ubpf ~= 0
for cnt = 1:length(ubpf)
leg(ct) = plot(fax_Hz(1:N),abs(R3(:,cnt)),':k'); % plot frequency response
txt{ct} = 'Bandwidth filter';
end
end
set(gca,'FontSize',24);
xlabel('Frequency [Hz]');ylabel('Normalized magnitude [-]');
title('Frequency domain');
legend(leg,txt,'FontSize',24);
axis([0 lpf+30 0 1.2]);
hold off;

% plot of time series of signal after each filter step
f3 = figure('units','normalized','outerposition',[0 0 1 1]);
hold on; grid minor;
plot(time,in(:,i),'-','Color',[0 0 0]); % original signal
plot(time,detrY,'-','Color',[1 0 0]); % after applying Matlab detrend function
plot(time,noDrift,'-','Color',[0 1 0]); % after removing polynomial best-fit ine
plot(time,f_y,'-','Color',[0 0.5 0]); % best-fit polynom
plot(time,FIL,'-','Color',[0 0 1]); % after FFT filtering
set(gca,'FontSize',24);
xlabel('Time [s]'); ylabel('Pressure [bar]');
title('Time series after each post-processing step');
legend('1. Measured signal', '2. After removing best-fit straight line',...
'3. After removing polynomial best-fit line', '4. Polynomia best-fit line',...
'5. After FFT-filtering','FontSize',24);
hold off;

%% SAVE OUTPUT

fileID = fopen(['.\Output\Pressure\Sensor_' num2str(i)...
'_filtered.txt'],'w'); % save filtered time series
fprintf(fileID,'%s\t%s\n','Time [s]',['Sensor' num2str(i) ' [bar]']);
fprintf(fileID,'%.8f\t%.8f\n',cat(1,time',FIL'));
fclose(fileID);

fileID = fopen(['.\Output\Pressure\Sensor_' num2str(i)...
'_Metadata.txt'],'w');  % save meta data
fprintf(fileID,'%s\t%s\n','original file:',file);
```

```
fprintf(fileID,'%s\t%s\n','sample frequency [Hz]:',num2str(fs));
fprintf(fileID,'%s\t%s\n','high-pass filter [Hz]:',num2str(hpf));
fprintf(fileID,'%s\t%s\n','low-pass filter [Hz]:',num2str(lpf));
fprintf(fileID,'%s\t%s\n','bandwidth filter [Hz]:',...
[num2str(lbpf) '-' num2str(ubpf)]);
fprintf(fileID,'%s\t%s\t%s\t%s\t%s\t%s\t%s\t%s\t%s\t%s\t%s\t%s\t%s\t%s...
\t%s\t%s\n','noise [Hz]:',num2str(noise));
fprintf(fileID,'%s\t%s\n','filter design:','butterworth');
fprintf(fileID,'%s\t%s\n','pressure unit:','bar');
fclose(fileID);

savefig(f1,['.\Output\Pressure\Sensor_' num2str(i) '_measured.fig']);
% save figures
savefig(f2,['.\Output\Pressure\Sensor_' num2str(i) '_spectrum.fig']);
savefig(f3,['.\Output\Pressure\Sensor_' num2str(i)...
'_postprocessing steps.fig']);

close all;

end
```

Second script: Pressure sensor signal integration

```
%%%%%%%%%%%%%%%%%%%%%%%%%%%%%%%%%%%%%%%%%%%%%%%%%%%%%%%%%%%%%%%%%%%%%%%%%%%%%%%
% Date: 11/05/2017
% Author: Maximilian Streicher, Phd student Ghent University.
% Email: Maximilian.Streicher@UGent.be (str.max1@gmx.de)
%
% Script: Integration of pressure sensors to obtain a force value
%%%%%%%%%%%%%%%%%%%%%%%%%%%%%%%%%%%%%%%%%%%%%%%%%%%%%%%%%%%%%%%%%%%%%%%%%%%%%%%
%
%
%
%% MANUAL USER INPUT

clc; clear all; close all;

dir = '.\Output\Pressure\'; % input directory
skiprows = 1; % rows to skip at the beginning of the input file
skipcol = 1; % colums to skip at the beginning of input file
del = '\t'; % delimiter in input file. space: ' ', tab: 't'
fs = 1000; % sampling frequency of pressure sensor signals [Hz]
Loc = [0.02 0.07 0.07 0.07 0.07 0.07 0.07 0.07 0.07 0.12 0.12 0.12 0.12];
% distance between pressure sensors in meters (starting from bottom)

%% LOAD DATA

Sens1 = dlmread([dir 'Sensor_1_filtered.txt'],del,skiprows,skipcol);
% preallocation of matrix
Sens = zeros(length(Sens1),length(Loc));

for i = 1:1:length(Loc)
Sens(:,i) = dlmread([dir 'Sensor_' num2str(i) '_filtered.txt'],...
'\t',skiprows,skipcol); % read in data from file
end

time = (0:1/fs:(length(Sens)-1)/fs)'; % generate time vector

%% RECTANGULAR INTEGRATION

Int = Sens(:,1).*(Loc(1)+Loc(2)/2); % first sensor above bottom

for i = 2:length(Loc)-1
tmp = Sens(:,i).*(Loc(i)/2+Loc(i+1)/2); % integration of pressure sensors
Int = Int + tmp;
```

```
end

tmp = Sens(:,end).*(Loc(i+1)/2); % upper sensor
Int = (Int + tmp).*100.*1; % conversion to kN/m (1 Bar = 100 kN/m)

%% VISUALISATION

f1 = figure('units','normalized','outerposition',[0 0 1 1]);
grid minor; hold on;
plot(time,Int,'-k');
set(gca,'FontSize',24);
xlabel('Time [s]'); ylabel('Force [kN/m]');
legend('Integrated pressure','FontSize',24);
hold off;

%% SAVE OUTPUT

fileID = fopen([dir '\Integrated_pressures.txt'],'w');
% save time series after integration
fprintf(fileID,'%s\t%s\n','Time [s]','Integrated Pressure [kN/m]');
fprintf(fileID,'%.8f\t%.8f\n',cat(1,time',Int'));
fclose(fileID);

savefig(f1,[dir 'Integrated_pressures.fig']); % save figure
```

First script: Pressure sensor signal peak detection

```
%%%%%%%%%%%%%%%%%%%%%%%%%%%%%%%%%%%%%%%%%%%%%%%%%%%%%%%%%%%%%%%%%%%%%%%%%%%%%%%
% Date: 11/05/2017
% Author: Maximilian Streicher, Phd student Ghent University.
% Email: Maximilian.Streicher@UGent.be (str.max1@gmx.de)
%
% Script: Peak detection method for integrated pressures
%%%%%%%%%%%%%%%%%%%%%%%%%%%%%%%%%%%%%%%%%%%%%%%%%%%%%%%%%%%%%%%%%%%%%%%%%%%%%%%
%
%
%
%% MANUAL USER INPUT

clc; clear all; close all;

dir = '.\Output\Pressure\'; % input directory
skiprows = 1; % rows to skip at the beginning of the input file
skipcol = 0; % colums to skip at the beginning of input file
del = '\t'; % delimiter in input file. space: ' ', tab: 't'
fs = 1000; % sampling frequency of pressure sensor signals [Hz]
sel = 0.02; % minimum magnitude difference between two consecutive
%  detected peaks [kN/m]
hpt = 0.02; % high pass threshold [kN/m]
dt = 2; % minimum time between impacts [s]
addpath('C:\Program Files\Matlab\ResearchR2015b\toolbox\peakfinder');
% add toolboxpath

%% LOAD DATA

Sens = dlmread([dir '\Integrated_pressures.txt'],del,skiprows,skipcol);
% read in integrated pressure data from file

%% PEAK DETECTION

[peakLoc peakMag] = peakfinder(Sens(:,2), sel, hpt, 1, 1);
% use Matlab peakfinder toolbox to find peaks. 1 stands for
% maxima and second 1 for including the endpoints

cnt = 1;
```

```
X = zeros(length(peakLoc),1);
Y = zeros(length(peakLoc),1);

for i = 1:length(peakLoc)

window = peakLoc(i)-dt*1000:1:peakLoc(i);
% filter values which are too close in time
n = find(ismember(peakLoc,window)==1);

if length(n) == 1 % check if only 1 peak was detected in the range of dt
X(cnt,1)=peakLoc(n);
Y(cnt,1)=peakMag(n);
cnt = cnt+1;

else
[mx I] = max(peakMag(n)); % check backwards if the last entrance in X and
% Y is part of the same impact and maybe overwrite

if peakMag(n(I)) >= Y(cnt-1)
X(cnt-1,1)=peakLoc(n(I));
Y(cnt-1,1)=peakMag(n(I));
else
end
end

end

Sens_events = [Sens(X(Y>=hpt),1) Y(Y>=hpt)]; % high pass threshold


%% VISUALISATION

f1 = figure('units','normalized','outerposition',[0 0 1 1]);
hold on; grid minor;
plot(Sens(:,1),Sens(:,2),'-','Color',[0 0 0]);
plot(Sens_events(:,1),Sens_events(:,2),'ob','MarkerSize',15);
set(gca,'FontSize',24);
xlabel('Time [s]'); ylabel('Force [kN/m]');
legend({'Integrated pressure','Peak event'},...
'FontSize',24,'Location','NorthWest');


%% SAVE OUTPUT

fileID = fopen([dir 'Events.txt'],'w'); % save peak events
fprintf(fileID,'%s\t%s\n','Time [s]','Events [kN/m]');
fprintf(fileID,'%.8f\t%.8f\n',cat(1,Sens_events(:,1)',Sens_events(:,2)'));
fclose(fileID);

fileID = fopen([dir 'Metadata.txt'],'w'); % save meta data
fprintf(fileID,'%s\t%s\n','high pass threshold [kN]:',num2str(hpt));
fprintf(fileID,'%s\t%s\n','min. difference in magnitude between 2...
 consecutive impacts [kN/m]:',num2str(sel));
fprintf(fileID,'%s\t%s\n','min. time difference between 2...
 detected impacts [s]:', num2str(dt));
fprintf(fileID,'%s\t%s\n','force unit:','kN/m');
fclose(fileID);

savefig(f1,[dir 'Events.fig']);  % save figure
```

References

Allsop, N. W. H., Bruce, T., Pearson, J., Franco, L., Burgon, J., and Ecob, C. (2004). Safety under wave overtopping - how overtopping processes and hazards are viewed by the pyblic. In *29th International conference on coastal engineering (ASCE)*, pages 1–12.

Altomare, C., Suzuki, T., Chen, X., Verwaest, T., and Kortenhaus, A. (2016). Wave overtopping of sea dikes with very shallow foreshores. *Coastal Engineering*, 116:236–257.

Altomare, C., Verwaest, T., Suzuki, T., and Trouw, K. (2015). Characterization of wave impacts on curve faced storm return walls within a stilling wave basin concept. In *34th International Conference on Coastal Engineering, Proceedings*, pages 1–12.

Andersen, T. L., Burcharth, H., and Gironella, X. (2011). Comparison of new large and small scale overtopping tests for rubble mound breakwaters. *Coastal Engineering*, 58(4):351 – 373.

Arnason, H. (2005). *Interactions between an incident bore and a free-standing coastal structure*. PhD thesis, University of Washington, Seattle.

Arnason, H., Petroff, C., and Yeh, H. (2009). Tsunami bore impingement onto a vertical columns. *Journal of Disaster Research*, 4:391–403.

Asakura, R., Iwase, K., Ikeya, T., Takao, M., Kaneto, T., Fujii, N., and Ohmori, M. (2002). The tsunami wave force acting on land structures. In *Proceedings of the 28th International Conference on Coastal Engineering, ASCE*, pages 1191–1202.

Bellotti, G., Van Doorslaer, K., Romano, A., Baelus, L., Caceres, I., De Rouck, J., and Franco, L. (2014). Forces on (flood)walls and buildings by wave overtopping. In *Hydralab IV Joint User meeting*, pages 1–10. Hydralab.

Blenkinsopp, C. and Chaplin, J. (2011). Void fraction measurements and scale effects in breaking waves in freshwater and seawater. *Coastal Engineering*, 58(5):417 – 428.

Blenkinsopp, C. E. and Chaplin, J. R. (2007). Void fraction measurements in breaking waves. *Proceedings of the Royal Society A: Mathematical, Physical and Engineering Sciences*, 463(2088):3151–3170.

Blenkinsopp, C. E., Turner, I. L., Allis, M. J., L., P. W., and E., G. L. (2012). Application of lidar technology for measurement of time-varying free-surface profiles in laboratory wave flume. *Coastal Engineering*, 68:1–5.

Bogaert, H., Léonard, S., Brosset, L., and Kaminski, M. (2010). Sloshing and scaling: Results from the sloshel project. In *20th International offshore and polar engineering conference (ISOPE)*, pages 88–97.

Bredmose, H., Bullock, G., and Hogg, A. (2015). Violent breaking wave impacts. part 3. effects of scale and aeration. *Journal of Fluid Mechanics*, 765:82–113.

Bredmose, H., Peregrine, D., and Bullock, G. (2009). Violent breaking wave impacts. part 2: modelling the effect of air. *Journal of Fluid Mechanics*, 641:389–430.

Buckingham, E. (1914). On physically similar systems; illustrations of the use of dimensional equations. *Physical Review*, 4:345–376.

Bullock, G., Obhrai, C., Peregrine, D., and Bredmose, H. (2007). Violent breaking wave impacts. part 1: Results from large-scale regular wave tests on vertical and sloping walls. *Coastal Engineering*, 54(8):602–617.

Bullock, G. N., Crawford, A. R., Hewson, P. J., Walkden, M. J. A., and Bird, P. A. D. (2001). The influence of air and scale on wave impact pressures. *Coastal Engineering*, 42(4):291–312.

Burcharth, H. and Andersen, T. (2009). Scale effects related to small physical modelling of overtopping of rubble mound breakwaters. In Franco, L., Tomasicchio, G., and Lamberti, A., editors, *Coastal Structures 2007*, pages 1532–1541. World Scientific.

Camfield, F. (1991). Wave forces on wall. *Journal of Waterways, Ports, Coastal and Ocean Engineering*, 177(1):76 – 79.

Cappietti, L., Simonetti, I., Esposito, A., Streicher, M., Scheres, B., Schüttrumpf, H., Hirt, M., Hofland, B., and Chen, X. (2018). Large-scale experiments of wave-overtopping loads on walls: Layer thicknesses and velocities. In *37th International conference on ocean, offshore and arctic engineering (OMAE)*, pages 1–6.

Chen, X. (2011). Hydrodynamic loads on buildings caused by overtopping waves. Master's thesis, TU Delft, Delft, The Netherlands.

Chen, X. (2016). *Impacts of overtopping waves on buildings on coastal dikes*. PhD thesis, TU Delft.

Chen, X., Altomare, C., Suzuki, T., and Uijttewaal, W. (2015). Forces on a vertical wall on a dike crest due to overtopping flow. *Coastal Engineering*, 95:94–104.

Chen, X., Hassan, W., Uijttewaal, W., Verwaest, T., Verhagen, H. J., Suzuki, T., and Jonkman, S. (2012). Hydrodynamic load on the building caused by overtopping waves. In *33rd International conference on coastal engineering (ICCE)*, pages 1–11.

Chen, X., Hofland, B., Altomare, C., and Uijttewaal, W. (2014). Overtopping flow impact on a vertical wall on a dike crest. In *34th International conference on coastal engineering (ICCE)*, pages 1–10.

Chen, X., Hofland, B., and Uijttewaal, W. (2016). Maximum overtopping forces on a dike-mounted wall with a shallow foreshore. *Coastal Engineering*, 116:89 – 102.

Chen, X., Jonkman, S. N., Pasterkamp, S., Suzuki, T., and Altomare, C. (2017). Vulnerability of buildings on coastal dikes due to wave overtopping. *Water*, 9(6).

Cross, R. (1967). Tsunami surge forces. *Journal of the Waterways and Harbors Division*, 93(4):201–231.

Cumberbatch, E. (1960). The impact of a water wedge on a wall. *Journal of Fluid Mechanics*, 7:353–374.

Cuomo, G., Allsop, W., and Takahashi, S. (2010). Scaling wave impact pressures on vertical walls. *Coastal Engineering*, 57(6):604–609.

De Rouck, J., Geeraerts, J., Troch, P., Kortenhaus, A., Pullen, T., and Franco, L. (2005). New results on scale effects for wave overtopping at coastal structures. In Allsop, N., editor, *Proceedings of ICE Coastlines, Structures and Breakwaters*, pages 29–43. Thomas Telford.

De Rouck, J., Van Doorslaer, K., Versluys, T., Ramachandran, K., Schimmels, S., Kudella, M., and Trouw, K. (2012). Full scale impact tests of an overtopping bore on a vertical wall in the large wave flume (gwk) in hannover. In *33rd International conference on coastal engineering (ICCE)*.

Den Heijer, F. (1998). Gofloverslag en krachten op verticale waterkeringsconstructies. Technical report, Rijkswaterstaat, Dienst Weg- en Waterbouwkunde, Delft, The Netherlands.

DHI Water & Environment (2003). *DHI Wave Amplifier Type 102E User Manual*. Horsholm, Denmark.

Endoh, K. and Takahashi, S. (1994). Numerically modeling personnel danger on a promenade breakwater due to overtopping waves. *Coastal Engineering Proceedings*, 1(24).

Eurotop (2016). *EurOtop 2016. Manual on wave overtopping of sea defences and related structures*.

FEMA (2000). *Coastal construction manual*. Washington DC, USA.

Frigaard, P. and Brorsen, M. (1995). A time-domain method for seperating incident and feflected irregular waves. *Coastal Engineering*, 24:205–215.

Frigaard, P. and Christensen, M. (1994). An absorbing wave-maker based on digital filters. In *Proceedings of the 24th International Conference on Coastal Engineering (ICCE)*, pages 168–180.

Frostick, L., McLelland, S., and T., M. (2011). *User guide to physical moelliong and experimentation: experience of the HYDRALAB network*. CRC Press/Balkema.

Fujima, K., Achmad, F., Shigihara, Y., and Mizutani, N. (2009). Estimation of tsunami force acting on rectangular structures. *Journal of Disaster Research*, 4:404–409.

Gallach Sánchez, D. (2018). *Experimental Study of Wave Overtopping Performance of Steep Low-Crested Structures*. PhD thesis, Ghent University.

Geeraerts, J., Boone, C., De Rouck, J., Kortenhaus, A., Van Damme, L., and Franco, L. (2005). Hazards from wave overtopping: field measurements on the zeebrugge breakwater. In *Proceedings ICS 2005 Second International Coastal Symposium*, page 14. Viggósson G.

Ghent University (2010). Wave flume manual. Technical report, Departement of Civil Engineering, Ghent University, Ghent, Belgium.

Goda, Y. (2010). *Random seas and design of maritime structures*. Advance series on ocean engineering 33. World Scientific.

Gruwez, V., Altomare, C., Suzuki, T., Streicher, M., Troch, P., Kortenhaus, A., and Cappietti, L. (2019). Validation of three open-source cfd models to large-scale experiments of wave impacts on sea dikes with a shallow foreshore. *To be defined*, -(-):–.

Gruwez, V., Vandebeek, I., Kisacik, D., Streicher, M., Altomare, C., Suzuki, T., Verwaest, T., Kortenhaus, A., and Troch, P. (2018). 2D overtopping and impact experiments in shallow foreshore conditions. *Coastal Engineering Proceedings*, 1(36):67.

Heller, V. (2011). Scale effects in physical hydraulic engineering models. *Journal of Hydraulic Research*, 49(3):293–306.

Higuera, P. (2017). olaflow: Cfd for waves. doi.org/10.5281/zenodo.1297013.

Hirt, M. (2017). Analyse wellenüberlauf-induzierter druckkräfte an auf seedeichen positionierten hochwasserschutzmauern. Master's thesis, RWTH Aachen, Aachen, Germany.

Hofland, B., Chen, X., Altomare, C., and Oosterlo, P. (2017). Prediction formula for the spectral wave period Tm-1,0 on mildly sloping shallow foreshores. *Coastal Engineering*, 123:21–28.

Hofland, B., Diamantidou, E., van Steeg, P., and Meys, P. (2015). Wave runup and wave overtopping measurements using a laser scanner. *Coastal Engineering*, 106:20 – 29.

Hofland, B., Wenneker, I., and Van Gent, M. (2013). *Description of the new Delta Flume*, pages 1346–1355. ICE publishing.

Hughes, S. (1995). *Physical models and laboratory techniques in coastal engineering*. Advanced series on ocean engineering 7. World Scientific.

Hughes, S. (2015). Hydraulic parameters of individual overtopping wave volumes. Technical report, Engineering Research Center, Colorado State University, Fort Collins, USA.

Hughes, S., Thornton, C., Van der Meer, J., and Scholl, B. (2012). Improvements in describing wave overtopping processes. In *Proceedings 33rd International conference on coastal engineering (ICCE)*.

Hughes, S. A. (2004a). Estimation of wave run-up on smooth, impermeable slopes using the wave momentum flux parameter. *Coastal Engineering*, 51(11):1085 – 1104.

Hughes, S. A. (2004b). Wave momentum flux parameter: a descriptor for nearshore waves. *Coastal Engineering*, 51(11):1067 – 1084.

IPCC (2014). Climate change 2014: Synthesis report. contribution of working groups i, ii and iii to the fifth assessment report of the intergovernmental panel on climate change. Technical report, IPCC, Geneva, Switzerland.

James, G., Witten, D., Hastie, T., and Tibshirani, R. (2013). *An introduction to statistical learning: with applications in R*. Springer, New York, USA.

Kihara, N., Niida, Y., Takabatake, D., Kaida, H., Shibayama, A., and Miyagawa, Y. (2015). Large-scale experiments on tsunami-induced pressure on a vertical tide wall. *Coastal Engineering*, 99:46 – 63.

Klammer, P., Kortenhaus, A., and Oumeraci, H. (1996). Wave impact loading of vertical face structures for dynamic stability analysis- prediction formulae. In *25th International conference on coastal engineering (ICCE)*.

Kleidon, P. (2004). Modelluntersuchungen zum wellenüberlauf eines geschütteten wellenbrechers und zur überlaufinduzierten gefährdung von personen auf kronenbauwerken. Master's thesis, TU Braunschweig, Braunschweig, Germany.

Ko, H. T.-S. and Yeh, H. (2018). On the splash-up of tsunami bore impact. *Coastal Engineering*, 131:1–11.

Kolkman, P. (1984). Consideration about the accuracy of discharge relations of hydraulic structures and the use of scale models for their calibration. In *Symposium on scale effects in modelling hydraulic structures*.

Kortenhaus, A., Gallach Sanchez, D., Streicher, M., Hohls, C., Trouw, K., Altomare, C., Suzuki, T., Thoon, D., Troch, P., and De Rouck, J. (2017). Wave-induced loads on coastal sea walls. In *Coastal structures and solutions to coastal disaster joint conference*, pages 1–7.

Kortenhaus, A. and Oumeraci, H. (1998). Classification of wave loading on monolithic coastal structures. In *26th International conference on coastal engineering (ICCE)*, pages 867–880.

Kortenhaus, A. and Oumeraci, H. (1999). Scale effects in modelling wave impact loading of coastal structures. In *Hydralab-workshop on experimental research and synergy effects with mathematical models*, page 10.

Kortenhaus, A., Oumeraci, H., Geeraerts, J., De Rouck, J., Medina, J., and González-Escrivá, J. (2004). Laboratory effects and further uncertainties associated with wave overtopping measurements. In *Proceedings of the 29th international conference on coastal engineering (ICCE)*, pages 4456–4468.

Larsen, B. E. and Fuhrman, D. R. (2018). On the over-production of turbulence beneath surface waves in reynolds-averaged navier–stokes models. *Journal of Fluid Mechanics*, 853:419 – 460.

Larsen, B. E., Fuhrman, D. R., and Roenby, J. (2019). Performance of interfoam on the simulation of progressive waves. *Coastal Engineering Journal*, 61(3):380–400.

Lubin, P. and Chanson, H. (2016). Are breaking waves, bores, surges and jumps the same flow? *Environmental Fluid Dynamics*, 17(1):47 – 77.

Lykke Andersen, T. and Frigaard, P. (2010). Lecture notes for the course in water wave mechanics. Technical report, Dept. of Civil Engineering, Aalborg University, Aalborg, Denmark.

Mansard, E. and Funke, E. (1980). The measurement of incident and reflected spectra using a least squares method. In *Proceedings of 32nd international conference on coastal engineering*, pages 154–169.

Marinov, K. K. (2017). Wave impacts on storm walls. a study on scale effects. Master's thesis, TU Delft, The Netherlands.

Martin, F. L., Losada, M. A., and Medina, R. (1999). Wave loads on rubble mound breakwater crown walls. *Coastal Engineering*, 37(2):149 – 174.

Masselink, G., Castelle, B., Scott, T., Dodet, G., Suanez, S., Jackson, D., and Floc'h, F. (2016). Extreme wave activity during 2013/2014 winter and morphological impacts along the atlantic coast of europe. *Geophysical Research Letters*, 45.

Mertens, T., DeWolf, P., Verwaest, T., Trouw, K., De Nocker, L., and Couderé, K. (2009). An integrated master plan for flanders future coastal safety. In *31st international conference on coastal engineering (ICCE)*, pages 4017–4028.

Oumeraci, H., Klammer, P., and Partenscky, H. (1993). Classification of breaking wave loads on vertical structures. *Journal of Waterway, Port, Coastal, and Ocean Engineering*, 119(4):381–397.

Oumeraci, H., Schüttrumpf, H., Sauer, W., Möller, J., and Droste, T. (2000). Physical model tests on wave overtopping with natural sea states. LWI-Bericht 852, TU Braunschweig.

Prandtl, L. (1904). Über Flüssigkeitsbewegungen bei sehr kleiner Reibung. In *3. Internationaler Mathematikerkongress*, pages 484–491.

Ramachandran, K., Genzalez, R. R., Oumeraci, H., Schimmels, S., Kudella, M., Van Doorslaer, K., De Rouck, J., Versluys, T., and Trouw, K. (2012). Loading of vertical walls by overtopping bores using pressure and force sensors- a large scale model study. In *33rd International conference on coastal engineering (ICCE)*, pages 1–15.

Ramsden, J. (1993). Tsunamis: Forces on a vertical wall caused by long waves, bores, and surges on a dry bed, report no. kh-r-54. Technical report, W.M. Keck Laboratory, California Institute of Technology.

Ramsden, J. D. (1996). Forces on a vertical wall due to long waves, bores and dry-bed surges. *Journal of Waterway, Port, Coastal, and Ocean Engineering*, 122(3):134–141.

Reynolds, O. (1883). An experimental investigation of the circumstances which determine whether the motion of water shall be direct or sinuous, and the law of resistance in parallel channels. In *Royal Society*, pages 874–99.

Robertson, I., Paczkowski, K., Riggs, H., and Mohamed, A. (2011). Tsunami bore forces on walls. In *Proceedings of the International Conference on Offshore Mechanics and Arctic Engineering - OMAE*.

Roeber, V. and Bricker, J. D. (2015). Destructive tsunami-like wave generated by surf beat over a coral reef during typhoon haiyan. *Nature Communications*, 6:1–9.

Romano, A., Bellotti, G., Briganti, R., and Franco, L. (2015). Uncertainties in the physical modelling of the wave overtopping over a rubble mound breakwater: The role of the seeding number and of the test duration. *Coastal Engineering*, 103:15–21.

Ruessink, G., Michallet, H., Bonneton, P., Mouazé, D., Lara, J., Silva, P., and Wellens, P. (2013). *Proceedings Coastal Dynamics*, chapter Globex: wave dynamics on a gently sloping laboratory beach, pages 1351–1362. Utrecht University.

Saponieri, A., Di Risio, M., Pasquali, D., Valentini, N., Aristodemo, F., Tripepi, G., Celli, G., Streicher, M., and Damiani, L. (2018). Beach profile evolution in front of storm seawalls: a physical and numerical study. In *36th International conference on coastal engineering (ICCE)*, pages 1–13.

Schüttrumpf, H. (2001). *Wellenüberlaufströmung an Seedeichen - Experimentelle und theoretische Untersuchungen*. PhD thesis, TU Braunschweig.

Schüttrumpf, H. and Oumeraci, H. (2005). Layer thicknesses and velocities of wave overtopping flow at seadikes. *Coastal Engineering*, 52(6):473–495.

Stolle, J., Takabatake, T., Nistor, I., Mikami, T., Nishizaki, S., Hamano, G., Ishii, H., Shibayama, T., Goseberg, N., and Petriu, E. (2018). Experimental investigation of debris damming loads under transient supercritical flow conditions. *Coastal Engineering*, 139:16–31.

Streicher, M., Hofland, B., and Lindenbergh, R. (2013). Laser ranging for monitoring water waves in the new Deltares Delta Flume. In *ISPRS Annual photogrammetry remote sensing spatial informatione science*, pages 1–6, Antalya, Turkey.

Streicher, M., Kortenhaus, A., Altomare, C., Gruwez, V., Hofland, B., Chen, X., Marinov, K., Scheres, B., Schüttrumpf, H., Hirt, M., Cappietti, L., Esposito, A., Saponieri, A., Valentini, N., Tripepi, G., Pasquali, D., Di Risio, M., Aristodemo, F., Damiani, L., Willems, M., Vanneste, D., Suzuki, T., Klein Breteler, M., and Kaste, D. (2017). WALOWA (wave loads on walls) : Large-scale experiments in the Delta Flume. In *International short course and conference on applied coastal research*, pages 69–80.

Streicher, M., Kortenhaus, A., Gruwez, V., Hofland, B., Chen, X., Hughes, S., and Hirt, M. (2018). Prediction of dynamic and quasi-static impacts on vertical sea walls caused by an overtopped bore. In *36th International conference on coastal engineering (ICCE)*, pages 1–15.

Streicher, M., Kortenhaus, A., Gruwez, V., Suzuki, T., Altomare, C., Saponieri, A., Pasquali, D., Valentini, N., Tripepi, G., Celli, D., Di Risio, M., Aristodemo, F., Damiani, L., Cappietti, L., Klein Breteler, M., and Kaste, D. (2019a). Overtopped wave loads on walls (WALOWA) - Numerical and physical modelling of large-scale experiments in the delta flume. In *Proceedings of the Hydralab+ Joint User Meeting*, pages 1–10.

Streicher, M., Kortenhaus, A., and Hohls, C. (2016). Analysis of post overtopping flow impacts on a vertical wall at the belgian coast. In *Coastlab 2016*, page 10.

Streicher, M., Kortenhaus, A., Marinov, K., Hirt, M., Hughes, S., Hofland, B., Scheres, B., and Schüttrumpf, H. (2019b). Classification of bore patterns induced by storm waves overtopping a dike crest and their impact types on dike mounted vertical walls – A large-scale model study. *Coastal Engineering Journal*, pages 1–19.

Suzuki, T., Altomare, C., Veale, W., Verwaest, T., Trouw, K., Troch, P., and Zijlema, M. (2017). Efficient and robust wave overtopping estimation for impermeable coastal structures in shallow foreshores using swash. *Coastal Engineering*, 122:108–123.

Suzuki, T., Altomare, C., Verwaest, T., Trouw, K., and Zijlema, M. (2015). Two-dimensional wave overtopping calculation over a dike in shallow foreshore by swash. In *Proceedings of the 34th International Conference on Coastal Engineering*, pages 1–1.

Suzuki, T., Verwaest, T., Hassan, W., W., V., Reyns, J., and Trouw, K. (2011). The applicability of swash model for wave transformation and wave overtopping: A case study for the flemish coast. In *Proceedings of the 5th international conference on advanced computational methods in engineering (ACOMEN 2011)*, pages 1–12, Liege, Belgium.

Tanimoto, K., Tsuruya, H., and Nakano, S. (1984). Experimental study of tsunami force and investigation of the cause of sea wall damage during 1983 nihonkai chubu earthquake. In *Proceedings 31st Japanese Conference Coastal Engineering*, pages 257–261, Liege, Belgium.

UNEP (2006). Marine and coastal ecosystems and human well- being: A synthesis report based on the findings of the millenium ecosystem assessment. Technical report, United Nations Environment Programm (UNEP) annual report.

U.S. Army Corps of Engineers (2002). *Coastal Engineering Manual, 1110-2-1110*. U.S. Army Corps of Engineers, Washington, D.C.

Van Der Meer, J., Hardeman, B., and Steendam, G. (2010). Flow depth and velocities at crest and landward slope of a dike, in theory and with the wave overtopping simulator. In *Proceedings of 32nd international conference on coastal engineering (ICCE)*, Shanghai, China.

Van Doorslaer, K., De Rouck, J., Van der Meer, J. W., and Trouw, K. (2012). Full scale wave impact tests on a vertical wall using the wave overtopping simulator. Technical report, Ghent University.

Van Doorslaer, K., Romano, A., De Rouck, J., and Kortenhaus, A. (2017). Impacts on a storm wall caused by non-breaking waves overtopping a smooth dike slope. *Coastal Engineering*, 120:93 – 111.

Van Gelder, P., Vrijling, J., and Hewson, P. (2001). *Probabilistic design tools for vertical breakwaters*, chapter Chapter 5.4: Uncertainty analysis of impact waves and scale corrections due to aeration. Balkema, Rotterdam, The Netherlands.

Van Gent, M. (1999a). Physical model investigations on coastal structures with shallow foreshores. Technical report, Delft Hydraulics (Deltares) Report H3608, Delft, The Netherlands.

Van Gent, M. (1999b). Wave run-up and wave overtopping for double peaked wave energy spectra. Technical report, Delft Hydraulics (Deltares) Report H3351-2, Delft, The Netherlands.

Van Gent, M. (2001). Wave runup on dikes with shallow foreshores. *Journal of Waterway, Port, Coastal, and Ocean Engineering*, 127:9.

Van Gent, M. (2015). The new delta flume for large-scale testing. In *36th IAHR World Congress*, pages 1–3.

Veale, W., Suzuki, T., Verwaest, T., Trouw, K., and Mertens, T. (2012). Integrated design of coastal protection works for wenduine, belgium. In *33rd International conference on coastal engineering*, Santander, Spain.

Verwaest, T., Hassan, W., Reyns, J., Balens, N., Trouw, K., Van Doorslaer, K., De Rouck, J., and Troch, P. (2011). Hydrodynamic loading of wave return walls on top of seaside promenades. In *6th International conference on coastal structures*, pages 568–576.

Verwaest, T., Van der Biest, K., Vanpoucke, P., Reyns, J., Vanderkimpen, P., De Vos, L., De Rouck, J., and Mertens, T. (2009). Coastal flooding risk calculations for the belgian coast. In *31st International Conference on Coastal Engineering (ICCE)*, pages 4193–4201.

Victor, L., Van der Meer, J., and Troch, P. (2012). Probability distribution on individual wave overtopping volumes for smooth impermeable steep slopws with low crest freeboards. *Coastal Engineering*, 64:87–101.

Weller, H. G., Tabor, G., Jasak, H., and Fureby, C. (1998). A tensorial approach to computational continuum mechanics using object-oriented techniques. *Computers in Physics*, 12(6).

Wenneker, I., Meesters, J., Hoffmann, R., and Francissen, D. (2013). Active wave absoprtion system arch. In *Proceedings Coastlab 2010*.

Wüthrich, D. (2017). Impact of a dry bed surge against structures with and without openingsh. In *Proceedigns of 37th IAHR world congress*.

Acknowledgements

The work described in this publication was supported by the European Community's Horizon 2020 Research and Innovation Programme through the grant to HYDRALAB-PLUS, Contract no. 654110.